

## **Copper Catalysts**

for Synthesis Gas Conversion

Promoter and Support Effects



## Copper Catalysts for Synthesis Gas Conversion – Promoter and Support Effects

ISBN: 978-94-6423-874-7

DOI: 10.33540/1266

 $\label{lem:composition} Cover design by Thomas Hartman \mid www.this illustrations.com \\ Printed by ProefschriftMaken \mid www.proefschriftmaken.nl$ 

The work described in this thesis was performed in the Materials Chemistry and Catalysis group, which is part of the Debye Institute for Nanomaterials Science, at Utrecht University.

# Copper Catalysts for Synthesis Gas Conversion – Promoter and Support Effects

Koperkatalysatoren voor de conversie van synthesegas – Effecten van promotor en drager

(met een samenvatting in het Nederlands)

#### **Proefschrift**

ter verkrijging van de graad van doctor aan de Universiteit Utrecht op gezag van de rector magnificus, prof.dr. H.R.B.M. Kummeling, ingevolge het besluit van het college voor promoties in het openbaar te verdedigen op

maandag 12 september 2022 des middags te 2.15 uur

door

#### **Remco Dalebout**

geboren op 25 september 1993 te Gorinchem

#### Promotoren:

Prof. dr. P.E. de Jongh

Prof. dr. K.P. de Jong

This research has received funding from the European Research Council (ERC) under the European Union's Horizon 2020 research and innovation program (ERC-2014-CoG, Grant agreement No. 648991)

## **Contents**

Chapter 1	Introduction	1		
Chapter 2	Interplay between carbon dioxide enrichment and zinc oxide promotion of copper catalysts in methanol synthesis	21		
Chapter 3	Insight into the nature of the zinc oxide promoter during methanol synthesis	39		
Chapter 4	Manganese oxide as a promoter for copper catalysts in $CO_2$ and $CO$ hydrogenation	65		
Chapter 5	Exploratory study of the synthesis of bimetallic copper—cobalt catalysts by impregnation and electroless deposition	93		
Summary and	l outlook	117		
Nederlandse	samenvatting	121		
References				
Acknowledgments / Dankwoord				
List of publications and presentations				
Curriculum v	itae	155		

### Chapter 1

## Introduction

#### 1.1 Catalysts

#### 1.1.1 Basic characteristics

When someone has heard of a catalyst before, it has often been explained as a car part that cleans the exhaust gases. However, there are many more types of catalysts used in the industrial production of almost any chemical, ranging from enzymes (biocatalysis) for the production of medicines to solid catalysts for gasoline and plastics production.  $^{1,2}$  A catalyst is in general a substance that is used to accelerate a chemical reaction from starting compound A to desired product B by lowering the activation barrier (**figure 1.1A**), while the substance itself is not consumed.  $^3$  For example, inside the three-way catalytic converter in gasoline-type cars several catalyzed reactions simultaneously occur: hydrocarbons, carbon monoxide (CO), and nitrogen oxides (NO<sub>x</sub>) in the high exhaust stream are converted into the less harmful carbon dioxide (CO<sub>2</sub>), water (H<sub>2</sub>O), and nitrogen gas (N<sub>2</sub>).  $^4$ 

Here, we focus on heterogeneous catalysts, which are solid catalysts used in liquid- or gas-phase reactions. The active compound in heterogeneous catalysts is often a metal (oxide or sulfide).

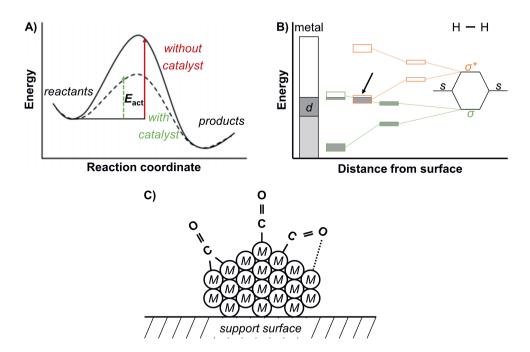


**Figure 1.1** (A) Energy diagram of a catalyzed and non-catalyzed chemical reaction with  $E_{\text{act}}$  representing the activation energy. (B) Transfer of electron density from the d-band of a metal to an anti-bonding orbital of a reactant (here  $\sigma^*$  of an  $H_2$  molecule). Back-donation (as indicated by the arrow) induces bond breaking. Adapted from ref. [3]. (C) Different binding modes of a CO molecule on a metal surface.

Zeolites are another important example of industrially applied heterogeneous catalysts, and they are also used as ion exchangers and molecular sieves in purification processes. These aluminosilicates have microporous channels, which act as molecular sieves, and often are solid acids that can isomerize or crack long-chain hydrocarbons. <sup>3,5</sup>

Reactions only occur on the surface of active catalysts, mostly transition metals, as reactants are activated on those surfaces for subsequent reaction steps by the specific electronic interaction between the metallic surface and the reactant (**figure 1.1B**). The electrons in the half-filled *d*-band of the transition metal are shared with anti-bonding orbitals of the reactant (so-called back-donation), thereby weakening or even breaking the bond in the reactant molecules. The degree of interaction between the reactant and the metal nanoparticle is governed by the extent of electron sharing. This is mainly determined by the active site, the matching between the electronic levels of the reactant and the Fermi level of the transition metal, and the orientation of the adsorbed molecule with respect to the metal surface. <sup>3</sup> For example, a CO molecule can adsorb in a bridging mode with two metal atoms or 'on top' of a surface atom (**figure 1.1C**). These different interactions with the surface lead to a distinct reactivity. <sup>6</sup>

The catalyst activity is greatly enhanced by small particles compared to macrocrystalline solids. As an example, the specific surface area of metal is enlarged a million times when a cube with a size of 1 cm is divided into 10-nm cubes. In these so-called nanomaterials the large specific surface area allows to use a low catalyst volume and mass: important parameters in industrial catalysis. <sup>3</sup>

Three essential aspects for catalysts are activity, selectivity, and stability. Ideally, the catalyst is highly active in producing the desired product, without any byproducts, for an infinite amount of time. The catalyst has a finite lifetime: many thermal, chemical, and mechanical deactivation modes can make the catalyst less active over time. <sup>7–9</sup> At elevated temperatures and pressures the mobility of the metal phase is enhanced, leading to particle growth and hence to a loss of active surface area. Furthermore, irreversible poisoning of the active sites by *e.g.* chloride and sulfur species <sup>10</sup>, but also the reversible oxidation of an active, reduced metal surface by *e.g.* CO<sub>2</sub> or H<sub>2</sub>O in the reaction atmosphere are chemical mechanisms for catalyst activity loss. Another important chemical factor is leaching, for example nickel loss due to gaseous nickel carbonyl formation during CO methanation at high CO partial pressures and low reaction temperatures. <sup>11</sup> Attrition of the catalyst in the reactor and carbon deposition could also (partially) block the porous structure of a catalyst, thereby limiting the access of reactants to reach and products to leave the active site. It is hence key to not only optimize activity and selectivity of a catalyst but simultaneously also the stability.

As nanometer-sized particles have a high surface-to-volume ratio, they are thermodynamically less stable than macrocrystalline solids. <sup>7</sup> Typically, the nanoparticles are deposited on a support to facilitate the preparation of the particles and to minimize their agglomeration and growth. This support is often chemically and thermally robust, such as graphite or silica <sup>12</sup>, but might also play a

significant role in catalyst activity. For example, reducible supports, such as titania and ceria, are known to be involved in the Mars-Van Krevelen reaction mechanism during CO oxidation, in which lattice oxygen is extracted from the support surface by the reactant and replenished by oxygen from the gas feed.  $^{13,14}$ 

#### 1.1.2 Carbon materials as model supports

Metal oxides such as silica, alumina, and zirconia are typical catalyst supports used in industry, because they withstand harsh reaction conditions and the resulting catalysts can be easily shaped into macroscopic bodies. <sup>15</sup> A major hurdle for fundamental investigation with these conventional oxide supports is that many promoter species (advantageous components in the catalyst formulation, discussed in detail in **section 1.4**) strongly interact with the support. <sup>16–18</sup> The great advantage of carbon materials as a support is that the interaction between the promoter species and carbon support is relatively weak <sup>18</sup>, thereby enhancing the intimacy between the metal particles and the promoter. Furthermore, the carbon surface can be modified with oxygen- and/or nitrogencontaining surface groups (**figure 1.2B**), which act can as anchoring points for metal nanoparticles but also as acid-base ligands to the active metal sites altering the catalytic performance. <sup>19–22</sup> Carbon

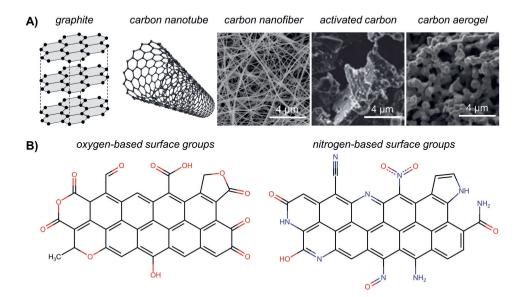


**Figure 1.2** (**A**) Various shapes of carbon materials with electron micrographs of carbon nanofiber, activated carbon and carbon aerogel adapted from refs. [23–25]. (**B**) Surface groups that can be present on carbon, based on ref. [26].

materials have a low density and hence are very suitable for transmission electron microscopy (TEM) and X-ray absorption (XAS) studies in contrast with, for example, titania. Hence, carbonaceous materials facilitate detailed studies of the promoter effects on the catalytic performance of supported metal nanoparticles.

Activated carbon and carbon black are the most important carbon materials from an industrial point of view (>900  $\cdot$  106 kg produced in 2005). <sup>26</sup> Activated carbons are prepared by carbonization of *e.g.* sawdust and coconut shells to charcoal and subsequent activation by steam or CO<sub>2</sub>. The resulting high porosity of the carbon material (up to 1.2 mL g<sup>-1</sup> due to micropores) is highly advantageous for purification purposes and the use as a catalyst support. Carbon blacks consist of amorphous, spherical particles of 10-500 nm in chain-like aggregates and are mainly used in the rubber industry (*ca.* 80%) to improve mechanical properties. <sup>27</sup> Carbon materials exist in many more various shapes, as illustrated in **figure 1.2A**. In academia, carbon nanotubes, nanofibers, and aerogels are frequently used as support materials. <sup>28–31</sup> Ordered mesoporous carbons can be obtained either by nanocasting mesoporous silica materials with dissolved carbon precursors, subsequent carbonization, and removal of the silica hard template, or directly *via* self-assembly processes. <sup>32–34</sup>

A practical advantage of carbonaceous supports is the high stability in acidic and basic solutions compared to silica and alumina. Also deposited precious metals, such as platinum and palladium, can be easily recovered by burning the carbon support. <sup>26,35,36</sup> Another important property of carbon materials is the high electrical conductivity, which is typically employed in fuel cells, electrolyzers, and supercapacitors. <sup>37,38</sup> In literature, carbon materials have been reported to even have a promoting role in the catalyst performance. For example, they might stabilize copper nanoparticles by confinement <sup>20,39–45</sup>, provide hydrogen spillover activity to the active site <sup>46</sup>, or change the activation energy of a reaction <sup>47,48</sup>. Throughout this thesis we extensively use graphitic carbon supports as they are ideal for the synthesis of supported model catalysts. A direct comparison between the use of a carbon and silica support on the catalyst effectiveness of copper in the methanol synthesis was not yet made and is presented in **chapter 3**.

#### 1.1.3 Impregnation as a key preparation method

There are numerous ways to prepare industrial and model catalysts. The industrially most preferred methods to synthesize (supported) metal catalysts is *via* impregnation and precipitation techniques. Precipitation is favored for highly loaded catalysts such as iron-based catalysts for the Haber-Bosch process. <sup>49</sup> The synthesis of supported metals, especially precious metals, is often done by impregnation of macroscopic bodies, as it is facile, low-cost, and fast. <sup>35,36</sup> Emerging laboratory-scale methods for catalyst synthesis include colloidal approaches, atomic layer deposition, and

electroless deposition. <sup>50</sup> In our work we typically used impregnation of fine powders as the main preparation method for catalysts, after which the catalysts are compacted, ground, and sieved into a specific grain size fraction before use.

For impregnation, a porous solid is exposed to a metal precursor solution which enters pores driven by capillary forces. The volume of the impregnation solution is either in excess (in the case of wet impregnation) or equal to the total porosity of the solid (for incipient wetness impregnation). After the impregnation, the material is dried to evaporate (most of) the solvent and to form small crystallites of mixed metal salt species in the pores of on the support. Finally, the dried impregnate is treated at elevated temperatures to transform the metal salt, often via a metal oxide, into metal nanoparticles. For most applications the last activation step involves a treatment of the metal oxide in a reductive atmosphere, such as  $H_2$ , CO, or syngas, to obtain the active metallic state of the nanoparticles.  $^{51-53}$ 

During this three-step procedure (impregnation  $\rightarrow$  drying  $\rightarrow$  activation, as presented in **figure 1.3**) it is key to uniformly deposit the metal precursor over the support surface. Research has shown that separation of the drying and activation steps helps to control the final particle size and redispersion. <sup>54</sup> The pH of the impregnation solution is a critical factor for the deposition of charged precursor complexes. At a pH higher than the point of zero charge (PZC) of the support, the support surface groups are negatively charged and cationic metal precursors such as  $[Pt(H_2O)_4]^{2+}$  adsorb (electrostatic adsorption). Likewise, anionic precursors such as  $[PtCl_4]^{2-}$  can adsorb at the positively charged surface groups at a pH > PZC of the support. However, a more uniform metal distribution can be obtained using an acidified impregnation solution with a lower pH than the PZC of the support surface, thereby enhancing electrostatic repulsion.

If carefully executed, incipient wetness impregnation and subsequent activation lead to a uniform spatial distribution of supported metal nanoparticles with a reasonable particle size control and

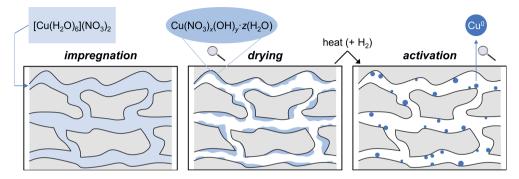


**Figure 1.3** Synthesis of supported nanoparticles by impregnation, drying, and subsequent activation. Salts are formed during drying, which are converted to nanoparticles after activation. Adapted from ref. [53].

moderate metal loadings up to 15 wt%. The metal loadings are limited by the solubility of the metal precursor in the impregnation solution. Incipient wetness impregnation is a relevant method, both industrially and academically, to prepare well-defined, copper-based catalysts.

In the remainder of this introduction, we first discuss several important CO/CO<sub>2</sub> hydrogenation reactions for which copper-based catalysts are being used (**section 1.2**). Subsequently, we discuss why copper is a particularly interesting metal for those reactions in **section 1.3**. The catalytic behavior of supported copper nanoparticles is often enhanced by the intentional addition of other components. How these so-called promoters enhance the catalytic behavior is described in **section 1.4**, both in a general manner and specifically focusing on copper-catalyzed CO/CO<sub>2</sub> hydrogenation.

#### 1.2 Synthesis gas conversion

A combination of H<sub>2</sub> and CO (synthesis gas or syngas), optionally containing some CO<sub>2</sub>, is the basis for the synthesis of a wide range of chemicals, including methanol and gasoline-type compounds. <sup>55,56</sup> It might play an important role in a transition towards a more sustainable society, as syngas can be obtained from alternative resources such as biomass and municipal waste, and its conversion might include direct CO<sub>2</sub> conversion. <sup>57</sup> Syngas is nowadays mainly produced from coal and petroleum residues by steam gasification (**equation (1.1)**). To compensate for the heat consumption due to this endothermic process, heat can be provided by a subsequent highly exothermic oxidation of solid carbon (**equation (1.2)**). At temperatures above 971 K the CO<sub>2</sub> formed during the oxidation reaction is in turn converted to additional CO (**equation (1.3)**), yielding an overall exothermic reaction to an N<sub>2</sub>-diluted, CO-rich syngas ('producer gas', **equation (1.4)**). <sup>58,59</sup> Also steam reforming of natural gas (**equation (1.5)**) <sup>60–62</sup>, gasification of biomass <sup>63</sup>, and simultaneous CO<sub>2</sub>/H<sub>2</sub>O splitting <sup>64</sup> are used or studied to obtain syngas. All carbon gasification processes are typically operated between 1073-1773 K and at *ca.* 30 bar pressure

	$\Delta_{\rm r} H^{\ominus}$ (kJ mol <sup>-1</sup> )	$\Delta_{r}S\Theta$ (J mol-1 K-1)	$\Delta_{\rm r}G\Theta$ (kJ mol-1)	
$C + H_2O \rightleftarrows CO + H_2$	+131	+134	+91.4	(1.1)
$C + O_2 \rightleftarrows CO_2$	-394	+2.88	-394	(1.2)
$C + CO_2 \rightleftarrows 2CO$	+172	+176	+120	(1.3)
$3C + H_2O + O_2 \rightleftarrows 3CO + H_2$	-89.8	+312	-183	(1.4)
$CH_4 + H_2O \rightleftarrows CO + 3H_2$	+206	+215	+142	(1.5)

depending on the carbonaceous resource. Natural gas yields the preferred high syngas purity (and composition) used for methanol synthesis, as the methane-rich source contains much less sulfur impurities (up to 50 ppm) than coal (up to 8,000 ppm). <sup>58,60</sup>

#### 1.2.1 Methanol synthesis

Methanol is a key chemical building block for the production of a wide range of chemicals including formaldehyde, olefins, acetic acid, and dimethyl ether, <sup>65,66</sup> and might play a role in the transition towards a more sustainable economy. <sup>66</sup> The annual methanol production is around 100 million tons, and the demand increases with about 4-5% per year. <sup>65,67,68</sup> Since the 1920's industrial-scale methanol production is based on syngas conversion <sup>69–71</sup>, although alternatives routes such as the direct partial oxidation of methane <sup>72–76</sup>, pure CO<sub>2</sub> hydrogenation <sup>77–81</sup>, and CO<sub>2</sub> electroreduction <sup>82–85</sup> to methanol are being investigated.

Methanol synthesis is generally performed at elevated temperatures (473-573 K) and pressures (40-100 bar), while exposing a  $Cu/ZnO/Al_2O_3$  catalyst to a syngas feed containing a small amount of  $CO_2$ .  $^{86,87}$  The copper (Cu) species are the main active component in this catalyst, while partially reduced zinc oxide ( $ZnO_x$ ) has a promoting function  $^{88,89}$ , and alumina ( $Al_2O_3$ ) plays a role in the structural stability  $^{71,90-92}$ . Characteristic for copper is its high selectivity (typically more than 98%) towards methanol, attributed to its limited ability to dissociate CO and to form C-C bonds, thereby also suppressing carbon deposition as a side product.  $^{39,46,93-97}$ 

The most important reactions occurring during methanol synthesis are the following: 98-102

	$\Delta_{\rm r} H^{\ominus}$ (kJ mol <sup>-1</sup> )	$\Delta_{r}S^{\ominus}$ (J mol <sup>-1</sup> K <sup>-1</sup> )	$\Delta_{\rm r}G^{\ominus}$ (kJ mol <sup>-1</sup> )	
$CO + 2H_2 \rightleftarrows CH_3OH$	-90.5	-219	-25.1	(1.6)
$CO_2 + 3H_2 \rightleftarrows CH_3OH + H_2O$	-49.3	-177	+3.48	(1.7)
$CO + H_2O \rightleftarrows CO_2 + H_2$	-41.1	-42.0	-28.6	(1.8)

Methanol formation from either CO or CO<sub>2</sub> (**equations** (1.6)-(1.7)) is exothermic (negative standard enthalpy of reaction,  $\Delta_r H^{\ominus}$ ). The hydrogenation reactions are entropically unfavorable (negative standard entropy of reaction,  $\Delta_r S^{\ominus}$ ), as reacting gas molecules finish up leading to a lower number of gas molecules. Under standard conditions, the resulting standard Gibbs free energy of reaction ( $\Delta_r G^{\ominus}$ ) is negative with an equilibrium constant  $\ln(K)$  of 4.4 for direct CO hydrogenation (**equation** (1.6)), indicating a thermodynamically favorable reaction at 298 K and 1 bar. However, above 410 K at 1 bar the  $\Delta_r G$  for this reaction becomes positive. Also, the (reverse) water-gas shift (WGS) reaction (**equation** (1.8)) may occur simultaneously with the CO and CO<sub>2</sub> hydrogenation.

To enhance the reaction rate elevated temperatures are typically applied, although this is thermodynamically less favored. Elevated pressures must be applied to drive the equilibria to the right-hand side at higher temperatures. Efficient heat removal and thermal management are needed. <sup>103</sup> **Figure 1.4** shows the CO + CO<sub>2</sub> equilibrium conversion levels as a function of pressure and temperature.

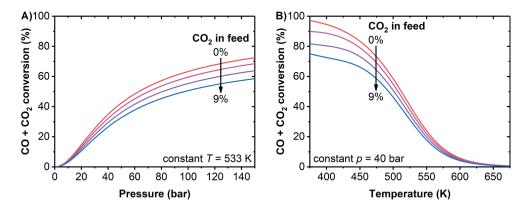


**Figure 1.4** Equilibrium  $CO + CO_2$  conversion levels (**A**) as a function of pressure at constant temperature and (**B**) as a function of temperature at constant pressure. Calculated from **equations (1.6)-(1.8)**, based on references [98–102]. The feed was composed of  $H_2/(CO + CO_2)/He = 60/30/10$  vol% and only MeOH,  $H_2$ , CO,  $H_2O$ ,  $CO_2$ , and He were considered as the possible compounds in the system.

Small amounts of CO<sub>2</sub> (2-6 vol%) are added to the syngas mixture to increase the catalyst activity. <sup>60,94,104–106</sup> It is now generally accepted that CO<sub>2</sub> is the main carbon source for methanol production, although CO hydrogenation is thermodynamically favored over CO<sub>2</sub> hydrogenation. <sup>104,107–109</sup> During methanol formation from CO<sub>2</sub>, H<sub>2</sub>O is formed (**equation (1.7)**), which in turn reacts with CO to generate CO<sub>2</sub> (**equation (1.8)**). In this way the H<sub>2</sub>O concentration in the reactor is low, which also avoids pronounced particle growth. In other words, a certain CO partial pressure must be present, especially at high syngas conversions, to remove H<sub>2</sub>O from the catalyst surface. <sup>106,110</sup> The equilibrium conversion is only slightly lower upon CO<sub>2</sub> enrichment of the feed (**figure 1.4**). Yet in the case of pure CO<sub>2</sub> hydrogenation the methanol formation is often much lower as high H<sub>2</sub>O amounts are produced at the catalyst surface, which are not removed by the WGS reaction (**equation (1.8)**). In fact, the reverse reaction can take place at elevated temperatures, resulting in the formation of additional CO and H<sub>2</sub>O. <sup>77–81</sup> In **chapter 2** we discuss the combined effect of CO<sub>2</sub> in the syngas feed and the catalyst composition on its performance in more detail.

Mechanistically, adsorbed CO<sub>2</sub> (CO<sub>2</sub>\*) is progressively hydrogenated on a Cu(111) surface with H\* *via* strongly bound formate (HCOO\*, -259 kJ mol<sup>-1</sup>) and formic acid (HCOOH\*) before scission of the C–O bond to obtain a hydroxymethoxy group (CH<sub>3</sub>O<sub>2</sub>\*). Subsequently, formaldehyde (CH<sub>2</sub>O\*) and methoxy species (CH<sub>3</sub>O\*) are formed before the final hydrogenation to methanol (CH<sub>3</sub>OH\*). During catalysis the Cu surface is mostly covered with formate species. <sup>111</sup> Also, CO\* can be successively hydrogenated to formyl (HCO\*), *via* formaldehyde, up to methanol. The rate-limiting step is either the formation of the methoxy group or, at high CO<sub>2</sub>-enrichment of the syngas, the final hydrogenation to methanol. <sup>111</sup> It has to noted that the reaction mechanism can change upon the catalyst composition, temperature, pressure, and feed composition, especially in the presence of zinc oxide. <sup>108</sup>

#### 1.2.2 Reverse water-gas shift reaction

Combustion of fossil fuels, mainly coal and natural gas, to produce energy and chemicals concomitantly generates  $CO_2$ , which contributes to global warming. Renewable alternatives are not yet mature enough to completely replace fossil fuels and are not easily incorporated into existing infrastructure. In 2019 the share of renewable energy consumption in the EU was only 18.9% (2.5 out of  $13.4 \cdot 10^6$  GWh). Only about 8.5% ( $1.1 \cdot 10^6$  GWh) of the total consumption of energy resources is used for the production of chemicals, whereas chemical production from renewables is just emerging (<0.1%).  $^{112}$  Capture of low-value  $CO_2$  from flue gasses (for instance in the steel industry) or natural gas and its conversion into high-value chemicals are hence attractive.  $^{113-115}$  The production of CO from  $CO_2$  *via* the reverse water-gas shift (RWGS) reaction (**equation (1.9)**) in excess of  $H_2$  yields syngas, which after drying could be incorporated into the existing infrastructure.  $^{116-120}$ 

$$\Delta_{\rm r} H\ominus ({\rm kJ\ mol^{-1}}) \quad \Delta_{\rm r} S\ominus ({\rm J\ mol^{-1}\ K^{-1}}) \quad \Delta_{\rm r} G\ominus ({\rm kJ\ mol^{-1}})$$
 CO<sub>2</sub> + H<sub>2</sub>  $\rightleftarrows$  CO + H<sub>2</sub>O +41.1 +42.0 +28.6 (1.9)

The RWGS reaction is an endothermic process (positive  $\Delta_r H^{\odot}$  value) and thus requires a constant energy input to proceed. It is performed at a temperature of 523-873 K and pressures of 1-20 bar.  $^{121}$  A typical catalyst consists of highly dispersed and metallic nanoparticles supported on (preferably reducible) metal oxides, such as ceria and titania. Noble metals, such as platinum, palladium, and rhodium, are frequently studied with a CO selectivity near 100%  $^{122-124}$  but are less attractive for commercialization due to their high market prices.

Supported copper particles are an interesting, low-temperature alternative for the RWGS reaction, which also plays a role during methanol synthesis (**section 1.2.1**). Up to date a K-Cu/Al<sub>2</sub>O<sub>3</sub> catalyst (5 wt% K, 17 wt% Cu) is the best-performing catalyst, producing CO with 99% selectivity at 533 K for a wide range of pressures and relatively low conversions (4-100 bar, 5-21% CO<sub>2</sub> conversion). <sup>121</sup> CO production is in competition with methanol formation from CO<sub>2</sub> (**equation (1.7)**) in CO<sub>2</sub>-rich syngas or pure H<sub>2</sub>/CO<sub>2</sub> feeds. The CO selectivity can be tuned by varying the reaction conditions, as methanol production is thermodynamically suppressed at higher temperatures and lower pressures. A main concern is stability as during the reaction H<sub>2</sub>O is formed, which might lead to excessive copper particle growth during operation. <sup>125</sup>

Currently, there are four different reaction mechanisms proposed for the RWGS reaction. Adsorbed CO<sub>2</sub> can either dissociate directly or *via* hydrogenation on a carbon-bound carboxyl (\*HOCO) or formate (\*HCOO) intermediate. Alternatively, the redox mechanism states that metallic Cu reduces CO<sub>2</sub> to CO, while H<sub>2</sub> closes the catalytic cycle by reducing the Cu+ to the metallic form by forming water. The challenge for supported copper catalysts is the balance between the CO selectivity, activity, and stability: elevated temperatures minimize methanol formation and increase the total activity, but both factors have adverse effects on the thermal stability.

#### 1.2.3 Higher alcohol synthesis

Copper-based catalysts have limited activity in C–C bond formation, leading to remarkably high methanol selectivities in syngas conversion. On the other hand, nanosized cobalt and iron surfaces can catalyze the formation of long-chain hydrocarbons *via* Fischer-Tropsch synthesis. Combining these two types of active metals in bimetallic systems could induce the production of long-chain alcohols. The synthesis of these higher alcohols from syngas is summarized in several excellent reviews. <sup>55,126–132</sup>

Alcohols of intermediate length ( $C_2$ - $C_5$ ) are attractive not only as fuels or fuel additives but also for many products such as paints, solvents, and adhesives. Longer-chain alcohols ( $C_{6+}$ ) are applied in the synthesis of detergents and surfactants.  $^{129}$  Nowadays, ethanol (as an important alcohol) is mainly produced by enzymatic fermentation or ethylene hydration, but these processes either interfere with food supplies or depend on oil reserves, respectively.  $^{55,126}$  Yet, no commercialized process with a heterogeneous catalyst for the higher alcohol production from syngas exists today.  $^{133-135}$ 

Next to copper-based catalysts many other catalyst systems are proposed, combining at least two but sometimes even four different active metals. <sup>55,129</sup> Rhodium is the only single metal which is capable to produce ethanol from syngas with reasonable selectivities (up to 54%) alongside with hydrocarbons at a high CO conversion (up to 39%), especially when promoted by manganese

oxides. <sup>136</sup> But due to its very high market price of €431,67 per gram (December 2020) <sup>137</sup> and its moderate activity it is not relevant for this application. Catalysts based on molybdenum sulfide have also been extensively investigated but need high pressures (50-100 bar) and suffer from a high CO<sub>2</sub> selectivity. <sup>128</sup> Efforts were also made to tweak the established Cu/ZnO/Al<sub>2</sub>O<sub>3</sub> methanol synthesis catalysts with base promoters, thereby increasing the selectivity to higher alcohols, but low activity and significant methanol selectivity are bottlenecks for this catalyst type. <sup>55</sup>

Currently, bimetallic copper—(cobalt/iron) based-catalysts are the most promising for the synthesis of long-chain alcohols. This dates back to the 1970's when the Institut Français du Pétrole (IFP) patented several potassium-promoted copper—cobalt (CuCoO<sub>x</sub>) bimetals. <sup>138,139</sup> The original patent claimed a higher alcohol selectivity up to 76% over such catalysts at 523 K and 60 bar during CO/CO<sub>2</sub> hydrogenation. However, catalyst and catalysis reproducibility appeared challenging for commercialization. <sup>133–135</sup> In the following years major efforts were made to understand several preparation parameters during co-precipitation and impregnation. Also, novel procedures to reproducibly stabilize the active CuCoO<sub>x</sub> phase are explored, such as the use of perovskites <sup>140–147</sup>, colloidal synthesis <sup>148–150</sup>, citrate complexation <sup>20,151–156</sup>, oxalate precipitation <sup>157</sup>, deposition-precipitation <sup>158,159</sup>, and variations thereof. The combination of these two metals is also relevant for electro- <sup>160–162</sup> and photocatalysis <sup>163</sup>, liquid-phase oxidation <sup>164,165</sup> and reduction <sup>140,166–170</sup> reactions, and gas-phase reactions such as phenol alkylation <sup>171</sup> and carbon nanotube synthesis <sup>172</sup>.

In our group Prieto  $et\,al.\,^{173}$  found experimentally and computationally that the optimal Cu/(Cu + Co) molar ratio is 0.30-0.35 to obtain a selective production of higher alcohols. The Cu–Co proximity and hence interaction was enhanced by stabilization of the Cu and Co species in a molybdate matrix, leading to a C<sub>2+</sub> alcohol selectivity of  $ca.\,27\%$  at low CO conversions (<2%). **Table 1.1** summarizes some recent CuCo-based catalyst formulations reported in high-impact

catalyst <sup>a</sup>	Cu/(Cu + Co)	H <sub>2</sub> /CO	О Т р	flow	X(%)	S	S (%c) c		ref.	
	molar ratio	ratio	(K)	(bar)	(h-1)	A (70)	C <sub>2+</sub> OH	HC	$CO_2$	_ 1 C1.
K-CuCo/MoO <sub>x</sub>	0.30	1	543	40	N.A.	<2	26.9 d	N.A.	N.A.	[173]
CuCo/N-C*	0.74	1	493	20	4,000	20.4	29.8	38.3	11.7	[20]
$CuCoMnO_x \\$	0.65	2	543	25	7,500	29.7	32.5	51.9	0.4	[174]
CuCo/KIT-6	0.25	2	543	30	9,000 b	83.3	43.5	38.4	1.8	[175]
$CuCoZnAlO_x \\$	0.33	1	553	60	12,000 b	6.0	21.8	28.7	30.0	[176]
$Na$ - $CoMnO_x$ + $CuZnAlZrO_x$	0.43	2	493	60	2,000 b	12.4	50.7	42.6	6.3	[177]

<sup>&</sup>lt;sup>a</sup> N-C = ordered mesoporous nitrogen-doped carbon, KIT-6 = ordered mesoporous silica, last entry = physical mixture. <sup>b</sup> In mL  $g_{cat}$   $^{-1}$  h  $^{-1}$ . <sup>c</sup> C<sub>2+</sub>OH = higher alcohols, HC = hydrocarbons. <sup>d</sup> Without taking CO<sub>2</sub> into account.

journals. Typically, a selectivity between 20-50%c to higher alcohols are reported with hydrocarbons and CO<sub>2</sub> as the main side products. Next to Co-rich catalysts, also Cu-rich catalysts can be selective to higher alcohols. The nature of the active site in these catalysts is far from clear: whereas Das and co-workers claim that only metallic Cu and Co are active <sup>20</sup>, others report that the higher alcohol activity results from a synergy between Cu<sup>+</sup> and Co<sup>0</sup> <sup>174</sup>, a stable Co<sub>2</sub>C/Cu<sup>0</sup> phase <sup>176</sup>, or a Co/Co<sub>2</sub>C interface altered by CO-inserting additives <sup>177</sup>. Computationally, a CuCo(211) stepped surface is selective towards ethanol at temperatures lower than 523 K, while a CuCo(111) close-packed surface has a high selectivity for methanol. <sup>178</sup> In **chapter 5** we report the synthesis of well-defined CuCo catalyst on graphitic carbon and their performance in higher alcohol synthesis.

#### 1.3 Copper as the main ingredient

Copper is a relatively abundant metal on Earth  $^{179}$ , explaining its relatively low cost of  $\mathfrak{C}6.38$  per kg compared to for example platinum ( $\mathfrak{C}29.84$  per gram) and palladium ( $\mathfrak{C}68.48$  per gram) (US market prices in December 2020)  $^{137}$ . The non-precious copper is a frequently used catalyst in the chemical industry, for example as the main component in methanol synthesis catalysts  $^{86.87}$  or as a reduction catalyst in iron-based Fischer-Tropsch catalysts  $^{180}$ .

Nanosized copper has the unique property to adsorb CO molecules with a binding energy (BE) of -83 kJ mol<sup>-1</sup> without breaking the C–O bond but to split H<sub>2</sub> molecules into H\* atoms upon adsorption ( $\Delta E = -28$  kJ mol<sup>-1</sup>). <sup>111</sup> In other words, the copper surface has a limited activity for directly breaking the C–O bond in a CO molecule, which has an activation barrier of +299 kJ mol<sup>-1</sup>. <sup>181</sup> CO<sub>2</sub> is adsorbed weakly onto a Cu(111) surface with a BE of -7.7 kJ mol<sup>-1</sup> and the direct scission of one of the C–O bonds in CO<sub>2</sub> still requires an activation energy of +171 kJ mol<sup>-1</sup>. Yet, by progressive hydrogenation of adsorbed CO<sub>2</sub> *via* formate (HCOO\*) and formic acid (HCOOH\*), the so-called H-assisted pathway, the C–O bond in formic acid can be split on a Cu(111) surface with an activation energy of +100 kJ mol<sup>-1</sup>. <sup>111</sup> This is one of the important reaction steps in methanol and CO<sub>2</sub> hydrogenation (**section 1.2**). This limited C–O bond breaking activity is due to the stable filled *d*-band of metallic Cu that lies low in energy with an electron configuration of [Ar]3d<sup>10</sup>4s<sup>1</sup> and thus a limited extent of back-donation to the anti-bonding orbitals of the C–O bond. In contrast, transition metals such as iron, nickel, and cobalt have partially filled *d*-bands higher in energy and hence are able to overcome the activation barrier for dissociative CO adsorption *via* back-donation. <sup>182</sup>

The thermodynamically most stable crystallographic structure of copper is the face-centered cubic (fcc) structure.  $^{183-186}$  A crystalline copper nanoparticle has various exposed surface planes, of which the (111) facet is thermodynamically the most stable configuration in vacuum with a surface energy of 1.33 J m<sup>-2</sup>. Other facets such as (100), (110), and (211) have higher surface energies of 1.49, 1.56,

and  $1.52 \,\mathrm{J}$  m<sup>-2</sup>, respectively. <sup>183</sup> However, the ratio of the exposed facets depends on the gas atmosphere, pressure, temperature, particle size, and the wettability of the support surface. Furthermore, copper nanoparticles have a dynamic shape during catalysis. For example, in a highly reducible syngas atmosphere copper nanoparticles of 4-6 nm spread out over a  $\mathrm{ZnO}_x$  surface, while in the presence of  $\mathrm{H}_2\mathrm{O}$  more spherical particles are formed. <sup>187,188</sup> **Figure 1.5A** shows the thermodynamically most stable distribution of surface planes of non-supported copper particles at varying temperatures and  $\mathrm{H}_2$  partial pressures. <sup>183</sup> The copper particle shape can furthermore be tuned by selective adsorption of ligands on crystallographic planes, thereby inducing preferential facet growth using colloidal synthesis (**figure 1.5B**). <sup>184–186</sup> Finally, copper nanoparticles have a relatively low melting point ( $T_{\rm m}$  for bulk Cu is 1358 K, for 10 nm spheres 1137 K, and for 3 nm spheres 620 K <sup>189</sup>) and hence we expect that they are highly deformable during reaction conditions.

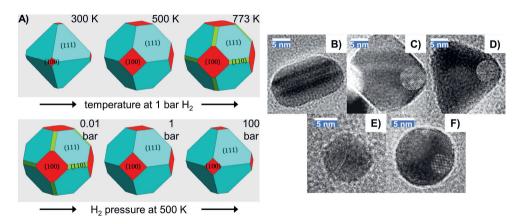


**Figure 1.5** (A) Wulff construction of thermodynamically most stable Cu nanoparticles at different temperatures and  $H_2$  pressures. Only (111) facets are covered with adsorbed H atoms at T < 500 K and  $p(H_2) > 1$  bar. Adapted from ref. [183]. (B-F) Various shapes of crystalline Cu nanoparticles (cylinder, cube (fcc), triangle, dodecahedron, sphere, respectively) obtained by colloidal synthesis in isooctane using docusate ligands and hydrazine as the reducing agent. Adapted from ref. [184].

#### 1.4 Promoters

This thesis discusses supported copper nanoparticles as catalysts, but to enable their full potential they are typically modified by additional metal (oxides) to obtain the desired activity, selectivity, and stability. These added metal (oxides) can be either regarded as a promoter or as a part of a bimetallic structure (if in the metallic form) or as a catalyst support. A promoter is defined as a material which enhances the catalyst performance by either modifying the properties of the

active component or by forming part of an intricate active site but has a limited or no activity on its own. It is typically present in low concentrations with respect to the active catalyst component. On the other hand, in bimetallic systems the individual components can both be active for the chemical reaction but display a distinct catalytic performance. In supported bimetals, such as the  $CuCoO_x$  system in **section 1.2.3**, the characteristics of both active metals are combined, particularly to steer the product selectivity. Similar amounts of both phases are mostly present in bimetallic systems in contrast to a promoter.

There is however no clear distinction whether an additional metal oxide acts as a promoter, part of a bimetallic system, or support. Furthermore, many distinct types of promotion exist and often depend on the specific reaction conditions. Typically, literature relates promoter effects to their structure in the initial and used state of a catalyst, while little information is available about the promoter during operation at relevant reaction conditions. Recent improvements in state-of-theart X-ray absorption spectroscopy (XAS) <sup>190–192</sup> enabled us to study the role of the promoter during catalysis, also named *operando* spectroscopy. In **chapters 3 and 4** we used *operando* XAS to observe time-resolved changes in zinc and manganese oxide promoters for copper-supported nanoparticles. In this section we first introduce several types of promotion after which we focus on zinc and manganese oxide promoters for supported copper catalysts.

#### 1.4.1 Distinct types of promotion

There are two types of promoters: textural and electronic promoters. <sup>7</sup> Textural promoters (**figure 1.6C**) can help to keep the catalytically active surface in a highly dispersed state by minimizing particle growth during catalyst synthesis and/or catalytic operation. A key factor is the strong metal—support interaction (SMSI), which can promote the catalyst stability. For example, the interaction between copper and silica, magnesia, or alumina is much stronger than between copper and activated carbon, thereby retarding the metal—adsorbate diffusion during catalyst synthesis and operation. <sup>18</sup>

Whether the intentional additive is either a support or a textural promoter is not well-defined but may be based on its relative amount in the catalyst formulation. For example, the alumina component in the methanol synthesis catalyst (Cu/ZnO/Al<sub>2</sub>O<sub>3</sub>) comprises only about 10 wt%, which hence can be more regarded as a structural promoter than a support. Besides enhancing the poison resistance by bonding sulfur impurities from the feed, alumina limits copper particle movement over the catalyst surface. <sup>193</sup> A similar stabilizing role of alumina (*ca.* 17 wt%) has been observed for macrocrystalline iron catalysts in CO oxidation. <sup>194</sup>

Promoters can also adjust the electronic properties of a catalyst, thereby enhancing the activity and/or selectivity. Alkali promoters, such as Na+ and K+ ions in the form of *e.g.* Na<sub>2</sub>O and K<sub>2</sub>O, are

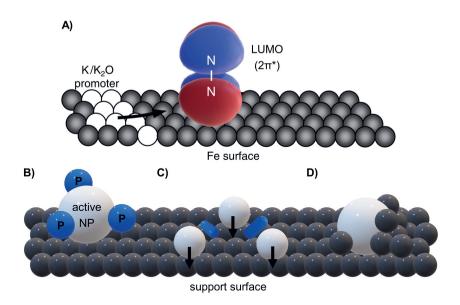


Figure 1.6 Different types of promotion. (A) A partially reduced, electropositive  $K_2O_x$  promoter donates electron density to a metal surface, which increases the back-donation of electron density from the reactant to the metal surface, thereby facilitating dissociative adsorption of the reactant. LUMO = lowest unoccupied molecular orbital. Based on refs. [195,196]. (B) A reducible metal oxide as an electronic promoter (P, blue) in close contact with a supported, active nanoparticle (NP, white). (C) A structural promoter (blue) separates the active NPs, thereby enhancing the dispersion. Interaction between the NPs and the support surface (indicated by the arrows) lowers the NP diffusion over the support surface. (D) A reducible support (black) as a promoter, which partially covers the active NPs.

an important class as they have a highly Lewis-basic nature in the partially reduced form and hence form a strong positive charge (**figure 1.6A**). They are typically used in Fischer-Tropsch synthesis, ethylene epoxidation, and ammonia synthesis to enhance the dissociation of the highly stable adsorbed CO and N<sub>2</sub>, respectively.  $^{197-200}$  Many different mechanisms are proposed to explain the role of alkali promoters.  $^{201}$  Generally, the electropositive alkali promoters become strongly polarized upon adsorption on a metallic surface and effectively donate electron density to the surface of the catalyst, thereby creating an electric dipole. As a result, the parallel coordination of the adsorbed reactant to the surface is favored over the terminally coordinated reactant due to the correlation between dipole moments of the dissociating reactant and the catalyst surface. Due to the increased electron density on the metal, the anti-bonding  $2\pi^*$  orbital of adsorbed reactants will accordingly be more filled, also called back-donation, thereby enhancing the dissociation of the reactant.  $^{3,195,201}$  Furthermore, the alkali promoters have a lower surface energy than transition metals (<0.6 vs >1.2 J m<sup>-2</sup>)  $^{202}$ , hence they diffuse to the surface of active nanoparticles and only a

few percent of alkali ions is more than sufficient to enhance the catalytic performance. The alkali promoters even might influence the exposed facets in iron-based surfaces ammonia synthesis. <sup>203</sup>

Other electronic promoters are reducible metal oxides (**figure 1.6B**). There are many ways how these materials promote the activity and/or selectivity of the catalyst, but the key feature is that there is a close intimacy between the active metal surface and the reducible promoter. This synergy is enhanced when the promoting metal oxide is in the (partially) reduced state. Reducible metal oxides are typically electron-withdrawing materials, thereby changing the oxidation state of the active surface species (for example ceria changes the Cu<sup>+</sup>/Cu<sup>0</sup> surface ratio in Cu/ZnO/Al<sub>2</sub>O<sub>3</sub> catalysts <sup>204</sup>). They could simultaneously help to keep the active phase in the reduced (*i.e.* active) phase. Other examples of promotion by reducible metal oxides is that they can alter the exposed facets or crystallographic structure of the active phase and change the surface tension of the active nanoparticles due to their strong interaction with the metal surface. <sup>7</sup>

Also the support can have a large electronic influence on the catalytic behavior, promoting the catalyst activity and selectivity (**figure 1.6D**). This is especially important for reactions which proceed at the interface between the active metal and the support, such as in CO oxidation on Pt/Fe<sub>3</sub>O<sub>4</sub> catalysts or for nanoparticles/clusters <2 nm. <sup>13</sup> Reducible oxidic supports such as ceria, titania, and niobia can be partially reduced by hydrogen spillover from the metal nanoparticles. As a result, the partially reduced support species partially cover the nanoparticles, thereby increasing the metal—support interface but lower the available metal surface. <sup>205</sup> Also support functionalization can alter the catalyst stability. For example, copper nanoparticles supported on aminopropyl-functionalized silica are stabilized during methanol synthesis by increasing the interparticle distance by the relatively large surface groups. Consequently, the diffusion of copper species is limited, compared to a non-functionalized silica support with mainly small silanol (Si–OH) groups. <sup>206</sup>

There is, however, an optimum in the surface coverage of active nanoparticles by an electronic promoter. At increasing promoter concentrations the active surface area decreases until the surface is fully covered with the promoter species. For instance, an optimum of 11 at% magnesia to carbon-supported copper nanoparticles enhanced the activity, selectivity as well as the stability in ester hydrogenolysis, but higher promoter loadings lowered the catalyst stability. <sup>19</sup> Finally, the location, amount, distribution, and local geometry of the promoting species all heavily influence the exact promoter effects. On top of that, the catalyst surface is dynamic during operation and hence *operando* characterization is needed to fully understand the promoter effects.

#### 1.4.2 Zinc oxide in supported copper catalysts

Zinc oxide (ZnO<sub>x</sub>) is produced on a scale of ca. 10,000 tons per year and is mostly used in the rubber industry (60%) to improve the thermal conductivity and mechanical properties.  $^{207,208}$  ZnO<sub>x</sub> is also industrially used as a promoter in methanol synthesis as well as in hydrogen production  $^{209-}$   $^{212}$ , Fe-based Fischer-Tropsch synthesis  $^{213-215}$ , and ester hydrogenolysis  $^{216}$ . It is slightly active for syngas conversion  $^{87,217,218}$ , but combined with CuO<sub>x</sub> species it forms a much more active catalyst formulation for methanol production.

For several decades, the role of the  $ZnO_x$  promoter in methanol synthesis catalysts has been investigated, both experimentally and computationally, in the typical  $Cu/ZnO/Al_2O_3$  catalyst as well as for Cu/ZnO model catalysts. Yet, the exact role of the  $ZnO_x$  promoter is still under debate.  $^{87,219-221}$  One of older hypotheses was that  $ZnO_x$  was only a stability promoter that increased the Cu dispersion.  $^{222,223}$  Later it became accepted that the synergy between the Cu and  $ZnO_x$  species was key. There are various reported mechanisms, e.g. variations in the  $ZnO_x$  oxidation state as a support change the morphology of small Cu nanoparticles and thereby the exposed Cu facets  $^{224}$ , and the hydrogen supply from  $ZnO_x$  to a Cu surface by spillover under  $H_2$ -deficient conditions  $^{225,226}$ . Now it is however generally accepted that the partial coverage of Cu nanoparticles by  $ZnO_x$  is the key factor for the promotional role of  $ZnO_x$ . An open question is still if under reaction conditions  $ZnO_x$  forms a layer over Cu particles  $^{225,227,228}$ , if the Cu surface is decorated with  $Zn^0$  atoms  $^{89,220}$ , or if a CuZn alloy is developed  $^{224,226,229}$ . Also it is still not clear if CuZn alloy formation at the surface is required  $^{81}$  or unfavorable  $^{221}$ .

The exact understanding of the ZnO<sub>x</sub> promoter is hampered by the challenge to study its structure during catalyst operation. For example, conversion level, particle size, activation procedure, and support might all influence the local coordination and speciation of ZnO<sub>x</sub>. <sup>18,39,46,93–95,104–106,188,220,230–234</sup> Furthermore, the reaction mechanism likely changes upon feed and catalyst composition. <sup>108</sup> To understand the dynamic role of the ZnO<sub>x</sub> during relevant industrial conditions, time-resolved and *operando* XAS needs to be used. In **chapter 3** we used this state-of-the-art technique at a high pressure during methanol synthesis to study the chemical nature and distribution of relevant promoting ZnO<sub>x</sub> species.

#### 1.4.3 Manganese oxide in supported copper catalysts

The world-wide consumption of manganese oxide  $(MnO_x)$  from manganese ores is more than 1.5 million tons per year of which ca. 95% is used for the production of iron–manganese alloys for the steel industry.  $^{235}$  Only a small portion of  $MnO_x$  is used as an electrolyte in batteries or a component in the catalyst industry.  $MnO_x$  is industrially used to promote the olefin selectivity for

CuFe-based Fischer-Tropsch synthesis catalysts.  $^{236,237}$  When changing the reactor pressure, the MnO<sub>x</sub> promoter can also enhance the selectivity to long-chain alcohols using similar CuFeO<sub>x</sub> catalysts, but this not yet commercialized.  $^{238-240}$  In literature several studies report using MnO<sub>x</sub> as a promoter for Cu-catalyzed reactions, including higher alcohol synthesis  $^{157,174,241-245}$ , ester hydrogenolysis  $^{19,216}$ , dimethyl ether (DME) synthesis and steam reforming  $^{246,247}$ , the aldehydewater shift reaction  $^{248}$ , and HCl oxidation  $^{249}$ .

MnO<sub>x</sub> is not frequently reported as a promoter for Cu-catalyzed CO and/or CO<sub>2</sub> hydrogenation to methanol. From the limited literature we can conclude that MnO<sub>x</sub> boosts the total activity, either attributed as a textural promoter by increasing the dispersion of small Cu nanoparticles <sup>250–253</sup> but also an electronic promoter due to a specific Cu–MnO<sub>x</sub> synergy <sup>253,254</sup>. In most cases MnO<sub>x</sub> is reported to also increase the methanol selectivity during hydrogenation of a CO<sub>2</sub>-rich syngas feed, ascribed to optimization of the Cu+/Cu<sup>0</sup> surface ratio <sup>251,255</sup> or the stabilization of specific reaction intermediates <sup>250</sup>. There are also hints that MnO<sub>x</sub> might increase the thermal stability, but its effect appears to be less pronounced than a ZnO<sub>x</sub> promoter. <sup>256,257</sup> There are still many open questions as some reports suggest the absence of any electronic promotion of Cu nanoparticles by MnO<sub>x</sub>, *i.e.* a Cu–MnO<sub>x</sub> synergy <sup>258</sup>, or that not the methanol selectivity but the CO selectivity increased upon MnO<sub>x</sub> addition <sup>256</sup>. In **chapter 4** we report the effects of the MnO<sub>x</sub> promoter on carbon-supported Cu catalysts in both CO and CO<sub>2</sub> hydrogenation under relevant reaction conditions and describe the MnO<sub>x</sub> speciation during operation with *operando* XAS at high pressure and temperature.

#### 1.5 Scope of this thesis

The aim of this thesis is to describe the influence of promoters, such as  $ZnO_x$  and  $MnO_x$ , on the performance of copper-supported catalysts in relevant hydrogenation reactions. These reactions include both the synthesis of methanol and the related water-gas shift reaction. In combination with electron microscopy and state-of-the-art *operando* XAS we ascribe the different catalytic performances to structural changes in the catalysts in the *ex situ* state as well as during operation. We make use of graphitic sheets as a model support to facilitate the intrinsic study of promoter effects, thereby mitigating any effect of hydroxylated surface groups which are typically present on metal oxide supports.

Chapter 2 focusses on the combined effect of  $CO_2$  enrichment of the synthesis gas and the presence of the  $ZnO_x$  promoter on the performance of supported copper model catalysts during methanol synthesis. Next to absolute methanol formation rates also the remarkable differences in the methanol selectivity are discussed between pure CO hydrogenation and combined  $CO/CO_2$  conversion. Furthermore, an optimum  $CO_2$  concentration in the syngas feed for maximum activity of these catalysts is established under industrially relevant reaction conditions.

**Chapter 3** concentrates on how the use of an oxidic support for  $CuZnO_x$  nanoparticles influences the extent of the  $Cu-ZnO_x$  interaction and hence their catalytic performance during high-pressure methanol synthesis. With the use of time-resolved XAS during methanol synthesis at high temperatures and pressures we were able to explain the differences in catalytic performance between using a graphitic and silica support and provide unprecedented insights into the state of the  $ZnO_x$  promoter during industrially relevant conditions.

In **chapter 4** we introduce  $MnO_x$  as a promoter for supported copper nanoparticles in CO and  $CO_2$  hydrogenation to methanol and CO. Using *operando* XAS we underline the synergistic effect between Cu and  $MnO_x$  and compare the catalyst performance to a conventional  $ZnO_x$  promoter.

**Chapter 5** covers the synthesis of supported, bimetallic  $CuCoO_x$  catalysts by two distinct preparation techniques: incipient wetness impregnation and electroless deposition/galvanic replacement. We describe the catalyst performance for CO hydrogenation to higher alcohols.

This thesis ends with summaries provided in both English and Dutch.

## Interplay between carbon dioxide enrichment and zinc oxide promotion of copper catalysts in methanol synthesis

#### **Abstract**

Methanol synthesis over  $Cu/ZnO/Al_2O_3$  is a key industrial reaction. Typically, a  $ZnO_x$  promoter and  $CO_2$  enrichment of the feed are applied to maximize the syngas conversion. However, understanding the effects of these additives on the performance of the Cu catalysts is obscured by the strong interaction between the  $ZnO_x$  promoter and oxidic supports. Here, we use Cu nanoparticles on graphitic support to study the interplay between  $CO_2$  concentration and  $ZnO_x$  promotion.  $CO_2$  enrichment enhanced the activity with an optimum at 3 vol% in the feed but only if the  $ZnO_x$  promoter was present, demonstrating the intricate interaction between the two. Interestingly, not only the activity but also the methanol selectivity was enhanced by  $CO_2$  enrichment, and even further by the addition of  $ZnO_x$ . Understanding not only the role of the individual components but also the interaction between them is important to design catalysts for processes with more flexible feed compositions.

**Based on**: Dalebout, R.; Visser, N.L.; Pompe, C.E.; de Jong, K.P.; de Jongh, P.E. Interplay between Carbon Dioxide Enrichment and Zinc Oxide Promotion of Copper Catalysts in Methanol Synthesis. *J. Catal.* **2020**, *392*, 150-158.

#### 2.1 Introduction

Methanol is a key chemical building block for the production of a wide range of chemicals including formaldehyde, olefins, acetic acid, and dimethyl ether. <sup>65,66</sup> The annual methanol production is around 100 million tons and the demand increases with about 4-5% per year. <sup>65,67,68</sup> Typically, a CO<sub>2</sub>-enriched synthesis gas feed (H<sub>2</sub>/CO/CO<sub>2</sub>) is passed over a Cu/ZnO/Al<sub>2</sub>O<sub>3</sub> catalyst at elevated temperatures (473-573 K) and pressures (40-100 bar). <sup>86,87</sup> Cu is the main active component in this catalyst, which is promoted by ZnO<sub>x</sub>, whereas Al<sub>2</sub>O<sub>3</sub> mainly serves for structural stability. <sup>88–91</sup> Other catalyst formulations such as Cu nanoparticles supported on ZrO<sub>2</sub> <sup>107</sup>, GaO<sub>x</sub> <sup>91</sup>, and CeO<sub>x</sub> <sup>204</sup> or in the presence of Al, Ga, Mg, Mn, and/or Zr <sup>93,233,234</sup>, NiGa<sub>x</sub>/SiO<sub>2</sub> <sup>259,260</sup>, GaPd<sub>2</sub>/SiO<sub>2</sub> <sup>261</sup>, and In<sub>2</sub>O<sub>3</sub>/ZrO<sub>2</sub> <sup>262</sup> have also been investigated.

Small amounts of  $CO_2$  (2-6 vol%) are generally added to the syngas mixture to increase the conversion of Cu-based methanol synthesis catalysts.  $^{60,94,104,105}$  Although CO can be directly hydrogenated to methanol  $^{94,105,108,263-265}$ , it has been clearly documented that in  $CO_2$ -enriched feed streams the vast majority of the methanol molecules originates from the hydrogenation of  $CO_2$  molecules  $^{104,107-109}$ . The water formed in this process drives the water-gas shift (WGS) reaction (CO +  $H_2O \rightleftharpoons CO_2 + H_2$ )  $^{109,266}$  by reacting with CO in the feed over a Cu surface. In this way constant but low concentrations of water and  $CO_2$  are sustained in the reaction atmosphere. Due to energy storage considerations, it can be desirable to operate the process with high concentrations of  $CO_2$  in the feed or even with a pure  $H_2/CO_2$  feed. However, hydrogenation of pure  $CO_2$  results in relatively high water concentrations, which give rise to a poor catalyst stability.  $^{125}$  Even though the redistribution of the  $ZnO_x$  promoter can also play a role, deactivation is mostly due to Cu particle growth, as investigated in detail in our lab  $^{206,267,268}$  and by others  $^{95,269-271}$ . Although the fact that slight  $CO_2$  enrichment increases the catalyst activity and decreases its stability, it is not yet known how and if the promoter plays a role in this.

Likewise, the influence of ZnO<sub>x</sub> on methanol synthesis is well known with a standard concentration of CO<sub>2</sub> in the feed <sup>60,87,94,104,107,220,272</sup>, but little is understood about its influence in different CO<sub>2</sub> concentrations or while hydrogenating pure CO. Martin *et al.* <sup>266</sup> showed that for a Cu/Al<sub>2</sub>O<sub>3</sub> catalyst the methanol formation rate increased by one order of magnitude upon ZnO<sub>x</sub> promotion in the absence of CO<sub>2</sub> in the feed, while Nielsen *et al.* <sup>264</sup> reported no significant change in the activity between 50 wt% Cu/Al<sub>2</sub>O<sub>3</sub> and Cu/ZnO/Al<sub>2</sub>O<sub>3</sub> catalysts, whereas Studt *et al.* <sup>108</sup> and Zander *et al.* <sup>273</sup> even reported a poisoning effect by ZnO<sub>x</sub> on the activity of an 86 wt% Cu/MgO catalyst. It hence seems that the effect of ZnO<sub>x</sub> also depends on the type of oxidic support used. ZnO<sub>x</sub> is known to have a relatively strong interaction with oxidic supports, which also depends on the reaction conditions. <sup>17,18,274</sup> As a result, a large fraction of the ZnO<sub>x</sub> might not be in the form of zinc oxide but rather present as for instance zinc aluminates or silicates. Hence, oxidic supports might hinder the understanding of the intrinsic influence of ZnO<sub>x</sub> on the performance of Cu catalysts. Graphite-like

materials as a non-oxidic support may limit these effects and has for example been used as a support for  $Cu(Zn)O_x$  particles in methanol synthesis  $^{39}$ , Ru particles in Fischer-Tropsch synthesis  $^{275}$ , and bimetallic CuNi in dimethyl carbonate synthesis  $^{276}$ .

A decisive factor in catalysis is the selectivity. Methanol synthesis from  $CO_2$ -containing syngas delivers a high selectivity, typically more than 98%.  $^{39,46,93-97}$  This remarkably high selectivity is typically attributed to the limited effectiveness of Cu to dissociate CO, thereby limiting the production of the thermodynamically more stable hydrocarbons. Even though the methanol selectivity is generally high, it is still relevant to investigate the nature of the side products and how the product distribution is influenced by the  $ZnO_x$  promoter and the  $CO_2$  concentration.

Here, we study the combined effect of different amounts of  $CO_2$  (including its absence) to the syngas feed and  $ZnO_x$  promotion on the methanol selectivity and formation rate on carbon-supported  $Cu(Zn)O_x$  model catalysts, to obtain insights into how these factors affect the performance of methanol synthesis catalysts. We use graphitic carbon as a model support for  $Cu(Zn)O_x$  nanoparticles as this avoids strong metal-support interactions <sup>18</sup> and hence is expected to limit spectator species such as zinc mixed metal oxides.

#### 2.2 Experimental

#### 2.2.1 Chemicals

Copper nitrate (Cu(NO<sub>3</sub>)<sub>2</sub>-3H<sub>2</sub>O, Acros Organics, 99%), zinc nitrate (Zn(NO<sub>3</sub>)<sub>2</sub>-6H<sub>2</sub>O, Sigma Aldrich,  $\geq$ 99%), high surface area graphite (TIMREX E-HSAG500, TIMCAL Graphite & Carbon), and nitric acid (HNO<sub>3</sub>, Merck, 65 wt%) were used as received. Reference was a commercial Cu/ZnO/Al<sub>2</sub>O<sub>3</sub>/MgO catalyst from Alfa Aesar, containing a Cu/Zn/Al/Mg ratio of 63.8/24.8/10.1/1.3 wt%. Silicon carbide (SiC, Alfa Aesar,  $\geq$ 98.8%, 46 grit) was sieved in a 212-425  $\mu$ m fraction, calcined at 1073 K for 10 h, subsequently washed with 65 wt% HNO<sub>3</sub> and rinsed with water until pH 7 was reached, and finally dried at 393 K overnight before use.

#### 2.2.2 Catalyst synthesis

Typically, ca.  $2.3 \, \mathrm{g}$  of powdered high surface area graphite (Brunauer-Emmett-Teller (BET) surface area  $509 \, \mathrm{m^2 \, g^{-1}}$ ) was dried at approximately 443 K under dynamic vacuum for  $1.5 \, \mathrm{h}$  to remove water from the pores. After cooling down to room temperature the fine carbon powder was (co-)impregnated to incipient wetness  $^{277}$ , defined as 95% of the total pore volume by  $N_2$  physisorption, under static vacuum with a  $0.1 \, \mathrm{M}$  HNO $_3$  solution containing  $1.8 \, \mathrm{M}$  copper (and  $1.0 \, \mathrm{M}$  zinc) nitrates. The impregnated support was subsequently dried at room temperature under

dynamic vacuum overnight and reduced at 503 K (ramp 2 K min<sup>-1</sup>) in a 100 mL min<sup>-1</sup> flow of 20 vol%  $H_2/N_2$  for 2.5 h. To be able to store and handle the catalyst in the oxidized state, it was exposed to a flow of 100 mL min<sup>-1</sup> of 5 vol%  $O_2/N_2$  for 1 h, heated to 473 K with a ramp of 1 K min<sup>-1</sup> and oxidized at 473 K in 15 vol%  $O_2/N_2$  for 1 h. The obtained X-Cu/C and X-CuZnO<sub>x</sub>/C catalysts, in which X represents the surface-averaged CuO size in the fresh catalyst, had a theoretical Cu weight loading of ca. 8.1  $\pm$  0.3 wt% and a ZnO loading of 0.1 or 5.3 wt%.

#### 2.2.3 Catalyst characterization

 $N_2$  physisorption isotherms were measured on a Micromeritics TriStar II Plus apparatus at 77 K. Prior to analysis the sample was dried at 443 K under an  $N_2$  flow overnight. The BET surface area was determined according to the IUPAC procedure. <sup>278</sup> Pore size distributions were established via a Barrett-Joyner-Halenda (BJH) analysis, using a carbon black statistical thickness curve  $(t = 2.98 + 6.45 \cdot (p/p_0) + 0.88 \cdot (p/p_0)^2)$  with a Faas correction. The total pore volume  $V_{\text{tot}}$  was derived from the amount of  $N_2$  adsorbed at  $p/p_0 = 0.995$ . The micropore volume  $V_{\text{micro}}$  was obtained via the t-plot method using the same statistical thickness curve fitted in the linear  $N_2$  monolayer adsorption regime. The mesopore volume  $V_{\text{meso}}$  was derived from integration of the adsorption-based BJH curve between 2 and 50 nm. Finally, the macropore volume  $V_{\text{macro}}$  was defined as the difference between the total pore volume and the sum of the t-plot micropore volume and BJH-derived mesopore volume.

Catalysts were imaged by transmission electron microscopy (TEM) on a Thermo Fisher Scientific Talos F200X apparatus, operating at 200 kV and equipped with a high-brightness field emission gun (X-FEG) and Super-X<sup>TM</sup> energy-dispersive X-ray (EDX) detectors. To this end, holey carbon film-coated Cu or Au grids (Agar, 300 mesh) were dry-loaded with finely ground sample (<25  $\mu$ m). Number-averaged CuO particle sizes ( $d_N$ ) were determined by measuring at least 350 individual particles at separate locations within the sample. These sizes were translated into surface-averaged ( $d_S$ ) and volume-averaged ( $d_S$ ) particle sizes, including the standard deviations in the width of the particle size distribution,  $via\ d_S \pm s_S = \sqrt{\frac{1}{N}\sum_{i=1}^N d_i^2} \pm \sqrt{\frac{1}{N-1}\sum_{i=1}^N (d_i-d_S)^2}$  and  $d_V \pm s_V = \sqrt[3]{\frac{1}{N}\sum_{i=1}^N d_i^3} \pm \sqrt{\frac{1}{N-1}\sum_{i=1}^N (d_i-d_S)^2}$ 

 $\sqrt{\frac{1}{N-1}\sum_{i=1}^{N}(d_i-d_V)^2}$ , in which  $d_i$  indicates the diameter of the i-th particle and N represents the total number of measured particles. Only the relevant part of the lognormal distribution (>1% of the modus) was considered for the calculation of average particle sizes.

Qualitative, chemical compositions were mapped by EDX spectroscopy, while imaging in high-angle, annular, dark-field, scanning transmission electron microscopy (HAADF-STEM) mode. The elemental maps were acquired using  $Velox^{TM}$  analytical imaging software. The acquisition time per EDX map was at least 15 min, and the probe current was around 700 pA.

Powder X-ray diffractograms were recorded on a Bruker AXS D2 Phaser diffractometer at room temperature with a fixed divergence slit. Samples were irradiated by Co K $\alpha$  radiation ( $\lambda$  = 1.790 Å) at 30 kV and 10 mA. Not only fresh catalysts, but also used catalysts were analyzed. These catalysts were slowly exposed to ambient conditions, separated from the SiC in the reactors, and finely ground prior to analysis.

Rietveld refinement was performed using Bruker DIFFRAC.SUITE TOPAS software by fitting CuO (monoclinic, C2/c) and ZnO (hexagonal,  $P6_3mc$ ) crystallographic data as Lorentzian functions between ca. 36 and 48°  $2\theta$ . No crystal strain or preferred orientation in the lattice planes were incorporated. The background was fitted as a first order Chebyshev polynomial, thereby taking the complete diffractogram into account. The y-coordinate of the O atom in CuO and the z-coordinate of the O atom in ZnO were refined. Crystallite sizes were obtained after the fitting converged to a minimum goodness-of-fit (GOF) value.

Temperature-programmed reduction (TPR) profiles were obtained on a Micromeritics AutoChem II 2920 apparatus. The sample (50 mg, <75  $\mu$ m granulites) was first dried *in situ* under an Ar flow at 50 mL min<sup>-1</sup> at 393 K for 30 min. The cooled sample was then exposed to 5 vol% H<sub>2</sub>/Ar at the same flow and heated to 873 K with a ramp of 2 K min<sup>-1</sup>. The formed H<sub>2</sub>O was captured with a dry ice/isopropanol cold trap, and the reduction profiles were recorded with a thermal conductivity detector (TCD).

#### 2.2.4 Catalyst testing

Catalysts were evaluated in a 16-reactor setup (Flowrence, Avantium) for 160 h, operating at 40 bar(g) and 533 K using an  $H_2/(CO + CO_2)$  molar ratio of 2. The catalysts powders were pelletized under a maximum pressure of 1 ton and sieved in granulites between 75-150  $\mu$ m. The stainless-steel reactors (inner diameter of 2.6 mm) were loaded with 178 mg 10-Cu/C, 51 mg 6-CuZnO<sub>x</sub>/C, or 6 mg commercial Cu/ZnO/Al<sub>2</sub>O<sub>3</sub>/MgO catalysts and diluted with inert SiC (grain fraction of 212-425  $\mu$ m). This resulted in inert SiC contents between 25 and 92 vol% of the total packed bed, thereby minimizing the error by dilution to a maximum of ca. 3%. <sup>279</sup> The size difference of the sieve fractions between the catalysts and diluent facilitated post-analysis by EM and X-ray diffraction (XRD).

An *in situ* reduction was performed in 2.8 mL min<sup>-1</sup> of 5 vol%  $H_2/N_2$  at 523 K for 3 h. The temperature was lowered to 393 K before the reactors were flushed with syngas ( $H_2/CO/He = 60/30/10$  vol%) at a GHSV of 400, 1,400, or 24,600 h<sup>-1</sup> for 1 h for the 10-Cu/C, 6-CuZnO<sub>x</sub>/C and commercial catalysts, respectively. The reactors were pressurized to 40 bar(g) and heated to the reaction temperature of 533 K with a ramp of 2 K min<sup>-1</sup>. After obtaining catalytic data for 40 h in an  $H_2/CO/He$  gas atmosphere a small amount of CO in the gas feed was replaced by  $CO_2$  and the new

gas composition was equilibrated for 1 h. After 30 h on stream in a  $CO_2$ -enriched feed, the  $CO_2$  content was stepwise further increased in a similar way up to  $H_2/CO/CO_2/He = 60/23/7/10 \text{ vol}\%$ .

The flows and catalyst loadings were adjusted to compensate for differences in Cu loading (8 vs 58 wt%) and packing densities of the sieved catalysts (0.52 vs 1.09 g mL<sup>-1</sup>) to achieve conversions in the same range. A tri-phase carbonyl trap (activated carbon,  $\gamma$ -Al<sub>2</sub>O<sub>3</sub>, ZnO) was located upstream of the CO feed to remove metal carbonyls and sulfur species. Products were periodically analyzed by online gas chromatography every 15 min. After catalysis, the samples were slowly exposed to air at 393 K.

#### 2.2.5 Calculation of catalyst activity and selectivity

The individual CO and CO<sub>2</sub> conversions ( $X_{\rm CO}$  and  $X_{\rm CO2}$ ) were calculated according to **equation (2.1)**, in which A represents the GC peak area of the corresponding compound obtained after the syngas mixture passed through a SiC-filled reference reactor (*i.e.* 'in') or through a catalyst-filled reactor (*i.e.* 'out'). The conversion levels were calibrated via He as an internal standard. The combined CO + CO<sub>2</sub> conversion (**equation (2.2)**) was calculated by taking the volume fractions of CO ( $\varphi_{\rm CO}$ ) and CO<sub>2</sub> ( $\varphi_{\rm CO2}$ ) in the syngas into account. The reported conversion levels were calculated from all products i formed (**equation (2.3)**) as the carbon mass balance ( $C_{\rm bal}$ ) was ca. 100 ± 1%c during all stages of catalysis. Here, Y is the yield, Q the volumetric flow rate, RF the response factor, and  $N_{\rm C}$  the number of carbon atoms.

$$X_{\text{CO}_{(2)}} = \frac{\left(A_{\text{CO}_{(2)}}/A_{\text{He}}\right)_{\text{in}} - \left(A_{\text{CO}_{(2)}}/A_{\text{He}}\right)_{\text{out}}}{\left(A_{\text{CO}_{(2)}}/A_{\text{He}}\right)_{\text{o}}} \cdot 100\% \, [\%]$$
 (2.1)

$$X_{\text{CO} + \text{CO}_2} = \frac{\varphi_{\text{CO}} \cdot X_{\text{CO}} + \varphi_{\text{CO}_2} \cdot X_{\text{CO}_2}}{\varphi_{\text{CO}} + \varphi_{\text{CO}_2}} [\%]$$
 (2.2)

$$X_{\text{CO (+ CO_2)}}^{\text{alt}} = \sum_{i=1}^{N} Y_i = \frac{\left[ \left( Q_{\text{CO}_2} \right)_{\text{out}} - \left( Q_{\text{CO}_2} \right)_{\text{in}} \right] + \sum_{i=1}^{N} \left( Q_i \right)_{\text{out}}}{\left( Q_{\text{CO}} \right)_{\text{in}} + \left( Q_{\text{CO}_2} \right)_{\text{in}}} \cdot 100\% \, [\%]$$
(2.3)

The Cu-normalized total activity and methanol formation rate were calculated via **equations (2.4)-(2.5)**. Here,  $F_{CO}$  and  $F_{CO2}$  represent the molar flow rates in the reaction feed of CO and CO<sub>2</sub>, respectively. The product selectivity S is calculated according to **equation (2.11)**.

Total activity = 
$$\frac{X_{\text{CO} (+ \text{CO}_2)}^{\text{alt}} \cdot (F_{\text{CO}} + F_{\text{CO}_2})}{m_{\text{Cu}} \cdot 100\%} \left[ \mu \text{mol}_{\text{CO} (+ \text{CO}_2) \text{ conv.}} g_{\text{Cu}}^{-1} s^{-1} \right]$$
 (2.4)

$$\text{Methanol formation rate} = \frac{\text{Total activity} \cdot S_{\text{MeOH}}}{100\%} \left[ \mu \text{mol}_{\text{MeOH form.}} \ g_{\text{Cu}}^{\text{-}1} \ s^{\text{-}1} \right]$$

The turnover frequency (TOF) was determined at an initial stage (**equation (2.6)**) and final stage (**equation (2.7)**) of catalysis. The initial TOF was calculated from the surface-averaged  $Cu(Zn)O_x$  size in the fresh catalyst ( $d_s^{initial}$ ) and the activity at t = 0 h, while the final TOF was obtained from the surface-averaged  $Cu(Zn)O_x$  size after catalysis ( $d_s^{final}$ ) and the activity at the corresponding time. The methanol-specific TOF<sub>MeOH</sub> was calculated according to **equation (2.8)**.

$$TOF_{initial} = \frac{X_{CO (+ CO_2)}^{alt}(t = 0 \text{ h}) \cdot (F_{CO} + F_{CO_2})}{Cu_{surf}(d_S^{initial}, m_{Cu})} \left[10^{-3} \text{ mol}_{CO (+ CO_2) \text{ conv.}} \text{ mol}_{Cu_{surf}}^{-1} \text{ s}^{-1}\right]$$
 (2.6)

$$TOF_{final} = \frac{X_{CO~(+~CO_2)}^{alt}(t = 100 \text{ h or } 150 \text{ h}) \cdot \left(F_{CO} + F_{CO_2}\right)}{Cu_{surf}\left(d_{S}^{final}, m_{Cu}\right)} \left[10^{-3} \text{ mol}_{CO~(+~CO_2)~conv.} \text{ mol}_{Cu_{surf}}^{-1} \text{ s}^{-1}\right]$$
 (2.7)

$$TOF_{MeOH} = \frac{TOF \cdot S_{MeOH}}{100\%} \left[ 10^{-3} \text{ mol}_{MeOH \text{ form.}} \text{ mol}_{Cu_{surf}}^{-1} \text{ s}^{-1} \right]$$
 (2.8)

The molar amount of Cu surface atoms in the catalyst (Cu<sub>surf</sub>) used in **equations (2.6)-(2.8)** was calculated according to **equation (2.9)**, which depends on the Cu dispersion ( $D_{\text{Cu}}$ , the ratio between Cu surface atoms and the total amount of Cu atoms) and the molar amount of Cu atoms in the catalyst ( $n_{\text{Cu}}$ ). In turn, the  $D_{\text{Cu}}$  depends on the Cu molar volume ( $V_{\text{m}}$ ) and particle area ( $A_{\text{m}}$ ), which are  $7.09 \cdot 10^{21}$  nm<sup>3</sup> and  $4.10 \cdot 10^{22}$  nm<sup>2</sup>, respectively. <sup>206</sup>

$$Cu_{surf} = D_{Cu} \cdot n_{Cu} = \frac{6 \cdot V_{m}}{A_{m} \cdot d_{S}} \cdot n_{Cu} \approx \frac{1.04 \text{ nm}}{d_{S}[\text{nm}]} \cdot n_{Cu} [\text{mol}_{Cu_{surf}}]$$
 (2.9)

Finally, the carbon atom-based selectivity of compound i ( $S_i$ ) was calculated according to **equation (2.10)**. For the CO<sub>2</sub>-free methanol selectivity, CO<sub>2</sub> was excluded as a product in the product distribution.

$$S_{i} = \frac{A_{i} \cdot N_{C,i}}{RF_{i}} \left[ \frac{\left(A_{CO_{2}}\right)_{out} - \left(A_{CO_{2}}\right)_{in}}{RF_{CO_{2}}} + \sum_{i=1}^{N} \frac{A_{i} \cdot N_{C,i}}{RF_{i}} \right]^{-1} \cdot 100\% \left[\%_{C}\right]$$
 (2.10)

#### 2.3 Results and discussion

#### 2.3.1 Structural properties of the catalysts

First, we discuss the particle size and elemental distribution in the catalysts as studied by electron microscopy and energy-dispersive X-ray (EDX) spectroscopy (**table 2.1**). **Figure 2.1** shows electron micrographs of two selected carbon-supported CuO catalysts, either promoted with ZnO<sub>x</sub> or not. <sup>50</sup> In bright-field transmission electron microscopy (BF-TEM) (frames C and A) particles of respectively *ca.* 5.4 nm and 9.3 nm (dark dots) are uniformly distributed over the support surface (light grey). Similarly sized and well-distributed nanoparticles were consistently found throughout these catalysts. Elemental mapping (frame E) shows that the ZnO<sub>x</sub> in the fresh 6-CuZnO<sub>x</sub>/C catalyst was evenly dispersed over the support surface and that the observed particles in BF-TEM (frames A and C) were hence mostly consisting of Cu(O). However, the elemental distribution after high-pressure methanol synthesis (frame F) is probably more representative of the catalyst during action and demonstrates a close intimacy between the Cu and Zn species. The

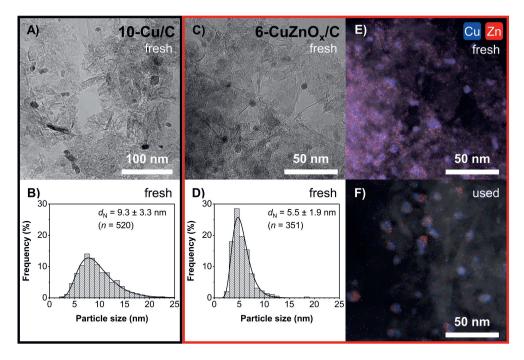


**Figure 2.1** (**A,C**) Representative BF-TEM images and (**B,D**) corresponding particle size distributions of (**A,B**) the fresh 10-Cu/C catalyst (8.1 wt%) and (**C,D**) the fresh 6-CuZnO<sub>x</sub>/C catalyst (7.7 wt% Cu, 5.3 wt% ZnO). Surface-averaged CuO particle sizes were  $9.9 \pm 3.3$  nm and  $5.7 \pm 1.8$  nm, respectively. Elemental distribution of Cu and Zn in (**E**) the fresh 6-CuZnO<sub>x</sub>/C catalyst in the same area of frame C and (**F**) the used 6-CuZnO<sub>x</sub>/C catalyst.

high surface area carbon support consisted of stacked graphitic sheets. As illustrated in **figure 2.2**, the carbon material exhibited a surface area of  $509~m^2~g^{-1}$  and a mesopore volume of  $0.36~mL~g^{-1}$ , while after Cu and Zn deposition  $297~m^2~g^{-1}$  and  $0.23~mL~g^{-1}$  were obtained. The high surface area of the carbon support clearly allowed a uniform distribution of nanoparticles over the support.  $^{22,276,280,281}$ 

**Table 2.1** Overview of structural properties of selected catalysts.

catalyst	loading (wt%)		TEM CuO p	article size (nm) <sup>a</sup>	XRD CuO crystallite	
catalyst	Cu	ZnO	$d_{ m S}$	$d_{ m V}$	size (nm) b	
10-Cu/C (fresh)	8.1	0	$9.9 \pm 3.3$	$10.4 \pm 3.5$	$15.9 \pm 0.5$	
10-Cu/C (used)	0.1		$11.6 \pm 4.4$	$12.5 \pm 4.7$	13 с	
10-CuZnO <sub>x</sub> /C	8.4	0.1	$9.3 \pm 3.8$	$10.0 \pm 4.1$	-	
6-CuZnO <sub>x</sub> /C (fresh)		5.3	$5.7 \pm 1.8$	$6.0\pm1.8$	$5.8 \pm 0.5$	
6-CuZnO <sub>x</sub> /C (used)	7.7		$8.7 \pm 3.0$	$9.2 \pm 3.1$	12 °	
Cu/ZnO/Al <sub>2</sub> O <sub>3</sub> /MgO	58.4	28.4	ca. 10		$5.8 \pm 0.1$	
(com cat) (fresh)	50.7	20.4				

<sup>&</sup>lt;sup>a</sup> Average CuO sizes with width of the particle size distribution. <sup>b</sup> Error indicates fitting error by Rietveld refinement of CuO. <sup>c</sup> Cu<sup>0</sup> crystallite size estimated from Scherrer equation at 59° 2θ, excluding CuO<sub>x</sub>.

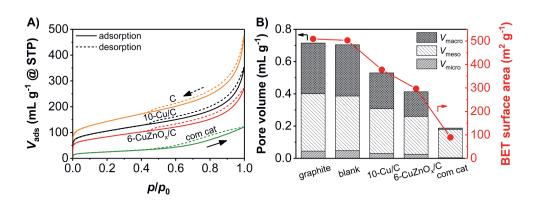
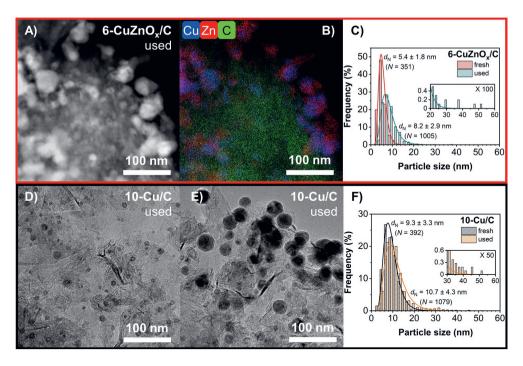


Figure 2.2 (A)  $N_2$  physisorption isotherms of native graphite and selected catalysts. (B) Corresponding pore volumes and BET surface areas. Blank = powdered graphite impregnated with HNO<sub>3</sub> and activated in the same way as the catalysts.

**Figure 2.1** (frames B and D) shows that the CuO particle sizes were distributed in a lognormal fashion for the fresh 10-Cu/C and 6-CuZnO<sub>x</sub>/C catalysts. Based on the histograms the particle size

distribution was also translated into a surface-averaged size, which is relevant for catalysis, and a volume-averaged size, which can be directly compared to X-ray diffraction (XRD) (table 2.1).  $^{282,283}$  Figure 2.3 presents local EM images of selected used catalysts and shows that a few agglomerates were present, which were not considered for the corresponding particle size averages to obtain a more relevant representation of the active particle size. The preparation and characterization of  $10\text{-CuZnO}_x/\text{C}$  catalysts containing 0.1 wt% ZnO was reproduced three times. For all three  $10\text{-CuZnO}_x/\text{C}$  catalysts similar number-averaged particle sizes  $(7.3 \pm 1.1 \text{ nm})$  and distributions were obtained, proofing that the catalyst synthesis was reproducible. All three carbon-supported catalysts shown in table 2.1 had a similar Cu loading  $(8.1 \pm 0.3 \text{ wt}\%)$ , which was confirmed by temperature-programmed reduction with  $H_2$   $(7.7 \pm 1.4 \text{ wt}\%)$ . These results show that the presence of sufficient ZnO<sub>x</sub>, as in the 6-CuZnO<sub>x</sub>/C catalyst, limited the growth of CuO<sub>x</sub> nanoparticles during catalyst synthesis.



**Figure 2.3** Selected local EM images of the (**A-B**) used 6-CuZnO<sub>x</sub>/C and (**D-E**) used 10-Cu/C catalysts after 160 h of catalysis. (**A**) HAADF-STEM image and (**B**) corresponding elemental distribution of Cu, Zn, and C in the same are as frame A. The most representative image of the used catalyst is shown in **figure 2.1**, taken from the same catalyst batch. (**D-E**) BF-TEM images at separate locations within the same EM sample. (**C,F**) Particle size distributions, comparing the fresh (the same as in frames B and D of **figure 2.1**) and used catalysts. Please note the low frequency of the larger particles in the used catalysts.

Powder X-ray diffraction patterns of the fresh 10-Cu/C and 6-CuZnO<sub>x</sub>/C catalysts (**figure 2.4**, frame A) showed, next to the graphite diffraction lines at  $30.7^{\circ}$ ,  $50.4^{\circ}$ , and  $64.1^{\circ}$   $2\theta$ , only diffractions attributed to CuO crystallites at  $37.9^{\circ}$ ,  $41.4^{\circ}$ ,  $45.2^{\circ}$ ,  $57.1^{\circ}$ ,  $62.9^{\circ}$ , and  $68.7^{\circ}$   $2\theta$ . The crystallite sizes were respectively ca. 16 and 6 nm and corresponded to the volume-averaged CuO particle sizes, derived from the BF-TEM particle size histograms, of  $10.4 \pm 3.5$  nm and  $6.0 \pm 1.8$  nm, respectively. No diffraction peaks due to ZnO were observed for the fresh 6-CuZnO<sub>x</sub>/C catalyst, which is in line with the high ZnO<sub>x</sub> dispersion observed in the fresh catalyst with elemental mapping (**figure 2.1**, frame E). After catalysis, the ZnO (partly) crystallized (**figure 2.4**, frame B), showing crystallites of 12 nm. This observation agreed with the fact that in the used 6-CuZnO<sub>x</sub>/C catalyst also some larger particles were found in the sample (**figure 2.3**, frame A). In both used 10-Cu/C and 6-CuZnO<sub>x</sub>/C catalysts (frame B) the diffractions at  $50.6^{\circ}$  and  $59.1^{\circ}$   $2\theta$  are attributed to 13 and 12 nm Cu<sup>0</sup> crystallites, respectively. Please note that these Cu<sup>0</sup> sizes are slightly smaller than the CuO sizes in the fresh catalysts (**table 2.1**), but this difference may be explained by the fact that not all Cu is in the metallic phase. Due to passivation of the samples after catalysis distinct phases of copper oxide were present.

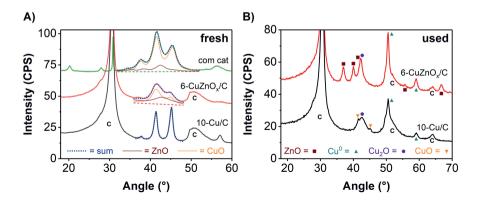


**Figure 2.4** Powder X-ray diffractograms of (**A**) selected fresh catalysts and (**B**) used catalysts after 160 h of catalysis and subsequent passivation. The diffractograms are vertically offset for clarity. The blue dotted lines represent Rietveld fittings, and the dashed lines describe the corresponding backgrounds. The peaks below  $35^{\circ}$   $2\theta$  in the com cat were due to mixed metal oxides, based on Al and/or Mg.

As a reference also a commercial Cu/ZnO/Al<sub>2</sub>O<sub>3</sub>/MgO methanol synthesis catalyst (com cat) prepared by co-precipitation <sup>39,86,89,95,269,284</sup> was included (**table 2.1**, **figure 2.2**). XRD analysis in **figure 2.3** (frame A) shows diffractions at 35°, 38° and 42°  $2\theta$  attributed to ZnO and with a width corresponding to an approximate crystallite size of 4 nm. The catalyst typically contained ca. 10 nm-sized Cu(O) particles <sup>89</sup> and 58 wt% Cu with a Zn/(Cu + Zn) molar fraction of 0.28, which was

similar to our 10-CuZnO<sub>x</sub>/C catalyst (0.35). The commercial catalyst is known to have a close intimacy of Cu and Zn species, whereas Al<sub>2</sub>O<sub>3</sub> mainly acts as a spacer. <sup>88,90,91</sup>

# 2.3.2 Influence of ZnO<sub>x</sub> on activity and selectivity during CO hydrogenation

First, we evaluated methanol synthesis with only CO and  $H_2$  in the feed (hence, without CO<sub>2</sub>). **Figure 2.5** (frame A) shows the CO conversion as a function of time for two selected catalysts, 10-Cu/C and  $6\text{-CuZnO}_x/C$ , as well as for the commercial  $\text{Cu/ZnO/Al}_2\text{O}_3/\text{MgO}$  catalyst to put our catalysts into perspective. The commercial catalyst was stable from the start, probably because it had already been exposed to temperatures >573 K  $^{39,89}$ , although the stabilizing effect by Al and/or Mg species may also play a role  $^{86}$ . For both carbon-supported catalysts an activation period of ca. 20 h was observed, which can be explained by the fact that this was the first time that they were subjected to 533 K and high pressure. The hollow symbols represent a duplicate test from the same catalyst batch, proving that the catalytic testing was reproducible. All these conversion levels are well below the thermodynamic equilibrium of 35.7%.  $^{98,285}$ 

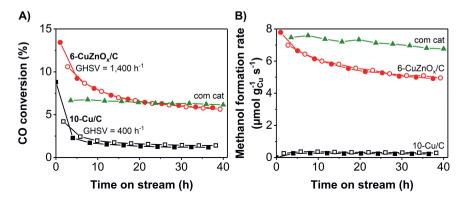


**Figure 2.5** (**A**) CO conversion and (**B**) methanol formation rate over time during CO hydrogenation. Hollow symbols represent a duplicate test from the same catalyst batch. Conditions: 533 K, 40 bar(g),  $H_2/CO/He = 60/30/10 \text{ vol}\%$ , flow = 152, 560, 620 mL min<sup>-1</sup> gcu<sup>-1</sup> and GHSV = 400, 1,400, 24,600 h<sup>-1</sup> for 10-Cu/C, 6-CuZnO<sub>x</sub>/C and com cat, respectively.

**Table 2.2** shows the CO conversion, also normalized to the Cu mass in the reactor, as well as the turnover frequencies based on the particle sizes in the fresh and used catalysts. Note that these different activities are not directly reflected in **figure 2.5** (frame A) as for these tests the flows and catalyst loadings were adjusted to compensate for differences in Cu loading and packing densities

**Table 2.2** Overview of catalytic results during CO hydrogenation in the absence of  $CO_2$ . The initial turnover frequency (TOF) was calculated using the CuO particle size in the fresh catalyst and the activity at t = 0. The final TOF was estimated from the CuO particle size after 160 h of catalysis and the activity at t = 40 h. The methanol selectivity included  $CO_2$  in the product distribution. The errors indicate the standard deviation between two measurements unless stated otherwise. Conditions were equal to **figure 2.5**. "Conv." = conversion.

catalyst	GHSV (h-1)	CO conv. (%)		CO conv. rate (µmol g <sub>Cu</sub> -1 s-1)		total turnover frequency (10 <sup>-3</sup> s <sup>-1</sup> ) <sup>a</sup>		MeOH selectivity (%c)	
		0 h	40 h	0 h	40 h	0 h	40 h	0 h	40 h
10-Cu/C	400	8.8	$1.3 \pm 0.1$	2.1	0.4	$1.6 \pm 0.6$	$0.3 \pm 0.1$	0	$63 \pm 5$
6-CuZnO <sub>x</sub> /C	1,400	15.1	$5.7 \pm 0.1$	21.5	6.5	$6.0 \pm 1.8$	$3.8 \pm 1.3$	48	$75 \pm 1$
com cat	24,600	6.8	6.2	8.7	7.7	3.0 b	2.7 <b>b</b>	89	88

<sup>&</sup>lt;sup>a</sup> The error in the TOF reflects the width in the CuO particle size distribution from BF-TEM. <sup>b</sup> The CuO crystallite size (from XRD) in the fresh catalyst was used in the calculation.

and to achieve conversion levels in the same range. By comparing the activities of the 10-Cu/C and 6-CuZnO<sub>x</sub>/C catalysts the ZnO<sub>x</sub> addition clearly led to an activity increase of about one order of magnitude. After 40 h on stream our 6-CuZnO<sub>x</sub>/C catalyst had a methanol turnover frequency of  $2.8 \cdot 10^{-3} \, s^{-1}$ , which was similar to the commercial Cu/ZnO/Al<sub>2</sub>O<sub>3</sub>/MgO catalyst with an activity of  $ca. 2.4 \cdot 10^{-3} \, s^{-1}$ . The turnover frequency of the 6-CuZnO<sub>x</sub>/C catalyst may be even higher as a few agglomerates were found in this catalyst but not considered in the particle size average (**figure 2.3**, frame A). As mentioned earlier in the introduction, only a few and somewhat contradictory studies are available regarding the effect of ZnO<sub>x</sub> while hydrogenating pure CO, which might be induced using (different) oxidic supports. Therefore, we studied the effect of ZnO<sub>x</sub> addition during CO hydrogenation while using an inert graphitic support.  $^{18}$ 

**Figure 2.5** (frame B) presents the evolution of the methanol formation rate over time. After the activation period all catalysts showed a stable methanol production. However, the methanol formation rate (and selectivity from **table 2.2**) was surprisingly low ( $<8 \mu mol g c u^{-1} s^{-1}$ ), even for the commercial catalyst, compared to what is typically reported for  $CO_2$ -enriched syngas conversion. <sup>39,96</sup> This might be induced by a slight deficiency in hydrogen <sup>285</sup> and the slightly high reaction temperature. Although there are few old studies available on  $Cu/ZnO/Al_2O_3$  catalysts <sup>94,105,263</sup>, as far as we are aware this is the first time that the methanol formation rates are reported for carbon-supported Cu particles in the presence and absence of  $ZnO_x$  during pure CO hydrogenation.

**Figure 2.6** displays the evolution of the other products formed over the 10-Cu/C and 6-CuZnO<sub>x</sub>/C catalysts, averaged over at least four separate measurement runs. In both cases CO<sub>2</sub> was the main side product, but also hydrocarbons, ethanol and, in the case of the 6-CuZnO<sub>x</sub>/C catalyst, dimethyl

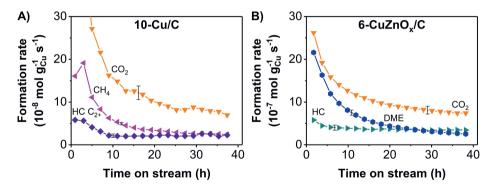


**Figure 2.6** Time evolution of side product formation rates during CO hydrogenation for the (**A**) 10-Cu/C and (**B**) 6-CuZnO<sub>x</sub>/C catalysts. Mind the order of magnitude difference between the frames. All points are the average over four or six separate measurement runs, with the error bars indicating the spread. Less than  $0.4 \pm 0.5 \cdot 10^{-8}$  and  $0.4 \pm 0.2 \cdot 10^{-7}$  mol gcu<sup>-1</sup> s<sup>-1</sup> ethanol was formed, respectively. HC = hydrocarbons, DME = dimethyl ether. Conditions were equal to **figure 2.5**.

ether (DME) were detected. The hydrocarbon formation rates were ca. 4 orders of magnitude lower than typically found in iron-based Fischer-Tropsch synthesis. <sup>286</sup> DME was probably formed by dehydration of methanol (2CH<sub>3</sub>OH  $\rightleftarrows$  (CH<sub>3</sub>)<sub>2</sub>O + H<sub>2</sub>O) <sup>226</sup> on the acidic oxygen vacancy sites on the ZnO<sub>x</sub> surface <sup>287,288</sup>. Interestingly, CO<sub>2</sub> was produced from CO, while no water or oxygen was present in the feed. Other oxygen sources such as ZnO<sub>x</sub> or contaminations in the feed, SiC diluent, and/or carbonyl trap do support the observed CO<sub>2</sub> production (as discussed in the next paragraph in detail). This CO<sub>2</sub> production can be explained by the co-formation of hydrocarbons, ethanol, and DME. The total formation rate of these compounds for the 10-Cu/C catalyst (5.1  $\pm$  1.1  $\cdot$  10-8 mol gcu<sup>-1</sup> s<sup>-1</sup>) was similar to the rate of produced CO<sub>2</sub> after 40 h of catalysis (6.9  $\pm$  3.1  $\cdot$  10-8 mol gcu<sup>-1</sup> s<sup>-1</sup>). An analogous observation was made for the 6-CuZnO<sub>x</sub>/C catalyst (6.3  $\pm$  1.7  $\cdot$  10-7 vs 7.2  $\pm$  1.8  $\cdot$  10-7 mol gcu<sup>-1</sup> s<sup>-1</sup>). Hence, the following reaction plausibly occurred (next to direct CO hydrogenation to methanol <sup>89,94,105,108,226,263-265)</sup>: 2xCO + (x+1)H<sub>2</sub>  $\rightleftarrows$  xCO<sub>2</sub> + C<sub>x</sub>H<sub>2x+2</sub>.

The contribution of impurities in the catalyst system to the CO<sub>2</sub> production was studied in more detail. A negligible number of Fe-based impurities, which are known to activate C–O bond splitting, was found in the graphite support, SiC diluent, and the nitrate salts as determined by ICP analysis (Mikrolab Kolbe, Germany), resulting in less than 11 ppm Fe (w/w) in the reactor. In addition, the SiC diluent and reactor walls did not show any conversion, and the carbon mass balance was 100% within error (1%). The carbonyl trap removed 0.96 wt% Fe(CO)<sub>5</sub>, 0.03 wt% Ni(CO)<sub>4</sub>, 618 ppm H<sub>2</sub>S, and 921 ppm COS after several catalyst tests according to ICP measurements <sup>92</sup>, while after refreshment of the trap no significant changes in the catalyst performance were observed, proving that the impurities in the CO gas feed did not influence the catalysts. Hence, we excluded any

significant contribution of metal impurities to possible CO<sub>2</sub> production in Cu-catalyzed pure CO hydrogenation.

As mentioned earlier, the gas feed might be one of the potential oxygen sources for the CO<sub>2</sub> production. The maximum possible amount of oxygen atoms from the gas feed was 4.4  $\mu$ mol in 40 h, contributing only 1% to the total CO<sub>2</sub> production. The carbon support contributed *ca.* 8% and 1% to the total CO<sub>2</sub> production for the 10-Cu/C and 6-CuZnO<sub>x</sub>/C catalysts, respectively, deduced from the surface group density on the graphite (0.161  $\pm$  0.002 nm<sup>-2</sup>) <sup>22</sup> and the comparison of the CO<sub>2</sub> yield between the catalysts and the native support. The ZnO<sub>x</sub> promoter in the 6-CuZnO<sub>x</sub>/C catalyst can provide a maximum of 4% to the CO<sub>2</sub> formation, assuming a complete reduction of the promoter. Hence, as the combined contributions of the feed, support, and ZnO<sub>x</sub> can only partially explain the CO<sub>2</sub> production in the 10-Cu/C and 6-CuZnO<sub>x</sub>/C catalysts during CO hydrogenation, the CO dissociation played a key role as an oxygen source.

An intriguing question is why the produced  $CO_2$  was not (entirely) consumed by hydrogenation to methanol. From literature it is known that  $CO_2$  is preferred over CO as the carbon source for methanol production at high temperatures.  $^{107,109}$  The  $CO_2$  concentration in these systems is very low with a corresponding partial pressure of 0.04 and 0.11 bar for, respectively, the 10-Cu/C and 6-CuZnO<sub>x</sub>/C catalysts after 40 h on stream, as  $CO_2$  was only generated during the reaction. To our knowledge this is the first time that these relatively low methanol selectivities in a pure  $H_2/CO$  feed have been reported and tentatively explained.

#### 2.3.3 Combined influence of CO2 and ZnOx

In industrial methanol production a  $CO_2$ -enriched syngas feed is typically used. <sup>60</sup> **Figure 2.7** (frame A) shows the effect of  $CO_2$  concentration in the syngas feed on the  $CO + CO_2$  conversion for carbon-supported Cu catalysts with and without  $ZnO_x$  as well as for the commercial catalyst. Please note that this is the net conversion, as we cannot determine the extent of (reverse) WGS taking place in the reactor. The conversion is taken after at least 30 hours on stream in a specific gas composition. Even 1 vol%  $CO_2$  in the feed (obtained by replacing 3% of the CO with  $CO_2$ ) increased the  $CO + CO_2$  conversion for the 6-Cu $ZnO_x/C$  catalyst from 5.7% to 11.9%, and with 3 vol%  $CO_2$  in the feed the maximum  $CO + CO_2$  conversion was reached, while with even higher  $CO_2$  content the conversion level again decreased, down to 6.8% with 7 vol%  $CO_2$  in the total feed. An effect of  $CO_2$  in syngas on the conversion has been observed earlier.  $^{60,87,94,104,105,107,220,272}$  A similar conversion increase was observed for the commercial catalyst for low and increasing  $CO_2$  concentrations, but the decline at higher concentrations was much less pronounced.

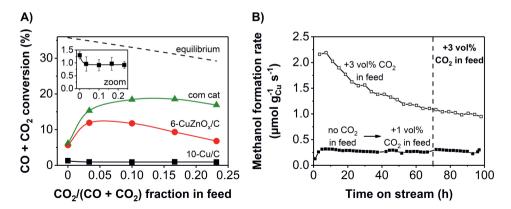


Figure 2.7 (A) Net  $CO + CO_2$  conversion at different syngas compositions. The catalysts were exposed to increasing  $CO_2$  contents in the feed at a constant  $H_2/(CO + CO_2)$  ratio. Values were determined after 30 h on stream in a specific gas composition (40 h on stream for no  $CO_2$  in feed). Error bars represent the standard deviations between 2 measurements. (B) Methanol formation rate of the 10-Cu/C catalyst when activated in different syngas compositions. The filled squares ( $\blacksquare$ ) represent the time-resolved data in frame A and are the average over two measurements. The empty squares ( $\square$ ) represent a single catalytic test in which the catalyst was directly introduced to a  $CO_2$ -enriched syngas feed after in situ reduction in  $H_2/N_2$  at 523 K. Conditions:  $H_2/(CO + CO_2)/He = 60/30/10$  vol%, further equal to figure 2.5.

The decrease in the conversion level for the 6-CuZnO<sub>x</sub>/C catalyst at higher CO<sub>2</sub> concentrations in the feed (frame A) can be explained by a combination of Cu particle growth,  $ZnO_x$  promotion loss, and/or Cu surface oxidation. TEM analysis (**table 2.1**) showed only a minor  $CuO_x$  particle growth to  $8.7 \pm 3.0$  nm in the used 6-CuZnO<sub>x</sub>/C catalyst, although probably a significant amount of the Cu atoms was in several larger particles (**figure 2.3**, frame A) but contributing little to the active surface area. XRD analysis of the used catalyst (**figure 2.4**, frame B) indicated a significant ZnO crystallization to approximately 12 nm, even though a close interaction between  $ZnO_x$  and Cu was preserved (**figures 2.1 and 2.3**). Another possible consequence of the higher  $CO_2$  concentration (and the additional  $H_2O$  formation), and hence a more oxidizing atmosphere, might be a higher oxygen coverage of the Cu surface, which is reported to render the catalyst less active. <sup>87,104,108</sup>

The influence of  $CO_2$  in the syngas feed on the activity of unpromoted supported Cu particles was so far not clear, as reported results varied depending on the type of oxidic support used.  $^{108,264}$  Furthermore, as we also found (**figure 2.7**, frame B), Cu-based catalysts can show a long activation period and performance might be influenced on the activation protocol, which is a topic of further study. However, based on carbon-supported model catalysts we clearly show that for unpromoted Cu nanoparticles, in the absence of any oxidic phase, the syngas conversion level (frame A) is not significantly influenced by the  $CO_2$  content. Hence, synergy between Cu nanoparticles and  $ZnO_X$  (or

another appropriate oxidic promoter) is clearly needed for effective  $CO_2$  hydrogenation, which plays such an important role in the industrial methanol synthesis process.  $^{108,217}$ 

**Figure 2.8** (frame A) presents the methanol selectivity of the catalysts in different syngas compositions, thereby not taking  $CO_2$  in account as a possible product in the product distribution, as a function of the  $CO_2$  content in the feed. Interestingly, a modest addition of  $CO_2$  boosted the methanol selectivity by ca.  $8\%_C$  for the 6-CuZnO<sub>x</sub>/C and 10-Cu/C catalysts. In  $CO_2$ -enriched syngas feeds the commercial catalyst reached a methanol selectivity of  $>99\%_C$ , which was also reported by our group at similar  $CO + CO_2$  conversion levels.  $^{96,289}$  The lower selectivity for the 10-Cu/C catalyst ( $89\%_C$ ) was also observed for a  $Cu/SiO_2$  catalyst ( $92\%_C$ ) and might be caused by its low conversion level.  $^{290}$  It must be noted that the hydrocarbon formation rate was similar in all syngas atmospheres ( $2.7 \cdot 10^{-7}$  mol gcu<sup>-1</sup> s<sup>-1</sup> or  $1.5 \cdot 10^{-4}$  s<sup>-1</sup> for the 6-CuZnO<sub>x</sub>/C catalyst), showing that the methanol selectivity increase was governed by an increased methanol formation rate. This remarkable improvement with the addition of a small amount of  $CO_2$  can be understood for the 6-CuZnO<sub>x</sub>/C catalyst by the DME suppression, as sufficient  $H_2O$  was generated via the  $CO_2$  hydrogenation to methanol. Additionally, the higher  $H_2O$  content seems to play a role in lowering of the C-O bond dissociation activity with respect to the methanol formation rate, as discussed in detail in **section 2.3.2**.

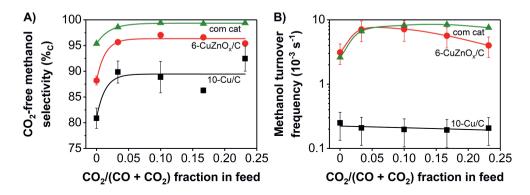


**Figure 2.8** (A) Carbon atom-based methanol selectivity, thereby not taking  $CO_2$  into account as a possible product in the product distribution (see also **equation (2.10)**). (B) methanol turnover frequency ( $TOF_{MeOH}$ ) at different syngas compositions. The data depiction and catalysis conditions are equal to **figure 2.5** (frame A). The  $TOF_{MeOH}$  was estimated using the CuO particle size after 160 h of catalysis. Error bars represent the standard deviations between two measurements (frame A) or reflect the width in the CuO size distribution in the used catalysts (frame B).

**Figure 2.8** (frame B) illustrates the methanol turnover frequency ( $TOF_{MeOH}$ ), serving as a combination of the  $CO_2$ -free methanol selectivity (frame A) and the  $CO + CO_2$  conversion (**figure 2.7**, frame A). For the  $ZnO_x$ -promoted catalysts, the trends in the  $TOF_{MeOH}$  reflect those of the  $CO + CO_2$  conversion. Also, our  $6-CuZnO_x/C$  catalyst performed in the same order of magnitude as the commercial catalyst, hence illustrating the relevance of our model catalyst study. The slightly lower conversion at higher  $CO_2$  contents in the feed might be explained by an increased loss of  $ZnO_x$  promoter effect by crystallization, dealloying and/or overcoverage over active Cu surface area  $^{125,220}$  compared to the stabilized commercial catalyst by metal oxides. For the 10-Cu/C catalyst the  $TOF_{MeOH}$  (frame B) did not change at all  $(2.1 \cdot 10^{-4} \text{ s}^{-1})$  upon  $CO_2$  enrichment of the feed, again strongly suggesting that the Cu catalyst alone is quite inactive in  $CO_2$  hydrogenation.

## 2.4 Conclusions

We prepared a series of carbon-supported  $CuZnO_x$  catalysts with a uniform distribution of Cu nanoparticles and, when present,  $ZnO_x$  in close contact with Cu during catalysis. While hydrogenating pure  $CO\ ZnO_x$  promoted the activity by about one order of magnitude and led next to methanol to the production of dimethyl ether. A maximum activity of the promoted catalyst was obtained with 3 vol%  $CO_2$  enrichment of the syngas, whereas the methanol formation rate over unpromoted Cu was not influenced by  $CO_2$  addition. Interestingly, alternative products (>10%c) such as  $CO_2$  and hydrocarbons were formed for all catalysts in the absence of  $CO_2$  in the feed in concomitance with methanol. The methanol selectivity of all catalysts was very high when  $CO_2$  was present in the feed.

# Acknowledgments

We thank Nienke Visser for the EDX imaging and Lisette Pompe for provision of several catalysts. Rolf Beerthuis and Jan Willem de Rijk are thanked for input during catalytic testing.

# Insight into the nature of the zinc oxide promoter during methanol synthesis

#### **Abstract**

Despite the great commercial relevance of zinc-promoted copper catalysts for methanol synthesis, the nature of the Cu-ZnO<sub>x</sub> synergy and the nature of the active Zn-based promoter species under industrially relevant conditions are still a topic of vivid debate. Detailed characterization of the chemical speciation of any promoter under high-pressure working conditions is challenging but specifically hampered by the large fraction of Zn spectator species bound to the oxidic catalyst support. We present the use of weakly interacting graphitic carbon supports as a tool to study the active speciation of the Zn promoter phase that is in close contact with the Cu nanoparticles using time-resolved X-ray absorption spectroscopy under working conditions. Without an oxidic support, much less Zn species needs to be added for maximum catalyst activity. A 5-15-minute exposure to 1 bar H<sub>2</sub> at 543 K only slightly reduces the Zn(II), but exposure for several hours to 20 bar H<sub>2</sub>/CO and/or H<sub>2</sub>/CO/CO<sub>2</sub> leads to an average Zn oxidation number of +(0.5-0.6), only slightly increasing to +0.8 in a 20 bar H<sub>2</sub>/CO<sub>2</sub> feed. This means that most of the added Zn is in a zero-valent oxidation state during methanol synthesis conditions. The Zn average coordination number is 8, showing that this phase is not at the surface but surrounded by other metal atoms (whether Zn or Cu), and indicating that the Zn diffuses into the Cu nanoparticles under reaction conditions. The time scale of this process corresponds to that of the generally observed activation period for these catalysts. These results reveal the speciation of the relevant Zn promoter species under methanol synthesis conditions and, more generally, present the use of weakly interacting graphitic supports as an important strategy to avoid excessive spectator species, thereby allowing to study the nature of relevant promoter species.

**Based on**: Dalebout, R.; Barberis L.; Totarella, G.; Turner, S.J.; La Fontaine, C.; de Groot, F.M.F.; Carrier, X.; van der Eerden, A.M.J.; Meirer, F.; de Jongh, P.E. Insight into the Nature of the ZnO<sub>x</sub> Promoter during Methanol Synthesis. *ACS Catal.* **2022**, *12*, 6628-6639.

# 3.1 Introduction

Methanol synthesis is an important, decades-old industrial process. Nowadays, a coprecipitated Cu/ZnO/Al<sub>2</sub>O<sub>3</sub> catalyst is used to hydrogenate CO<sub>2</sub> to methanol in a CO-rich environment. It has been well established that the methanol is predominantly formed from CO<sub>2</sub> rather than from CO. The role of the CO is to supply CO<sub>2</sub> *via* the reaction with water, which also keeps the water level low. <sup>60,94,104–106,291</sup> Generally accepted is that Cu is the main active component where ZnO<sub>x</sub> plays a crucial role in promoting the catalyst activity with about an order of magnitude. <sup>39,88–91,291</sup> Yet, the exact role of the ZnO<sub>x</sub> promoter is still under debate <sup>219–221</sup>, especially due to a lack of detailed knowledge on the ZnO<sub>x</sub> speciation, structure, and its interaction with Cu under the typical methanol synthesis conditions at 473-573 K and 20-100 bar <sup>86,87</sup>.

Various hypotheses exist to explain the role of the  $ZnO_x$  promotion. It has been suggested that  $ZnO_x$  increases the Cu dispersion and thereby the active Cu surface area  $^{222,223}$  and that the promoter supplies hydrogen to the Cu surface by spillover  $^{225,226}$ . The oxidation state of  $ZnO_x$  can also play a role in the morphological change of small Cu particles due to a varying degree of the  $Cu-ZnO_x$  interaction, thereby varying the exposed Cu surface planes.  $^{224}$  However, by now it is universally accepted that the coverage of Cu nanoparticles with partially reduced ZnO is essential for the enhanced methanol production. An open question is still whether the promotion is due to the formation of a  $ZnO_x$  layer on the Cu particles  $^{225,227,228,292}$ , to the formation and migration of  $ZnO_x$  interaction  $^{193,225,227}$ . Research is typically performed on catalysts supported on metal oxides, which may obscure the active  $ZnO_x$  phase by the formation of mixed  $ZnO_x$  metal oxides, and hence may significantly differ from the relevant speciation and distribution of the active fraction of the  $ZnO_x$  promoter.

It is accepted that  $ZnO_x$  (partially) covers the Cu nanoparticles in reducing conditions. The fractional coverage of Cu with  $ZnO_x$  during reaction conditions is mainly influenced by three factors: the feed composition, governing the degree of  $ZnO_x$  reduction, the  $ZnO_x$  loading, and the Cu particle size. For example, Kuld *et al.*  $^{220}$  showed that by applying various feeds during catalyst activation an optimal Zn coverage over a Cu surface of 0.47 was achieved using a  $Cu/ZnO/Al_2O_3$  catalyst of constant composition during  $CO/CO_2$  hydrogenation at ambient pressure. Yet, contradictory results for the optimal Zn coverage were reported by varying the  $ZnO_x$  loading under different reaction conditions.  $^{294,295}$  Also in a pure  $H_2/CO_2$  feed an optimal Zn coverage of 0.20, or an atomic Zn/Cu ratio of 1.2-1.6, was reported for Cu/ZnO catalysts.  $^{225,227,228,296,297}$  The question remains what the actual state of the  $ZnO_x$  is during working conditions in different feeds at high pressure, *e.g.*  $H_2/CO$  feed, syngas enriched with a relevant amount of  $CO_2$  (2-6 vol%  $^{60,94,104,105,291}$ ), or an  $H_2/CO_2$  feed.

Much effort has been devoted to studying the interaction and oxidation state of ZnO<sub>x</sub> species in CuZn-based catalysts in the calcined state <sup>295,298–300</sup> and before/after <sup>96,230,299,301–303</sup> or during <sup>221,298,304–307</sup> exposure to reducing atmospheres at (near-)ambient pressures (up to 8 bar). Based on those results, it is still inconclusive whether the oxidation state of ZnO<sub>x</sub> slightly changes <sup>301,302,304</sup> and whether Cu–Zn alloys are formed <sup>221,303</sup> or not <sup>299,301,305,306</sup>. For example, recent studies reported the formation of a Cu–Zn alloy in a Cu/ZnO/Al<sub>2</sub>O<sub>3</sub> catalyst during a (CO<sub>2</sub>/)H<sub>2</sub> treatment at 15 bar and 533 K <sup>80</sup>, but this alloy formation was absent for a Cu/ZnO/faujasite catalyst with almost a 1-to-1 ratio of Cu and Zn <sup>81</sup>. A unique tool that since very recently allows to gain insight into the Zn oxidation state and speciation under realistic high-pressure conditions and in the working state is X-ray absorption spectroscopy (XAS). Very recently Divins *et al.* <sup>292</sup> published an interesting *operando* study at 20-40 bar in a CO<sub>2</sub>-enriched syngas feed using silica and alumina supports, ascribing the active ZnO<sub>x</sub> speciation to a distorted ZnO<sub>x</sub> phase with a maximum content of 9 at% Zn<sup>0</sup> atoms but most of the Zn species present as metal oxides.

Summarizing: a major obstacle until now to know the nature of the active state of the  $ZnO_x$  promoter is that typically a large fraction of Zn spectator species is present as formates, oxides, or mixed metal phases, and is often due to the interaction with the oxidic catalyst support.  $^{18,80,81,96,232,234,292}$  Hence, the active promoter species represent only a fraction of the Zn species present in the system, and averaged information, such as the Zn oxidation state and coordination number, are not representative for the active  $ZnO_x$  promoter species.

We present graphitic carbon as a support with very limited interaction with Cu and  $ZnO_x$ .  $^{18,232}$  In combination with a relatively low  $ZnO_x$  loading it allows us to study specifically the  $ZnO_x$  in contact with the Cu nanoparticles during methanol synthesis and its speciation and interaction with the Cu, based on time-resolved XAS experiments under working conditions, also as a function of different feed compositions.

# 3.2 Experimental

# 3.2.1 Catalyst synthesis

A series of CuZnO<sub>x</sub>/C catalysts, with similar Cu weight loadings  $(8.0 \pm 0.4 \text{ wt}\%)$  but varying Zn/Cu molar ratios, were prepared via incipient wetness impregnation following a published method. <sup>291</sup> In brief, powdered high surface area graphite (TIMREX E-HSAG500, TIMCAL Graphite & Carbon) was dried at ca. 443 K under dynamic vacuum for 1.5 h. The support was impregnated at room temperature under static vacuum to 95% of the total pore volume with an acidified aqueous solution containing 1.8 M copper nitrate (Acros Organics, 99%) and 0-1.8 M zinc nitrate (Sigma Aldrich,  $\geq$ 99%). Subsequently, the impregnated support was dried overnight at room temperature under dynamic vacuum and further reduced at 503 K (ramp 2 K min<sup>-1</sup>) in a 100 mL min<sup>-1</sup> flow of

20 vol%  $H_2/N_2$  for 2.5 h. After cooling to room temperature, the sample was exposed to a flow of 100 mL min<sup>-1</sup> flow of 5 vol%  $O_2/N_2$  for 1 h, heated to 473 K with a ramp of 1 K min<sup>-1</sup> and oxidized at 473 K in 15 vol%  $O_2/N_2$  for 1 h.

The Cu/C (8.1 wt% Cu), ZnO<sub>x</sub>/C (9.9 wt% ZnO) and CuZnO<sub>x</sub>/SiO<sub>2</sub> catalysts were synthesized following the same procedure as for the CuZnO<sub>x</sub>/C catalysts using the respective metal nitrate(s). Only for the ZnO<sub>x</sub>/SiO<sub>2</sub> catalyst (10.0 wt% ZnO) a different heat treatment was applied: the dried impregnate was heated to 723 K (ramp 2 K min<sup>-1</sup>) in a 200 mL min<sup>-1</sup>  $g_{cat}$ -1 flow of 2 vol% NO/inert for 1 h. <sup>289</sup> Both SiO<sub>2</sub>-based catalysts were supported on silica gel (25-75  $\mu$ m, Davisil<sup>TM</sup>, grade 643, Sigma Aldrich,  $\geq$ 99%). All catalysts are named CuZn-X/C or CuZn-X/SiO<sub>2</sub>, in which X represents the molar Zn/(Cu + Zn) ratio expressed as percentage. Please note that the 6-CuZnO<sub>x</sub>/C catalyst discussed in **chapter 2** is the same as the CuZn-35/C catalyst in this chapter. A commercial Cu/ZnO/Al<sub>2</sub>O<sub>3</sub>/MgO catalyst from Alfa Aesar, containing a Cu/Zn/Al/Mg ratio of 63.8/24.8/10.1/1.3 wt%, served as a reference.

#### 3.2.2 Catalyst characterization

 $N_2$  physisorption isotherms were recorded on a Micromeritics TriStar II Plus apparatus at 77 K. The samples were first dried at 443 K (or at 573 K for the SiO<sub>2</sub> support) under an N<sub>2</sub> flow overnight. The BET surface area was determined according to the IUPAC procedure. <sup>278</sup> A Barrett-Joyner-Halenda (BJH) analysis was applied to obtain pore size distributions, using either a carbon black or Harkins-Jura statistical thickness curve. The single-point total pore volume  $V_{\text{tot}}$  was determined at  $p/p_0 = 0.995$ . Integration of the differential pore size distribution (derived from the adsorption branch) between 2 and 50 nm yielded the mesoporosity. The micropore volume  $V_{\text{micro}}$  was calculated using the t-plot method.

**Transmission electron microscopy (TEM) imaging** was performed on an FEI Tecnai 20 apparatus, operating at 200 kV. High-angle, annular, dark-field scanning transmission electron microscopy (HAADF-STEM) images were obtained on a Thermo Fisher Scientific Talos F200X apparatus, operating at 200 kV. With the same apparatus chemical maps were recorded using energy-dispersive X-ray (EDX) detectors. The EM samples for the carbon-supported catalysts were prepared by deposition of an ethanolic dispersion of the catalyst onto holey carbon film-coated Cu or Au grids (Agar, 300 mesh). As adequate TEM measurements on the silica-supported catalysts as such were not possible, they were ultramicrotomed. The catalysts were embedded in a two-component epoxy resin (Struers, EpoFix), which was heated overnight at 333 K, and cut in 60-70 nm slices on a Leica Ultracut E. The slices were deposited on the aforementioned Au grids, which were made hydrophilic by glow discharge in a Cressington 208 carbon coater. At least 350 individual particles at various locations within the sample were measured to determine the

number-averaged Cu(Zn)O<sub>x</sub> particle sizes  $(d_N)$  with the standard deviation  $(s_N)$  representing the width of the size distribution. These mean sizes were translated into surface-averaged particle sizes  $(d_S)$  via  $d_S \pm s_S = \sqrt{\frac{1}{N}\sum_{i=1}^N d_i^2} \pm \sqrt{\frac{1}{N-1}\sum_{i=1}^N (d_i-d_S)^2}$ , with  $d_i$  the i-th particle size and N the total number of measured particles. Only the relevant part of the lognormal distribution (>1% of maximum) was considered for the calculation of the average particle sizes.

**Powder X-ray diffractograms** were recorded on a Bruker AXS D2 Phaser diffractometer at room temperature with a fixed divergence slit. Samples were irradiated by Co K $\alpha$  radiation ( $\lambda$  = 1.790 Å) at 30 kV and 10 mA. Not only fresh catalysts, but also used catalysts were analyzed. These were exposed to ambient conditions, separated from the SiC in the reactors, finely ground, and characterized without any further pretreatment.

Temperature-programmed reduction (TPR) profiles were obtained on a Micromeritics AutoChem II 2920 apparatus. The sample (50 mg, <75 μm granulites) was first dried *in situ* under an Ar flow at 1 L min<sup>-1</sup> g<sub>sam</sub>-<sup>1</sup> at 393 K for 30 min. The cooled sample was then exposed to 5 vol% H<sub>2</sub>/Ar at the same flow and heated to 873 K with a ramp of 2 K min<sup>-1</sup>. The formed H<sub>2</sub>O was captured with a dry ice/isopropanol cold trap, and the reduction profiles were recorded with a thermal conductivity detector (TCD). The H<sub>2</sub> reduction profiles of the CuZn-15/C and CuZn-15/SiO<sub>2</sub> catalysts (25-75 μm) were also obtained at a temperature ramp of 5 K min<sup>-1</sup> in a 0.5 L min<sup>-1</sup> g<sub>sam</sub>-<sup>1</sup> flow without prior drying to directly compare with the H<sub>2</sub> treatment during XAS.

Time-resolved, *operando* X-ray absorption spectroscopy (XAS) measurements on simultaneously the Cu (8979 eV) and Zn K-edges (9659 eV) were performed at the SOLEIL synchrotron (ROCK beamline). <sup>308</sup> Typically, *ca.* 3.5 mg catalyst (25-75 μm sieve fraction) was loaded in a quartz capillary (ID 1.5 mm, 50 μm thick), which was tightly glued into a frame connected to gas feed lines. A hot gas blower (FMB Oxford) ensured heating of the capillary. After the capillary was leak-checked at 20 bar, XAS data was obtained in He at room temperature. The catalyst was exposed to a 15 mL min<sup>-1</sup> flow of 20 vol% H<sub>2</sub>/He and heated to 543 K (ramp 5 K min<sup>-1</sup>) with a hold time of 5-15 min at ambient pressure. After the H<sub>2</sub> treatment the capillary was cooled to 453 K prior to introducing a syngas feed (H<sub>2</sub>/CO/He = 60/30/10 vol%) at 15 mL min<sup>-1</sup>. Within *ca.* 100 min the capillary was pressurized to 20 bar, and subsequently the temperature was increased to 533 K (ramp 5 K min<sup>-1</sup>) and held for 160 min. For the CuZn-15/C catalyst the feed was subsequently switched to H<sub>2</sub>/CO/CO<sub>2</sub>/He = 60/27/3/10 vol%, recording XAS spectra for 160 min, and after that to H<sub>2</sub>/CO<sub>2</sub>/He = 67.5/22.5/10 vol%. Finally, XAS data were recorded after cooling to room temperature at 20 bar and in the last experienced gas atmosphere.

During all treatments XAS spectra were recorded while scanning the X-ray energy from 8.70 to 10.65 keV (20 averaged scans per 10 s) in transmission mode using a Si(111) quick-XAS monochromator. Methanol production and gas compositions were recorded with a mass

spectrometer (Cirrus, MKS) at ambient pressure. If the measurement involved CO, a conditioned carbonyl trap was used upstream the capillary to capture metal carbonyl compounds. ZnO (abcr, 99.999%), CuO (Sigma Aldrich, 99.999%), Cu<sub>2</sub>O (Sigma Aldrich,  $\geq$ 99.99%), in-house synthesized Zn<sub>2</sub>SiO<sub>4</sub>, all mixed with boron nitride (Sigma Aldrich, 98%), and Cu (6  $\mu$ m) and Zn (5  $\mu$ m) foils were used as references, with their spectra being recorded at room temperature under air.

The macrocrystalline  $Zn_2SiO_4$  reference was prepared via a solid-state reaction based on the review of Takesue  $et~al.~^{309}$  ZnO (0.73 g, Puratronic®, abcr Chemicals, 99.999%) and an excess of silica gel (0.59 g, Davisil<sup>TM</sup>, grade 643, Sigma Aldrich,  $\geq$ 99%) (Zn/Si molar ratio of 1/1.1) were finely ground with a pestle and mortar for at least 20 min. The mixed powder was heated in a tubular furnace to 1373 K (ramp 5 K min<sup>-1</sup>) in an N<sub>2</sub> flow for 4 h. After the solid-state reaction 1.25 g Zn<sub>2</sub>SiO<sub>4</sub> was obtained and finely ground before use. **Figure 3.1** shows X-ray diffraction (XRD) patterns of the initial ZnO + SiO<sub>2</sub> mixture and the final Zn<sub>2</sub>SiO<sub>4</sub> material. Crystalline Zn<sub>2</sub>SiO<sub>4</sub> was obtained with only a minor amount of the initial powders present. The excess of silica gel led to a higher conversion level of the ZnO into Zn<sub>2</sub>SiO<sub>4</sub>, whereas the leftover amorphous SiO<sub>2</sub> did not influence the XAS data on the Zn K-edge. All patterns were measured on a Bruker D8 Advance apparatus with Co K $\alpha$  radiation ( $\lambda$  = 1.790 Å) at 30 kV and 40 mA with a variable divergence slit.

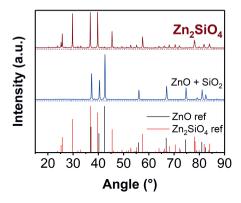


Figure 3.1 XRD patterns of the in-house synthesized  $Zn_2SiO_4$  material and the initial  $ZnO + SiO_2$  mixture (solid lines), alongside with ZnO and  $Zn_2SiO_4$  reference data (bars). Note that the diffraction peaks of the amorphous (SiO<sub>2</sub>) are barely visible.

The XAS spectra were processed using the Demeter software package. <sup>310</sup> Spectra were normalized and background-subtracted by fitting a line to the pre-edge region and cubic splines to the post-edge region. Spectra were energy-aligned using the Cu and Zn metal foil reference spectra, located between the second and third ionization chambers, and measured simultaneously with the samples.

Prior to analyses of the XAS data at the XANES region, the number of principal components was assessed by principal component analysis (PCA) of the complete time series. In all cases the cumulative variance explained (CVE) of the first three principal components covered more than 99.99% of the variance of the data, suggesting that three principal components were sufficient to describe the data by multivariate curve resolution (MCR). Note that a principal component in PCA is not a pure chemical phase but can represent a linear combination of pure chemical components in a constant ratio throughout the time series.

The *in situ* XAS data at the XANES region was analyzed with linear combination fitting (LCF) using the Athena software. For the Cu K-edge, a spectrum of the macrocrystalline Cu<sub>2</sub>O reference at 298 K was used for the Cu<sup>+</sup> state, while representative samples were used as references for the Cu<sup>+</sup> and Cu<sup>0</sup> states: a spectrum of the sample recorded at 298 K in a He atmosphere and recorded at 543 K in an H<sub>2</sub>/He atmosphere, respectively. For the Zn K-edge, the average Zn oxidation number (ON) was estimated using Zn metal foil as reference for the Zn<sup>0</sup> state and macrocrystalline ZnO and Zn<sub>2</sub>SiO<sub>4</sub> as reference for the Zn<sup>2+</sup> state. The LCF was performed in Athena on the normalized  $\mu(E)$  spectra in the region between -20 to 30 eV from the absorption edge.

MCR with constraints was performed on the data matrix using alternating least squares (ALS), employing an in-house code written in Matlab®. MCR-ALS decomposes a matrix  $\mathbf{X}$  such that  $\mathbf{X} = \mathbf{CS} + \mathbf{E}$ , where  $\mathbf{E}$  is minimized using ALS. Here,  $\mathbf{X}$  represents the data arranged in a way that every row is a spectrum recorded at various times, *i.e.* different row index. MCR-ALS allows to set constraints for the matrix decomposition, which, in comparison to singular value decomposition (SVD) used in PCA, can help in obtaining more meaningful eigenspectra (or spectral profiles) in  $\mathbf{S}$  in terms of spectra that more closely resemble spectra of pure chemical components. Here, the constraints that are especially useful in the analysis of time-resolved XAS data are non-negativity and closure, assuming that spectra do not contain negative values and that the concentration of the element studied is constant. MCR-ALS will then decompose the data matrix into non-negative eigenspectra in  $\mathbf{S}$  and concentration profiles in  $\mathbf{C}$  that sum to unity. We analyzed the data using these constraints and three components, as determined by PCA as mentioned before. Based on these results, we further varied the number of components between two and four and the number of iterations, thereby comparing the obtained MCR-ALS eigenspectra with the reference data, before selecting the final number of components and iterations.

The EXAFS data was fitted using the Artemis software. The amplitude reduction factor  $(S_0^2)$  was calculated from the EXAFS analysis of the known reference materials and used as a fixed parameter during the fitting procedure for the spectra recorded at room temperature. The coordination number (CN), energy correction term ( $\Delta E_0$ ), the Debye-Waller factor ( $\sigma^2$ ), and the shift in the interatomic distance compared to the FEFF model structure ( $\Delta R$ ) were used as free parameters during the fitting. Multiple k-weight fittings were employed to derive the structural parameters. The

typical distance fit range was 1.4-3.0 Å for Cu K-edge fitting and 1.0-2.3 Å for Zn K-edge fitting in the Fourier transform. No phase correction was applied.

#### 3.2.3 Catalyst testing

A 16-reactor setup (Flowrence, Avantium) was used to evaluate the catalyst performance for methanol synthesis at 40 bar(g) and 533 K for at least 100 h. The powdered catalysts were pressed, crushed, and sieved into granules of 75-150  $\mu$ m and were loaded (3-180 mg) in the stainless-steel reactors (ID 2.6 mm). The catalysts were diluted with SiC (212-245  $\mu$ m fraction, Alfa Aesar,  $\geq$  98.8%, 46 grit), resulting in SiC contents between 22 and 88 vol% of the total packed catalyst bed. <sup>279</sup> The SiC had been previously calcined at 1073 K for 10 h, washed with 65 wt% HNO<sub>3</sub>, rinsed with MilliQ water until pH 7 was reached, and dried in static air at 393 K overnight. The varying catalyst loadings enabled us to achieve similar CO (+ CO<sub>2</sub>) conversions (*ca.* 10%). The difference in sieve fractions between the catalysts and diluent facilitated post-analysis by EM and XRD.

An in situ reduction was performed in 2.8 mL min-1 of 5 vol% H<sub>2</sub>/N<sub>2</sub> at 523 K for 3 h after which the temperature was lowered to 393 K. The reactors were exposed to a 2.2 mL min<sup>-1</sup> flow of CO<sub>2</sub>-free syngas  $(H_2/CO/He =$ 60/30/10 vol%) or CO<sub>2</sub>-enriched syngas  $(H_2/CO/CO_2/He =$ 60/27/3/10 vol%), leading to a flow of 0.2-2.1 L min<sup>-1</sup> gcu<sup>-1</sup> and a gas-hourly space velocity (GHSV) of 400-53,200 h<sup>-1</sup>. The reactors were pressurized to 40 bar(g), heated to 533 K (ramp 2 K min<sup>-1</sup>). and the reaction was run for at least 100 h, Alternatively, the ZnOx/C and ZnOx/SiO2 catalysts were alternately exposed to the pre-defined H<sub>2</sub>/CO/He and H<sub>2</sub>/CO/CO<sub>2</sub>/He feeds. A tri-phase carbonyl trap (activated carbon, y-Al<sub>2</sub>O<sub>3</sub>, ZnO) was located upstream of the CO feed to remove metal carbonyls and sulfur species. Products were periodically analyzed by online gas chromatography every 15 min. After catalysis, the samples were slowly exposed to air at 393 K. Details on the calculations of catalyst activity and selectivity are given in section 2.2.5. The stability of the catalyst activity was calculated by **equation (3.1)**.

Stability = 
$$\frac{X_{\text{CO (+ CO_2)}}^{\text{alt}}(t = 100 \text{ h})}{X_{\text{CO (+ CO_2)}}^{\text{alt}}(t = 50 \text{ h})} \cdot 100\% \text{ [\%]}$$
(3.1)

## 3.3 Results and discussion

# 3.3.1 Structural properties of the catalysts

**Figure 3.2** shows representative electron micrographs, including elemental maps, of  $CuZn-15/SiO_2$  (frames A-C) and CuZn-15/C (frames D-F) catalysts both with 8.1 wt% Cu and 1.8 wt% ZnO. Note that the number in the catalyst names refers to the Zn/(Cu + Zn) fraction of

15 at%. The silica as support consists of aggregated spheres of ca. 8 nm, whereas the graphitic carbon has a sheet-like morphology of a few nanometers thick. Both materials have a high specific surface area (>260 m<sup>2</sup> g<sup>-1</sup>) and ca. 50-60% of the total pore volume consists of mesopores (see also **figure 2.2** in the previous chapter), making these materials suitable supports for model catalyst studies.

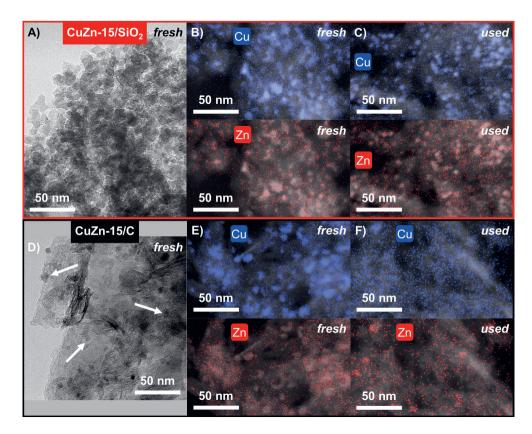


**Figure 3.2** Representative EM images of the (A-C) CuZn-15/SiO<sub>2</sub> and (D-F) CuZn-15/C catalysts. Frames A and D involve BF-TEM, and frames B-C and E-F involve HAADF-STEM with an elemental map overlay. Number-averaged Cu(Zn)O<sub>x</sub> particle sizes are  $3.4 \pm 0.8$  nm (frames B-C) and  $4.2 \pm 1.7$  nm (frame D) for the fresh CuZn-15/SiO<sub>2</sub> and CuZn-15/C catalysts, respectively. The used catalysts (frames C and F) are after 150 and 100 h of catalysis in an  $H_2/CO/CO_2$  feed, respectively.

Frame A shows no clear  $Cu(Zn)O_x$  nanoparticles on the silica support, demonstrating that it was challenging to distinguish metal particles on the silica support due to the limited phase contrast. Only by imaging ultramicrotomed slices we were able to obtain a representative HAADF-STEM

micrograph with an elemental map (frame B).  $Cu(Zn)O_x$  particles of ca. 3-4 nm (bright spots) were observed for the  $CuZn-15/SiO_2$  catalyst, corresponding to mainly Cu species (blue dots) and  $ZnO_x$  species (red dots). The distribution of Cu and  $ZnO_x$  looked similar after 150 h of catalysis (frame C), which is probably more representative for the catalyst during catalysis.

When using a graphitic support (frame D)  $\text{CuO}_x$  nanoparticles of ca. 4 nm were clearly discernable by TEM and well-distributed (dark spots indicated with white arrows) on the carbon surface (light grey). The distribution was confirmed by the elemental maps of Cu and Zn species, projected on a HAADF-STEM image (frame E). There was a strong correlation between the location of the Cu nanoparticles and the distribution of the  $\text{ZnO}_x$  species, both in the fresh CuZn-15/C catalyst and after catalysis (frames E-F). The characteristics of the full series carbon-supported  $\text{CuZnO}_x/\text{C}$  catalysts with varying Cu/Zn ratios, both in the fresh and used state, are presented in **table 3.1** and shows similar  $\text{Cu(Zn)O}_x$  particle sizes ( $d_N = 5$ -9 nm) with varying  $\text{ZnO}_x$  loadings. The catalysts were extensively characterized by  $N_2$  physisorption, X-ray diffraction and  $H_2$  reduction profiling, but only a concise discussion is presented for clarity. Overall, we showed that in both catalysts well-distributed  $\text{Cu(Zn)O}_x$  particles of similar size were present and that the relatively thin sheets of graphitic carbon as a model support facilitated the determination of the particle sizes by electron microscopy.

**Table 3.1** Number-averaged  $Cu(Zn)O_x$  particle sizes of the  $CuZnO_x/C$ ,  $CuZn-15/SiO_2$ , and  $ZnO_x/SiO_2$  catalysts in the fresh and used state (after 100 h of catalysis in an  $H_2/CO/CO_2$  feed) by TEM analysis. Independent of the  $ZnO_x$  loading, the number-averaged  $Cu(Zn)O_x$  particle size was 5.1 nm, while with (almost) no  $ZnO_x$  the average size was 8.9 nm. After catalysis, the  $Cu(Zn)O_x$  particles grew to an average of 9.5 nm in all catalysts.

catalyst	loadi	ng (wt%)	d <sub>N</sub> [CuO] (nm)		
cuturyst	Cu	ZnO	fresh	used	
Cu/C	8.1	0	$9.3 \pm 3.3$	11.0 ± 6.7 a	
CuZn-1/C	8.4	0.1	$8.5 \pm 3.7$	$10.8 \pm 5.8$ a	
CuZn-5/C	8.4	0.6	$5.1 \pm 2.4$	$11.8 \pm 9.0$	
CuZn-15/C	8.1	1.8	$4.2 \pm 1.7$	$10.0\pm6.2$	
CuZn-25/C	7.9	3.4	$5.6 \pm 2.2$	$6.3 \pm 2.3$ a	
CuZn-35/C	7.7	5.3	$5.4 \pm 1.8$	$6.9 \pm 3.8$	
CuZn-50/C	7.4	9.5	$5.1 \pm 2.3$	$9.9 \pm 7.4$	
$CuZn-15/SiO_2$	8.0	1.8	$3.4 \pm 0.8$ <sup>b</sup>	$5.9 \pm 2.7$ $\alpha$	

<sup>&</sup>lt;sup>a</sup> After 150 h of catalysis. <sup>b</sup> Obtained from HAADF-STEM images.

# 3.3.2 Influence of the support and feed composition

In this section we compare the catalytic performance of  $CuZn-15/SiO_2$  and CuZn-15/C catalysts, which were prepared and tested in the same way and have similar  $Cu(Zn)O_x$  particle sizes and  $ZnO_x$  loadings but only have a different support. **Figure 3.3** shows the methanol formation rate under industrially relevant temperature and pressure as a function of time in an  $H_2/CO$  feed as well as in an  $H_2/CO/CO_2$  feed (mimicking industrially relevant conditions  $^{60,94,104,105,291}$ ). **Table 3.2** provides additional information on the conversion levels, turnover frequencies (TOFs), and  $Cu(Zn)O_x$  particle growth during catalysis.

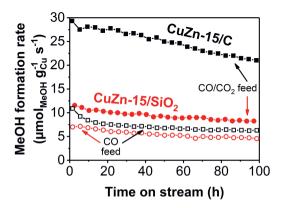


**Figure 3.3** Methanol formation rate of the CuZn-15/SiO<sub>2</sub> (red circles) and CuZn-15/C (black squares) catalysts in a CO<sub>2</sub>-free (open symbols) or -enriched (filled symbols) syngas feed. The data points of the CuZn-15/C catalyst in  $H_2/CO$  and  $H_2/CO/CO_2$  are the average over 4 and 2 separate runs, respectively. Conditions: 533 K, 40 bar(g),  $H_2/CO/He = 60/30/10$  vol% or  $H_2/CO/CO_2/He = 60/27/3/10$  vol%.

The TOF for the carbon-supported catalyst  $(3.9-15.3 \cdot 10^{-3} \text{ s}^{-1})$  was always higher than for the silicasupported catalyst  $(1.6-3.0 \cdot 10^{-3} \text{ s}^{-1})$  (**table 3.2**). Strikingly, the beneficial effect of CO<sub>2</sub> enrichment of the syngas feed on the methanol formation rate was much larger for the CuZn-15/C catalyst (factor 3.5) than for the CuZn-15/SiO<sub>2</sub> catalyst (factor 1.7) (**figure 3.3**). Upon CO<sub>2</sub> enrichment the methanol selectivity increased from 83 to 99 %c and from 85 to 98 %c after 100 h on stream for, respectively, the CuZn-15/SiO<sub>2</sub> and CuZn-15/C catalysts, in line with earlier published results  $^{291}$  and significantly higher than recently reported for CuZnO<sub>x</sub>/Al<sub>2</sub>O<sub>3</sub>  $^{292}$ . In literature enhancement factors upon CO<sub>2</sub> enrichment of 2-4 are reported for Cu/ZnO/Al<sub>2</sub>O<sub>3</sub> catalysts depending on the reaction conditions  $^{104,105,232}$ , and differences were also observed between silica- and aluminasupported CuZnO<sub>x</sub> particles  $^{292}$ . However, our results, obtained in the same reaction conditions and with similar Cu particles sizes, unequivocally proves that promotion with a given amount of ZnO<sub>x</sub>

**Table 3.2** Catalytic performance of the  $CuZn-15/SiO_2$  and CuZn-15/C catalysts, with or without  $CO_2$  in the feed. Errors represent the standard deviation between 2 or 4 separate measurements unless stated otherwise. Conditions: 533 K, 40 bar(g),  $H_2/CO/He = 60/30/10$  vol% or  $H_2/CO/CO_2/He = 60/27/3/10$  vol%.

catalyst	CO <sub>2</sub>	flow	CO (+ CO <sub>2</sub> ) conv. (%)		TOF (10 <sup>-3</sup> s <sup>-1</sup> ) <sup>a</sup>	
	in feed	(mL min <sup>-1</sup> g <sub>cat</sub> <sup>-1</sup> )	50 h	100 h	initial <sup>b</sup>	final <sup>c</sup>
CuZn-15/SiO <sub>2</sub>	no	21.1	12.2	10.4	$3.0 \pm 0.7$	$1.6 \pm 0.7$
	yes	63.8	5.8	5.0	$2.6 \pm 0.6$	$3.0\pm1.3~^{d}$
CuZn-15/C	no	$35.2 \pm 0.1$	$9.1 \pm 0.4$	$8.2 \pm 0.3$	$4.9 \pm 1.9$	$3.9 \pm 1.5$
	yes	$87.5 \pm 0.2$	$11.6 \pm 0.3$	$9.6 \pm 0.6$	$11.2 \pm 4.4$	$15.3 \pm 8.4$

<sup>&</sup>lt;sup>a</sup> Error reflects the width in the CuO particle size distribution. <sup>b</sup> Calculated from the average CuO size in the fresh catalyst and activity at t = 0 h. <sup>c</sup> Calculated from the average CuO size in the used catalyst and activity at t = 100 h. <sup>d</sup> After 150 h of catalysis.

is much more efficient using a carbon than using an oxide support. Under all conditions the  $ZnO_x$  promotion is more effective in the CuZn-15/C catalyst than in the  $CuZn-15/SiO_2$  catalyst, but the effect is especially pronounced with  $CO_2$  enrichment of the feed.

It is known that  $ZnO_x$  itself can also act as a methanol synthesis catalyst, albeit with a lower activity than in combination with Cu.  $^{87,217,218}$  Supported  $ZnO_x$  species without Cu were investigated under similar reaction conditions to check if the catalysis by  $ZnO_x$  on graphitic carbon contributed significantly. The  $ZnO_x/SiO_2$  and  $ZnO_x/C$  catalysts have the same ZnO loading (both 10 wt%) with  $ZnO_x$  particle sizes of 7.7 and ca. 4.5 nm, respectively. **Figure 3.4** shows the CO (+ CO<sub>2</sub>) conversion *versus* time on stream in the presence and absence of  $CO_2$  and for both an oxidic and a carbon support.

Irrespective of the syngas composition, carbon-supported  $ZnO_x$  species were more active than silica-supported  $ZnO_x$  species, even when taking the slightly different Zn surface areas into account. TEM analysis showed no Zn-based nanoparticles in the fresh  $ZnO_x/SiO_2$  catalyst, whereas they were present in the  $ZnO_x/C$  catalyst. During pure CO hydrogenation the  $ZnO_x/C$  catalyst had a significant conversion of ca. 2% (of which ca. 1.3% was methanol). The activity of both supported  $ZnO_x$  species clearly decreased in the presence of  $CO_2$ . The conversion level was restored when switching back to an  $H_2/CO$  feed. This demonstrates that the negative  $CO_2$  effect on the conversion is not related to e.g. irreversible changes in the catalyst morphology but can be attributed to the significant reduction of ZnO in a  $CO_2$ -free feed, making it a more efficient methanol synthesis catalyst. Yet, the activity of the supported  $ZnO_x$  was too small to explain the overall effects of  $CO_2$ -enrichment in methanol synthesis of  $CuZnO_x$ -based catalysts. Nevertheless, these results clearly show that an oxide support has a strong interaction with the  $ZnO_x$  and leads to a different speciation than for the weaker interacting carbon supports.

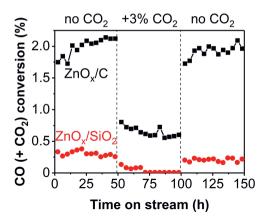


**Figure 3.4** CO (+ CO<sub>2</sub>) conversion of silica- and carbon-supported ZnO<sub>x</sub> (10 wt%) in various syngas compositions. Label '+3% CO<sub>2</sub>' in the total feed corresponds to a CO<sub>2</sub>/(CO + CO<sub>2</sub>) volume fraction of 0.10. Conditions: 533 K, 40 bar(g),  $H_2/(CO + CO_2)/He = 60/30/10$  vol%, 21.9 mL min<sup>-1</sup>  $g_{cat}$ -1.

#### 3.3.3 Influence of the ZnO<sub>x</sub> loading on activity and stability

For the carbon-supported catalysts we investigated in more detail the effect of the  $ZnO_x$  loading on the activity and stability of supported Cu nanoparticles. **Figure 3.5** shows the specific activity as a function of the  $ZnO_x$  loading in a syngas atmosphere with and without  $CO_2$  (please note the logarithmic scale) for ca. 5.1 nm Cu nanoparticles supported on either a carbon support (black lines)

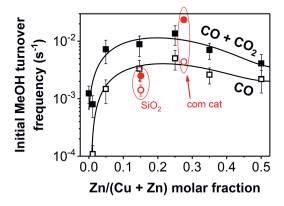


**Figure 3.5** Initial methanol turnover frequency (TOF<sub>MeOH</sub>) of CuZnO<sub>x</sub>/C (black squares) and metal oxide-supported (red circles) catalysts in an  $H_2/CO$  (open symbols) or an  $H_2/CO/CO_2$  (filled symbols) feed (at t=0). 'SiO<sub>2</sub>' = CuZn-15/SiO<sub>2</sub> catalyst. 'com cat' = commercial, co-precipitated Cu/ZnO/Al<sub>2</sub>O<sub>3</sub>/MgO catalyst (58 wt% Cu, ca. 10 nm CuO particles). Conditions: 533 K, 40 bar(g),  $H_2/CO/He = 60/30/10$  vol% or  $H_2/CO/CO_2/He = 60/23/7/10$  vol%.

or an oxide support (red markers). The activity increased when  $CO_2$  was in the feed for all studied  $ZnO_x$ -promoted catalysts. After the initiation period all catalysts had a methanol selectivity >97% c in  $CO_2$ -enriched syngas. The highest  $TOF_{MeOH}$  values were obtained for carbon-supported catalysts with Zn/(Cu+Zn) molar fractions between 0.15 and 0.25, irrespective of the presence of  $CO_2$  in the feed. These  $ZnO_x$  loadings are lower than the well-established optimal loading for the commercially used  $Cu/ZnO/Al_2O_3/MgO$  methanol synthesis catalyst as well as for other oxide-based Cu catalysts in literature (Zn/(Cu+Zn) content of 29-47 at%). 86.89,220,225,227,228,284,294-297

Another key factor in catalysis is the stability. In **figure 3.6** this stability is defined as the ratio between the activity after 100 h and after 50 h on stream. The addition of only 5 at%  $ZnO_x$  was sufficient to increase the catalyst stability from  $74 \pm 8\%$  to  $84 \pm 3\%$  upon syngas conversion. Further increasing the  $ZnO_x$  content to 15-35 at% maximized the stability to  $91 \pm 2\%$  and  $83 \pm 3\%$  in an  $H_2/CO$  and  $H_2/CO/CO_2$  feed, respectively. In the most heavily promoted CuZn-50/C catalyst the stability was somewhat lower. We ascribe the stability improvement for intermediate amounts of  $ZnO_x$  to the fact that the presence of 15-35 at%  $ZnO_x$  clearly limited the  $CuZnO_x$  particle growth during catalysis as evident from TEM analysis (**table 3.1**). Hence,  $ZnO_x$  is not only an activity promoter but also a stability promoter for carbon-supported Cu catalysts.

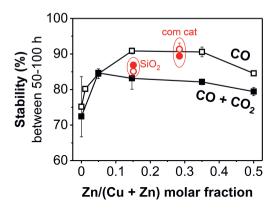


**Figure 3.6** Stability between 50 and 100 h on stream of  $CuZnO_x/C$  catalysts (black squares), the  $CuZn-15/SiO_2$  catalyst, and a commercial  $Cu/ZnO/Al_2O_3/MgO$  catalyst (com cat) (red circles) in a  $CO_2$ -free or -enriched syngas feed. Error bars represent the standard deviation between two separate measurements. Conditions: 533 K, 40 bar(g),  $H_2/CO/He = 60/30/10$  vol% or  $H_2/CO/CO_2/He = 60/23/7/10$  vol%. After 50 h on stream all catalysts had a CO (+  $CO_2$ ) conversion of Ca. 10%, unless stated otherwise in **table 3.2**.

## 3.3.4 Catalyst evolution during reduction in H<sub>2</sub>

From literature it is known that the coverage of the Cu surface with ZnO<sub>x</sub> species <sup>220</sup> and the reduction degree of these ZnO<sub>x</sub> species <sup>221,301</sup> are parameters that determine the effectiveness of ZnO<sub>x</sub> as a promoter. However, mostly metal oxides are employed to support CuZnO<sub>x</sub> particles, which can result in the formation of spectator species such as zinc silicates and aluminates <sup>39,96,307</sup>, hampering the study of the active fraction of the ZnO<sub>x</sub> promoter. The presence of the mixed Zn metal oxides may hence obscure the results also of *operando* X-ray absorption spectroscopy (XAS) measurements. Hence, our hypothesis was that our use of a carbon support would allow us to much better study the formation, oxidation state, and structure of the relevant ZnO<sub>x</sub> promoter by time-resolved, *operando* XAS at simultaneously the Cu and Zn K-edges at 20 bar and up to 533 K.

A first piece of information about the interaction between  $CuO_x$  and  $ZnO_x$  species can be derived from the reduction profiles. **Figure 3.7** shows the *ex situ*  $H_2$  reduction profiles of the  $CuZn-15/SiO_2$  and CuZn-15/C catalysts. The theoretically maximum Cu surface coverage by a monolayer of Zn atoms is 75-95% for these catalysts with 15 at%  $ZnO_x$ . The maximum CuO reduction temperature  $(T_{max})$  as well as the offset temperature for reduction  $(T_{offset})$  were clearly lower for the CuZn-15/C catalyst than for the  $CuZn-15/SiO_2$  catalyst  $(T_{max})$  of 465 vs 475 vs 475 vs 434 vs 434 vs 7 respectively). Hence, the CuO is more easily reduced on a carbon support than on a silica support. We ascribe this to a stronger interaction of  $CuO_x$  with silica.

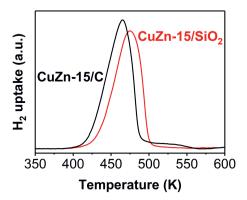


**Figure 3.7** Ex situ reduction in 0.5 L min<sup>-1</sup> g<sub>cat</sub><sup>-1</sup> flow of 5 vol% H<sub>2</sub>/Ar at 5 K min<sup>-1</sup> in 1 bar, mimicking the conditions used during *in situ* H<sub>2</sub> treatment monitored by XAS.

The reducibility of the  $CuZn-15/SiO_2$  and CuZn-15/C catalysts was also investigated with in situ XAS under similar conditions as for the ex situ  $H_2$  treatments. Time-resolved X-ray absorption spectra

at the Cu K-edge (we refer the interested reader to **figure S3.1** at the end of this chapter) were analyzed by fitting linear combinations of the macrocrystalline references to extract the Cu oxidation state evolutions, showing that the CuO species in both catalysts were fully reduced to Cu<sup>0</sup> *via* the formation of Cu<sup>+</sup> upon an H<sub>2</sub> treatment up to 543 K for 5-15 min. This was confirmed by a more in-depth study using multivariate analysis in which no prior information on the component spectra was imposed but which yielded eigenspectra that corresponded well to the macrocrystalline Cu references (see **figure S3.1**). This full reduction of CuO in ZnO<sub>x</sub>-promoted CuO nanoparticles has also been reported in literature. <sup>221,292,306,311</sup>

During the H<sub>2</sub> treatment we also studied changes in the ZnO<sub>x</sub> oxidation state by *in situ* XAS. **Figure 3.8** presents the time-resolved, normalized X-ray absorption near edge structures (XANES) and first derivatives at the Zn K-edge before and upon the H<sub>2</sub> treatment. We start with ZnO<sub>x</sub> species in the Zn(II) oxidation state for both CuZn-15/SiO<sub>2</sub> (frames A and C) and CuZn-15/C (frames B and D) catalysts, as clear from the comparison to the first derivative of the ZnO reference.

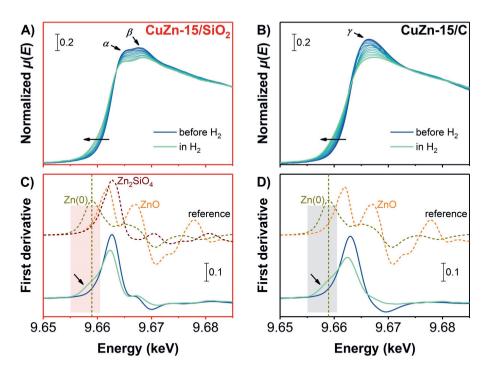


**Figure 3.8** (**A-B**) Time-resolved, normalized absorption and (**C-D**) corresponding first derivatives of *in situ* XANES spectra at the Zn K-edge of the (**A,C**) CuZn-15/SiO<sub>2</sub> and (**B,D**) CuZn-15/C catalysts (solid lines). The spectra are depicted in the initial state at 298 K, during a treatment in 20 vol%  $H_2/He$  up to 543 K in 1 bar each ca. 5.7 min, and finally in an  $H_2$  atmosphere at 453 K. Dashed lines show the first derivatives of the macrocrystalline ZnO, Zn<sub>2</sub>SiO<sub>4</sub>, and Zn foil references at 298 K.

Upon heating in an  $H_2$  atmosphere the Zn K-edge shifted to a lower energy (indicated by the arrows), showing that partially reduced  $ZnO_x$  was formed in both catalysts. The dominant features were still due to the presence of  $Zn^{2+}$ , as clear from the peak at 9.6626 keV on the first derivatives, although its intensity had slightly decreased.

Interestingly, the CuZn-15/SiO<sub>2</sub> catalyst (frame A) displayed two distinct peaks in the normalized XANES spectra (indicated with  $\alpha$  and  $\beta$ ). This peak combination has been reported before and is ascribed to the presence of zinc silicates in a single phase such as Zn<sub>2</sub>SiO<sub>4</sub>, <sup>96,309,312–314</sup> Yet, the CuZn-15/C catalyst (frame B) only had one single, broad peak (indicated with y), in line with a ZnOx phase which was also observed in electron microscopy (figure 3.2, frame E). The estimated, average Zn oxidation number (ON) was slightly lower for the CuZn-15/C catalyst than for the CuZn-15/SiO<sub>2</sub> catalyst (+1.3 vs +1.6). Multivariate analysis on the Zn K-edge is more challenging than for the Cu K-edge, as the XAS signal is lower. Extraction of the components suggests the presence of three distinct phases for the CuZn-15/SiO<sub>2</sub> catalyst (we refer the interested reader to the multivariate analysis in figure S3.2 at the end of this chapter). The eigenspectrum of one of the components resembles that of Zn<sub>2</sub>SiO<sub>4</sub> and its contribution is relatively stable throughout the experiment, indicating the presence of a substantial amount of Zn spectator species in the CuZn-15/SiO<sub>2</sub> catalyst. For the carbon-supported catalyst a significant contribution of a compound with a relatively high absorption at lower energies is found. The phases do not fully match with the macrocrystalline Zn references, which indicates highly dispersed species of low crystallinity and/or not very well-defined mixed phases. This confirms the impact of the support on the ZnO<sub>x</sub> speciation: on an oxidic support the majority of the Zn species is irreducibly bound to the oxidic support and a fraction of the Zn is bound in silicate species, while on a carbon support a highly dispersed ZnOx phase with an average Zn oxidation number significantly lower than +2 is present, which might be due to a high defect density in the ZnO (creating oxygen vacancies and a lower average ZnO state) or possibly the intermixing of fully reduced Zn in the compounds.

## 3.3.5 Nature of the ZnO<sub>x</sub> under working conditions

The *in situ* H<sub>2</sub>-treated catalysts were used for high-pressure methanol synthesis by CO, CO/CO<sub>2</sub>, and CO<sub>2</sub> hydrogenation. Upon catalysis no significant changes in the oxidation state and local coordination of the Cu<sup>0</sup> were detected, in line with results published earlier. <sup>80,230</sup> **Figure 3.9** shows the normalized, *operando* XAS spectra on the Zn K-edge in the XANES region after 160 min in an H<sub>2</sub>/CO feed and after 160 min of subsequent H<sub>2</sub>/CO/CO<sub>2</sub> feed for the CuZn-15/SiO<sub>2</sub> (frames A and C) and CuZn-15/C (frames B and D) catalysts. The numerical results in CO<sub>2</sub> hydrogenation are presented in **table 3.3**. Note that due to the XAS setup restrictions, the amount of catalyst and hence the conversion was limited. For the CuZn-15/SiO<sub>2</sub> catalyst, the ZnO<sub>x</sub> was only slightly further reduced during methanol synthesis (frames A and C) with an estimated Zn ON of +1.1. This was

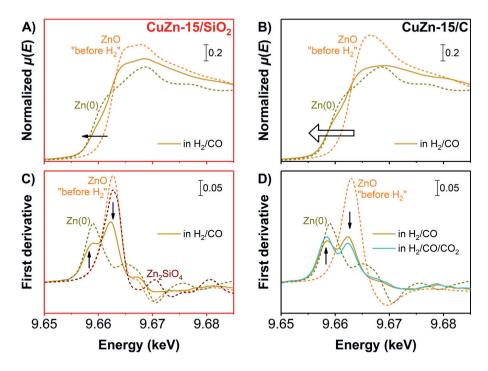


**Figure 3.9** (**A-B**) Normalized absorption and (**C-D**) corresponding first derivatives of *operando*, normalized XANES spectra at the Zn K-edge of the (**A,C**) CuZn-15/SiO<sub>2</sub> and (**B,D**) CuZn-15/C catalysts (solid lines). Depicted during  $H_2/CO$  (and subsequent  $H_2/CO/CO_2$ ) conversion at 20 bar and 533 K, each after 160 min. Gas compositions:  $H_2/CO/He = 60/30/10$  vol% and  $H_2/CO/CO_2/He = 60/27/3/10$  vol%. Dashed lines show the initial catalyst state (ZnO), macrocrystalline  $Zn_2SiO_4$ , and Zn foil at 298 K.

confirmed by a measurement after cooling the catalyst down to room temperature to obtain sharper features (average Zn ON of +1.2). Features that were attributed to zinc silicates were dominant at all stages in the XAS spectra for the CuZn-15/SiO<sub>2</sub> catalyst, as confirmed by multivariate analysis (see also **figure S3.2**). The fact that only a slight reduction of the Zn(II) is observed when using oxidic supports and that the Zn species strongly interact with the support is in line with earlier reports using oxidic supports. <sup>80,96</sup>

Remarkably, in the CuZn-15/C catalyst a large fraction of metallic Zn was formed during methanol synthesis at 20 bar (**figure 3.9**, frames B and D). This observation was confirmed by multivariate analysis, which showed a resemblance of the independently extracted eigenspectrum of the Zn species to the XAS spectrum of metallic Zn (see also **figure S3.2**). The average Zn ON was only ca. +0.6. Assuming that the Zn species are either in the Zn(II) or Zn(0) oxidation state, this means that about 70% of the Zn species was completely reduced. With the addition of 3 vol%  $CO_2$  in the feed, a slightly less reducing gas atmosphere was created. Nevertheless, the Zn ON decreased

**Table 3.3** Average Zn oxidation number (ON) by XANES analysis, and average Zn coordination number (CN) and bond length (R) by EXAFS analysis. The CNs and Rs are determined for the first Zn–O and Zn–M (M = Cu or Zn) shells using a fixed  $S_0^2$  value of the reference materials. The first-shell Zn–O CN of macrocrystalline ZnO is 4 with R = 1.97 Å ( $S_0^2 = 0.89 \pm 0.05$ ), and the first-shell Zn–Zn CN of Zn<sup>0</sup> foil is 12 with R = 2.66 Å ( $S_0^2 = 0.71 \pm 0.07$ ).

stage during	CuZn-15/SiO <sub>2</sub>			CuZn-15/C			
XAS	Zn ON	Zn CN	R (Å)	Zn ON	Zn CN	R (Å)	
before H <sub>2</sub>	$2.00 \pm 0.19$	4 ±1 (Zn–O)	1.97	$1.92 \pm 0.14$	4 ±1 (Zn–O)	1.97	
in H <sub>2</sub>	$1.63 \pm 0.16$	$3.7 \pm 0.4  (Zn-O)$	1.97	$1.27 \pm 0.13$	$3.8 \pm 0.5  (Zn-O)$	1.94	
in H <sub>2</sub> /CO	1.11 ± 0.16	$2.6 \pm 0.5  (Zn-O)$	1.95	0.59 ± 0.11	$1.8 \pm 0.2  (Zn-O)$	1.92	
		$2.2 \pm 1.4 (Zn-M)$	2.55	$0.39 \pm 0.11$	$6.1 \pm 1.3  (\mathrm{Zn-M})$	2.54	
in H <sub>2</sub> /CO/CO <sub>2</sub>	-	-	-	$0.45 \pm 0.11$	$1.7 \pm 0.3  (Zn-O)$	1.92	
					$6.1 \pm 1.3  (\mathrm{Zn-M})$	2.54	
in H <sub>2</sub> /CO <sub>2</sub>	-	-		$0.56 \pm 0.11$	$2.0 \pm 0.2  (Zn-O)$	1.92	
			_		$8.0 \pm 0.8  (\mathrm{Zn-M})$	2.53	
after catalysis	1 22 + 0 16	$2.6 \pm 0.5  (Zn-O)$	1.96	0.70 + 0.10	$2.0 \pm 0.2  (Zn-O)$	1.94	
	$1.22 \pm 0.16$	$2.2 \pm 1.4  (Zn-M)$	2.55	$0.78 \pm 0.12$	$8.0 \pm 0.8  (Zn-M)$	2.54	

further with time to ca. +0.5 after nearly 3 h in the  $H_2/CO/CO_2$  feed, which is probably rather an effect of time than feed composition. Upon switching to a pure  $H_2/CO_2$  feed, the average Zn ON slightly increased to +(0.6-0.8). An increase is expected in a more oxidizing gas feed, as it is also predicted computationally that there will be a slight dependence of the ON (and hence probably the Zn coverage) on the exact feed composition.  $^{220}$  However, even under these conditions most of Zn species remain in the fully reduced state under *operando* conditions. This means that the relatively high Zn ONs in methanol synthesis systems reported until now (in the presence of an oxidic support) can probably be explained by a strong promoter–support interaction, and hence a large fraction of the Zn promoter species is being chemically bound to the oxidic support (and hence inactive). In contrast, our use of a weakly interacting carbon support allows to assess an average Zn oxidation state and coordination number that are much more representative of the true nature of the active ZnO<sub>x</sub> promoter phase during methanol synthesis.

Several hypotheses have been postulated for the  $ZnO_x$  speciation during Cu-catalyzed methanol synthesis. Firstly, the beneficial effect of the  $ZnO_x$  promoter was ascribed to the so-called strong metal–support interaction (SMSI) with slightly reduced ZnO having a high affinity for the  $Cu^0$  metal and partially covering the Cu nanoparticle surface.  $^{301,315}$  Alternative explanations involve the influence of  $ZnO_x$  on the structure of the Cu nanoparticles. For instance, it was proposed that specific steps sites were exceptionally active sites on the  $Cu^0$  surface and that these step sites were stabilized by  $Zn^0$  atoms.  $^{89,108,230}$  Metallic Cu and Zn are quite miscible; up to 33 at% Zn can dissolve

in Cu (solid solution) at temperatures between 473 K and the melting point (>1175 K).  $^{316}$  Some groups proposed that the active site was related to the decoration of Cu<sup>0</sup> nanoparticles with Zn<sup>0</sup> atoms and shallow diffusion of Zn<sup>0</sup> atoms into the Cu surface.  $^{220,224}$  However, results from *ex situ* and low-pressure studies have limited value, as it is known that the catalytically active phase dynamically adjusts to the working conditions.  $^{317}$  A recent high-pressure *operando* study, based on oxidic supports, concluded that a distorted ZnO<sub>x</sub> layer was the majority phase under working conditions with at most 9% of the Zn being present as Zn<sup>0</sup> atoms.  $^{292}$  Our experiments clearly show that, if a strong interaction of the Zn species with an oxide support is avoided, a much more truthful picture of the active fraction of the Zn promoter species under high-pressure methanol synthesis conditions is obtained, and that this fraction is clearly reduced to zero-valent Zn upon prolonged methanol synthesis conditions (**figure 3.9**).

Zooming in on the local coordination of the Cu and Zn atoms during high-pressure methanol synthesis, we analyzed the extended X-ray absorption fine structure (EXAFS) region of the XAS data. Figure 3.10 shows the EXAFS data on the Zn K-edge in R-space for the CuZn-15/SiO<sub>2</sub> (frame A) and CuZn-15/C (frame B) catalysts in the initial state and upon heating in an H<sub>2</sub> atmosphere. Selected EXAFS fitting parameters are available in table 3.3. The initial spectra of both catalysts have a main peak at 1.50 Å in the Fourier transform, which corresponds to first-shell Zn-O bonds such as in ZnO with a bond length of 1.97 Å. The R-space of the CuZn-15/SiO<sub>2</sub> catalyst (frame A) closely resembles that of the Zn<sub>2</sub>SiO<sub>4</sub> reference, showing that a majority of the Zn atoms is bound to the oxide support, as reported before. 96 No contribution of second-shell Zn-Zn bonds was observed (frames A-B) (which could be expected in crystalline ZnO at 2.91 Å in the non-phase corrected Fourier transform, corresponding to a real bond length of 3.2 Å 305), indicating the absence of larger ZnO crystallites in both samples and in line with the high ZnOx dispersion observed by TEM (figure 3.2). During in situ H<sub>2</sub> reduction the Zn-O bond intensity at 1.50 Å apparently decreased for both catalysts, but this was simply due to the increasing measurement temperature 301 as the overall peak intensities were significantly increased in the spectra taken at room temperature after catalysis (purple lines in frames C-D) compared to the spectra taken during the last stage of catalysis at high temperature. It is important to note that in neither of the catalysts Zn<sup>0</sup> formation was observed during reduction in atmospheric-pressure H<sub>2</sub> (the Zn–Zn or Zn–Cu bond fingerprint is expected at 2.30 Å in the non-phase corrected Fourier transform, its position is indicated with an unlabeled arrow in the frames). After the in situ H2 reduction the first-shell Cu-Cu coordination number (CN) in metallic Cu was ca. 11 (for bulk Cu<sup>0</sup> this CN is 12) and it remained unchanged for both catalysts, independent of the exact feed. This means that no change in the Cu nanoparticles was observed upon exposure to working conditions: neither a significant fraction of oxidized copper nor the presence of highly dispersed copper. This is in agreement with the fully reduced Cu observed in the spectra at the XANES region.

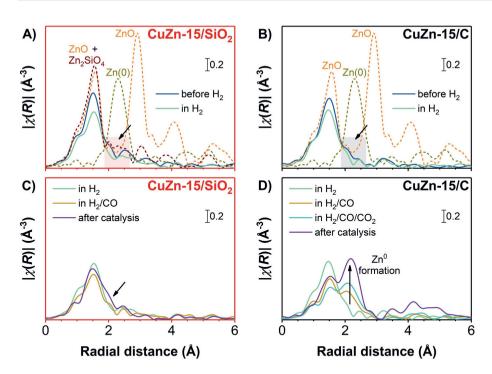


**Figure 3.10** Fourier-transformed EXAFS spectra at the Zn K-edge of the (**A,C**) CuZn-15/SiO<sub>2</sub> and (**B,D**) CuZn-15/C catalysts (solid lines). (**A-B**) Depicted during *in situ* reduction in the initial state at 298 K and in an H<sub>2</sub> atmosphere at 453 K after an H<sub>2</sub> treatment at 1 bar (for conditions, see **figure 3.8**). (**C-D**) Depicted during high-pressure H<sub>2</sub>/CO (and subsequent H<sub>2</sub>/CO/CO<sub>2</sub>) conversion at 533 K and 20 bar (for conditions, see **figure 3.9**) and after catalysis. Dashed lines depict the macrocrystalline ZnO, Zn<sub>2</sub>SiO<sub>4</sub>, and Zn foil references. The unlabeled arrows indicate the position of Zn–Zn or Zn–Cu bond formation.

We continue the EXAFS analysis under *operando* methanol synthesis conditions by focusing on the Zn local surrounding. **Figure 3.10** (frames C-D) shows selected R-spaces from the EXAFS data on the Zn K-edge for both catalysts. For the CuZn-15/SiO<sub>2</sub> catalyst during CO hydrogenation, only a very minor fraction of metallic Zn was observed (signal around 2.30 Å indicated with the arrow in frame C), in line with earlier reports on oxide-supported catalysts.  $^{292,301,315}$  Nevertheless a change was observed, as the first-shell Zn–O CN decreased from 4 (as in bulk ZnO and Zn<sub>2</sub>SiO<sub>4</sub>) to 2.6  $\pm$  0.5 and a very low second-shell Zn–Zn or Zn–Cu (from here onwards denoted as Zn–M) CN of 2.2  $\pm$  1.4 was obtained (for bulk Zn<sup>0</sup> this CN is 12). This indicates a very slight change in the average Zn surroundings, but due to the minor changes and the very similar Zn–Zn and Zn–Cu bonding distances it is not possible to analyze this in detail. Overall, the signal remains dominated by features that are attributed to Zn silicate species, and there is very little difference between the reduced fresh catalyst and that under working conditions.

Interestingly, the CuZn-15/C catalyst (frame D) displayed substantial changes when switching to working conditions, which was already expected from the zero-valent Zn as evidenced by the XANES analysis (**figure 3.9** (frame B)). An average Zn–M bond length of 2.54 Å (close to that of 2.66 Å of the Zn<sup>0</sup> foil reference) and a quite high Zn–M CN of  $6.1 \pm 1.3$  were obtained. This is clear supporting evidence for the large fraction of zero-valent Zn species in the active catalysts. Upon prolonged exposure (while slightly enriching the feed with CO<sub>2</sub>), the increase in coordination number continues to a Zn<sup>0</sup> CN of ca. 8. This means that most of the Zn promoter species is present in metal nanoparticles. The very similar Zn–Zn and Zn–Cu bonding distances do not allow to unequivocally derive the nature of these metal nanoparticles. However, very likely the zero-valent Zn is in Cu–Zn nanoparticles. The high Zn–M coordination number suggests that the Zn does not remain as ad-atoms or a monolayer on the outside of the Cu particle. The diffusion coefficient of Zn<sup>0</sup> in Cu<sup>0</sup> strongly depends on the Cu particle size and temperature <sup>189,318,319</sup> but is high enough to support a full distribution of the Zn<sup>0</sup> throughout the relatively small Cu<sup>0</sup> particles at the time scale of hours.

Interestingly, the time scale of the formation of highly coordinated zero-valent Zn is quite in line with the generally observed activation period for Cu methanol synthesis catalysts exposed to high-pressure working conditions.  $^{88,291}$  To our knowledge no clear explanation for this activation period has so far been reported in academic literature, but our results suggest that the gradual reduction of Zn(II) to active Zn(0) promoter species might be a principal factor in this activation.

Figure 3.11 summarizes the results of our study by depicting the ZnO<sub>x</sub> speciation in silica- and carbon-supported Cu catalysts containing 15 at% Zn/(Cu + Zn) after reduction as well as during high-pressure methanol synthesis. On both supports, the Cu<sup>2+</sup> nanoparticles (depicted in dark blue) were fully reduced to Cu<sup>0</sup> nanoparticles in 5-15 min exposure to 1 bar H<sub>2</sub> at 543 K. Even during highpressure methanol synthesis with a H<sub>2</sub>/CO<sub>2</sub> feed, no significant subsequent change in the oxidation state of the Cu was observed. Using an oxidic support, which is standard in commercial catalysts and most academic studies, it was difficult to derive detailed information about the speciation of the Zn component (depicted in red) that was active as a promoter. Only slight changes in the average Zn speciation were observed (in line with earlier literature), as the signal was dominated by Zn species that had a strong interaction with the oxidic support (depicted as a layer of ZnSiO<sub>x</sub>), and these species remained dominant under all (also methanol synthesis) conditions. In contrast, using a much less strongly interacting carbon support, allowed us to follow the fraction of the Zn species that was closely affiliated with the Cu nanoparticles, and hence most likely represents the active Zn promoter species during catalysts. Under methanol synthesis conditions, the relevant ZnO<sub>x</sub> phase is in a deeply reduced state with an average Zn oxidation number of only +0.6. Assuming that only Zn<sup>2+</sup> and Zn<sup>0</sup> species exist, this means that ca. 70% of the ZnO is fully reduced to Zn<sup>0</sup>. The Zn–M coordination number was as high as 8 during methanol synthesis working conditions, showing that the Zn<sup>0</sup> is almost fully coordinated with other metal atoms, and has likely mostly diffused into the

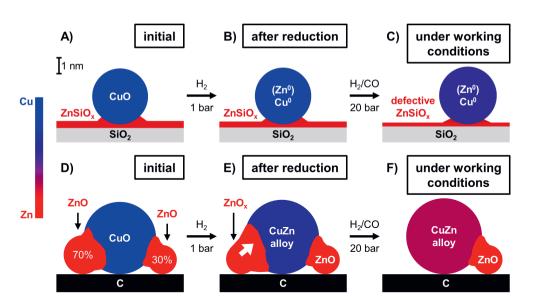


**Figure 3.11** Schematic representation of the  $ZnO_x$  speciation in the (**A-C**)  $CuZn-15/SiO_2$  and (**D-F**) CuZn-15/C catalysts, depicted (**A,D**) in the initial state, (**B,E**) after reduction and (**C,F**) under working conditions at 20 bar and 533 K. The various shades of between blue (Cu) and red (Zn) in the CuZn particles represent the relative extent of  $Zn^0$  incorporation into the  $Cu^0$  nanoparticles based on the estimated Zn ONs from the XANES analysis.

Cu nanoparticles. It is likely that this Zn speciation for the active promoter species is also relevant for the more conventional oxide-supported catalysts, to which much more Zn must be added to reach an optimum promoter effect, which is probably explained by the fact that a large fraction of the added Zn is not active as promoter.

## 3.4 Conclusions

Cu nanoparticulate catalysts on graphitic carbon were prepared, and compared to  $SiO_2$ -supported catalysts, to better understand the interaction between the Cu and the Zn-based promoter species and the speciation of Zn acting as a promoter during high pressure methanol synthesis. With a modest amount of  $ZnO_x$  promoter, the methanol formation for the  $CuZnO_x/C$  catalyst was significantly faster than for a  $CuZnO_x/SiO_2$  catalyst with similar Cu particle size in a pure  $H_2/CO$  feed. This difference was even much more pronounced in a  $CO_2$ -enriched syngas feed. Importantly, the use of graphitic carbon model supports allowed us to reveal the true speciation of the active fraction of the Zn-based promoter under commercially relevant methanol synthesis conditions. The vast majority of the Zn(II) is reduced all the way to Zn(0) during methanol synthesis at 20 bar. Also the Zn coordination number was high, making it likely that the Zn(0) diffused into

the Cu nanoparticles. The characteristic time for this diffusion corresponds to the activation time that is generally observed with this type of catalysts. For the first time this gives direct insight into the nature of the active fraction of the Zn-based promoter in high pressure methanol synthesis, not obscured by the commonly large fraction of Zn species that strongly interacts with an oxidic support, and hence dominates the structural characterization results.

# **Acknowledgments**

Laura Barberis, Giorgio Totarella, Petra de Jongh, and Xavier Carrier (Sorbonne University) are thanked for all the help with performing the XAS experiments. Laura Barberis, Ad van der Eerden, Frank de Groot, and Mahnaz Ghiasi Kabiri helped with the analysis of the XAS data, and we are thankful for that. We acknowledge SOLEIL (France) for provision of synchrotron radiation facilities, and we would like to thank Camille La Fontaine and Valérie Briois for assistance in using the ROCK beamline, for the help with the data interpretation, and the design of the experimental method. We also thank Savannah Turner for performing electron microscopy imaging by EDX and Giorgio Totarella for ultramicrotomy of the silica samples. Lisette Pompe is thanked for the synthesis of several catalysts, and finally we would like to thank Rolf Beerthuis and Jan Willem de Rijk for useful input during catalytic testing.

# **Supplementary figures**

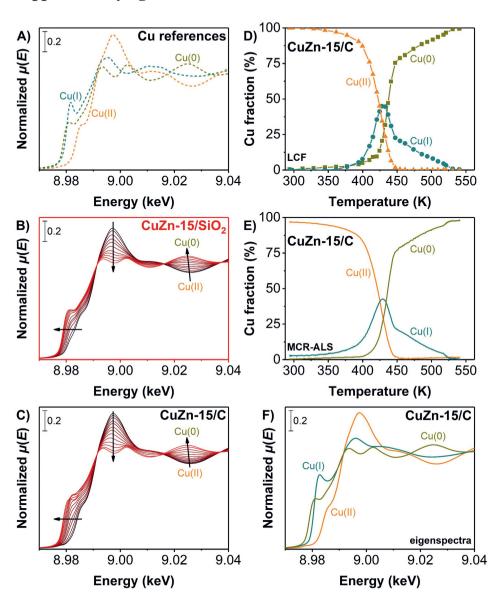


**Figure S3.1** Time-resolved XANES spectra at the Cu K-edge of the (**A**) macrocrystalline references in air at 298 K, and of the (**B**) CuZn-15/SiO<sub>2</sub> and (**C**) CuZn-15/C catalysts during an H<sub>2</sub> treatment (solid lines from black to red). The Cu oxidation state evolution of the CuZn-15/C catalyst during this treatment, determined by (**D**) LCF and (**E**) MCR-ALS (500 iterations) with (**F**) extracted eigenspectra. Conditions: 20 vol% H<sub>2</sub>/He, from 298 to 541 K (ramp 5 K min<sup>-1</sup>), 1 bar.

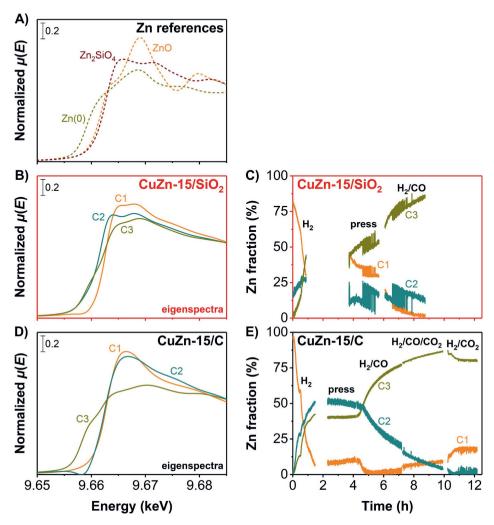


**Figure S3.2** (A) Macrocrystalline Zn references at 298 K. (B,D) Extracted eigenspectra and (C,E) corresponding concentration profiles by multivariate analysis (MCR-ALS) of time-resolved XAS spectra at the Zn K-edge of the (B-C) CuZn-15/SiO<sub>2</sub> (5,000 iterations) and (D-E) CuZn-15/C catalysts (25,000 iterations). The concentration profiles are presented at various stages during the experiments ( $H_2$  = during an  $H_2$  treatment from 298 to 543 K; press = during pressurization to 20 bar in an  $H_2$ /CO feed at 478 K;  $H_2$ /CO<sub>x</sub> = during catalysis at 533 K and 20 bar). The extracted components do not resemble pure Zn-based compounds but either represent a relatively stable combination of various Zn-based compounds. Deviations can also be due to differences in the particle size, temperature effects, the relatively weak XAS signal, and the interference with Cu forming metastable phases. The eigenspectrum of component C2 in frame A mostly represents Zn<sub>2</sub>SiO<sub>4</sub> and its contribution is relatively stable throughout the experiment, indicating the presence of a substantial amount of Zn spectator species in the CuZn-15/SiO<sub>2</sub> catalyst.

# Manganese oxide as a promoter for copper catalysts in CO<sub>2</sub> and CO hydrogenation

#### **Abstract**

In this chapter, we discuss the role of manganese oxide (MnO<sub>x</sub>) as a promoter in Cu catalysts supported on graphitic carbon during hydrogenation of CO<sub>2</sub> and CO. MnO<sub>x</sub> is a selectivity modifier in an  $H_2/CO_2$  feed and is a highly effective promoter in an  $H_2/CO$  feed. Interestingly, the presence of MnO<sub>x</sub> suppresses the methanol formation from CO<sub>2</sub> (turnover frequency (TOF) of  $0.7 \pm 0.2 \cdot 10^{-3} \, s^{-1}$  at 533 K and 40 bar) and enhances the low-temperature reverse water-gas shift reaction (TOF =  $5.7 \pm 2.0 \cdot 10^{-3} \, s^{-1}$ ) with a selectivity to CO of 87%c. Using time-resolved X-ray absorption spectroscopy (XAS) at high temperature and pressures, we find significant adsorption of CO<sub>2</sub> to the MnO, which is reversed if CO<sub>2</sub> is removed from the feed: a feature which is not observed for ZnO<sub>x</sub>-promoted catalysts (see also **chapter 3**). A low concentration of H atoms might explain the formation of CO instead of methanol. This work reveals fundamental differences in the promoting effect of MnO<sub>x</sub> and ZnO<sub>x</sub> and contributes to a better understanding of the role of reducible oxide promoters in Cu-based hydrogenation reactions.

**Based on**: Dalebout, R.; Barberis L.; Visser, N.L.; van der Hoeven, J.E.S.; van der Eerden, A.M.J.; Stewart, J.A.; Meirer, F.; de Jong, K.P.; de Jongh, P.E. Manganese Oxide as a Promoter for Copper Catalysts in CO<sub>2</sub> and CO Hydrogenation, *ChemCatChem*, **2022**, *accepted*.

# 4.1 Introduction

Promoters are found in many supported catalysts. <sup>320,321</sup> They are generally present in low concentrations and, while usually being catalytically inactive for a specific reaction, they substantially boost catalyst activity, selectivity, and/or stability. <sup>7</sup> For instance, in methanol production from CO<sub>2</sub>-enriched syngas (H<sub>2</sub>/CO) the addition of a ZnO<sub>x</sub> promoter to the Cu/Al<sub>2</sub>O<sub>3</sub> system leads to an activity enhancement of an order of magnitude, as presented in **chapters 2-3**. <sup>39,89</sup> This activity increase has made the Cu/ZnO/Al<sub>2</sub>O<sub>3</sub> catalyst the established industrial catalyst for the synthesis of methanol from syngas since the 1960s. <sup>87</sup> Another interesting feature of this reaction is that it has been shown that it is the CO<sub>2</sub> in the feed that is converted into methanol <sup>94,104,105,291</sup>, and hence this system can form an important starting point for Cu-catalyzed pure CO<sub>2</sub> hydrogenation.

Elucidating the change in catalyst properties induced by various feed compositions is of significant importance. The rising CO<sub>2</sub> concentration in the atmosphere has pushed the interest in research to convert CO<sub>2</sub> in large industrial processes such as methanol synthesis from syngas. Yet, catalysts for use in a feed purely based on CO<sub>2</sub> and H<sub>2</sub> face challenges. For example, without CO in the feed Cu/ZnO/Al<sub>2</sub>O<sub>3</sub> catalysts face faster thermal growth of the Cu particles and a significantly lower methanol selectivity. <sup>95</sup> The Cu particle growth is accelerated by the extra water formed during CO<sub>2</sub> hydrogenation to either methanol (**equation (1.7)**) or CO (the reverse water-gas shift (RWGS) reaction, **equation (1.9)**). CO<sub>2</sub> hydrogenation to methanol is an exothermic reaction but entropically very unfavorable, hence high pressures are needed to reach reasonable equilibrium conversion (*e.g.* 26.2%c methanol at 40 bar and 473 K with an H<sub>2</sub>/CO<sub>2</sub> ratio of 3). On the other hand, the RWGS reaction is endothermic and entropically slightly favorable. It is hence expected that control over the experimental conditions such as pressure, temperature, and gas composition is key to selectively obtain the desired product. Additionally, promoters can play a key role in product selectivity.

Reducible metal oxides are particularly effective promoters in gas-phase hydrogenation reactions. Their rich chemistry is based on the changes in the oxidation state of the metal, facile and reversible creation of oxygen vacancies, and metal—metal interactions of the oxide.  $^{108,273,322-324}$  Starting from a high oxidation state, reduction to a lower metal oxidation state forms an oxygen vacancy. In turn, this results in an excess of electrons, which is redistributed to the cation empty energy level causing a change in the oxidation state of the cation  $M^{n_1}$  to  $M^{(n-1)+}$ . For this reason, metals that contain half-filled d and f orbitals, and hence have a variety of stable oxidation states, typically are redox active.  $^{14,325}$  The presence of electropositive sites (vacancies) can have important effects during catalysis, particularly influencing the adsorption properties of reactants and intermediate species, *e.g.* favoring  $CO_2$  adsorption and activation due to its electrophilic character.  $^{250,326,327}$  Improvements in catalytic performance in methanol synthesis resulting from the use of reducible

oxides as promoters in Cu-based catalysts have been reported for many reducible oxides, with  $ZnO_x$  being the most recurrent, but the nature of the metal–metal oxide interaction has been far from fully understood.  $^{220,252,323,328,329}$ 

MnO<sub>x</sub> is an interesting oxide as Mn has a rich variety of metal oxidation states (+2, +3, +4, +5, +6, +7), low cost, and high abundancy. Despite this, only limited literature is available regarding the use of MnO<sub>x</sub> as a promoter in hydrogenation reactions, specifically for Cu-catalyzed CO<sub>2</sub> and/or CO hydrogenation. MnO<sub>x</sub> has been reported to boost the total activity, either attributed to changing the size and dispersion of the Cu nanoparticles <sup>250–253,330</sup>, to electronic promotion due to a specific Cu-MnO<sub>x</sub> synergy <sup>253,254,330</sup>, or to its influence on the concentration of basic surface sites that increase the CO<sub>2</sub> dissociation activity <sup>330</sup>. As an example of electronic promotion, for NO reduction by CO the formation of oxygen vacancies in  $(CuMn)_3O_4$ , specifically  $Cu^{(y-1)+}-\Box-Mn^{(x-1)+}$ , is reported to be the main active site for N<sub>2</sub> production as proven by in situ spectroscopy and DFT calculations. <sup>327</sup> MnO<sub>x</sub> is also reported to increase the methanol selectivity during high-pressure hydrogenation of a CO<sub>2</sub>rich syngas feed, which is proposed to be due to the presence of surface Cu<sup>+</sup> species <sup>251,255</sup> or stabilization of specific reaction intermediates 250. There are also hints that MnOx might increase the thermal stability of Cu nanoparticles <sup>330</sup>, but its effect appears to be less pronounced than for a ZnO<sub>x</sub> promoter <sup>256,257</sup> and mechanistic details remain unclear. There are still many open questions as other reports suggest the absence of any electronic promotion of Cu nanoparticles by MnO<sub>x</sub> <sup>258</sup> or that not the selectivity to methanol but to CO increased upon MnO<sub>x</sub> addition <sup>256</sup>.

The complexity of supported catalysts, *e.g.* partial mixture of the oxidic promoter and oxidic support, has partly been responsible for the limited knowledge about the role of reducible oxides in catalysis. <sup>18,232</sup> Recently, we reported that a silica support for ZnO<sub>x</sub>-promoted Cu nanoparticles plays a significant role in reducing the efficacy of the ZnO<sub>x</sub> promoter due to the formation of a large fraction of inactive Zn spectator species bound to the silica (**chapter 3**). The use of an inert support such as graphitic carbon allows reducing this complexity and enables a more targeted investigation of structure, properties, and catalytic functioning of reducible oxide-promoted catalysts.

Another reason why the promotion of Cu nanoparticles by reducible oxides is far from fully understood is the dynamic nature of the catalysts under working (high-pressure) conditions <sup>331</sup> and hence the need for *operando* studies. *In situ* X-ray absorption spectroscopy (XAS) is a powerful technique with the ability to elucidate the nature of metal–oxide species under reaction conditions. <sup>80,81,332</sup> In this work, *operando* XAS has been employed as a tool to study the dynamic changes in Cu and Mn interaction by following the oxidation state, electronic structure, and local bonding environment during *in situ* reduction and high temperature and pressure CO<sub>2</sub> and/or CO hydrogenation to methanol.

Here, we investigate the impact of MnO<sub>x</sub> as a reducible oxide promoter on the activity, selectivity, and stability of the Cu-catalyzed hydrogenation of CO and CO<sub>2</sub>. The nature of the MnO<sub>x</sub>-Cu

interaction and the changes in the  $MnO_x$  phase upon changing the feed composition are studied by in situ XAS. We also highlight the fundamental difference in the promoting effect between  $MnO_x$  and  $ZnO_x$ .

# 4.2 Experimental

#### 4.2.1 Chemicals

Copper nitrate (Cu(NO<sub>3</sub>)<sub>2</sub>·3H<sub>2</sub>O, Acros Organics, 99%), manganese nitrate (Mn(NO<sub>3</sub>)<sub>2</sub>·4H<sub>2</sub>O, Acros Organics), high surface area graphite (XG Sciences, xGnP® graphene nanoplatelets, grade C-500 HP, Brunauer-Emmett-Teller (BET) surface area of 490 m<sup>2</sup> g<sup>-1</sup>, total pore volume of 0.84 mL g<sup>-1</sup>), and nitric acid (HNO<sub>3</sub>, Merck, 65%) were used as received. As a reference we used a series of CuZnO<sub>x</sub> nanoparticles supported on graphitic carbon with varying Zn/Cu molar ratios but similar Cu particles sizes, as previously discussed in **chapter 3**. Silicon carbide (SiC, Alfa Aesar, ≥98.8%, 46 grit) was pressed and sieved in a 212-425 µm fraction, calcined at 1073 K for 10 h, subsequently washed with 65% HNO<sub>3</sub>, rinsed with water until pH 7 was reached, and finally dried at 393 K overnight before use.

# 4.2.2 Catalyst synthesis

A series of CuMnO<sub>x</sub>/C catalysts, with similar Cu weight loadings (8.4 wt%) but varying Mn/Cu molar ratios, were prepared via incipient wetness impregnation, according to a previously reported method. 19 Typically, ca. 2 g of high surface area graphite was dried at 443 K under dynamic vacuum for 1.5 h. After cooling to room temperature the fine carbon powder was (co-)impregnated to incipient wetness, which means that the added liquid corresponds to 95% of the total pore volume  $(0.84 \text{ mL g}^{-1})$  as measured by N<sub>2</sub> physisorption at a  $p/p_0$  value of 0.995, under static vacuum with a 0.1 M HNO<sub>3</sub> aqueous solution of ca. 1.8 M copper nitrate and up to 0.9 M manganese nitrate. The impregnated support was equilibrated at room temperature under static vacuum for 2 h prior to drying under dynamic vacuum for 24 h. The dried material was transferred to an Ar-filled glovebox and subsequently divided over two plug-flow reactors (1 g each) without exposure to air. The dried precursor was decomposed at 503 K (ramp 0.5 K min-1) in an N<sub>2</sub> flow of 100 mL min-1 g-1 for 1 h. After cooling to 303 K the material was exposed to 10 vol% O<sub>2</sub>/N<sub>2</sub> for 3 h and subsequently to pure N<sub>2</sub> for 30 min. Finally, the sample was reduced at 443 K (ramp 2 K min<sup>-1</sup>) in a 100 mL min<sup>-1</sup> g<sup>-1</sup> flow of 10 vol% H<sub>2</sub>/N<sub>2</sub> for 2 h, directly followed at 673 K (ramp 2 K min<sup>-1</sup>) for 1 h. A part of the reduced catalyst was stored in an Ar-filled glovebox, whereas the remainder was slowly passivated in air at room temperature. The obtained CuMnO<sub>x</sub>/C catalysts are named CuMn-X/C, in which X represents the molar Mn/(Cu + Mn) fraction in percentages. An  $MnO_x/C$  catalyst (7.2 wt% Mn) was in a similar manner. The Cu/C catalyst used in this chapter is the same as discussed in **chapters 2-3**.

#### 4.2.3 Catalyst characterization

**Structural characterization.** Catalysts were imaged by transmission electron microscopy (TEM) using a Thermo Fisher Scientific Talos L120C apparatus, operating at 120 kV. The samples were prepared by loading finely ground, dry sample (<25 µm) onto holey carbon film-coated Cu grids (Agar, 300 mesh). At least 540 individual particles at various locations within the sample were measured to determine the number-averaged CuO<sub>x</sub> particle sizes ( $d_{\rm N}$ ). Also surface-averaged sizes ( $d_{\rm S}$ ) were calculated using  $d_{\rm S} \pm s_{\rm S} = \sqrt{\frac{1}{N}\sum_{i=1}^N d_i^2} \pm \sqrt{\frac{1}{N-1}\sum_{i=1}^N (d_i - d_{\rm S})^2}$ , in which  $s_{\rm S}$  represents the width of the lognormal particle size distribution,  $d_i$  the diameter of the i-th particle, and N the total number of measured particles. Only the relevant part of the lognormal distribution (>1% of maximum) was considered for the calculation of the average particle sizes.

Powder X-ray diffractograms of the catalysts were recorded in the reduced state and after air exposure on a Bruker AXS D8 Advance diffractometer at room temperature with a variable divergence slit. Samples were exposed to Co K $\alpha$  radiation ( $\lambda$  = 1.790 Å) at 30 kV and 45 mA. The Scherrer equation was used to calculate the CuO $_{\rm x}$  crystallite sizes from the peak widths, thereby taking the instrumental line broadening of the X-ray diffraction (XRD) apparatus (ca. 0.1°) into account. All diffractograms were normalized between 0 and 1, *i.e.* between the lowest intensity at 20° and the maximum peak intensity due to the (002) reflection of graphite at 30.9°.

Temperature-programmed reduction (TPR) by  $H_2$  was performed on a Micromeritics AutoChem II 2920 apparatus. Prior to the reduction the samples (50 mg each, <75  $\mu$ m granulites) were dried at 393 K under an Ar flow of 50 mL min<sup>-1</sup> for 30 min and cooled to room temperature. Reduction profiles were recorded with a thermal conductivity detector when the samples were exposed to a 5 vol%  $H_2$ /Ar flow of 25 mL min<sup>-1</sup> up to 973 K with a ramp of 2.5 K min<sup>-1</sup>.  $H_2$ O was captured with a dry ice/isopropanol cold trap.

**XAS analysis.** *Operando*, quick X-ray absorption spectroscopy measurements on simultaneously the Cu (8979 eV) and Mn K-edge (6540 eV) were performed at the SOLEIL synchrotron (ROCK beamline).  $^{308}$  Typically, 2-4 mg CuMn-11/C, CuMn-33/C, or MnO<sub>x</sub>/C catalyst (25-75  $\mu$ m sieve fraction) was loaded in a quartz capillary (internal diameter 1.2 mm, 20-50  $\mu$ m thick), which was tightly glued into a frame connected to gas feed lines. A hot gas blower (FMD Oxford) controlled heating of the capillary. After the capillary was leak-checked at 20 bar, XAS data was obtained in He at room temperature. The catalyst was exposed to a 10 mL min-1 flow of 20 vol%

 $H_2/He$  and heated to 543 K (ramp 2.5 K min<sup>-1</sup>) at ambient pressure with a hold time of 20-30 min (or 130 min for the MnO<sub>x</sub>/C catalyst).

After the  $H_2$  treatment the capillary containing the CuMn-11/C catalyst was cooled to 453 K prior to introducing a syngas feed ( $H_2/CO/He = 60/30/10 \text{ vol}\%$ ) at 10 mL min<sup>-1</sup>. Within *ca*. 100 min the capillary was pressurized to 20 bar after which the temperature was increased to 533 K (ramp 2.5 K min<sup>-1</sup>) and held for 160 min. The feed was switched to  $H_2/CO/CO_2/He = 60/27/3/10 \text{ vol}\%$ , recording spectra for at least 200 min, and similarly to  $H_2/CO_2/He = 67.5/22.5/10 \text{ vol}\%$ . The CuMn-33/C catalyst was only measured under the  $H_2/CO_2$  atmosphere. Finally, spectra were recorded for both catalysts after cooling to room temperature under 20 bar of  $H_2/CO_2$ .

During all treatments XAS spectra were obtained in the rocking mode, switching from the Cu K-edge (8.70-9.86 keV, 50 scans, 35 s) to the Mn K-edge (6.40-7.10 keV, 60 scans, 40 s) using 10 s to switch between each edge. The setup was configured in the transmission mode using as Si(111) quick-XAS monochromator. The product gas compositions were recorded with a mass spectrometer (Cirrus, MKS) at ambient pressure. When flowing CO gas, a carbonyl trap was used upstream of the capillary reactor. MnO (Sigma Aldrich, 99%), MnCO<sub>3</sub> (abcr, 99.985%), Mn<sub>2</sub>O<sub>3</sub> (Sigma Aldrich, 99%), MnO<sub>2</sub> (Sigma Aldrich,  $\geq$ 99%), CuO (Sigma Aldrich, 99.999%), Cu<sub>2</sub>O (Sigma Aldrich,  $\geq$ 99.99%), all mixed with boron nitride (Sigma Aldrich, 98%), as well as Cu (6 µm) and Mn (4 µm) foils were used as references with the spectra being recorded at room temperature under air. The XAS spectra were processed using the Demeter software package  $^{310}$ , as described in more detail in section 3.2.2 for the Zn K-edge. For specifically these data: for the principle component analysis (PCA) only two principle components were needed to cover more than 99.99% of the cumulative variance explained (CVE), and for the linear combination fitting (LCF) crystalline MnO and MnCO<sub>3</sub> were used as references for the Mn(II) oxidation state and Mn<sub>2</sub>O<sub>3</sub> was used as reference for the Mn(III) oxidation state.

#### 4.2.4 Catalyst testing

Catalysts were assessed in a 16-reactor setup (Flowrence, Avantium) for at least 80 h, operating at 20-40 bar(g) and 473-533 K using various  $CO_2$  and CO feeds. The catalyst powders were pelletized and sieved into granules with a size of 75 to 150  $\mu$ m. The stainless steel reactors (internal diameter 2.6 mm) were loaded with similar amounts of catalysts (ca. 26 or 39 mg) and diluted with 400-450 mg inert SiC (sieve fraction of 212-425  $\mu$ m), resulting in SiC contents of ca. 83 vol% of the total packed bed. <sup>279</sup> The size difference of the sieve fractions of the catalysts and the diluent facilitated separation after catalysis and hence post-analysis by EM and XRD.

Two separate catalytic tests were performed to evaluate the influence of various parameters, such as the gas composition, temperature, pressure, and flow rate, on the catalyst performance. Prior to

both tests, the catalysts were *in situ* reduced in a 20 vol%  $H_2/N_2$  flow at 10.9 mL min<sup>-1</sup> and 543 K for 2 h after which the temperature was lowered to 393 K. During the first test (see **figure 4.3** for an overview as a function of time) the reduced catalysts were exposed to a 2.2 mL min<sup>-1</sup> flow of  $H_2/CO_2/He = 67.5/22.5/10$  vol% at 690 mL min<sup>-1</sup>  $g_{Cu}^{-1}$  and a gas-hourly space velocity (GHSV) of  $ca.1,800 \, h^{-1}$ , after which the reactors were pressurized to 40 bar(g) and heated to 533 K at 5 K min<sup>-1</sup>. After 22 h the temperature was lowered to 473 K and consecutively increased in steps of 10 K to 533 K, recording data for 15 h at each reaction condition. In the same test, this temperature protocol was directly repeated in a flow of  $H_2/CO/He = 60/30/10$  vol% at 40 bar(g). In the second test (see **figure 4.8** for an overview as a function of time), freshly reduced catalysts were exposed to varying gas compositions ( $H_2/CO_2/He$ ,  $H_2/CO/CO_2/He = 60/27/3/10$  vol%, and  $H_2/CO_2/He$ ) at a pressure of 20 bar, maintaining constant flow rate of 1.0 mL min<sup>-1</sup>  $g_{Cu}^{-1}$  at  $ca. 2,700 \, h^{-1}$  and temperature of 533 K. In the same test, this specific protocol was directly repeated at a pressure of 40 bar.

A tri-phase carbonyl trap (active carbon,  $\gamma$ -Al<sub>2</sub>O<sub>3</sub>, ZnO) was located between the CO feed and the reactor to remove metal carbonyls and sulfur species. Products were analyzed by online gas chromatography every 15 min. After catalysis, the samples were slowly exposed to air at 338 K. Details on the calculations of activity and selectivity are given in **section 2.2.5**. The gas hourly space velocity (GHSV) was calculated by **equation (4.1)** using  $\rho_{\text{packing}}$  as the packed bed density of the sieved catalyst without considering the dilution by SiC.

GHSV = 
$$\frac{Q_{\text{feed}} \cdot \rho_{\text{packing}}}{m_{\text{cat}}} [h^{-1}]$$
 (4.1)

#### 4.3 Results

### 4.3.1 Structural properties of the catalysts

A main challenge in studying the influence of a promoter is to vary the promoter content while keeping all other variables constant, such as the size of the metal nanoparticles.  $^{19,333}$  **Figure 4.1** (frames A-H) shows electron micrographs of selected CuMnO<sub>x</sub>/C catalysts with the corresponding particle size distributions. The surface-averaged particle sizes are summarized in **table 4.1** (note that the Cu/C catalyst is the same as the one presented in **chapters 2-3**). All Cu(Mn)O<sub>x</sub>/C catalysts had a Cu loading of ca. 8.5 wt%, but their Mn/(Cu + Mn) molar content ranged from 0 to 33 at%, as indicated in the sample name. For example, the CuMn-11/C catalyst contained 11 at% MnO<sub>x</sub>. In all cases a good spatial distribution of the CuO<sub>x</sub> nanoparticles (black dots) over the sheet-like carbon support (light grey) was obtained. The average particles sizes were between 5 and 7 nm, irrespective of the MnO<sub>x</sub> loading (**table 4.1**). The Cu/C catalyst had slightly larger particles (10 nm) as it is challenging to synthesize small CuO<sub>x</sub> particles supported on carbon without any additives.  $^{334}$  MnO<sub>x</sub> is thus also a structural promoter in Cu/C catalysts by enhancing or stabilizing a smaller Cu particle

size. An MnO<sub>x</sub>/C catalyst with 7.2 wt% Mn was prepared as a reference. The catalyst synthesis  $^{19}$  was reproducible as shown by three batches of the CuMn-20/C catalyst, which had surface-average particle sizes of  $5.5 \pm 1.9$  nm.  $5.7 \pm 1.6$  nm, and  $5.1 \pm 1.7$  nm, respectively.

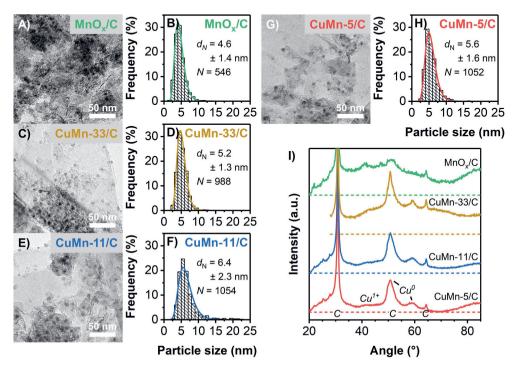


**Figure 4.1** (**A**,**C**,**E**,**G**) TEM images and (**B**,**D**,**F**,**H**) corresponding particle size distributions of the MnO<sub>x</sub>/C, CuMn-33/C, CuMn-11/C, and CuMn-5/C catalysts, respectively. The Cu/C catalyst is presented in **figure 2.1**. (**I**) XRD patterns of selected CuMnO<sub>x</sub>/C catalysts in the reduced state; vertically offset for clarity.

**Table 4.1** Surface-averaged CuMnO<sub>x</sub> particle diameters (in nm) of CuMnO<sub>x</sub>/C catalysts in the fresh and used state determined by TEM. The particles were passivated under ambient conditions prior to the measurement.

catalyst	fresh	used
Cu/C	$9.9 \pm 3.3$	11.6 ± 4.4 a
CuMn-5/C	$5.8 \pm 1.6$	$6.3 \pm 1.8$
CuMn-11/C	$6.9 \pm 2.3$	$6.5 \pm 2.0$
CuMn-20/C	$5.5 \pm 1.9$	$6.7 \pm 2.4$
CuMn-33/C	$5.4 \pm 1.3$	$6.6 \pm 2.1$
MnO <sub>x</sub> /C	$4.8 \pm 1.4$	$9.3 \pm 4.0$

<sup>&</sup>lt;sup>a</sup> After 160 h of catalysis as described in **chapter 2**.

The presence of crystalline phases was detected by X-ray powder diffraction (XRD), both after catalyst synthesis in the reduced state and after passivation. The diffractograms of selected reduced catalysts are shown in **figure 4.1** (frame I). After catalyst preparation, during which temperatures up to 673 K were used, the crystallinity of the carbon support was preserved, as demonstrated by the (002) diffraction line of graphite at 30.9°. The peaks at 50.9° and 59.5° for the CuMn-5/C and CuMn-11/C catalysts correspond to metallic Cu crystallites with an average size of only 3-4 nm, whereas for the CuMn-33/C catalyst the peaks are attributed to Cu $^0$  crystallites with a size of ca. 7-8 nm. Specifically focusing on MnO $_x$ , no crystalline Mn phases were detected in any of the catalysts. The amorphous background of the diffractograms increased when more MnO $_x$  was present in the catalyst, which suggests that the MnO $_x$  promoter was highly dispersed and/or amorphous.

#### 4.3.2 Interaction between Cu and MnOx

We investigated the interaction of  $MnO_x$  with Cu in our carbon-supported samples by ex situ reduction by  $H_2$  as well as in situ, time-resolved X-ray absorption spectroscopy (XAS). **Figure 4.2** (frame A) shows the ex situ reduction profiles of selected catalysts. Note that probably all carbon surface groups were already reduced before this measurement, as the catalysts were  $H_2$ -treated at 673 K during catalyst synthesis. The Cu-free  $MnO_x$  species were (partially) reduced around 587 K, as indicated by the arrow. The reduction profiles changed significantly with the addition of Cu: a peak around 433 K was observed, corresponding to the reduction of CuO to  $Cu^{0.335,336}$ , while the high-temperature reduction of  $MnO_x$  became much less pronounced. Furthermore, the offsets of the reduction peaks around 433 K were slightly higher for the CuMn-33/C (407 K) than for the CuMn-11/C catalyst (396 K). The increase in the reduction temperature at higher  $MnO_x$  loadings is a general trend observed across all  $CuMnO_x/C$  catalysts. Hence, from the ex situ reduction profiles it appears that Cu influences the reduction of  $MnO_x$ , indicating close contact between Cu and  $MnO_x$ , but in situ XAS is needed to study in more detail what happens.

**Figure 4.2** (frames B-F) shows the evolution of the oxidation states of the Cu and Mn species during *in situ* H<sub>2</sub> treatment. The oxidation states were obtained by fitting linear combinations (LCF analysis) of the macrocrystalline references to the time-resolved XAS data depicted in **figure S4.1** at the end of this chapter for the interested reader. In all Cu-based catalysts (frames C-D) the CuO clearly was reduced in a two-step process to Cu<sup>0</sup> *via* the formation of Cu+, which is a typical two-step conversion also reported in literature. <sup>306,335</sup> Furthermore, the Cu species in the CuMn-11/C catalyst had an oxidation state slightly below +2 (+1.90, frame C), while the CuMn-33/C catalyst contained fully oxidized CuO (frame D). The CuO reduction was not significantly affected by the presence of MnO<sub>x</sub>.

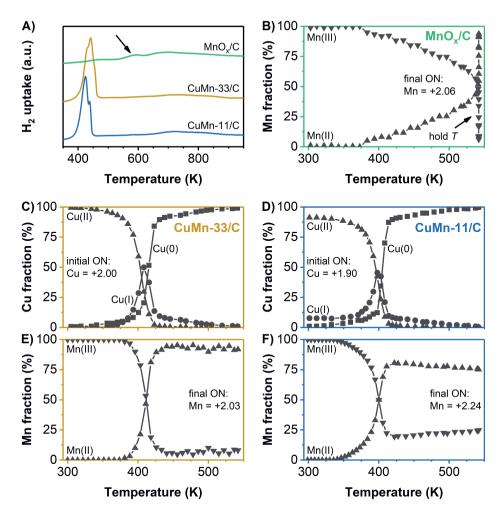


**Figure 4.2** (A) Reduction profiles of selected CuMnO<sub>x</sub>/C catalysts, which are vertically offset for clarity and normalized by the support amount (50 mg catalyst). The arrow indicates the (partial) reduction of MnO<sub>x</sub> species. Conditions: dried at 393 K in Ar, TPR with 5 vol%  $H_2$ /Ar, ramp 2.5 K min<sup>-1</sup>, 0.5 L min<sup>-1</sup>  $g^{-1}$ . (B-F) Results from linear combination fitting (LCF) of the Cu and Mn oxidation states of the CuMn-11/C, CuMn-33/C, and MnO<sub>x</sub>/C catalysts, derived from time-resolved XAS measurements. Conditions: 20 vol%  $H_2$ /He, ramp 2.5 K min<sup>-1</sup>, ca. 2.5-3.3 L min<sup>-1</sup>  $g^{-1}$ . ON = oxidation number.

Focusing on the Mn species, in the absence of Cu the  $MnO_x$  was slowly reduced from  $Mn_2O_3$  to mainly MnO upon holding for 2 h at 543 K (frame B), in agreement with the *ex situ* H<sub>2</sub> profiling (frame A). On the contrary,  $Mn_2O_3$  in the  $CuMnO_x/C$  catalysts (frames E-F) was reduced at a much lower temperature around 405 K and exactly at the same temperature as CuO. The combined reduction proceeded at a slightly lower temperature in the CuMn-11/C catalyst (400 K) than in the

CuMn-33/C catalyst (410 K), in line with the *ex situ* reduction by  $H_2$  (frame A). Hence, with *in situ* XAS we showed that (virtually) all  $MnO_x$  was influenced by the close vicinity of Cu and that Cu induced the reduction of  $Mn_2O_3$  at a very low temperature as soon as metallic Cu was formed.

The  $MnO_x$  species consisted of (amorphous)  $Mn_2O_3$  in the initial state, whereas upon heating in an  $H_2$  atmosphere the Mn oxidation number (ON) decreased to between +2 and +3. The  $Mn_2O_3$  species were reduced to a somewhat lesser extent in the CuMn-11/C catalyst (+2.24, frame F), while a higher extent of reduction took place in the CuMn-33/C catalyst (+2.03, frame E). The same Mn ON was obtained for the Cu-free  $MnO_x/C$  catalyst (+2.05) after a prolonged exposure at 543 K (frame B). The Cu and Mn oxidation states were confirmed by a more in-depth study using multivariate analysis in which no prior information on the component spectra was imposed and which yielded eigenspectra that corresponded well to the macrocrystalline Cu and Mn references with only a minor variation in the white line intensities (**figure S4.1**). Hence, we demonstrated for the first time that closely interacting Cu catalyzed the  $Mn_2O_3$  reduction at much lower temperatures and determined the real Mn oxidation state in reduced  $CuMnO_x/C$  catalysts using time-resolved, in situ XAS.

# 4.3.3 Impact of MnOx on the catalyst activity and selectivity

The catalytic performance of the Cu catalysts in  $CO_2$  and CO hydrogenation was influenced by the presence of  $MnO_x$ . **Figure 4.3** shows a typical measurement in an  $H_2/CO_2$  feed (frame A) and

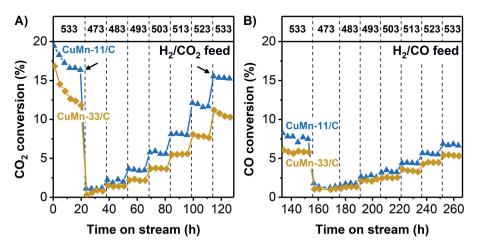


**Figure 4.3** (A) CO<sub>2</sub> and (B) CO conversion as a function of time for selected CuMnO<sub>x</sub>/C catalysts, measured in a single test. The numbers in the top banners represent the reaction temperatures in K. Conditions: 40 bar(g), 690 mL min<sup>-1</sup> gcu<sup>-1</sup>, ca. 1,800 h<sup>-1</sup>, 3.2 mg Cu, H<sub>2</sub>/CO<sub>2</sub>/He = 67.5/22.5/10 vol% or H<sub>2</sub>/CO/He = 60/30/10 vol%.

consecutively in an  $\rm H_2/CO$  feed (frame B) at 40 bar pressure but different reaction temperatures. All catalysts lost activity during the first 22 h on stream at 533 K (frame A) after which the conversion was relatively stable, especially at lower temperatures (473-513 K). When returning to the same reaction conditions after 92 h of catalysis only a slight additional loss of activity was observed, *e.g.* from 16.1% to 15.5% for the CuMn-11/C catalyst (indicated by the arrows in frame A). This means that, although carbon supports are known to have a relatively weak interaction with metal nanoparticles  $^{18}$ , these catalysts are remarkably stable. In all cases we worked at conversion levels well below the thermodynamic equilibrium (*e.g.* 22.1% at 533 K in the  $\rm H_2/CO_2$  feed) to study the intrinsic catalytic properties of these materials. The non-promoted Cu/C catalyst showed a considerable particle growth to at least *ca.* 12 nm, which was also observed in similar hydrogenation reactions (**chapter 2**, **table 2.1**), while the Cu particle size was stable in CuMnO<sub>x</sub>/C catalysts (*e.g.* from  $5.8 \pm 1.6$  to  $6.3 \pm 1.8$  nm for the CuMn-5/C catalyst) (see also **table 4.1**). In other words, it is the MnO<sub>x</sub> promoter that induces the unexpectedly high stability in these carbon-supported catalysts by suppressing the Cu particle growth.

**Figure 4.4** (frame A) shows the CO<sub>2</sub> conversion of selected catalysts as a function of temperature. based on the same Cu mass (3.2 mg) for each catalyst. The Cu/C reference catalyst showed a CO<sub>2</sub> conversion up to 12.2% at 533 K, while the MnO<sub>x</sub>/C reference sample did not show any significant CO<sub>2</sub> conversion. Combining MnO<sub>x</sub> species and Cu nanoparticles only slightly increased the CO<sub>2</sub> conversion for intermediate MnO<sub>x</sub> contents compared to the non-promoted Cu/C catalyst. The CuMn-11/C catalyst had a conversion of 15.2% at 533 K with an estimated turnover frequency (TOF) of  $6.4 \pm 2.2 \cdot 10^{-3}$  s<sup>-1</sup>, which is in the same order of magnitude as for the Cu/C catalyst  $(7.5 \pm 2.5 \cdot 10^{-3} \, \text{s}^{-1})$ . At all measured temperatures, an MnO<sub>x</sub> content of 5-11 at% was sufficient to optimize the total activity, while at higher MnOx loadings the conversion decreased. Frame B shows the Arrhenius plots of the selected catalysts (assuming zero-order kinetics, which is reasonable at the low conversion levels), which are translated in frame C to the apparent activation energy  $E_a$  as a function of the Mn content. The  $E_a$  to convert CO<sub>2</sub> appears to be independent of the Mn content and has an average value of 88.1 ± 1.4 kJ mol<sup>-1</sup>, suggesting that in each of these catalysts the active site for CO<sub>2</sub> conversion is the same. For each promoted catalyst, the E<sub>a</sub> for CO formation  $(95.7 \pm 1.9 \text{ kJ mol}^{-1})$  is higher than the  $E_a$  for methanol formation  $(59.0 \pm 1.2 \text{ kJ mol}^{-1})$ . Frame D presents the pre-exponential factor A as a function of the Mn loading using the average E<sub>a</sub> for CO<sub>2</sub> conversion as a fixed value. The CuMn-5/C and CuMn-11/C catalysts have a slightly larger A, describing a higher probability of catalytic turnover and/or a higher density of active sites, and is in agreement with the higher total activity of these catalysts. However, the impact of MnO<sub>x</sub> on the Cu activity in CO2 conversion is minor.

The performance of the CuMnO<sub>x</sub>/C catalysts was also evaluated for the hydrogenation of CO, consecutive to the CO<sub>2</sub> hydrogenation experiment. **Figure 4.5** (frame A) shows the CO conversion as a function of the reaction temperature for selected catalysts. Please note the smaller scale on the

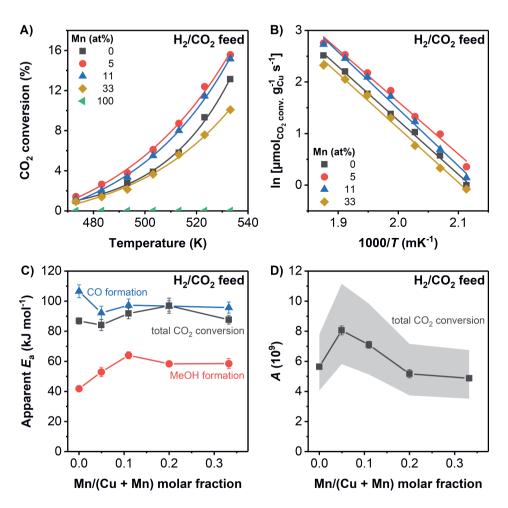


**Figure 4.4** (A)  $CO_2$  conversion as a function of temperature for selected  $CuMnO_x/C$  catalysts determined from the activity after ca. 15 h at each temperature, neglecting the initiation period at 533 K. The data are fitted by an exponential curve. (B) Arrhenius plots based on the total amount of converted  $CO_2$  using linear fits without restrictions. (C) Apparent activation energy as a function of the Mn content, determined for the total  $CO_2$  conversion, MeOH formation, and CO formation. (D) Apparent pre-exponential factor as a function of the Mn content based on the total  $CO_2$  conversion using a fixed activation energy of  $88.1 \pm 1.4$  kJ mol<sup>-1</sup>. The error bars represent the error in the determination of the pre-exponential factor, while the shaded area indicates the width induced by the error in the fixed activation energy. Conditions: 40 bar(g),  $690 \text{ mL min}^{-1} \text{ gcu}^{-1}$ , ca.  $1,800 \text{ h}^{-1}$ , 3.2 mg Cu,  $H_2/CO_2/He = 67.5/22.5/10 \text{ vol}\%$ .

ordinate compared to **figure 4.4** (frame A). The MnO<sub>x</sub>/C and Cu/C catalysts showed a very limited activity, but the CO conversion was greatly enhanced by the addition of MnO<sub>x</sub> to supported Cu nanoparticles. In our series, the MnO<sub>x</sub> content of 11 at% showed the highest total activity at each

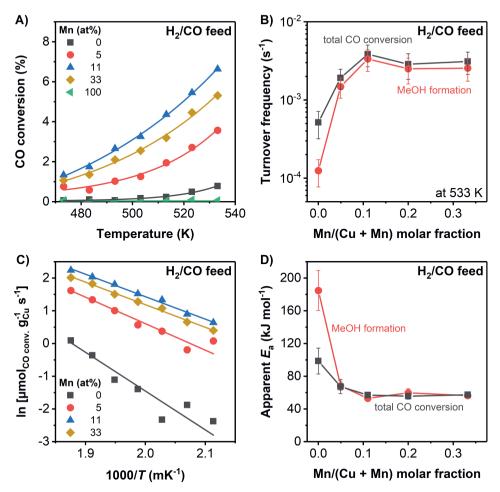


**Figure 4.5** (**A**) CO conversion as a function of temperature for selected CuMnO<sub>x</sub>/C catalysts determined from the activity after ca. 15 h at each temperature, neglecting the initiation period at 533 K. The data are fitted by an increasing exponential curve. (**B**) Turnover frequency as a function of the Mn content determined at 533 K using surface-averaged particle size of the used catalysts. (**C**) Arrhenius plots using linear fits without restrictions. (**D**) Apparent activation energy as a function of the Mn content, determined for the total CO conversion and MeOH formation. Conditions: 40 bar(g), 690 mL min<sup>-1</sup> gcu<sup>-1</sup>, ca. 1,800 h<sup>-1</sup>, 3.2 mg Cu, H<sub>2</sub>/CO/He = 60/30/10 vol%.

tested reaction temperature. As an example, at 533 K the CO conversion increased from 0.8% for the Cu/C catalyst to 6.6% for the CuMn-11/C catalyst. When taking the surface-averaged particle size in the used catalysts into account (**table 4.1**), the MnO<sub>x</sub> promotion led to a total TOF enhancement of an order of magnitude as shown in frame B. This promotional effect is even more pronounced when focusing on the methanol formation  $(0.12 \pm 0.05 \text{ to } 3.3 \pm 1.0 \cdot 10^{-3} \text{ s}^{-1})$ . Using

Arrhenius plots of the CuMnO<sub>x</sub>/C catalysts in the H<sub>2</sub>/CO feed (frame C), the apparent activation energy  $E_a$  for the total CO conversion (frame D) was determined. The large activity increase upon MnO<sub>x</sub> promotion is explained by a ca. 1.7 times decrease in the  $E_a$  from 99 ± 16 to 57.3 ± 1.3 kJ mol<sup>-1</sup>. Our results clearly show that MnO<sub>x</sub> acts as a very efficient activity promoter for supported Cu nanoparticles in CO hydrogenation, while having little effect in an H<sub>2</sub>/CO<sub>2</sub> feed.

CO<sub>2</sub> hydrogenation over supported Cu nanoparticles can lead to the formation of either CO or methanol.  $^{120,121}$  For example, at 533 K and 40 bar in our  $_{\rm H_2/CO_2}$  feed the thermodynamically expected selectivity to CO is 55.2%c at an equilibrium CO<sub>2</sub> conversion of 22.1%. **Figure 4.6** (frame A) shows the selectivity to CO in CO<sub>2</sub> hydrogenation at 533 K as a function of the MnO<sub>x</sub> content (filled symbols). For comparison, the same experiments were performed with the CuZnO<sub>x</sub>/C catalyst series from **chapter 3** and are included in the frame (hollow symbols). In an  $_{\rm H_2/CO_2}$  feed the major product was CO (>72%c) for all catalysts, which was formed by the reverse water-gas shift (RWGS) reaction in concentrations much higher than the equilibrium concentration (dashed line in frame A). This might be related to an ineffective catalyzation of methanol synthesis. Remarkably, MnO<sub>x</sub> promotion had no effect on CO selectivity and remained high at 86%c, while ZnO<sub>x</sub> addition slightly decreased the CO selectivity from 86%c to 73%c.

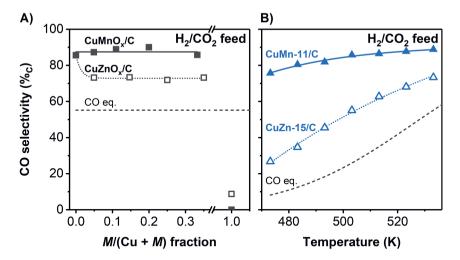


**Figure 4.6** Selectivity to CO during CO<sub>2</sub> hydrogenation, as a function of (**A**) MnO<sub>x</sub> or ZnO<sub>x</sub> loading at 533 K (M = Mn or Zn metal) and (**B**) reaction temperature (CO<sub>2</sub> conversion = 1.1-15.1% and 4.8-20.2% for CuMn-11/C and CuZn-15/C catalysts, respectively). The selectivity was determined after 15 h at each reaction condition. The dashed lines refer to the expected carbon-based CO selectivity at thermodynamic equilibrium, *e.g.* at 533 K the equilibrium composition is  $H_2/CO/CO_2/H_2/H_2/H_2 = 61.1/2.9/18.4/5.2/2.3/10$  vol%. Conditions: 40 bar(g), 690 mL min<sup>-1</sup> gcu<sup>-1</sup>, *ca.* 1,800 h<sup>-1</sup>, 3.2 mg Cu,  $H_2/CO_2/H_2 = 67.5/22.5/10$  vol%.

**Figure 4.6** (frame B) shows the selectivity to CO in an H<sub>2</sub>/CO<sub>2</sub> feed at 533 K as a function of temperature. The CuMn-11/C catalyst is compared to a reference CuZn-15/C catalyst from the CuZnO<sub>x</sub>/C catalyst series of **chapter 3**, which has a similar Cu-to-promoter ratio. For both catalysts more CO is produced at increasing temperatures, as expected for the endothermic RWGS reaction (**equation (1.9)**). Interestingly, at all tested temperatures the CuMn-11/C catalyst was much more selective to CO than the CuZn-15/C catalyst, especially at low temperatures. This makes the CuMn-11/C catalyst a low-temperature RWGS catalyst with respect to ZnO<sub>x</sub>-promoted Cu particles. In **section 4.3.4** we further explore this remarkable difference between MnO<sub>x</sub> and ZnO<sub>x</sub> promotion of Cu-based catalysts in hydrogenation reactions.

Reaction conditions such as temperature, pressure, and gas flow per catalyst volume are key to tune the catalyst performance, specifically for CO<sub>2</sub> hydrogenation. <sup>118</sup> **Figure 4.7** shows for the CuMn-11/C catalyst and at 20 bar pressure, the effect of the gas flow expressed as gas hourly space velocity (GHSV) by **equation (4.1)** on the Cu mass-normalized CO formation rate (frame A) and the CO selectivity (frame B). The CO formation rate increased from 8.7 to 24.4 µmol gcu<sup>-1</sup> s<sup>-1</sup> for a higher gas flow per catalyst volume by a factor of 6. Also the CO selectivity slightly increased from 95%c to 98%c upon increasing the GHSV. These observations indicate that the methanol formation is suppressed at higher flow rates by promoting the desorption of adsorbed CO from the catalyst

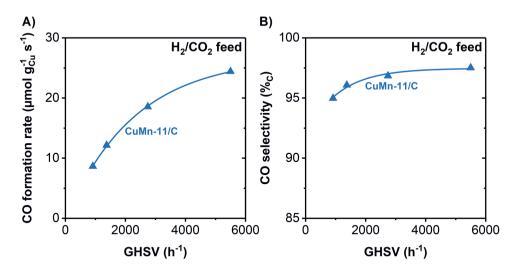
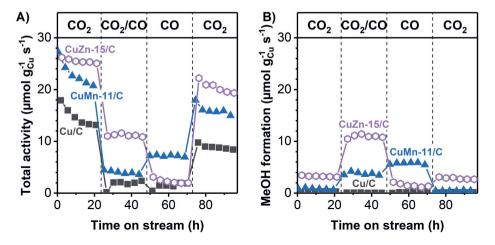


Figure 4.7 (A) CO formation rate and (B) CO selectivity as a function of gas hourly space velocity (GHSV) for the CuMn-11/C catalyst. The only other product was methanol with traces of CH<sub>4</sub> (<0.3%<sub>C</sub>). Conditions: 533 K, 20 bar(g), 1.1-6.4 mg Cu,  $H_2/CO_2/He = 67.5/22.5/10$  vol%. Under these conditions the thermodynamic equilibrium concentration consists of 82.3 %<sub>C</sub> CO. The data are fitted by an exponential curve.

surface, possibly by effectively removing adsorbed  $H_2O$ . Hence, supported  $CuMnO_x$  is an effective RWGS catalyst at low temperature and high GHSV.

# 4.3.4 Comparison between MnO<sub>x</sub> with the ZnO<sub>x</sub> promoter

An interesting question is whether the  $MnO_x$  promoter acts in a similar manner as the well-established  $ZnO_x$  promoter for methanol synthesis. **Figure 4.8** presents the catalytic performance of selected promoted Cu-based catalysts at 20 bar for the hydrogenation of either  $CO_2$ , CO, or a combination to methanol, mimicking the conditions during the *operando* XAS experiments. The activity of the CuMn-11/C catalyst is directly compared to a  $CuZnO_x/C$  reference catalyst with a Zn/(Cu + Zn) molar fraction of 0.15 and similar Cu particle size (see also **chapter 3**). All catalysts stabilized within the first 22 h in a pure  $H_2/CO_2$  feed (frame A). Only a slight additional loss of activity was observed when returning to the same reaction conditions after 74 h of catalysis.



**Figure 4.8** (**A**) Total activity in terms of converted  $CO_2$  and/or CO and (**B**) methanol formation rate as a function of time on stream for the Cu/C and CuMn-11/C catalysts as well as for a reference CuZn-15/C catalyst. Conditions: 533 K, 20 bar, 1.0 L min<sup>-1</sup>  $g_{Cu}$ -1, ca. 2,700 h<sup>-1</sup>, 2.1 mg Cu, feeds:  $H_2/CO_2/He = 67.5/22.5/10$  vol%,  $H_2/CO_2/CO/He = 60/3/27/10$  vol%, and  $H_2/CO/He = 60/30/10$  vol%.

The ZnO<sub>x</sub> promoter behaved as expected from literature in the various feed compositions <sup>77,94,108</sup>: frame A shows a higher activity for the CuZn-based catalyst in H<sub>2</sub>/CO<sub>2</sub> than in H<sub>2</sub>/CO, mainly due to an increased RWGS reaction activity leading to *ca.* 87%c CO, while frame B shows that the

highest methanol formation was observed when a small amount of CO<sub>2</sub> was added to the syngas feed.

The behavior of the MnO<sub>x</sub> promoter is quite different: the 3 vol% CO<sub>2</sub> in H<sub>2</sub>/CO gave a very low total activity (frame A) and methanol formation rate (frame B) for the CuMn-11/C catalyst. Another striking difference is that in the absence of CO<sub>2</sub> in the feed, MnO<sub>x</sub> promotion is much more effective than ZnO<sub>x</sub> promotion. Specifically, the total activity and the selectivity to methanol (80 vs 68%c), and hence the methanol formation (5.8 vs 1.3  $\mu$ mol gcu<sup>-1</sup> s<sup>-1</sup>), were ca. 4.5 times higher for MnO<sub>x</sub> promotion than for the ZnO<sub>x</sub>-promoted catalyst. A third major difference is that in an H<sub>2</sub>/CO<sub>2</sub> feed the MnO<sub>x</sub>-promoted catalyst had a much lower methanol selectivity than the CuZn-15/C catalyst (4%c vs 13%c). These observations were observed at a pressure of either 20 or 40 bar and irrespective of the Cu/promoter ratio. These results suggest that the interaction of CO<sub>2</sub> with the MnO<sub>x</sub> promoter is fundamentally different than with the ZnO<sub>x</sub> promoter.

#### 4.3.5 MnO<sub>x</sub> speciation measured with *operando* spectroscopy

The oxidation state and local surroundings of Cu and Mn species and the evolution of the MnO<sub>x</sub> structure were studied by XAS experiments under working conditions (also termed *operando*) of 20 bar and 533 K at the ROCK beamline of SOLEIL, simultaneously at the Cu and Mn K-edges. **Figure 4.9** shows a selection of normalized X-ray absorption spectra and corresponding first derivatives in the X-ray absorption near-edge structure (XANES) energy region. The spectra of several MnO<sub>x</sub> references are shown in frames A-B. Spectra for the CuMn-33/C and CuMn-11/C catalysts in an  $H_2$  atmosphere and during subsequent  $CO_2$  hydrogenation are given in frames C-F. The speciation of the fully reduced Cu in the CuMnO<sub>x</sub>/C catalysts (**figure 4.2**) did not change during catalysis, not even in the more oxidizing gas feed of  $H_2/CO_2$ , in line with literature on CuZnO<sub>x</sub> catalysts  $^{80,230}$ . The result was confirmed by a more in-depth multivariate analysis (data not shown).

Focusing on the promoter, the MnO<sub>x</sub> in the CuMn-33/C catalyst (frame C) consisted of almost exclusively Mn(II)–O with an Mn ON of +2.03 after the *in situ* H<sub>2</sub> treatment. During 3.5 h of high-pressure CO<sub>2</sub> hydrogenation the white line of MnO at 6554.7 eV shifted to a lower energy by 2.2 eV (as indicated by the arrow) and after catalysis resembled the MnCO<sub>3</sub> reference. This reference is typical for Mn(II) strongly coordinated to a carbonate species, or in other words *via* an oxygen bond to CO<sub>2</sub> (*i.e.* Mn(II)–O–CO<sub>2</sub>). This spectral shift was already observed during pressurization to 20 bar in H<sub>2</sub>/CO<sub>2</sub> at 453 K in *ca.* 2 h (**figure 4.10**), conditions that are well below typical methanol synthesis reaction temperatures and pressures. <sup>86,87</sup> To verify the formation of an Mn(II)–O–CO<sub>2</sub>-like compound we cooled the CuMn-33/C catalyst to room temperature in H<sub>2</sub>/CO<sub>2</sub> (denoted as "after cat.") to obtain a more pronounced spectrum, still resembling that of the MnCO<sub>3</sub> reference. Please note that after catalysis no crystalline MnCO<sub>3</sub> was observed in the XRD patterns of the

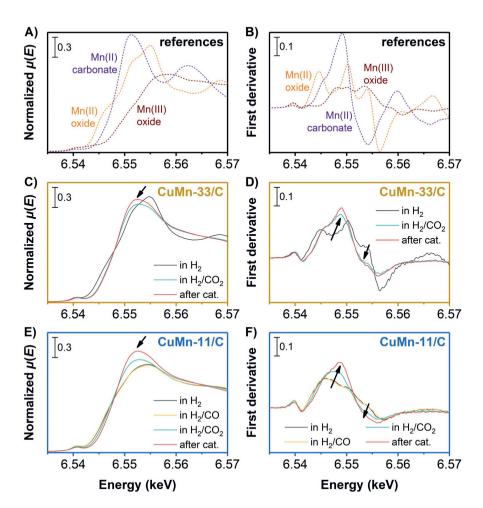


**Figure 4.9** (**A**) Reference (Mn<sub>2</sub>O<sub>3</sub>, MnO, and MnCO<sub>3</sub>) XANES spectra and (**B**) corresponding first derivatives on the Mn K-edge at 298 K. (**C-F**) *Operando* XANES spectra and corresponding first derivatives on the Mn K-edge of the (**C-D**) CuMn-33/C and (**E-F**) CuMn-11/C catalysts. Depicted (1) in an H<sub>2</sub> atmosphere at 453 K after a treatment in 20 vol% H<sub>2</sub>/He up to 543 K in 1 bar for *ca*. 25 min, (2) during subsequent H<sub>2</sub>/CO and H<sub>2</sub>/CO<sub>2</sub> conversion at 20 bar and 533 K after 160-210 min, and (3) after catalysis in H<sub>2</sub>/CO<sub>2</sub> at 20 bar and 298 K. Gas compositions: H<sub>2</sub>/CO/He = 60/30/10 vol% and H<sub>2</sub>/CO<sub>2</sub>/He = 67.5/22.5/10 vol%. The arrows indicate the formation of Mn(II) coordinated to a carbonated species upon H<sub>2</sub>/CO<sub>2</sub> conversion.

CuMnO<sub>x</sub>/C catalysts (data not shown). The average Mn ON did not further change during catalysis (*ca.* +2.04 at room temperature in a 20 bar H<sub>2</sub>/CO<sub>2</sub> feed, see also **table 4.2**), in line with a non-redox phase transition like that from Mn(II)–O to Mn(II)–O–CO<sub>2</sub>. The two isosbestic points at 6548 and 6558 eV provide a strong indication that Mn(II)–O binds CO<sub>2</sub> to form only one other species. <sup>337</sup> Also in the first derivative plot of the normalized absorption (frame D) the resemblance

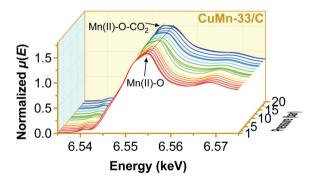


**Figure 4.10** Operando XANES spectra of the CuMn-33/C catalyst during pressurization in an  $H_2/CO_2$  atmosphere at 453 K, displaying gradual transformation of Mn(II)-O to Mn(II)-O-CO<sub>2</sub>. This process took 110 min. Conditions:  $H_2/CO_2/He = 67.5/22.5/10 \text{ vol}\%$ , 15 mL min<sup>-1</sup>.

**Table 4.2** Percentual distribution of Mn(III)–O, Mn(II)–O, and Mn(II)–O–CO<sub>2</sub> species and the Mn oxidation number (ON) by fitting linear combinations (LCF) of the XANES data using macrocrystalline references (Mn<sub>2</sub>O<sub>3</sub>, MnO, and MnCO<sub>3</sub>). Average Mn coordination number (CN) and bond length (R) by EXAFS analysis.

stage during	g XANES analysis				EXAFS analysis <sup>a</sup>	
XAS	Mn(III)-O	Mn(II)-O	Mn(II)-O-CO <sub>2</sub>	Mn ON	Mn CN	R (Å)
before H <sub>2</sub>	100 ± 1.4	0 ± 1.0	_	+3.00	2.4 ± 0.2 (Mn–O)	1.90
					-	2.99
in H <sub>2</sub> 24.1 ± 1.	24.1 ± 1.8	$75.9 \pm 1.5$	-	+2.24	$3.9 \pm 0.3  (Mn-O)$	2.05
111 112	24.1 ± 1.0				$4.4 \pm 1.7  (Mn-Mn)$	3.13
in $H_2/CO$ 24.2 ± 1.9	242 ± 10	$75.8 \pm 1.6$		+2.24	$3.8 \pm 0.4  (Mn-O)$	2.05
	/ J.O I 1.0		+2,24	$6.7 \pm 3.0  (Mn-Mn)$	3.14	
in H <sub>2</sub> /CO/CO <sub>2</sub> 24.	247 ± 10	$4.7 \pm 1.9$ $75.3 \pm 1.6$	-	+2.25	$3.8 \pm 0.3  (Mn-O)$	2.05
	24./ 11./				$6.7 \pm 2.6  (Mn-Mn)$	3.14
in H <sub>2</sub> /CO <sub>2</sub>	$14.5 \pm 0.9$	$48.4 \pm 2.1$	$37.1 \pm 1.2$	+2.14	4.0 ± 0.9 (Mn–O)	2.06
after catalysis	$5.5 \pm 1.0$	$48.9 \pm 2.1$	$45.6 \pm 1.3$	+2.05	$5.0 \pm 1.5  (Mn-O)$	2.10

<sup>&</sup>lt;sup>a</sup> The CNs and Rs are determined for the first Mn–O and second Mn–Mn shells using a fixed  $S_0^2$  value of the reference materials. The first-shell Mn–O CN is 6 with  $R = 2.20 \, \text{Å}$  ( $S_0^2 = 0.81$ ) and  $R = 1.99 \, \text{Å}$  ( $S_0^2 = 0.9$ ) for MnO and Mn<sub>2</sub>O<sub>3</sub>, respectively. The second-shell Mn–Mn CN is 6 with  $R = 3.15 \, \text{Å}$  ( $S_0^2 = 0.81$ ) and  $R = 3.13 \, \text{Å}$  ( $S_0^2 = 0.9$ ) for MnO and Mn<sub>2</sub>O<sub>3</sub>, respectively.

of the catalyst spectra in an H<sub>2</sub>/CO<sub>2</sub> feed and the MnCO<sub>3</sub> reference is clear (as indicated by the arrows). Hence, *operando* XAS in an H<sub>2</sub>/CO<sub>2</sub> feed strongly suggests the formation of Mn(II) strongly bound to a carbonate species because of the CO<sub>2</sub> interaction with Mn(II)–O.

The influence of the gas composition on the MnO<sub>x</sub> speciation is studied in more detail for the CuMn-11/C catalyst (frames E-F). After the *in situ* reduction, we started with a mixed MnO<sub>x</sub> phase with an average Mn ON of +2.24 (see also **figure 4.2**), which is in between the MnO (Mn(II)) and Mn<sub>2</sub>O<sub>3</sub> (Mn(III)) references. The spectral features of the CuMn-11/C did not change during more than 2.5 h of H<sub>2</sub>/CO conversion. Even subsequent enrichment of the syngas feed with 3 vol% CO<sub>2</sub>. which had a large influence on the promoter in the case of ZnOx-promoted methanol synthesis 94,104,105,291, did not influence the shape of the spectra (data not shown). Yet, with the switch to an H<sub>2</sub>/CO<sub>2</sub> feed, an Mn(II)-O-CO<sub>2</sub> complex was formed (frames E-F). These observations are supported by multivariate analysis on the Mn K-edge of the CuMn-11/C catalyst during subsequent changes in feed gas composition (figure \$4.2). In particular, the Mn speciation remained constant until the introduction of the H<sub>2</sub>/CO<sub>2</sub> feed, after which a clear fingerprint of an Mn(II) carbonatelike compound was observed and became dominant after ca. 3 h. The formation of an Mn(II)-O-CO<sub>2</sub> complex during catalysis (figure 4.8) indicates a strong CO<sub>2</sub> adsorption on the Mn promoter and probably a local depletion of adsorbed H atoms, which may explain the lower total activity and methanol selectivity of the CuMnO<sub>x</sub>/C catalysts when CO<sub>2</sub> is present in the feed. Therefore, during working conditions CO<sub>2</sub> has a strong impact on the local surroundings of the Mn species in CuMnO<sub>x</sub>/C catalysts, thereby influencing the MnO<sub>x</sub> promotion.

To differentiate between Mn(II)–O strongly binding CO<sub>2</sub> and crystalline MnCO<sub>3</sub> formation, it is important to consider the local coordination of the Mn atoms in the MnO<sub>x</sub> promoter during high-pressure CO<sub>2</sub> and CO hydrogenation by inspecting the extended X-ray absorption fine structure (EXAFS) energy region. **Figure 4.11** shows the Fourier-transformed EXAFS region of macrocrystalline Mn references in standard conditions (frame A) and the CuMn-33/C (frame B) and CuMn-11/C (frame C) catalysts in the reduced state, during working conditions in an  $H_2/CO_2$  feed, and after catalysis. The coordination numbers (CNs) and bond lengths from the EXAFS data analysis are summarized in **table 4.2**. After the *in situ* reduction two significant signals were observed in both catalysts: the first-shell Mn–O bond at R = 1.55 Å and next an Mn–Mn bond at R = 2.65 Å, both resembling the MnO reference. In the CuMn-11/C catalyst the signal corresponding to the Mn–Mn bond is less intense than for the CuMn-33/C catalyst and significantly lower than for the Mn–Mn bond of the Mn<sub>2</sub>O<sub>3</sub> reference. This result indicates a short-range ordering of the MnO<sub>x</sub> promoter in the CuMn-11/C catalyst, in line with the theoretical partial coverage of MnO<sub>x</sub> over the Cu<sup>0</sup> surface in this catalyst (73%).

The local environment of the MnO<sub>x</sub> promoter did not change upon high-pressure conversion of  $H_2/CO$ . Also enriching the syngas feed with 3 vol%  $CO_2$  for 4 h did not change the state of the MnO<sub>x</sub> promoter, but that might be due to the slow  $CO_2$  introduction at 20 bar. Only when  $CO_2$  was hydrogenated under working conditions, the spectra for both catalysts (**figure 4.11**) significantly changed: the signal at R = 2.65 Å corresponding to the second-shell Mn–Mn bond of MnO<sub>x</sub> decreased, and therefore resembled the Mn(II) carbonate reference. Interestingly, for the

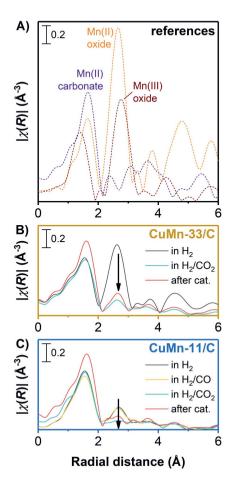


**Figure 4.11** Fourier-transformed EXAFS spectra at the Mn K-edge of (**A**) macrocrystalline references (Mn<sub>2</sub>O<sub>3</sub>, MnO, and MnCO<sub>3</sub>) at 298 K, (**B**) CuMn-33/C and (**C**) CuMn-11/C catalysts. The spectra of the catalysts are depicted (1) in an H<sub>2</sub> atmosphere at 453 K after *in situ* reduction and (2) during high-pressure H<sub>2</sub>/CO and subsequent H<sub>2</sub>/CO<sub>2</sub> conversion at 533 K (for exact conditions, see **figure 4.9**).

CuMn-33/C catalyst a fraction of the MnO phase remained present after catalysis, whereas for the CuMn-11/C catalyst the second-shell Mn–Mn bond peak completely vanished. The decrease in this peak intensity might be attributed to redispersion of the MnO<sub>x</sub> phase <sup>19</sup>, which is supported by the XRD analysis of the used CuMnO<sub>x</sub>/C catalysts in which no crystalline MnO<sub>x</sub> phases were observed (data not shown). Using *operando* XAS at simultaneously the Cu and Mn K-edges we unequivocally showed that the MnO<sub>x</sub> promoter is predominantly in the MnO phase after *in situ* reduction and high-pressure CO hydrogenation, whereas during CO<sub>2</sub> hydrogenation the promoter speciation changes drastically and an Mn(II)–O–CO<sub>2</sub>-like surface is formed.

# 4.4 Discussion

We observed a strong change in the  $MnO_x$  speciation in an  $H_2/CO_2$  feed with *operando* XAS, while such effects were absent for  $ZnO_x$  in oxide-supported  $CuZnO_x$  catalysts.  $^{292,301,315}$  We investigated the thermodynamic properties of the formation of  $MnCO_3$  (as a representation for the Mn(II)–O– $CO_2$  complex) and  $ZnCO_3$  in high-temperature  $CO_2$  hydrogenation  $^{98}$  to understand the different behavior of the  $MnO_x$  and  $ZnO_x$  promoters. **Equations (4.2)-(4.3)** show the thermodynamic parameters for the reactions of MnO and ZnO with  $CO_2$  at 533 K and 1 bar. Interestingly, under these conditions the formation of  $MnCO_3$  is favored (negative  $\Delta_r G$ ), whereas ZnO cannot spontaneously react with  $CO_2$  to form  $ZnCO_3$  (positive  $\Delta_r G$ ). Even though the negative entropy ( $\Delta_r S$ ) shows that the Gibbs free energy becomes more negative at higher pressure (*e.g.* 20 bar),  $CO_2$  significantly binds stronger to MnO than to ZnO.

$$\Delta_{\rm r} H_{533\rm K} \, (\rm kJ \; mol^{-1}) \quad \Delta_{\rm r} S_{533\rm K} \, (\rm J \; mol^{-1} \; K^{-1}) \quad \Delta_{\rm r} G_{533\rm K} \, (\rm kJ \; mol^{-1})$$
 
$$MnO_{(8)} + CO_{2\,(9)} \rightleftarrows MnCO_{3\,(8)} \qquad -101 \qquad -164 \qquad -13.6 \qquad \textbf{(4.2)}$$

$$ZnO_{(s)} + CO_{2(g)} \rightleftarrows ZnCO_{3(s)}$$
 -68.7 -169 +21.6 (4.3)

The binding of CO<sub>2</sub> to MnO can represent various structures (**figure 4.12**). For example, it can indicate strongly adsorbed CO<sub>2</sub> on the manganese and oxygen atoms of Mn(II)–O (structure A) or the closely related formation of crystalline MnCO<sub>3</sub> (structure B). For the first structure it implies that the Mn(II)–O–CO<sub>2</sub>-type complex only forms at the surface of the MnO<sub>x</sub> promoter and hence lacks long-range crystallinity, while for the second structure the diffusion of CO<sub>2</sub> into the MnO is required. During catalysis we observed that the methanol productivity is influenced in a reversible

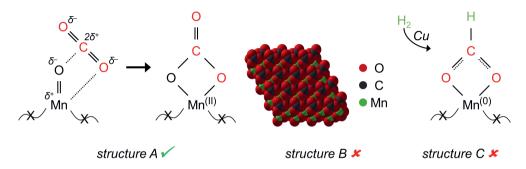


**Figure 4.12** Theoretically possible structures for the Mn(II)–O–CO<sub>2</sub>-type complex of which only structure A is supported by our data.

manner by changing between  $CO_2$ -rich gas and pure syngas feeds (**figure 4.8**) and after catalysis no crystalline  $MnCO_3$  was observed in the XRD patterns of the  $CuMnO_x/C$  catalysts (data not shown), making the second structure unlikely. Also the low Mn CN of  $4.0 \pm 0.9$  for the first-shell Mn-O bond in an  $H_2/CO_2$  feed is in line with structure A, while it makes the formation of crystalline  $MnCO_3$  (having a corresponding Mn-O CN of 6) highly unlikely. Alternatively, the  $Mn(II)-O-CO_2$ -like structure might be envisioned as an adsorbed, oxygen-bound formate ( $HCOO^*$ ) species, which is a reaction intermediate typically found in Cu-catalyzed  $CO_2$  hydrogenation  $^{111}$ , on an  $Mn^0$  surface formed following an H atom spillover from the  $Cu^0$  surface (structure C). According to the binary phase diagram up to 26 at%  $Mn^0$  can dissolve into  $Cu^0$  nanoparticles at 533 K, forming a CuMn solid solution in coexistence with  $Cu_5Mn$  and  $Cu_3Mn$  phases.  $^{316}$  Yet, no metallic Mn was observed in the XANES (**figure 4.9**) or EXAFS analysis (**figure 4.11**), which would be needed to support the  $Mn^0$ -HCOO structure, thereby making the formation of formates on the  $MnO_x$  promoter surface also highly unlikely. Hence, the spectral change upon  $H_2/CO_2$  exposure is most probably related to the formation of strongly bound  $CO_2$  to Mn(II)-O (structure A).

It must be noted that MnC<sub>2</sub> (amongst the Mn carbides) is a stable compound under the studied reaction conditions, while Zn carbides are highly unstable. This suggests that MnC<sub>2</sub> might be (partially) formed during catalyst synthesis by the strong interaction between the graphite support and MnO in the presence of H<sub>2</sub> with concomitant H<sub>2</sub>O formation. However, **figure 4.2** does not show any signal that can be attributed to MnC<sub>2</sub>. Furthermore, the formation of MnC<sub>2</sub> from CO<sub>2</sub> under working conditions would require the scission of the C–O bond in the CO molecule, which is not expected to take place on Cu nanoparticles <sup>39,94,95</sup>, an MnO surface, or a Cu–MnO<sub>5</sub> interface.

The first step in CO<sub>2</sub> hydrogenation is the adsorption of CO<sub>2</sub> on a catalyst surface (also termed CO<sub>2</sub>\*), which can either dissociate into O\* and CO\* directly or via a hydrogenated, carbon-bound carboxyl (HOCO\*). The binding strength of the adsorbed CO on a Cu/oxide interface is a key factor for the product selectivity in CO2 hydrogenation. 118 A weak CO\* binding to the interface facilitates the desorption of CO\* from the surface, while stronger bound CO\* is likely to further hydrogenate to a carbon-bound formyl species (HCO\*), one of the possible intermediates leading to the formation of methanol, <sup>326</sup> **Figure 4.6** shows that the CO selectivity is not influenced upon MnO<sub>x</sub> promotion of the supported Cu nanoparticles, while for the CuZnO<sub>x</sub>/C catalysts the CO selectivity decreased from 86 to 73%c in favor of methanol. This can be explained by the weak interaction of CO\* with Mn(II)-O or the Cu/MnO interface, while CO\* has probably a stronger interaction with ZnO<sub>x</sub>. Another important factor for the product selectivity is the surface coverage of adsorbed H atoms and CO<sub>2</sub>, which both are needed to form either CO or methanol. To complete one turnover from CO<sub>2</sub> to CO requires only one H<sub>2</sub> molecule (i.e. two H\* atoms) while three H<sub>2</sub> molecules are needed to produce one methanol molecule. The observed Mn(II)-O-CO2 structure in the CuMnO<sub>x</sub>/C catalysts by operando XAS (figures 4.9-4.10) indicates a high CO<sub>2</sub>\* coverage on the MnO promoter, and hence a locally low H2-to-CO2 ratio. In this way, the relatively low H\* surface concentration may suppress the hydrogenation of formyl species (HCO\*), or the related oxygen-bound formate species (HCOO\*)  $^{111}$ , to methanol and can explain the decrease in the methanol formation when CO<sub>2</sub> is added to the H<sub>2</sub>/CO feed (**figure 4.8**).

**Figure 4.13** schematically depicts the proposed MnO<sub>x</sub> speciation in CuMnO<sub>x</sub>/C. The MnO<sub>x</sub> structure in the CuMn-33/C catalyst (frames A-B) is discussed first. After *in situ* H<sub>2</sub> reduction the average Mn ON of the MnO<sub>x</sub> promoter in the CuMn-33/C catalyst is +2.03 (**figure 4.2**, frame E), and there is close contact between the Cu and Mn as evidenced by the reduction profile (**figure 4.2**, frame A). As the amount of MnO<sub>x</sub> corresponds to a 2.1-3.4 monolayer coverage of Mn atoms at the Cu<sup>0</sup> surface, the majority of the MnO is probably in a layer around the Cu<sup>0</sup> particles. As the MnO<sub>x</sub> loading was relatively high in this catalyst, also separate MnO particles can be envisioned (**figure 4.1**). These particles are in close proximity to Cu<sup>0</sup> nanoparticles as the reduction of Mn<sub>2</sub>O<sub>3</sub> to MnO at intermediate temperatures is facilitated, as shown by *ex situ* H<sub>2</sub> profiling (**figure 4.2**, frame A). Upon CO<sub>2</sub> hydrogenation and subsequently after catalysis a significant amount of MnO is left in the CuMn-33/C catalyst (**figure 4.11**, frame B). Mn(II)-O-CO<sub>2</sub> compounds probably only form at the MnO surface, as the diffusion of the required CO<sub>2</sub> into the MnO is limited. <sup>338</sup> This suggests the formation of a layered Cu<sup>0</sup>-MnO-Mn(II)-O-CO<sub>2</sub> structure (from core to surface) in an H<sub>2</sub>/CO<sub>2</sub> feed.

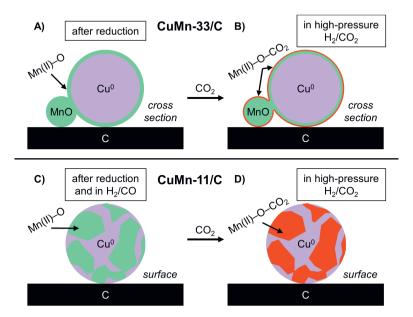


**Figure 4.13** Schematic representation of the proposed  $MnO_x$  speciation in the **(A-B)** CuMn-33/C and **(C-D)** CuMn-11/C catalysts, depicted **(A,C)** after *in situ* reduction (and high-pressure CO hydrogenation) and **(B,D)** during  $CO_2$  hydrogenation. Note that a limited amount of  $Cu_xMn$  alloys might be formed at each case.

The MnO<sub>x</sub> speciation of the CuMn-11/C catalyst (**figure 4.13**, frames C-D) has similar features as the CuMn-33/C catalyst after *in situ* H<sub>2</sub> reduction and high-pressure catalysis. The main difference is that the MnO<sub>x</sub> content is much lower, corresponding to *ca.* 0.7 monolayers of Mn on the CuO<sub>x</sub> nanoparticles. As a result, upon CO<sub>2</sub> hydrogenation almost all MnO<sub>x</sub>, mostly at the surface of Cu<sup>0</sup> particles, is transformed in an Mn(II)–O–CO<sub>2</sub> compound, supported by the nearly complete depletion of the Mn–Mn peak resembling MnO in EXAFS analysis (**figure 4.11**, frame C).

# 4.5 Conclusions

Cu particles on graphitic carbon were prepared to study the MnO<sub>x</sub> promotion in the hydrogenation of either CO<sub>2</sub> or CO. In an H<sub>2</sub>/CO feed only a modest amount of MnO<sub>x</sub>, in close interaction with Cu, was sufficient to enhance the activity of Cu/C thereby producing mainly methanol, and was much more effective than a CuZnO<sub>x</sub>/SiO<sub>2</sub> catalyst with a similar promoter content. In CO<sub>2</sub> hydrogenation MnO<sub>x</sub> promotion also increased the total activity with a selectivity to CO up to 87%c while retaining this high selectivity irrespective of the Mn content, even at lower temperatures (473 K), making CuMnO<sub>x</sub>/C a low-temperature reverse water-gas shift catalyst. From X-ray absorption spectroscopy studies at high temperature and pressure we can explain this by the reversible formation of an Mn(II)–O–CO<sub>2</sub> complex, which has not been observed for the ZnO<sub>x</sub> promoter. This surface-specific Mn speciation may indicate a high coverage of adsorbed CO<sub>2</sub> on MnO<sub>x</sub>, while the local H atom coverage is relatively low; essential to suppress subsequent hydrogenation to methanol and lead to the desorption of adsorbed CO. This gives a direct insight into the nature of MnO<sub>x</sub> promotion in Cu-based syngas conversion and allows a more rational use of reducible oxides in catalyst design.

# Acknowledgments

We are very grateful to Laura Barberis who contributed greatly to this chapter: she synthesized some catalysts, performed catalyst testing, and wrote substantial parts. Nienke Visser designed the catalyst synthesis protocol. Laura Barberis, Giorgio Totarella, Petra de Jongh, and Xavier Carrier (Sorbonne University) are thanked for performing the XAS experiments. Laura Barberis, Florian Meirer, and Ad van der Eerden helped with the analysis and interpretation of the XAS data. We acknowledge SOLEIL (France) for provision of synchrotron radiation facilities, and we would like to thank Camille La Fontaine and Valérie Briois for assistance in using the ROCK beamline, for the help with the data interpretation, and the design of the experimental method.

# Supplementary figures

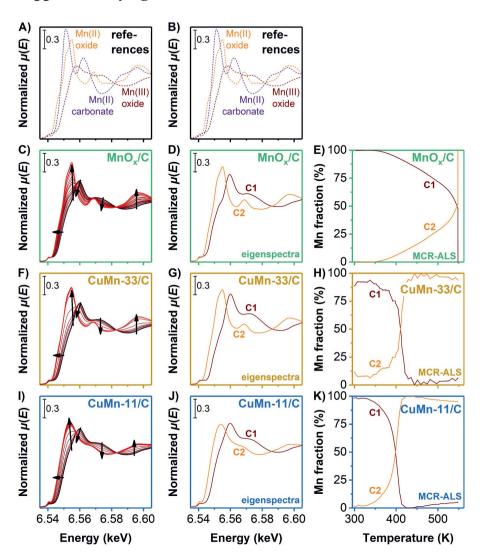
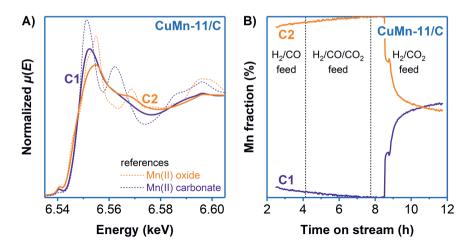


Figure S4.1 (A-B) Macrocrystalline Mn references at 298 K. (B,F,I) Time-resolved XANES spectra at the Mn K-edge of the (C) MnO<sub>x</sub>/C, (D) CuMn-33/C, and (E) CuMn-11/C catalysts during an H<sub>2</sub> treatment (solid lines from black to red). (D,G,J) Extracted eigenspectra and (E,H,K) corresponding concentration profiles by multivariate analysis (MCR-ALS) of the (D-E) MnO<sub>x</sub>/C, (G-H) CuMn-33/C, and (J-K) CuMn-11/C catalysts. The extracted components C1 and C2 clearly have a good resemblance to the macrocrystalline Mn(III)—O and Mn(II)—O references. Yet, for the CuMn-11/C catalyst the whiteline of component C2 is significantly lower than for the corresponding reference. The trends in the concentration profiles resemble the LCF analysis in figure 4.2. Conditions: 20 vol% H<sub>2</sub>/He, from 298 to 541 K (ramp 2.5 K min<sup>-1</sup>), 1 bar.



**Figure S4.2** (**A**) Extracted eigenspectra and (**B**) corresponding concentration profiles obtained by multivariate analysis (MCR-ALS) of time-resolved, *operando* XAS spectra at the Mn K-edge of the CuMn-11/C catalyst during various stages of the experiment (all at 20 bar and 533 K;  $H_2/CO$  feed =  $H_2/CO/He = 60/30/10$  vol%;  $H_2/CO/CO_2$  feed =  $H_2/CO/CO_2$ /He = 60/30/3/10 vol%;  $H_2/CO_2$  feed =  $H_2/CO/He = 67.5/22.5/10$  vol%). The first 2 h in frame B correspond to pressurization and reactor heating in the  $H_2/CO$  feed. The extracted eigenspectra reasonably match the macrocrystalline Mn(II) oxide and Mn(II) carbonate references at 298 K (dashed lines in frame A). Intensity differences can be ascribed to temperature and particle size effects. Please note that it is not possible to directly compare the Mn fraction obtained by MCR-ALS (frame B) to LCF (**table 4.2**), as for MCR-ALS only two components were considered during the analysis.

# Exploratory study of the synthesis of bimetallic copper-cobalt catalysts by impregnation and electroless deposition

#### **Abstract**

Intimacy between different surface atoms plays a key role in bimetallic catalysts, for example in Cu-Co catalysts to obtain a high selectivity to long-chain alcohols upon CO hydrogenation. A major hurdle, however, is the preparation of bimetallic catalysts with high intimacy and to maintain this intimacy under reaction conditions. In this chapter we explore the effect of the synthesis method and Cu/Co ratio on the structural properties of supported CuCoO<sub>x</sub> nanoparticles. We show that CuCoO<sub>x</sub> nanoparticles of 3-4 nm can be synthesized by the coimpregnation of a graphite support with Cu and Co species, and their particle size is rather insensitive to a variation of preparation parameters. The stable particle size is due to the addition of Co. thereby limiting the total particle growth during catalyst synthesis. Yet, larger CuCo crystallites of ca. 7 nm can be prepared by a mild oxidation and subsequent reduction of supported CuCoO<sub>x</sub> nanoparticles. Alternatively, we also show that electroless deposition (or galvanic replacement) of the outer layer of pre-deposited Co nanoparticles with metallic Cu via the redox reaction of Cu+ ions in oleylamine with metallic Co is an effective method to prepare silica-supported CuCoO<sub>x</sub> nanoparticles with a high Cu-Co intimacy. These particles better retain the intimacy between Cu and Co during CO hydrogenation than the impregnated catalysts but have lower activities. More research is needed to better understand the interesting observations between the preparation methods.

# 5.1 Introduction

The choice of the active metal is based on the adsorption strength of key intermediates in the reaction, which its turn depends on the extent and nature of electron density sharing between adsorbates (reactants, intermediates, and products) and the active metal. This determines not only the activity but also the selectivity in a catalyzed reaction. For example, rhodium is the only single metal that can effectively form C–C bonds on its surface but has a moderate activity for C–O bond breaking of adsorbed CO molecules. As a result, upon CO hydrogenation long-chain alcohols, especially ethanol, can be formed with a product selectivity up to 40 %c. <sup>339</sup> Yet, rhodium is not commercially relevant for ethanol synthesis due to its high price and relatively modest activity compared to homogeneous catalysts. <sup>137</sup>

To limit the use of precious metals, it is considered to partially replace it by less precious metal or to replace it completely by a combination of two less precious metals that mimic the same properties. For the synthesis of alcohols by CO hydrogenation, bimetallic CuCo (oxides) are interesting. In laboratory-scale CO hydrogenation, the combination of Co and Cu can lead to the production of long-chain alcohols.  $^{55}$  This bimetallic system is for instance also relevant for the activation of  $H_2O_2$  to form free radicals for the degradation of organic pollutants, and the Cu and Co redox pairs have a wider pH stability window compared to the typically used  $Fe^{2+}/Fe^{3+}$  redox pair.  $^{340-342}$ 

The intimacy between the Cu and Co plays a key role in the catalyst performance. The CO hydrogenation activity to form long-chain alcohols is either attributed to  $Cu^0/CoO_x^{140,168}$ ,  $Cu^0/Co_2C^{176}$ ,  $Co/Co_2C^{177}$ , or synergy between  $Cu^+$  and  $Co^{0.174}$ . The close interaction between Cu and  $Co^{0.174}$  is also important for a high activity in oxidation reactions: it is believed that lattice  $Cu^{2+}$  ions partially exchanges lattice  $Co^{2+}$  in  $CuO/Co_3O_4$ , thereby creating lattice strain and active oxygen vacancies. <sup>156,343</sup> Next to electronic effects,  $Co^{0.167,344}$  and *vice versa* <sup>172</sup>.

One of the major challenges is to prepare surfaces with Cu and Co in close vicinity, as macrocrystalline CuCo alloys are not thermodynamically stable below 800 K. 345,346 At these temperatures, the solubility of Co within Cu is very limited and *vice versa*. As the mixing enthalpy is +10 kJ mol<sup>-1</sup> at an equimolar Cu–Co composition, the entropy gain upon mixing is important to establish CuCo alloying. <sup>189,202,319,347</sup> Also the different reducibility of Cu and Co oxides to their metallic form is a challenge and can result in metal segregation. <sup>173</sup> Yet, in nanosized CuCo a small window of stable CuCo surface compositions might be kinetically allowed as surface species melt at a significantly lower temperature than bulk materials (especially for nanoparticles smaller than 10 nm) and atom diffusion is faster at the nanoscale. <sup>189,202,319,347</sup>

Several preparation routes have been proposed to stabilize the active  $CuCo(O_x)$  phase and to minimize metal segregation during catalyst operation. For example, Prieto *et al.* <sup>173</sup> stabilized both Cu and Co species in a molybdate matrix using co-precipitation. Other procedures to stabilize the active  $CuCoO_x$  phase are reported, such as the use of perovskites <sup>140–147</sup>, colloidal synthesis <sup>148–150</sup>, citrate complexation <sup>20,151–156</sup>, oxalate precipitation <sup>157</sup>, deposition-precipitation <sup>158,159</sup>, dipcoating <sup>172,348,349</sup>, and variations thereof. Recently, the synthesis of a modified zeolitic imidazolate framework (ZIF) and subsequent carbonization/pyrolysis obtains embedded CuCo alloys in nitrogen-functionalized carbon materials. <sup>160,169,343,350,351</sup> Yet, these emerging techniques for the synthesis of bimetallic CuCo catalysts might be challenging to scale up.

Galvanic replacement, also known as electroless deposition, is an industrially widely used technique for the synthesis of electrodes, to modify metal surfaces, and to coat CoP with a copper layer in the semiconductor industry. <sup>352,353</sup> At a smaller scale this method is applied to synthesize bimetallic and also hollow nanostructures with good control over the particle composition. <sup>354,355</sup> The galvanic replacement is a redox reaction between metal ions in solution and a solid metallic phase without the use of an external current. The reaction is solely driven by the difference in the reduction potentials of the metal ions in solution and the ions that emerge from the metallic phase. In this way the metal ions from solution are reduced and deposited on the metallic phase, simultaneously with the oxidation of the metallic phase and its (partial) dissolution. The reaction is self-limiting: after the top layer is replaced by the more noble metal, the replacement stops. This allows very even coating of surfaces and nanostructures.

In this exploratory chapter we discuss the synthesis and properties of bimetallic CuCo nanoparticles supported on graphitic carbon or silica in detail. To this end, we compared two preparation methods: more conventional incipient wetness co-impregnation (see also **section 1.1.3**) of a graphite support and a new method: partial galvanic replacement of predeposited Co particles on silica by a surface layer of Cu. We explore the influence of the preparation parameters and applied new combinations, such as impregnation under vacuum and using a functionalized support as well as applying galvanic replacement on pre-deposited Co nanoparticles. We used CO hydrogenation as a probe reaction to examine the stability of the bimetallic catalysts.

# 5.2 Experimental

# 5.2.1 Surface oxidation of graphite

 $\it Ca.10$  g of high surface area graphite (xGnP® C-500 HP, XG Sciences) was dispersed in 400 mL 65 vol% HNO<sub>3</sub> (Merck) in a 1 L round-bottom flask. The mixture was heated to 353 K and held for 2 h at this temperature while magnetically stirring at 1000 rpm. The evolving NO<sub>x</sub> gasses were trapped in downstream H<sub>2</sub>O bottles. After the heating step the mixture was quickly quenched by

addition of *ca*. 500 mL cold, demineralized H<sub>2</sub>O. The material was washed and decanted until the effluent reached a pH of 6-7. The obtained oxidized graphite (oxC) was dried at 393 K at static air for several days and finely crushed afterwards. Further drying was at 423 K for 2 h under dynamic vacuum (*ca*. 1 mbar) and transferred to an Ar-filled glovebox before use.

#### 5.2.2 Catalyst synthesis

**CuCoO**<sub>x</sub>/**oxC** catalysts by impregnation. First, ca. 1 g of oxC was evacuated under dynamic vacuum at room temperature to remove the Ar from the pores. An aqueous impregnation solution of Cu and Co nitrates (Acros Organics, >99%), acidified to pH 1 with HNO<sub>3</sub> (Merck, 65 vol%), was used to impregnate ca. 90 vol% of the pores of oxC (total pore volume = 0.86 mL g<sup>-1</sup>) under static vacuum while heavily stirring. After 1 h of equilibrating the liquid within the sample at static vacuum, the impregnate was dried under dynamic vacuum (ca. 1 mbar) at room temperature for 24 h, resulting in ca. 1.3 g of dried pre-catalyst. Around 1.1 g of this material was loaded into a tubular reactor without exposure to air and reduced using a bottom-up flow of 200 mL min<sup>-1</sup> gcat<sup>-1</sup> of 5 vol% H<sub>2</sub>/N<sub>2</sub> and heating to 623 K (ramp 0.5 K min<sup>-1</sup>) for 2 h. The reactor was flushed with nitrogen at room temperature before the reduced powder was transferred to an Ar-filled glovebox. In this way CuCoO<sub>x</sub>/oxC catalysts with a total metal loading of 10 wt% but varying Cu/(Cu + Co) molar ratios were synthesized.

**Co/SiO<sub>2</sub> catalyst by impregnation**. Silica gel (Davicat® SI 1351, Grace Davison) was dried under dynamic vacuum at 573 K up to 3 h and impregnated with an HNO<sub>3</sub>-acified, aqueous solution containing Co nitrate as previously described. After equilibration and drying under vacuum, the material was heat-treated in a tubular reactor at 573 K (ramp 2 K min<sup>-1</sup>) for 1 h in an N<sub>2</sub> flow and subsequently reduced at 723 K (ramp 5 K min<sup>-1</sup>) for 2 h in a 10 vol%  $H_2/N_2$  flow at 100 mL min<sup>-1</sup>  $g_{cat}$ -1. The reduced 8.5 wt% Co/SiO<sub>2</sub> sample (according to ICP-OES) was stored in an Ar-filled glovebox.

CuCoO<sub>x</sub>/SiO<sub>2</sub> catalysts by galvanic replacement (GR). Inspired on the synthesis procedure from Nafria *et al.* <sup>356</sup> the CuCoO<sub>x</sub>/SiO<sub>2</sub> catalysts were prepared by galvanically replacing predeposited Co<sup>0</sup> nanoparticles on SiO<sub>2</sub> by Cu<sup>(2)+</sup> ions using Schlenk line techniques. First, *o*-dichlorobenzene (Sigma Aldrich, 99%), oleylamine (OLA, Sigma Aldrich, 70%), and demineralized water (H<sub>2</sub>O) were dried under dynamic vacuum and flushed with N<sub>2</sub> at elevated temperatures. Typically, 15 mL of 10 mM copper(I) chloride (Sigma Aldrich, >99%) or copper(II) nitrate in respectively degassed oleylamine or water was cold-injected to 200 mg reduced Co/SiO<sub>2</sub> sample. This resulted in a theoretical molar Cu/(Cu + Co) ratio of 0.3-0.4. The mixture was quickly heated (60 K min<sup>-1</sup>) to either 458 or 363 K for 30 min. The CuCoO<sub>x</sub>/SiO<sub>2</sub> catalysts were retrieved by centrifugation and redispersion (5-7 times) in the used solvent and ethanol. The catalysts were

dried in static air at 333 K for 1 h, at 393 K overnight and under dynamic vacuum at 353 K for 3 h. Organic ligands were removed by first drying the catalyst at 393 K (ramp 5 K min<sup>-1</sup>) for 30 min in pure N<sub>2</sub>, subsequently for 30 min in 20 vol% O<sub>2</sub>/N<sub>2</sub> for, and finally at 723 K (ramp 5 K min<sup>-1</sup>) for 1 h at a flow of 200 mL min<sup>-1</sup>  $g_{cat^{-1}}$ . A reference  $CuCoO_x/SiO_2$  catalyst (3.9 wt% Co, 2.3 wt% Cu, according to ICP-OES) was prepared by co-impregnation to incipient wetness (as described for the  $Co/SiO_2$  sample) and treated in a 200 mL min<sup>-1</sup>  $g_{cat^{-1}}$  N<sub>2</sub> flow at 573 K (ramp 2 K min<sup>-1</sup>) for 1 h. All catalysts are denoted as X-CuCo/[sup] with X = the Cu/(Cu + Co) molar ratio with [sup] either oxC or  $SiO_2$ .

**Equations (5.1)-(5.4)** show the standard reduction potentials relative to the normal hydrogen electrode (NHE, at 298 K, 1 atm, and in H<sub>2</sub>O) involved in the synthesis of bimetallic CuCo nanoparticles by galvanic replacement. The combination of these half reactions shows that Co has to be in the Co<sup>0</sup> oxidation state to enable Cu<sup>+</sup> or Cu<sup>2+</sup> ions to spontaneously deposit on the Co<sup>0</sup> surface without applying an external current (**equations (5.5)-(5.6)**). <sup>357</sup> This is also a practical disadvantage as metallic Co is readily oxidized in air and hence the reaction must be performed in an inert or reducing atmosphere.

$$Cu^{2+} + 2e^{-} \rightleftharpoons Cu^{0}$$
  $E^{\Theta} = +0.34 \text{ V}$  (5.1)

$$Cu^{+} + e^{-} \rightleftharpoons Cu^{0}$$
  $E\Theta = +0.52 \text{ V}$  (5.2)

$$Co^{2+} + 2e^{-} \rightleftharpoons Co^{0}$$
  $E\Theta = -0.28 \text{ V}$  (5.3)

$$Co^{3+} + e^{-} \rightleftharpoons Co^{2+}$$
  $E^{\Theta} = +1.92 \text{ V}$  (5.4)

$$2Cu^{+} + Co^{0} \rightleftharpoons 2Cu^{0} + Co^{2+}$$
  $\Delta E^{\ominus} = +0.80 \text{ V}$   $\Delta G^{\ominus} = -155 \text{ kJ mol}^{-1}$  (5.5)

$$Cu^{2+} + Co^{0} \rightleftharpoons Cu^{0} + Co^{2+}$$
  $\Delta E = +0.62 \text{ V}$   $\Delta G = -120 \text{ kJ mol}^{-1}$  (5.6)

#### 5.2.3 Catalyst characterization

Acid-base titration and PZC determination. The amount of acidic surface groups on graphite was determined on a TitraLab TIM880 Titration set-up. To this end, 20 mg carbon material was dispersed in 65 mL 0.1 M KCl (Acros Organics,  $\geq$ 99%) in H<sub>2</sub>O. Throughout the whole procedure the solution was stirred at 500 rpm and purged with N<sub>2</sub> to remove dissolved CO<sub>2</sub> from the solution. After 5 min of purging the dispersed carbon material was titrated with 0.01 M NaOH (Merck,  $\geq$ 99%) in 0.1 M aqueous KCl. The acid surface group density was calculated using the BET surface area obtained from N<sub>2</sub> physisorption. The point of zero charge (PZC) was determined by stepwise dispersing small amounts of graphite in an aqueous 0.1 M Ba(NO<sub>3</sub>)<sub>2</sub> solution while

measuring the pH. The PZC was reached when the pH did not significantly change upon sample addition.

**EM imaging**. Catalysts were imaged by transmission electron microscopy (TEM) on an FEI Tecnai 20 apparatus, operating at 200 kV. High-angle, annular, dark-field scanning transmission electron microscopy (HAADF-STEM) images were obtained on a Thermo Fisher Scientific Talos F200X apparatus, operating at 200 kV. With the same apparatus chemical maps were acquired using energy-dispersive X-ray (EDX) detectors and  $Velox^{TM}$  analytical imaging software. To this end, finely ground sample (<25  $\mu$ m) was dispersed in ethanol and deposited onto holey carbon film-coated Cu or Au grids (Agar, 300 mesh). Number-averaged CuO particle sizes ( $d_N$ ) were determined by measuring at least 280 individual particles at various locations within the sample. Only the relevant part of the lognormal distribution (>1% of the modus) was considered for the calculation of average particle sizes.

 $N_2$  physisorption.  $N_2$  physisorption isotherms were recorded on a Micromeritics TriStar II Plus apparatus at 77 K. The samples were first dried at 443 K (or at 573 K for the SiO<sub>2</sub> support) under an  $N_2$  flow overnight. The BET surface area was determined according to the IUPAC procedure.  $^{278}$  A Barrett-Joyner-Halenda (BJH) analysis was used to obtain pore size distributions, using either a carbon black or Harkins-Jura thickness curve. The single-point total pore volume  $V_{\text{tot}}$  was determined at  $p/p_0 = 0.995$ . Integration of the adsorption branch of the pore size distribution between 2 and 50 nm obtained the mesoporosity. The micropore volume  $V_{\text{micro}}$  was calculated by using the t-plot method with the same thickness curves.

TG-MS analysis. Mass loss by thermogravimetric analysis (TGA) was recorded on a PerkinElmer TGA 8000 apparatus connected to a Hiden Analytical HPR-20 mass spectrometer. The carbon support stability was probed by reduction of a vacuum-dried Co/C impregnate in 5 vol% H<sub>2</sub>/Ar (100 mL min<sup>-1</sup>) at 623 K (ramp 2 K min<sup>-1</sup>) for 8 h. The effective Co loading was determined by drying a Co/C catalyst (as synthesized according to **section 5.2.2**) at 393 K in Ar (80 mL min<sup>-1</sup>) for 30 min, cooling down to 323 K, and a full oxidation at 1073 K (ramp 5 K min<sup>-1</sup>) in 20 vol% O<sub>2</sub>/Ar (80 mL min<sup>-1</sup>). The oxidation temperature to remove organic ligands on CuCoO<sub>x</sub>/SiO<sub>2</sub> catalysts prepared by GR was determined by the same oxidative TG-MS procedure. The mass loss patterns and mass spectrometry (MS) profiles were corrected for buoyancy effects.

**TPR and TPO profiling.** Temperature-programmed reduction (TPR) by  $H_2$  and oxidation (TPO) by  $O_2$  were performed on a Micromeritics AutoChem II 2920 apparatus. Prior to the reduction the sample (60-75 mg) was dried at 393 K under an Ar flow of 50 mL min<sup>-1</sup> for 30 min and cooled down to room temperature. Reduction profiles were recorded with a thermal conductivity detector (TCD) when the  $CuCoO_x/oxC$  samples were exposed to a 5 vol%  $H_2/Ar$  flow of 170-570 mL min<sup>-1</sup>  $g_{sam}$ -1 up to 1073 K with a ramp of 2-5 K min<sup>-1</sup>. Similarly, oxidation profiles were recorded in a 5 vol%  $O_2/He$ 

flow of 180 mL min<sup>-1</sup>  $g_{sam^{-1}}$ . H<sub>2</sub>O was captured with a dry ice/isopropanol cold trap. MS data was recorded on a Hiden Analytical OGA apparatus.

**XRD analysis**. Powder X-ray diffractograms of the reduced and air-exposed catalysts were recorded on a Bruker AXS D8 Advance or D2 Phaser diffractometer at room temperature. Samples were irradiated by Co K $\alpha$  radiation ( $\lambda$  = 1.790 Å) at 30 kV and 45 mA. The Scherrer equation was used including the instrumental breadth of the XRD apparatus (ca. 0.1°) to determine crystallite sizes. All diffractograms were normalized between 0 and 1 and vertically stacked.

#### 5.2.4 Synthesis gas conversion experiments

Powdered catalysts were pressed into granulites between 75-150  $\mu$ m and were loaded (32-61 mg) in stainless steel reactors (ID 2.6 mm) in a 16-reactor setup (Flowrence, Avantium). The catalysts were diluted with SiC (212-245  $\mu$ m fraction, Alfa Aesar,  $\geq$ 98.8%, 46 grit), resulting in a SiC content *ca.* 87 vol% of the total packed catalyst bed. <sup>279</sup> The SiC had been previously calcined at 1073 K for 10 h, washed with 65 vol% HNO<sub>3</sub>, rinsed with MilliQ water until pH 7 was reached, and dried in static air at 393 K overnight. The difference in sieve fractions between the catalysts and diluent facilitated post-analysis by EM and XRD.

An *in situ* reduction was performed in at least 1.5 L min<sup>-1</sup>  $g_{CuCo}^{-1}$  of 5-10 vol%  $H_2/N_2$  for 3.5 h at 523 K for Cu/oxC, 623 K for all other  $CuCoO_x/oxC$  catalysts or 723 K for the  $SiO_2$ -supported catalysts after which the temperature was lowered to 393 K. The reactors were exposed to a 2.5-3.8 mL min<sup>-1</sup> flow of  $CO_2$ -free syngas ( $H_2/CO/He = 60/30/10$  vol%), leading to a gas-hourly space velocity (GHSV) of 1,900 h<sup>-1</sup>. The reactors were pressurized to 40 bar(g), heated to 533 K (ramp 2-5 K min<sup>-1</sup>), and held for at least 125 h. The  $CuCoO_x/oxC$  catalysts were exposed to varying amounts of  $CO_2$  in the feed (up to 3 vol%) but did not have any effect on the catalyst performance. The  $CuCoO_x/SiO_2$  catalysts were also tested at 60 bar(g) after 82 h on stream. A tri-phase carbonyl trap (active carbon,  $\gamma$ -Al<sub>2</sub>O<sub>3</sub>, ZnO) was located upstream the CO feed to remove metal carbonyls and sulfur species. Products were periodically analyzed by online gas chromatography every 23 min. After catalysis, the samples were slowly exposed to air at 393 K. The calculations of activity, selectivity, and stability are detailed in **section 2.2.5**.

#### 5.3 Results and discussion

#### 5.3.1 Structural properties of the impregnated catalysts

We functionalized the surface of the graphitic support via liquid-phase oxidation in HNO<sub>3</sub> according to a published method. <sup>334</sup> **Figure 5.1** shows for the pristine and oxidized graphite the

acid-base titration curves (frame A),  $N_2$  physisorption isotherms (frame B), X-ray diffraction patterns (frame C), and point of zero charge (PZC) determination (frame D). The pristine graphite has a native acidic surface group density of 0.14 nm<sup>-2</sup> (frame A). <sup>358</sup> Upon oxidation the acidic surface group density increased 5-fold to 0.66 nm<sup>-2</sup> (frame A), while the decrease in surface area and total pore volume was only 14% (frame B). Also, the crystallinity of the carbon material remained intact upon surface oxidation (frame C). The strength of the acidic groups increased, as indicated by a decrease of the PZC from 3.2 to 2.1 (frame D). These values are important as they reflect the local pH in the pores of the graphite during catalyst synthesis *via* impregnation at a high support surface area to liquid volume ratio (0.8 mL g<sup>-1</sup> = ca. 48 wt%). From this characterization we conclude that the liquid-phase oxidation of graphitic carbon is an appropriate method to introduce acidic surface groups. These might serve as anchoring points for metal species and influence the local pH in the pores during catalyst preparation.

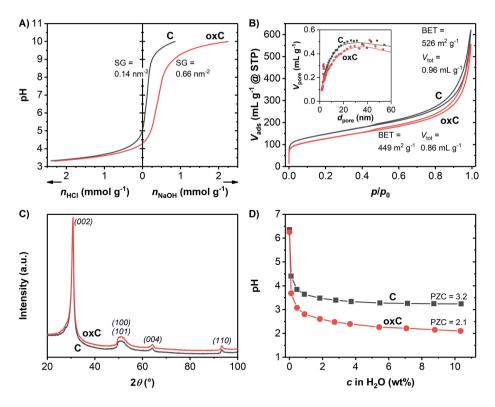


**Figure 5.1** Characterization of graphite (C) and oxidized graphite (oxC) supports. (**A**) Acid-base titration curves, also indicating acidic surface group (SG) densities. (**B**)  $N_2$  physisorption isotherms (inset = volume-based pore size distribution). (**C**) Vertically offset XRD patterns with peaks attributed to crystallographic planes. (**D**) PZC determination.

Using the oxidized graphite, we synthesized a series of  $CuCoO_x/oxC$  catalysts via incipient wetness co-impregnation and subsequent reduction at 623 K, all with a total CuCo loading of 10 wt% but varying Cu/Co ratios. **Figure 5.2** shows representative transmission electron microscopy (TEM) images (frames A-E) and corresponding particle size distributions of the catalysts (frames F-J). In each case a uniform spatial distribution of  $CuCoO_x$  particles (black dots) over the graphitic support (light grey) was obtained. The Cu/oxC catalyst (frame A) had significantly larger  $CuO_x$  particles (5.8  $\pm$  2.1 nm) than the  $(Cu)CoO_x/oxC$  catalysts (2-4 nm) (frames B-E), even though the reduction temperature was lower (523 vs 623 K). An enhanced Cu dispersion by  $CoO_x$  was also reported in

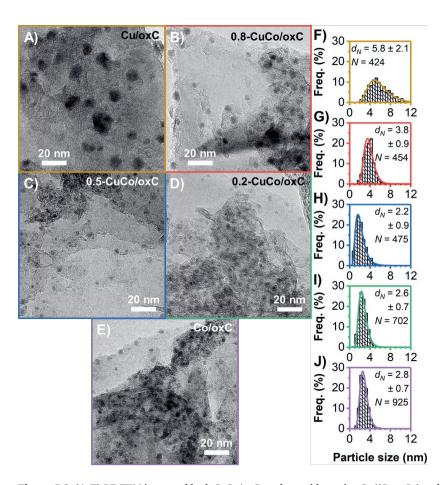


**Figure 5.2** (A-E) BF-TEM images of fresh CuCo/oxC catalysts with varying Cu/(Cu + Co) molar ratios: 1, 0.8, 0.5, 0.2, and 0, respectively. (F-J) Particle size distributions and number-averaged particles sizes in nm. The catalysts were reduced in 5 vol%  $H_2/N_2$  at 623 K (ramp 0.5 K min<sup>-1</sup>) for 2 h (at 523 K for Cu/oxC to minimize Cu particle growth).

literature for impregnated SBA-15 and for  $CuCoO_x/C$  prepared by ZIF pyrolysis.  $^{160,167}$  The  $CoO_x$  acts as a textural promoter, enhancing the Cu dispersion upon catalyst synthesis by impregnation.

**Figure 5.3** shows the spatial distribution of Cu (frame A) and Co (frame B) species in the 0.2-CuCo/oxC catalyst probed by energy-dispersive X-ray (EDX) spectroscopy. The nanoparticles (white dots) mostly consisted of Co species, but the Cu species were generally located in the same position, suggesting a strong intimacy between the two components. The ratio of the intensity of the Cu/Co signals in the corresponding X-ray spectrum matches the theoretical Cu/(Cu + Co) ratio of 20 at% (namely, 21.4 at%), showing that Cu and Co species were uniformly distributed in the fresh catalyst.

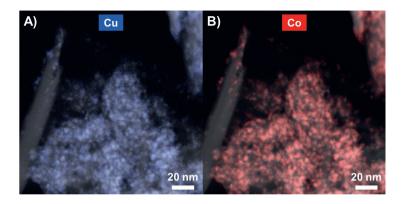


**Figure 5.3** EDX maps with an overlay of the corresponding HAADF-STEM image of the fresh, impregnated 0.2-CuCo/oxC catalyst for **(A)** Cu and **(B)** Co in the same area.

The reducibility of the carbon-supported CuCoO<sub>x</sub> nanoparticles was studied with H<sub>2</sub> reduction profiling (**figure 5.4**). The peaks between 420-460 K are mainly attributed to the reduction of CuO to Cu<sup>0</sup>. The temperature onset of these reduction peaks increased from *ca.* 395 K to 433 K with increasing Co loading. Interestingly, the total H<sub>2</sub> consumption around this temperature is 3.5 and 1.9 times higher than only corresponding to the reduction of CuO to Cu<sup>0</sup> for the 0.2-CuCo/oxC and 0.5-CuCo/oxC catalysts, respectively. The additional H<sub>2</sub> uptake implies that CoO<sub>x</sub> was reduced simultaneously with CuO around 450 K, suggesting that more than 36% of the CoO<sub>x</sub> in the catalysts (as CoO) was reduced due to the close intimacy to Cu species. This means that Cu increases the reducibility of CoO<sub>x</sub>. As the catalysts were previously H<sub>2</sub>-treated at 623 K (523 K for the Cu/oxC catalyst) during catalyst synthesis, probably most carbon surface groups were already removed before the H<sub>2</sub> reduction profiling. In literature metallic Cu and Co were formed at a much higher temperature (520 and 920 K) in respectively a co- precipitated K-Cu/MoO<sub>x</sub> and K-Co/MoO<sub>x</sub>

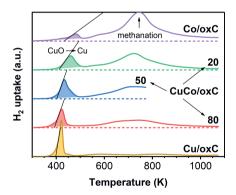


**Figure 5.4** Reduction profiles of air-exposed CuCo/oxC catalysts with tangent lines at the peaks around 420-460 K. The numbers indicate the Cu content in at%. The patterns are vertically offset for clarity. Conditions: dried at 393 K in Ar, cooled down to RT, reduction with 5 vol% H<sub>2</sub>/Ar, ramp 2 K min<sup>-1</sup>, 170-330 mL min<sup>-1</sup> g<sup>-1</sup>.

catalyst, while a bimetallic CuCo phase was formed upon reduction around 630 K in the combined K-CuCo/MoO<sub>x</sub> catalyst. <sup>173</sup> For Al<sub>2</sub>O<sub>3</sub>-supported CuCoO<sub>x</sub> particles the main reduction peak was reported around 575 K, while CuO reduced at 467 K in Cu/Al<sub>2</sub>O<sub>3</sub>. <sup>168</sup> Hence, the reduction temperatures on our graphitic carbon support are significantly lower than for CuCoO<sub>x</sub> particles on oxidic support (see further also **figure 5.10** (frame B) for our CuCoO<sub>x</sub>/SiO<sub>2</sub> catalysts), suggesting a close intimacy between the Cu and Co species.

Next to the intimacy between the catalyst components, catalyst stability under working conditions is a highly relevant parameter. For example, during  $H_2$  reduction profiling shown in **figure 5.4** support methanation was observed at 745 K for the Co/oxC catalyst. The stability of the carbon support is further studied in a reducing atmosphere by heating graphitic carbon as well as a Co/C impregnate in a hydrogen feed while recording the mass loss. The bare carbon support had a negligible mass loss, but also the Co/C catalyst showed only a minor (2.1 wt%) mass loss upon holding for 8 h at 623 K. This suggests that the support methanation was limited when the catalysts were reduced at this temperature during catalyst synthesis or before catalysis.

The minimal support degradation upon reduction of the Co/C catalyst was verified with an additional, separate experiment to determine the effective Co loading after a full oxidation. **Figure 5.5** (frame A) shows the mass loss upon oxidation as a function of temperature for the carbon support and the Co/C catalyst with a theoretical Co loading of 10.0 wt%. The carbon material in both samples was fully oxidized to CO<sub>2</sub> in a two-step process (frame B). The pure graphite was completely oxidized at 1025 K, while the conversion of the Co/C catalyst to Co<sub>3</sub>O<sub>4</sub> was finished around 900 K, showing that Co catalyzed the oxidation of graphitic carbon. The effective Co<sub>3</sub>O<sub>4</sub> loading was 14.0 wt% (*i.e.* 10.3 wt% Co) after the total oxidation, which agrees with the theoretical

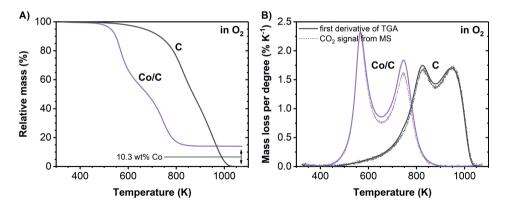


**Figure 5.5** (A) Mass loss of the 10.0 wt% Co/C catalyst and C support when heating in an oxidative atmosphere. (B) First derivatives of the mass loss patterns in an oxidative atmosphere and normalized CO<sub>2</sub> signals from MS. Conditions: dried at 393 K in Ar, cooled down to RT, measurement with 20 vol% O<sub>2</sub>/Ar, ramp 5 K min<sup>-1</sup>, 80 mL min<sup>-1</sup>.

Co loading. Hence, the carbon support with deposited Co(-rich) nanoparticles is stable in a reducing atmosphere up to 623 K as the effective Co loading did not change.

#### 5.3.2 Robustness of the CuCoO<sub>x</sub>/oxC catalyst synthesis by impregnation

Impregnation of graphite to incipient wetness, subsequent drying, and activation is a facile method to synthesize  $CuCoO_x/oxC$  catalysts. Yet, little is known about the influence of various preparation parameters on the average  $CuCoO_x$  particle and crystallite sizes and the size distribution. **Table 5.1** lists the effect of varying heat treatment parameters for graphite-supported  $CuCoO_x$  nanoparticles with 20 at% Cu and 80 at% Co. In almost all cases, an average  $CuCoO_x$  size of 3-4 nm was obtained, regardless of the support functionalization, the gas atmosphere  $(H_2, N_2, O_2, or CO)$ , and the impregnation solvent  $(H_2O \text{ or EtOH})$ . The 0.2-CuCo/oxC catalyst discussed in **section 5.3.1** had been reduced at 623 K (first entry), resulting in an average particle size of  $2.6 \pm 0.7$  nm. An additional heat treatment in  $N_2$  up to 773 K only slightly increased the average size to  $3.8 \pm 1.0$  nm. The TEM particle sizes of all catalysts were in line with the crystallite sizes derived from XRD, suggesting that the nanoparticles consist of single crystallites. Only after reduction in  $H_2$  at 673 K the 0.2-CuCo/C catalyst had slightly larger particles with a broader distribution  $(6.0 \pm 4.4 \text{ nm})$  compared to the other catalysts in **table 5.1**, probably due to the high mobility of reduced  $CuCoO_x$  over the flat graphitic surface and the higher total metal loading, *i.e.* smaller interatomic distance. Overall, the synthesis of graphite-supported, Co-rich  $CuCoO_x$  nanoparticles

**Table 5.1** Number-averaged particle sizes of 0.2-CuCo/oxC and 0.2-CuCo/C catalysts synthesized under various conditions. Treatment abbreviations:  $R = \text{reduction in } 5 \text{ vol} \% \text{ H}_2$ ,  $HT = \text{heat treatment in } N_2$ ,  $OX = \text{oxidation in } 5 \text{ vol} \% \text{ O}_2$ , CO = reduction in 10 vol % CO, number = temperature in K. In all cases a flow of 200 mL min<sup>-1</sup>  $g_{\text{cat}}^{-1}$  was used.

support	treatment	ramp (K min <sup>-1</sup> )		total loading (wt%)	TEM: <i>d</i> <sub>N</sub> (nm)	XRD: d <sub>Cu2O/CoO</sub> (nm)
oxC	R623	0.5	2	10	$2.6 \pm 0.7$	3.0
	R623-HT723	0.5-2	2-1	10	$3.5 \pm 0.9$	3.4
	R623-HT773	2-2	2-2	10	$3.8 \pm 1.0$	_
	HT523-R623-HT773	5-5-5	2-4-2	10	$4.1\pm1.4$	2.8
	HT523- $wet^a$	5	4	10	$4.8 \pm 1.8$	N.A.
С	HT523-OX303-R623	2-cool-2	2-3-2	11	$3.0 \pm 1.2$	3.5
	OX493-R623	2-2	2-2	11	$4.1\pm2.2$	3.6
	OX473-R623	2-2	5-2	11	$3.0\pm1.0$	3.0
	HT523	0.5	4	15	$2.6 \pm 0.7$	3.2
	HT523-R673	0.5-2	4-2	15	$6.0 \pm 4.4$	$3.9(6.7)^{d}$
	R623- <i>EtOH</i> <b>b</b>	2	2	10	$3.7 \pm 1.2$	-
	CO673- <i>EtOH b</i>	2	2	10	$4.3\pm1.3$	$3.7(5.7)^{d}$
oxC-300 <sup>c</sup>	R623	2	2	5.4	$3.6 \pm 1.1$	2.7
	R623-wet a	5	2	5.4	$4.0\pm1.4$	N.A.

<sup>&</sup>lt;sup>a</sup> In an  $H_2O$ -saturated feed. <sup>b</sup> With an ethanolic impregnation solution. <sup>c</sup> Oxidized graphite with BET of 236 m<sup>2</sup>  $q^{-1}$  and  $V_{tot}$  of 0.28 mL min<sup>-1</sup>. <sup>d</sup>  $d_{CuO/CoO}$  in parentheses.

by incipient wetness impregnation yields well-defined nanoparticles of 3-4 nm, irrespective of several preparation parameters.

The synthesis of Co-rich CuCoO<sub>x</sub> nanoparticles larger than 3-4 nm can be required for a specific catalytic performance, for example to avoid excessive methane formation upon syngas conversion. <sup>359</sup> We envisioned to achieve larger nanoparticles by using various synthesis parameters as listed in **table 5.1** but did not result in significantly varied sizes. To explore an alternative strategy to vary the particle size, we discuss a specific method in more detail: oxidation of the impregnate at various temperatures and subsequent reduction. **Figure 5.6** shows the O<sub>2</sub> uptake profiles for the first oxidation step in the 0.2-CuCo/oxC catalyst synthesis. At 538 and 736 K two major peaks corresponding to graphite combustion to CO<sub>2</sub> and H<sub>2</sub>O were observed, resembling the mass loss in **figure 5.5** (frame B). The small peak at 463 K indicated the oxidation of mixed metal nitrates with the release of NO<sub>x</sub> gases, suggesting the start of the phase transformation to CuCoO<sub>x</sub> nanoparticles. Three various oxidation temperatures were accordingly chosen for the first step in the catalyst synthesis: 463 K which mimics the start of the CuCoO<sub>x</sub> phase formation, 523 K which

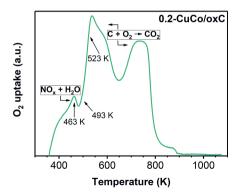


**Figure 5.6** O<sub>2</sub> uptake profiles as a function of temperature for the 0.2-CuCo/oxC impregnate. The impregnate was *ex situ* dried under vacuum at room temperature, stored in an Ar glovebox, and loaded from the glovebox without exposure to air. Conditions:  $2 \text{ K min}^{-1}$ ,  $5 \text{ vol}\% \text{ O}_2/\text{He}$ ,  $180 \text{ mL min}^{-1} \text{ g}_{\text{cat}}^{-1}$ .

is just below the temperature of significant support degradation, and an intermediate temperature of 493 K.

**Figure 5.7** presents electron micrographs (frames A-C) and corresponding particle size distributions (frames D-F) of the 0.2-CuCo/oxC catalysts after an initial oxidation treatment at the various temperatures (463, 493, and 523 K). We observed the formation of ultrasmall particles/clusters after oxidation at 463 K (frame A), showing the start of the phase transformation to CuCoO<sub>x</sub> nanoparticles at this temperature. At higher temperatures (frames B-C) CuCoO<sub>x</sub> particles of around 3 nm were formed, in line with the observations listed in **table 5.1**.

After the initial oxidation treatment at various temperatures, the 0.2-CuCo/oxC catalysts were subsequently reduced in an  $H_2$  atmosphere at 623 K to obtain the active metal phase. **Figure 5.7** (frames G-L) shows EM images and accompanying particle size distributions of the reduced 0.2-CuCo/oxC catalysts after their exposure to air at room temperature. Around 3 nm CuCoO<sub>x</sub> particles (frame G) were formed for the reduced catalyst, which was previously oxidized at 463 K. However, significantly larger particles and size distributions of  $4.2 \pm 2.6$  and  $7.0 \pm 4.9$  nm were obtained for the reduced catalysts, which were previously oxidized at 493 K (frame H) and 523 K (frame I), respectively. The larger particle sizes and distributions can be explained by the partial support combustion in these catalysts, leading to an effective higher Cu + Co loading (13.1, 16.1, and 18.9 wt% for oxidation at 463, 493, and 523 K, respectively, according to mass loss analysis) and hence a smaller interatomic distance. Larger particles were not observed in the 0.2-CuCo/oxC catalysts after the initial oxidation treatment (frames B-C) but only after subsequent reduction (frames H-I), as Cu and Co oxides have a significantly lower mobility than metallic Cu and Co.  $^{360}$ 

Hence, heat treatments by mild oxidation and subsequent reduction is an effective method to obtain larger CuCo particles in impregnated carbon supports.

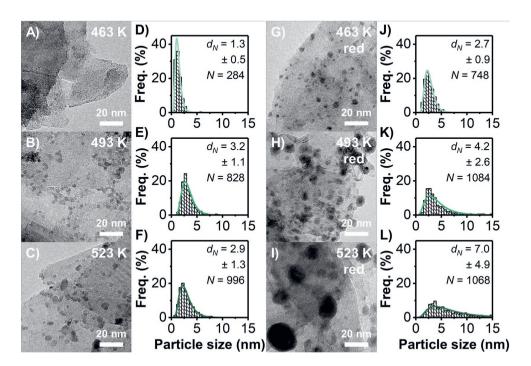


**Figure 5.7** Representative TEM images and corresponding particle size distributions of the 0.2-CuCo/oxC catalyst (**A-F**) prepared *via* an oxidation treatment of the dried impregnate at 463, 493, or 523 K and (**G-L**) subsequent reduction at 623 K. Conditions: 5 vol% O<sub>2</sub>/N<sub>2</sub> or 5 vol% H<sub>2</sub>/N<sub>2</sub>, ramp 2 K min<sup>-1</sup>, hold 2 h, 200 mL min<sup>-1</sup> g<sub>cat</sub><sup>-1</sup>.

**Figure 5.8** shows the XRD patterns of the 0.2-CuCo/oxC catalysts prepared by various oxidation treatments and subsequent reduction at 623 K. At higher oxidation temperatures the formation of a crystalline  $\text{CuCo}_2\text{O}_4$  phase (indicated with  $\beta$ ) was observed. After subsequent reduction at 623 K a diffraction peak at 51.6° was observed, located between the (111) peaks of Cu<sup>0</sup> and Co<sup>0</sup>. Hence, most probably a mixed CuCo phase was formed with a crystallite size around 7-9 nm. Here, we showed that well-defined and robust CuCoO<sub>x</sub> nanoparticles of 3-4 nm are obtained for many impregnated, Co-rich CuCoO<sub>x</sub>/oxC catalysts and that a subsequent oxidation-reduction treatment allows the growth into larger particles around 7 nm.

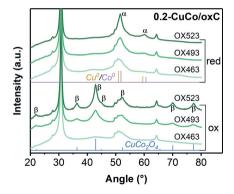


**Figure 5.8** XRD patterns of the fresh 0.2-CuCo/oxC catalysts prepared via various oxidation treatments and subsequent reduction at 623 K (see also **figure 5.7**). The reduced catalysts were measured without exposure to air.  $\alpha$  = CuCo peaks,  $\beta$  = CuCo<sub>2</sub>O<sub>4</sub> peaks.

### 5.3.3 Galvanic replacement as an alternative catalyst preparation

Galvanic replacement (GR), or electroless deposition, is an alternative procedure to synthesize bimetallic particles. For instance, Co@Cu core-shell colloids can be prepared, which are subsequently deposited on a support.  $^{356}$  We explored a new strategy: to synthesize supported  $^{C0}$  nanoparticles on silica gel (BET = 340 m² g $^{-1}$ ,  $V_{tot}$  = 1.20 mL g $^{-1}$ ) by incipient wetness impregnation and subsequently to selectively deposit a Cu layer on the Co nanoparticles using GR. The initial  $^{C0}$ SiO2 impregnate was heated in  $^{N2}$  at 573 K and subsequently  $^{H2}$  at 723 K to obtain the catalyst and had a Co loading of 8.5 wt% (according to ICP-OES analysis). After the initial  $^{N2}$  treatment, the  $^{C0}$ O<sub>4</sub> crystallite size in the  $^{C0}$ SiO<sub>2</sub> catalyst was 8.1 nm, as derived from XRD, and is in line with the 7-12 nm-sized  $^{C0}$ O<sub>5</sub> particles observed by TEM in the subsequently reduced catalyst, which were typically located within agglomerates up to 100 nm (data not shown).

The reduced Co/SiO<sub>2</sub> catalyst was used as a (partial) sacrificial template to deposit Cu<sup>0</sup> from a solution containing Cu<sup>(2)+</sup> ions onto the Co<sup>0</sup> nanoparticles. Here we discuss two selected CuCoO<sub>x</sub>/SiO<sub>2</sub> catalysts prepared by GR with either Cu(NO<sub>3</sub>)<sub>2</sub> as the Cu precursor in an aqueous solution or with CuCl as the Cu precursor dissolved in oleylamine (OLA). For both catalysts, a Cu/(Cu + Co) ratio of 0.38 upon GR was expected. Galvanic replacement was successful: Cu was deposited onto both catalysts according to ICP-OES analysis, which resulted in a molar Cu/(Cu + Co) ratio of 0.34 and 0.21 for the catalysts prepared in H<sub>2</sub>O and OLA, respectively. This means that almost all Cu<sup>2+</sup> ions in aqueous environment were reduced to Cu<sup>0</sup> and deposited on Co<sup>0</sup> nanoparticles, while ca. 55% of the Cu<sup>+</sup> ions was deposited on the Co<sup>0</sup> nanoparticles in the CuCoO<sub>x</sub>/SiO<sub>2</sub> catalyst by the OLA-based synthesis. Furthermore, ca. 1.1-1.2 times more Cu was

deposited onto both catalysts than Co was dissolved, thereby taking the different charge of the Cu precursors into account using **equations (5.5)-(5.6)**, and might indicate partial Co leaching.

**Figure 5.9** shows chemical maps of the two selected  $CuCoO_x/SiO_2$  catalysts prepared with  $H_2O$  (frames A-F) or OLA (frames G-L) as GR solvent. Cu and Co species with much smaller Co particles were obtained using an aqueous-based synthesis (frames A-B) than in the initial  $Co/SiO_2$  catalyst. The smaller Co particle size in the  $CuCoO_x/SiO_2$  catalyst can be explained by the slightly acidic

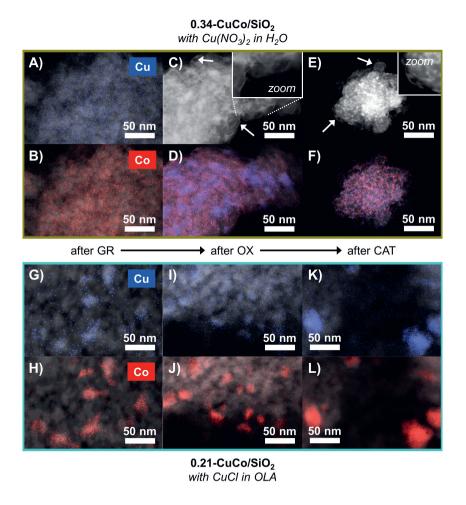


**Figure 5.9** Chemical maps with HAADF-STEM overlays of two selected CuCoO<sub>x</sub>/SiO<sub>2</sub> catalysts prepared with (**A-F**) Cu(NO<sub>3</sub>)<sub>2</sub> as Cu precursor in H<sub>2</sub>O as solvent or with (**G-L**) CuCl as Cu precursor in oleylamine (OLA) as solvent. Samples are depicted after galvanic replacement (GR), an oxidation treatment at 723 K (OX) and 60 h of syngas conversion (CAT). Frames C and E show the HAADF-STEM images with zoomed insets and arrows indicating CoSiO<sub>x</sub>. Frames D and F show the corresponding combined Cu + Co chemical maps.

solution (ca. pH 3.8) of the aqueous GR solution. At this pH H+ ions can oxidize the Co<sup>0</sup> nanoparticles to Co<sup>2+</sup> ( $\Delta E = +0.06$  V,  $\Delta G = -11$  kJ mol<sup>-1</sup>), which can lead to partial dissolution and redispersion of Co nanoparticles. Note that the driving force is larger for the oxidation of Co<sup>0</sup> by Cu<sup>2+</sup> ( $\Delta E^{\ominus} = +0.62$  V,  $\Delta G^{\ominus} = -120$  kJ mol<sup>-1</sup>), *i.e.* galvanic replacement. When OLA is used as GR solvent, particles of ca. 14 ± 5 nm were observed (frames G-H) with a strong correlation between the position of the Cu and Co species, indicating the formation of CuCoO<sub>x</sub> nanoparticles.

After GR and subsequent washing, the surface of the OLA-prepared  $CuCoO_x/SiO_2$  catalyst was still covered with adsorbed OLA molecules, as clear from the mass loss when heating in  $O_2$ . **Figure 5.9** (frames C-D and I-J) shows the elemental distribution of two selected  $CuCoO_x/SiO_2$  catalysts after the oxidation treatment at 723 K to remove organic ligands. For the catalyst prepared in an aqueous solution,  $CuO_x$  nanoparticles of  $12 \pm 5$  nm were formed, which had a limited correlation to the position of the Co species (frame D). Several 3 nm-sized  $CoO_x$  particles as well as needle-like and mainly Co-based structures were present in the catalyst as indicated by the white arrows (frame C). A similar catalyst structure was observed for the catalyst after prolonged syngas conversion (frames E-F). For the OLA-prepared  $CuCoO_x/SiO_2$  catalyst no notable change in the average particle size and the relative position of the Cu and Co was observed neither upon ligand removal (frames I-J) nor during long-term exposure to syngas (frames K-L). Hence, it seems that after ligand removal the high intimacy between Cu and Co species is maintained using OLA as GR solvent but is limited using an aqueous solution for the synthesis.

**Figure 5.10** (frame A) presents XRD patterns of the two selected CuCoO<sub>x</sub>/SiO<sub>2</sub> catalysts after GR and the subsequent ligand removal by oxidation as well as a silica reference. The CuCoO<sub>x</sub>/SiO<sub>2</sub>

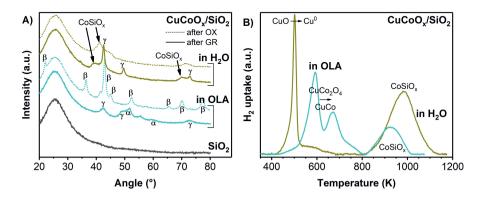


**Figure 5.10** (**A**) XRD patterns of selected  $CuCoO_x/SiO_2$  catalysts prepared with OLA or  $H_2O$  as solvent. Depicted after galvanic replacement (GR) and after oxidation at 723 K in synthetic air (OX). The diffractograms are vertically offset for clarity.  $\alpha$  = CuCo peaks,  $\beta$  =  $CuCo_2O_4$  peaks,  $\gamma$  =  $Cu_2O/CoO$ . (**B**) Reduction profiles of similar  $CuCoO_x/SiO_2$  catalysts after removal of ligands (OX). Conditions: dried in Ar at 393 K, reduction with 5 vol%  $H_2/Ar$ , ramp 5 K min<sup>-1</sup>, ca. 570 mL min<sup>-1</sup>  $g_{cat}$ -1.

prepared in an aqueous solution contained  $Cu_2O$  and/or CoO with a crystallite size of  $\it{ca}$ . 10 nm without crystalline  $Co^0$ . It therefore seems that the  $Co^0$  nanoparticles were indeed (partially) dissolved and redeposited with the additional formation of several larger crystallites, which were not detected by EM analysis. After GR using OLA as the solvent crystalline  $Cu^0/Co^0$  with  $Cu_2O/CoO$  domains were observed, which were transformed into a  $CuCo_2O_4$  phase with a crystallite size of 12.0 nm upon oxidation, in agreement with EM analysis in **figure 5.9** (frames C-D). Hence, the  $CuCoO_x/SiO_2$  catalyst prepared in OLA has well-defined  $CuCo_2O_4$  crystallites/nanoparticles of 12-14 nm, which might be favorable for catalysis.

The intimacy between the Cu and Co species in the CuCoO<sub>x</sub>/SiO<sub>2</sub> can also be derived from H<sub>2</sub> reduction profiling. Figure 5.10 (frame B) shows the reduction profiles of the two oxidized CuCoO<sub>x</sub>/SiO<sub>2</sub> catalysts, prepared by using H<sub>2</sub>O or OLA as the solvent. Two separate reduction peaks were observed for the H<sub>2</sub>O-prepared CuCoO<sub>x</sub>/SiO<sub>2</sub> catalyst: a sharp peak at 501 K due to the reduction of CuO to Cu0 361 and a broad, large peak at 982 K attributed to the reduction of CoSiO<sub>x</sub> <sup>56,362</sup>. The fact that CoO<sub>x</sub> was not simultaneously reduced with CuO points to the lack of a close intimacy between the Cu and Co in this catalyst and to an extensive reaction of highly dispersed CoO<sub>x</sub> with the silica support most likely during the reduction experiment. For the catalyst prepared in OLA, the H<sub>2</sub> reduction profile featured three distinct peaks. The peaks at 592 and 670 K are ascribed to a two-step reduction of CuCo<sub>2</sub>O<sub>4</sub> to bimetallic CuCo, whereas the peak at 921 K indicated a small fraction of CoSiO<sub>x</sub>. These CuCo<sub>2</sub>O<sub>4</sub> reduction temperatures were in the same temperature region as reported for CuCoO<sub>x</sub>/Al<sub>2</sub>O<sub>3</sub> catalysts <sup>168</sup> and significantly higher than for our CuCoO<sub>x</sub>/oxC catalysts (**figure 5.4**), indicating a strong interaction between the oxidic support and CuCoO<sub>x</sub> nanoparticles and a high intimacy between Cu and Co. Here, we showed for the first time that applying GR on pre-deposited Co<sup>0</sup> nanoparticles is a suitable method to synthesize CuCoO<sub>x</sub>/SiO<sub>2</sub> catalysts with a high intimacy between Cu and Co species.

#### 5.3.4 Catalyst stability during CO hydrogenation

Bimetallic CuCo (oxide) catalysts are relevant for various gas- and liquid-phase reactions, as described in the introduction (**section 5.1**). Yet, they are highly sensitive to metal segregation due to their thermodynamic instability, and this separation is especially enhanced in a reducing atmosphere at high temperatures and pressures. We used high-pressure CO hydrogenation as a tool to assess the stability of the bimetallic CuCo (oxide) catalysts under reducing conditions by following the product distribution over time. Highly intimate, metallic Cu and Co species are able to catalyze the formation of long-chain alcohols <sup>55,173</sup>, whereas separate Cu and Co particles give selectivity to methanol and hydrocarbons, respectively. Furthermore, methane can be formed on Co particles. <sup>359</sup>

The Cu-Co distribution is visualized in **figure 5.11** for the impregnated 0.2-CuCo/oxC catalyst by EDX spectroscopy after 150 h of high-temperature and -pressure CO hydrogenation, Frames A-D show agglomerates of ca. 50 nm, indicated by the orange window. These particles consisted of a Corich core and a Cu-rich shell, suggesting the formation of Co@Cu core-shell particles during catalysis. According to EDX spectra (frames E-G) the large CuCoO<sub>x</sub> particles were significantly enriched with Cu (frame F) with respect to the overall Cu distribution in the 0.2-CuCo/oxC catalyst (frame E). On the other hand, in a region with smaller particles (light blue window) a depletion of Cu occurred (frame G). The reason why Cu is mainly located at the outside of the large particle (orange window) after high-pressure CO hydrogenation is probably related to the different surface tension of reaction intermediates with Cu and Co during reaction, 363 Note that under vacuum or inert conditions the surface tension of Cu of lower than of Co, influenced by the lower melting point of bulk Cu (1358 K) compared to bulk Co (1768 K). 189,364 Interestingly, the 0.21-CuCo/SiO2 catalyst prepared by GR in OLA (figure 5.9, frames K-L) maintained the high intimacy between Cu and Co species after catalysis, yet a support effect cannot be excluded here. Here we showed that the Cu species become mobile at high temperatures and pressures in a reducing atmosphere, which resulted in the segregation of the Cu and Co species.

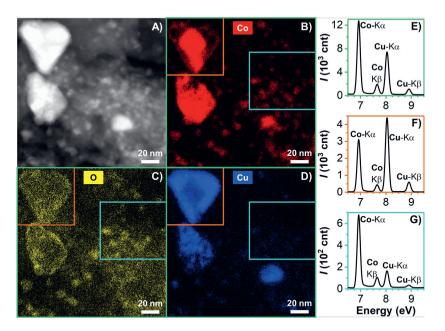


**Figure 5.11** (A) HAADF-STEM image and (B-D) EDX maps of the used 0.2-CuCo/oxC catalyst in the same area for Co, O, and Cu, respectively. (E-G) EDX spectra corresponding to the colored areas. Conditions catalysis: 523 K, 40 bar,  $H_2/\text{CO}/\text{He} = 60/30/10 \text{ vol}\%$ , 150 h.

**Figure 5.12** (frame A) shows the total activity as a function of time for the impregnated  $CuCoO_x/oxC$  catalysts with varying Cu/(Cu+Co) ratios but equal Cu+Co reactor loadings. A significantly higher conversion was obtained when more Co was present in the catalyst. For the 0.8-CuCo/oxC and Cu/oxC catalysts the conversion was very low. Co-rich catalysts were more stable during CO hydrogenation. The activity of the  $CuCoO_x/SiO_2$  catalysts prepared by CO as a function of time is shown in frame C. The CO in the  $CuCo/SiO_2$  catalyst prepared in CO did not show significant activity, which we attributed to the large portion of non-reduced  $CoSiO_x$  and the lack of Cu-Co intimacy, as was determined by CO reduction profiling (**figure 5.10**, frame CO). At 40 bar only a small amount of hydrocarbons (of which CO and CO representation of CO hydrogenation (frame CO) but had a significantly lower activity than the co-impregnated CO catalyst (frame CO) with a similar metal composition. The activity of the CO actalyst CO catalyst (frame CO) with a similar metal composition. The activity of the CO actalyst CO catalyst CO in the CO in

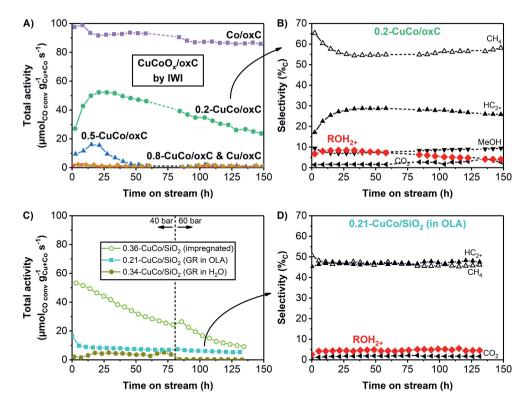


**Figure 5.12** CO conversion as a function of time for (**A**) impregnated  $CuCoO_x/oxC$  catalysts with equal Cu + Co reactor loadings and (**C**) selected  $CuCoO_x/SiO_2$  catalysts prepared by galvanic replacement. Frame C includes a co-impregnated 0.36- $CuCo/SiO_2$  reference catalyst. (**B,D**) Product distribution as a function of time for the impregnated 0.2-CuCo/oxC and galvanically replaced 0.21- $CuCo/SiO_2$  catalysts, respectively.  $ROH_{2+} = C_{2+}$  alcohols;  $HC_{2+} = C_{2+}$  hydrocarbons. Conditions: 523 K, 40 (or 60) bar,  $H_2/CO/H_0 = 60/30/10$  vol%.

was also lower compared to a co-impregnated 0.36-CuCo/SiO<sub>2</sub> catalyst (frame C), which has a slightly higher Cu content. This lower activity might be attributed to some inactive CoSiO<sub>x</sub> species (**figure 5.10**, frame B) and the relatively large CuCoO<sub>x</sub> particle size (**figure 5.9**, frames G-L), thus a lower active surface area. Interestingly, the stability of the 0.21-CuCo/SiO<sub>2</sub> catalyst prepared in OLA was much higher than for the two impregnated catalysts: 0.2-CuCo/oxC (frame A) and 0.36-CuCo/SiO<sub>2</sub> (frame C). This remarkable stabilization suggests that GR is a suitable method to obtain a more stable CuCoO<sub>x</sub> structure compared to impregnation.

**Figure 5.12** (frame B) presents the product distribution of the most active, impregnated  $CuCoO_x/oxC$  catalyst, 0.2-CuCo/oxC, as a function of time. Methane was the main product, which can be due to the presence of small (<3 nm) Co nanoparticles typically having a high surface pressure of adsorbed H atoms during hydrogenation reactions.  $^{359}$  Mostly hydrocarbons but also methanol were produced in significant amounts. Up to  $8.5\%_C$  of long-chain alcohols with a chain growth probability (a) of  $0.463 \pm 0.019$  were obtained, which is a significantly lower selectivity to long-chain alcohols than recently reported in literature for CuCo-based catalysts (>20%c).  $^{20,173-177}$  After ca. 30 h of catalysis the long-chain alcohol selectivity slowly decreased, which can be explained by gradual  $CuCoO_x$  segregation as is supported by EM analysis (**figure 5.11**). These catalysts with a Cu-Co intimacy may be suitable bimetallic catalysts for reactions under milder conditions than those used in this study, such as aerobic oxidation reactions in the liquid phase  $^{156,164}$  and radical reactions for organic pollutant removal.  $^{340,341}$ 

Focusing on the product distribution of the  $0.21\text{-CuCo/SiO}_2$  catalyst prepared in OLA (frame D), more long-chain hydrocarbons, less methane, and no methanol were produced compared to the 0.2-CuCo/oxC catalyst (frame B). These observations suggest the absence of extended Cu surfaces. Interestingly, the galvanically replaced catalyst has a stable but low production of long-chain alcohols with a selectivity of  $4.5\%_C$  and an  $\alpha$  of  $0.38 \pm 0.05$ . This stability is supported by the close intimacy between the Cu and Co species in the fresh as well as the used catalyst, as derived by EM analysis (**figure 5.9**, frames K-L). These results strongly indicate that in all tested catalysts a high intimacy between Cu and Co exists, leading to the production of long-chain alcohols upon CO hydrogenation, but a support effect cannot be excluded. Whereas for the active, impregnated CuCoO<sub>x</sub>/oxC catalysts the metals slowly segregate over time, leading to the production of both methanol and hydrocarbons, the  $0.21\text{-CuCo/SiO}_2$  prepared by GR has intimately mixed Cu and Co and no separate Cu nanoparticles but separate Co nanoparticles.

The Anderson-Schulz-Flory (ASF) distribution for the hydrocarbon formation can be used to extract additional textural properties of the catalysts as it depends on the distribution of Cu and Co surface atoms. The chain growth probability ( $\alpha$ ) describes the chance of CH<sub>2</sub>\* insertion in an adsorbed hydrocarbon over chain termination of the hydrocarbon. The ASF plots of the impregnated CuCoO<sub>x</sub>/oxC catalysts in **figure 5.13** (frame A) show that the  $\alpha$  decreased from 0.792  $\pm$  0.009 for

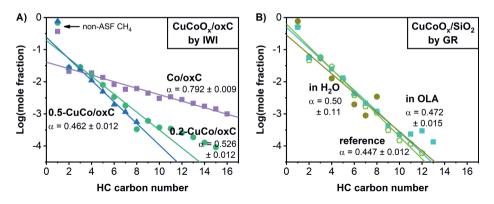


**Figure 5.13** ASF plots of hydrocarbon formation for (**A**) CuCoO<sub>x</sub>/oxC catalysts prepared by impregnation and (**B**) the 0.21-CuCo/SiO<sub>2</sub> catalyst prepared by GR and a co-impregnated CuCoO<sub>x</sub>/SiO<sub>2</sub> reference. Impregnated CuCoO<sub>x</sub>/oxC catalysts form a large portion of non-ASF methane, attributed to small Co nanoparticles.

Co/oxC to  $0.526 \pm 0.012$  and  $0.462 \pm 0.012$  for the 0.2-CuCo/oxC and 0.5-CuCo/oxC catalysts, respectively. This means that the high chain propagation property of a pure Co surface is mitigated by the local presence of Cu, showing the intimacy between Cu and Co species. Furthermore, significantly more methane was produced in all impregnated  $\text{CuCoO}_x/\text{oxC}$  catalysts than expected from the ASF distribution, indicating the presence of small Co nanoparticles or clusters. <sup>359</sup> The galvanically replaced 0.21-CuCo/SiO<sub>2</sub> catalyst prepared in OLA (frame B) had a significantly lower  $\alpha$  of  $0.472 \pm 0.015$ . Also, the amount of produced methane was as expected, based on the ASF distribution. This means that the 0.21-CuCo/SiO<sub>2</sub> catalyst did not contain small, metallic Co nanoparticles. Interestingly, CO hydrogenation is an effective tool to assess the stability and the extent of phase segregation of CuCoO<sub>x</sub> particles in a reductive atmosphere and harsh conditions. Using this technique, we demonstrated that with galvanic replacement as the preparation method for supported CuCoO<sub>x</sub> nanoparticles, a higher CuCo phase stability yet lower activity was obtained than for impregnation for reasons not fully understood.

#### 5.4 Conclusions

We explored the influence of various synthesis methods on the textural properties of supported, bimetallic CuCo nanoparticles, using co-impregnation and galvanic replacement. We showed that the presence of Co in graphite-supported Cu nanoparticles limits the Cu particle growth during catalyst synthesis by co-impregnation. The impregnation procedure is robust and yielded 3-4 nm CuCoO<sub>x</sub> nanoparticles on a graphitic support, but larger particles of ca. 7 nm were obtained by using a mild oxidation and subsequent reduction. Galvanic replacement using pre-deposited Co<sup>o</sup>

nanoparticles on a silica support partially replaced by  $Cu^0$  in oleylamine is an effective method to prepare  $CuCoO_x$  nanoparticles with a high Cu-Co intimacy. The stability of the supported CuCo bimetals was probed by CO hydrogenation at high temperature and pressure. In all catalysts, a Cu-Co intimacy was observed as indicated by the production of long-chain alcohols, except for the galvanically replaced  $CuCoO_x/SiO_2$  catalyst prepared in an aqueous solution, which probably contained a significant amount of cobalt silicate. Surprisingly, the catalyst prepared by galvanic replacement had a higher CuCo phase stability than for impregnated catalysts under harsh reductive conditions but a lower activity, although a support effect cannot be excluded in this respect.

### Acknowledgments

We thank Willem Eijsvogel and Brecht Herremans for their scientific contributions to galvanic replacement. Nynke Krans is thanked for the EDX analysis and Dennie Wezendonk for the mass loss experiments. We are also grateful for Jan Willem de Rijk who helped with the catalytic testing.

# Summary and outlook

Understanding catalyst performance and its dependence on the structure of the individual catalyst's components is important to enhance the economical (and sometimes even environmental) impact and adds to the rational design of new generations of catalysts. Typically, catalysts contain multiple components that improve the activity, selectivity, and/or lifetime. A prime example of such a component is a promoter, which boosts the catalyst performance without significantly being active for the reaction itself. The role and structure of promoters are often studied remotely from industrially relevant conditions, while it is well known that catalysts are dynamic entities under working conditions at high temperatures and pressures. Also, the influence of the promoter is often challenging to discern from the roles of the other components within the catalyst, such as a strongly interacting support, thereby hampering the identification of the active state of the promoter.

This thesis covers the role of several promoters in supported copper catalysts used in the conversion of syngas ( $H_2/CO$ , hence CO hydrogenation) and during  $CO_2$  hydrogenation. We extensively used graphitic carbon as a model support instead of the frequently used metal oxides, to facilitate analysis by transmission electron microscopy and X-ray absorption spectroscopy (XAS). Reactions were performed at high temperatures and pressures, but even more importantly, the catalysts were also characterized under working conditions as much as possible.

**Chapter 1** provides a detailed background of the catalyst components and hydrogenation reactions allowing the reader to become acquainted with the topics discussed in the following chapters. Impregnation as a catalyst synthesis technique is discussed, and the uniqueness of copper (Cu) in catalysis is highlighted. We thoroughly describe distinct types of promotion, thereby specifically focusing on zinc oxide ( $ZnO_x$ ), manganese oxide ( $MnO_x$ ), and cobalt (Co) promoters for Cucatalyzed reactions.

In **chapter 2** we treat the  $ZnO_x$  promoter. From literature it is well known that promotion by  $ZnO_x$  and the  $CO_2$  enrichment of syngas enhance the copper catalyst activity for this reaction, but little is reported on the mutual influence of these two activity-enhancing effects. In this chapter we present the combined effect of  $ZnO_x$  and  $CO_2$  promotion on the catalyst performance using carbon-

supported copper catalysts. We find that without  $CO_2$  in the syngas feed, the activity of the supported Cu nanoparticles is boosted by an order of magnitude by  $ZnO_x$  promotion, and alternative products are formed next to the main product methanol, regardless of the presence of the  $ZnO_x$  promoter. Unpromoted Cu nanoparticles are not affected by  $CO_2$  addition in the syngas feed. For the  $ZnO_x$ -promoted catalyst, a maximum activity is obtained with 3 vol%  $CO_2$ . The methanol selectivity of all catalysts is very high when  $CO_2$  is present in the syngas feed. The results in this chapter showed that the combined effect of  $ZnO_x$  promotion and  $CO_2$  enrichment of the syngas to enhance the catalyst performance is complex and was unraveled using graphitic carbon as a model support.

In **chapter 3** we elaborate on the structure of the  $ZnO_x$  promoter during methanol synthesis using *operando* XAS. A comparison is made between oxide- and carbon-supported Cu nanoparticles. Our experiments clearly show that  $ZnO_x$ -promoted Cu nanoparticles supported on carbon produce methanol faster than supported on silica in a pure  $H_2/CO$  feed but especially in a  $CO_2$ -enriched syngas feed. In literature the active state of the  $ZnO_x$  promoter is thought to contain Zn in its divalent state. Using a graphitic support for Cu nanoparticles the true speciation of the active fraction of the Zn-based promoter was elucidated under industrially relevant temperature and pressure. Strikingly, a significant part of the relevant  $ZnO_x$  promoter is reduced all the way to  $Zn^0$  during catalysis, likely forming Cu-Zn alloys. In this chapter we present the use of weakly interacting graphitic supports as an important strategy to avoid the excessive presence of promoter speciator species.

In **chapter 4**, the effect of  $MnO_x$  promotion is presented. With *in situ* XAS, we find that the promoter is reduced from the Mn(III) to (mainly) Mn(II) oxidation states at the same temperature at which the CuO nanoparticles are reduced to metallic Cu, showing close intimacy and direct interaction between  $MnO_x$  and Cu. During CO as well as  $CO_2$  hydrogenation only a small amount of  $MnO_x$  is needed to improve the activity, selectivity to methanol, and stability. The selectivity during  $CO_2$  hydrogenation is further influenced by the temperature, pressure, and gas flow. More importantly, the  $MnO_x$  promoter is fundamentally different than the  $ZnO_x$  promoter discussed in chapters 2 and 3. Using XAS under working conditions we show that  $CO_2$  in a syngas feed strongly binds to  $MnO_x$  which probably forms an  $MnCO_3$  phase. This carbonate formation is absent for the  $ZnO_x$  promoter and hence clarifies the lower activity of the  $MnO_x$ -promoted Cu nanoparticles in a  $CO_2$ -enriched syngas feed.

In **chapter 5** we introduce Co as a modifier for supported Cu catalysts. A combination of the high methanol selectivity of Cu and the ability of Co to form C–C bonds can in principle lead to the formation of long-chain alcohols upon CO hydrogenation. This chapter focuses on the preparation and the catalyst formulation of bimetallic CuCo nanoparticles, where catalysis is used to determine the stability at high temperature and high syngas pressure. We present impregnation as a suitable

method to prepare bimetallic CuCo catalysts with varying Cu/Co ratios, yielding supported nanoparticles with a size around 3 nm. This technique is not very sensitive to synthesis parameters, such as the support functionalization, gas atmosphere during activation, and nature of the impregnation solvent. Larger nanoparticles of 7 nm were synthesized by activating the impregnates by a mild oxidation and a subsequent reduction. We also find that with galvanic replacement (or electroless deposition) a Cu layer can be selectively deposited on supported Co nanoparticles. These catalysts better retain the intimacy between Cu and Co during CO hydrogenation at high temperatures and pressures than the impregnated catalysts but have lower activities. The intimately mixed Cu and Co lead to a stable production of  $5\%_c$  long-chain alcohols, while separate Co nanoparticles mainly produce hydrocarbons.

All together, we show the effect and structure of several promoters on the catalyst performance of supported Cu catalysts in syngas conversion and CO<sub>2</sub> hydrogenation. High surface area carbon materials are typically regarded as less useful catalyst supports than oxides for non-noble metals. One of the main reasons is the lack of compressibility of graphitic carbon to shape the final catalyst into macroscopic bodies, a method typically used industrially. However, in this thesis we show that carbonaceous materials are important model supports to study the relevant promoter structure by facilitating the characterization by electron microscopy and XAS. This strategy is also applicable to other catalyst types. As discussed in chapter 3, we also find a positive side effect of graphitic carbon as a model support: less promoter material is needed to maximize the methanol formation by the Cu nanoparticles than when an oxidic support is used, showing that the promoter is more efficiently used in carbon-supported catalysts. Hence, carbon-metal oxide composites as a support for nanoparticles may be a good option to lower the promoter material costs while retaining sufficient structural stability for shaping the catalysts in macroscopic bodies. We present that carbon-supported metal catalysts are valuable model systems for academic research that may be less distant from industrially used catalysts than you might have thought.

# **Nederlandse samenvatting**

Katalysator, dragermateriaal, promotor, synthesegas: deze termen vormen een belangrijke basis voor het begrip van het onderwerp van dit proefschrift, namelijk het gebruik van promotoren om de katalytische prestatie van koper te bevorderen. Maar wat is een katalysator, wat wordt bedoeld met synthesegas en hoe zit het met promotoren?

Een katalysator is een stof die een bepaalde chemische reactie versnelt. Een belangrijk voorbeeld van een (chemische) katalysator is te vinden in de uitlaat van een auto. Een katalysator bestaat veelal uit een collectie van vele kleine metaaldeeltjes van maar enkele nanometers groot (1 nanometer = 0.000000001 meter), die aangebracht worden op een dragermateriaal. Een drager kan het best beschreven worden als een spons met heel veel poriën en die daardoor een groot specifiek oppervlak heeft. Het geheel vormt de katalysator en is in het geval van de veelgebruikte koolstofdrager in dit proefschrift een zwart poeder (vergelijkbaar met Norit®).

De reden dat zulke kleine deeltjes gebruikt worden, is dat hun actieve oppervlak per gram materiaal enorm groot is. Stel je een knikker voor met een diameter van 1 centimeter. Wanneer deze wordt opgedeeld in piepkleine bolletjes van 10 nanometer ("nanodeeltjes"), dan wordt het oppervlak maar liefst een miljoen keer groter. Het is precies dit grote oppervlak dat een sleutelrol speelt in de functionaliteit van een katalysator, omdat een chemische reactie doorgaans alleen plaatsvindt aan het oppervlak.

Het tweede onderdeel van een katalysator is het dragermateriaal dat meestal niet bijdraagt aan de activiteit van de katalysator. Toch is het wel van cruciaal belang voor de stabiliteit, omdat er een drijvende kracht is voor de enorm kleine nanodeeltjes om samen te smelten tot één groot geheel waardoor het actieve oppervlak afneemt. Dit proces wordt versneld wanneer de katalysator onder hoge temperatuur en druk gebruikt wordt.

Katalysatoren worden al vele decennia toegepast om materialen, zoals brandstoffen, plastics en medicijnen, op grote schaal te produceren. Daarbij zijn drie elementen van de katalysator van groot belang: de mate waarin de katalysator de chemische reactie versnelt (activiteit), de formatie van het gewenste product met een minimale hoeveelheid aan bijproducten (selectiviteit) en de levensduur

van de katalysator (stabiliteit). Al deze aspecten dragen bij aan de effectiviteit van omzetting, bijvoorbeeld in de chemische industrie, en daarmee worden het energieverbruik en de afvalstroom verminderd en worden uiteindelijk dus kosten bespaard en milieu gespaard. Daarom is het begrip van katalysatoren, hun synthese en hun gebruik, de wetenschapsdiscipline van de katalyse, zo belangrijk.

Koper is een goed ingrediënt voor katalysatoren: het komt relatief veel voor op de aarde en is daardoor relatief duurzaam en goedkoper dan veelgebruikte edelmetalen (ongeveer vijfduizend keer dan bijvoorbeeld platina). Het metaal is al decennia de hoofdcomponent in de katalysator voor onder andere de reactie van waterstof (H<sub>2</sub>) met koolstofmonoxide (CO) naar methanol. Reacties van waterstof met andere moleculen worden hydrogenatiereacties genoemd. Methanol is een belangrijke bouwsteen voor de chemische industrie waarvan jaarlijks maar liefst meer dan honderd miljoen ton wordt geproduceerd. Het gasmengel van H<sub>2</sub> en CO, waaruit onder andere methanol wordt geproduceerd, is zo belangrijk dat het een eigen naam heeft gekregen: "synthesegas". Naast methanol kunnen vele andere stoffen, zoals benzine en diesel, uit synthesegas gevormd worden met behulp van katalysatoren.

Vergeleken met edelmetalen heeft koper wel een nadeel: koperen nanodeeltjes hebben een relatief lage katalytische activiteit. Om de volledige potentie te benutten worden vaak toevoegingen gebruikt om zo de gewenste activiteit, selectiviteit en stabiliteit te verkrijgen. Deze additieven worden ook wel promotoren genoemd. Zinkoxide is hiervan onder chemici een bekend voorbeeld; het verhoogt de activiteit van koperkatalysatoren voor de synthese van methanol uit synthesegas. Mangaanoxide als een promotor voor de door koper gekatalyseerde conversie van synthesegas wordt minder vaak gebruikt, maar is zeker niet minder interessant. Ondanks de vele studies over de rol van de promotor in katalytische reacties is nog niet alles bekend en is soms nog veel controverse over wat op nanoniveau gebeurt.

En dan komt de lastige vraag: hoe kunnen we al deze diverse materialen bekijken? Nanodeeltjes zijn namelijk niet met het blote oog zichtbaar. Microscopie is een van de technieken die in elk hoofdstuk van dit proefschrift genoemd wordt. Met behulp van elektronen in plaats van zichtbaar licht kunnen deeltjes van slechts enkele nanometers worden bekeken. Het interessantst is hoe de katalysator eruitziet tijdens een chemische omzetting die vaak plaatsvindt op hoge temperatuur en bij hoge druk zoals in methanolsynthese. Onder die omstandigheden ziet een katalysator er meestal anders uit dan aan de open lucht op kamertemperatuur, omdat onder ruwe omstandigheden de nanodeeltjes continu vervormen en zich verplaatsen over het dragermateriaal. Hieraan wordt veel aandacht besteed in dit proefschrift. Door het meten van absorptie van röntgenstralen door de katalysator ("röntgenstralenabsorptiespectroscopie") kunnen de structuur en positie van de promotoren ontrafeld worden onder veelgebruikte reactiecondities. Deze techniek heeft zich in de

afgelopen paar jaar sterk ontwikkeld en vormt een belangrijk gereedschap in ons onderzoek om de meest interessante rol van de katalysator te bestuderen.

De keuze van het dragermateriaal is erg belangrijk om de structuur van de promotor te kunnen onderzoeken. Een veelgemaakte keuze voor industriële katalysatoren is silicium- of aluminiumoxide, omdat deze materialen mechanisch zeer sterk zijn, alsook erg stabiel zijn in veel verschillende gasatmosferen op een hoge temperatuur en bij hoge druk. Een groot nadeel is echter dat de promotor vaak een sterke wisselwerking heeft met deze dragermaterialen, waardoor de chemische structuur van de promotor flink verandert. Hierdoor kan de promotor de katalytische prestatie van de koperdeeltjes minder goed bevorderen en gaat de effectiviteit van de promotor deels verloren. De keuze voor het dragermateriaal is gevallen op grafiet dat de eigenschap heeft om metalen nanodeelties en promotoren maar relatief zwak te binden. Verder heeft grafiet een vlakke morfologie vergeleken met veelgebruikte metaaloxides. karakterisatie elektronenmicroscopie en röntgenstralenabsorptie-spectroscopie vergemakkelijkt.

#### Wat te vinden is in dit proefschrift

In dit proefschrift beschrijf ik de structuur van promotoren en hun bijdrage aan de katalytische prestatie van gedragen koperkatalysatoren, alsook hoe hier het dragermateriaal een rol in speelt. De katalysatoren zijn uitvoerig getest voor de omzetting van synthesegas, een gasmengsel van waterstof en koolstofmonoxide, onder hoge temperatuur en druk. Ook de reactie van waterstof met koolstofdioxide (CO<sub>2</sub>) onder soortgelijke condities is bestudeerd. De zinkoxidepromotor wordt als eerste besproken in hoofdstukken 2 en 3, waarna de rol van de mangaanoxidepromotor wordt aangesneden in hoofdstuk 4. Het laatste hoofdstuk presenteert het effect van kobalttoevoeging op gedragen koperkatalysatoren.

**Hoofdstuk 1** geeft een uitvoerige achtergrond over het dragermateriaal, de bereiding en het gebruik van katalysatoren, specifiek voor koperkatalysatoren in hydrogenatiereacties, om zo de volgende hoofdstukken beter te kunnen begrijpen. Speciale aandacht wordt hierbij besteed aan wat bekend is in de wetenschappelijke literatuur over de rol van zink-, mangaan- en kobaltoxides als doelbewuste additieven voor koperkatalysatoren.

Het vervolg van het proefschrift richt zich als eerste op zinkoxide als promotor voor koperkatalysatoren voor de synthese van methanol uit synthesegas. Naast het toevoegen van zinkoxide heeft ook het toevoegen van een paar procent CO<sub>2</sub> in het synthesegasmengsel invloed op de katalytische activiteit. **Hoofdstuk 2** voegt deze twee belangrijke parameters in de methanolsynthese samen.

Eerst wordt het effect van het zinkoxide tijdens de omzetting van puur synthesegas naar methanol besproken. Het toevoegen van zinkoxide aan de koperdeeltjes zorgt ervoor dat de activiteit ongeveer tien keer zo hoog wordt en dat de koperdeeltjes zowel methanol als dimethylether vormen. CO2-verrijking van het synthesegas heeft een positief effect: een maximale activiteit wordt bereikt wanneer 3% CO2 in het synthesegas aanwezig is. Voor de koperkatalysator zonder zinkoxide is dit verhaal anders; hiervoor blijkt de methanolproductie niet beïnvloed te worden door de toevoeging van CO2.

In dit hoofdstuk is ook aandacht voor de selectiviteit van de katalysator. In afwezigheid van  $CO_2$  worden alternatieve producten zoals  $CO_2$  en koolwaterstoffen geproduceerd, ongeacht of de zinkoxidepromotor is toegevoegd of niet. Dit is een bijzondere observatie, omdat voor de synthese van methanol over op koper gebaseerde katalysatoren doorgaans een selectiviteit van meer dan 98% wordt gerapporteerd. Een soortgelijke selectiviteit wordt inderdaad bereikt door het toevoegen van minimaal 1%  $CO_2$  in de gastoevoer.

Nadat de optimale CO<sub>2</sub>-concentratie in het synthesegasmengsel was vastgesteld voor onze koolstofgedragen koperkatalysatoren, hebben we de structuur van de zinkoxidepromotor onder relevante reactiecondities onder de loep genomen. In **hoofdstuk 3** wordt de staat van de promotor beschreven onder reactiecondities, waarbij we de focus leggen op de rol van het dragermateriaal. Eerst hebben we een serie koperkatalysatoren gesynthetiseerd met een constante lage koperbelading en met variërende hoeveelheden van de zinkoxidepromotor. Deze serie hebben we vergeleken met een soortgelijke katalysator gebaseerd op een siliciumdioxidedrager op de katalytische prestatie onder hoge temperatuur en druk. We zien dat de zinkoxidepromotor ongeveer vijf keer zo efficiënt wordt gebruikt wanneer de katalysator een koolstofdrager bevat in plaats van een siliciumdioxidedrager.

Deze bijzondere observatie verklaren we met behulp van röntgenstralenabsorptiespectroscopie op hoge temperatuur en bij hoge druk. Ons onderzoek laat zien dat een groot deel van de zinkoxidepromotor tijdens de reactie is gereduceerd tot zinkmetaal. Tot nu toe dacht men dat het zinkoxide nauwelijks gereduceerd werd onder reactiecondities. In dit hoofdstuk tonen wij aan dat op koolstofgedragen katalysatoren dit grotendeels wel het geval is. Hierbij hebben we aangetoond dat het gebruik van een koolstofdrager een geschikt hulpmiddel is om de eigenschappen van de zinkoxidepromotor te bestuderen.

In **hoofdstuk 4** maken we de stap naar een alternatieve promotor: mangaanoxide. Een reeks van koperkatalysatoren met variërende hoeveelheden mangaanoxide op een koolstofdrager zijn gesynthetiseerd. Met behulp van röntgenstralenabsorptiespectroscopie zien we dat de promotor dicht in de buurt is van de koperen nanodeeltjes en dat de promotor een directe wisselwerking ermee heeft. We vinden dat een kleine hoeveelheid mangaanoxide (5 tot 11%) in de katalysator een positief effect heeft op de alle drie belangrijkste punten tijdens katalyse: activiteit (in zowel een CO<sub>2</sub>-

rijke gastoevoer als de conversie van synthesegas), selectiviteit (naar methanol) en stabiliteit. Tijdens de hydrogenatiereactie van puur  $CO_2$  naar methanol wordt voor het merendeel koolstofmonoxide gevormd in plaats van methanol. Dit zou nuttig kunnen zijn om  $CO_2$  om te zetten en om synthesegas te vormen voor de chemische industrie. We laten in onze experimenten zien dat de selectiviteit naar methanol of koolstofmonoxide gestuurd kan worden door de temperatuur, druk en toevoersnelheid tijdens de reactie te veranderen.

Een belangrijke vraag die in dit hoofdstuk wordt beantwoord is of de mangaanoxidepromotor een andere werking heeft dan de zinkoxidepromotor zoals besproken in hoofdstukken 2 en 3. Tot onze verrassing is de mangaanoxidepromotor minder effectief wanneer er ook maar een beetje  $CO_2$  in het synthesegas aanwezig is: een resultaat dat in sterk contrast staat met de zinkoxidepromotor. Dit fundamenteel verschil kunnen we uitleggen met experimenten met röntgenstralenabsorptie onder hoge temperatuur en druk. Hierbij hebben we gevonden dat het  $CO_2$  in de gastoevoer sterk bindt aan het mangaanoxide, waarbij waarschijnlijk ook een laagje mangaancarbonaat wordt gevormd. Deze vorm van de promotor is blijkbaar minder effectief om de katalytische prestatie van de koperen nanodeeltjes te bevorderen.

Ten slotte is kobalt een erg interessant metaal dat de katalytische prestatie van gedragen koperkatalysatoren kan beïnvloeden. Waar koperen nanodeeltjes methanol vormen uit synthesegas op hoge temperatuur en bij hoge druk, zijn kobaltdeeltjes in staat om benzineachtige moleculen zoals koolwaterstoffen en alcoholen te produceren onder deze omstandigheden. De combinatie van deze twee metalen kan in principe verschillende soorten alcoholen opleveren, waarvan ethanol de bekendste is. Het is echter een grote uitdaging om beide metalen dicht bij elkaar te houden.

In **hoofdstuk 5** verkennen we het effect van twee types preparatiemethodes en de samenstelling op de structuur van gedragen koper-kobaltnanodeeltjes, waarbij we katalyse hebben gebruikt als een manier om de stabiliteit te onderzoeken. De twee methodes zijn impregnatie en de zogeheten galvanische vervanging, technieken die veelvuldig gebruikt worden in de chemische industrie voor het bereiden van respectievelijk katalysatoren en elektrodes, maar nog niet eerder direct met elkaar vergeleken zijn. Door middel van impregnatie zien we dat het toevoegen van kobalt aan koperen nanodeeltjes leidt tot kleine nanodeeltjes met een grootte van 3 tot 4 nanometer. Deze methode is bestand tegen uiteenlopende parameters tijdens de bereiding, zoals de temperatuur en gassoort. Ook de synthese van grotere koper-kobaltnanodeeltjes van 7 nanometer is mogelijk. Met galvanische vervanging kan kopermetaal specifiek worden afgezet op kobaltnanodeeltjes die van tevoren zijn geplaatst op een siliciumdioxidedrager. Het gebruik van deze bereiding leidt tot een redelijk stabiele katalysatorstructuur onder hoge temperatuur en druk in synthesegas maar vooralsnog een lage activiteit.

Samenvattend hebben we het effect en de structuur van uiteenlopende promotoren voor koperkatalysatoren onderzocht tijdens de conversie van synthesegas of een mengsel van waterstof en CO<sub>2</sub>. Het begrijpen van zowel de rol van de individuele componenten van de katalysator als de wisselwerkingen tussen hen is belangrijk om katalysatoren te ontwikkelen voor processen met flexibele gascomposities. Hierbij is het gebruik van koolstofdragers een belangrijke methode om de relevante promotorstructuur te bestuderen bijvoorbeeld met elektronenmicroscopie en röntgenstralenabsorptiespectroscopie: een strategie die ook ingezet kan worden voor andere types katalysatoren. Ten slotte hebben we laten zien dat gelegeerde koper–kobaltkatalysatoren gesynthetiseerd kunnen worden met relatief simpele technieken en met een goed gedefinieerde structuur. Deze katalysatoren zouden gebruikt kunnen worden voor chemische reacties onder milde condities, zoals oxidatiereacties of voor het verwijderen van organische vervuilingen in een vloeistof (een alternatief voor zogenaamde op ijzer gebaseerde Fentonchemie).

## References

- (1) Hagen, J. Heterogeneously Catalyzed Processes in Industry. In *Industrial Catalysis: A Practical Approach*; Wiley-VCH Verlag GmbH & Co. KGaA: Weinheim, Germany, 2015; pp 261–298.
- (2) Choi, J.-M.; Han, S.-S.; Kim, H.-S. Industrial Applications of Enzyme Biocatalysis: Current Status and Future Aspects. *Biotechnol. Adv.* **2015**, *33* (7), 1443–1454.
- (3) Chorkendorff, I.; Niemantsverdriet, J. W. *Concepts of Modern Catalysis and Kinetics*, 2nd ed.; Wiley-VCH Verlag GmbH & Co. KGaA: Weinheim, Germany, 2013.
- (4) Heck, R. M.; Farrauto, R. J.; Gulati, S. T. *Catalytic Air Pollution Control: Commercial Technology*, 3rd ed.; John Wiley & Sons, Inc.: Hoboken, New Jersey, 2009.
- (5) Kokotailo, G. T.; Lawton, S. L.; Olsen, D. H.; Meier, W. M. Structure of Synthetic Zeolite ZSM-5. *Nature* 1978, 272 (5652), 437–438.
- (6) Hadjiivanov, K. I.; Vayssilov, G. N. Characterization of Oxide Surfaces and Zeolites by Carbon Monoxide as an IR Probe Molecule. Adv. Catal. 2002, 47, 307–511.
- (7) Argyle, M. D.; Bartholomew, C. H. Heterogeneous Catalyst Deactivation and Regeneration: A Review. *Catalysts* **2015**, *5* (1), 145–269.
- (8) Cerqueira, H. S.; Caeiro, G.; Costa, L.; Ramôa Ribeiro, F. Deactivation of FCC Catalysts. J. Mol. Catal. A 2008, 292 (1–2), 1–13.
- (9) Crabtree, R. H. Deactivation in Homogeneous Transition Metal Catalysis: Causes, Avoidance, and Cure. Chem. Rev. 2015. 115 (1), 127–150.
- (10) Twigg, M. V.; Spencer, M. S. Deactivation of Supported Copper Metal Catalysts for Hydrogenation Reactions. Appl. Catal. A 2001, 212 (1–2), 161–174.
- (11) Shen, W. M.; Dumesic, J. A.; Hill Jr., C. G. Criteria for Stable Ni Particle Size under Methanation Reaction Conditions: Nickel Transport and Particle Size Growth via Nickel Carbonyl. *J. Catal.* **1981**, 68 (1), 152–165.
- (12) Takeda, N.; Torimoto, T.; Sampath, S.; Kuwabata, S.; Yoneyama, H. Effect of Inert Supports for Titanium Dioxide Loading on Enhancement of Photodecomposition Rate of Gaseous Propionaldehyde. J. Phys. Chem. 1995, 99 (24), 9986–9991.
- (13) Bliem, R.; van der Hoeven, J.; Zavodny, A.; Gamba, O.; Pavelec, J.; de Jongh, P. E.; Schmid, M.; Diebold, U.; Parkinson, G. S. An Atomic-Scale View of CO and H<sub>2</sub> Oxidation on a Pt/Fe<sub>3</sub>O<sub>4</sub> Model Catalyst. *Angew. Chem. Int. Ed.* **2015**, *54* (47), 13999–14002.
- (14) Puigdollers, A. R.; Schlexer, P.; Tosoni, S.; Pacchioni, G. Increasing Oxide Reducibility: The Role of Metal/Oxide Interfaces in the Formation of Oxygen Vacancies. ACS Catal. 2017, 7 (10), 6493–6513.
- (15) Kraushaar-Czarnetzki, B.; Müller, S. P. Shaping of Solid Catalysts. In Synthesis of Solid Catalysts; de

- Jong, K. P., Ed.; Wiley-VCH Verlag GmbH & Co. KGaA; Weinheim, Germany, 2009; pp 173-199.
- (16) Marchi, A. J.; Di Cosimo, J. I.; Apesteguía, C. R. Effects of the Preparation Conditions on the Reducibility of Cu-Co Based Oxides. *Catal. Today* 1992, 15 (3–4), 383–394.
- (17) Sun, Y.; Chen, L.; Bao, Y.; Zhang, Y.; Wang, J.; Fu, M.; Wu, J.; Ye, D. The Applications of Morphology Controlled ZnO in Catalysis. *Catalysts* **2016**, *6* (12), 1–44.
- (18) Chatterjee, R.; Kuld, S.; van den Berg, R.; Chen, A.; Shen, W.; Christensen, J. M.; Jensen, A. D.; Sehested, J. Mapping Support Interaction in Copper Catalysts. Top. Catal. 2019, 62 (7–11), 649–659.
- (19) Beerthuis, R.; Visser, N. L.; van der Hoeven, J. E. S.; Ngene, P.; Deeley, J. M. S.; Sunley, G. J.; de Jong, K. P.; de Jongh, P. E. Manganese Oxide Promoter Effects in the Copper-Catalyzed Hydrogenation of Ethyl Acetate. *J. Catal.* 2020, 394, 307–315.
- (20) Das, S.; Sengupta, M.; Lippi, R.; Patel, J.; Bag, A.; Nayak, C.; Jha, S. N.; Bordoloi, A. Insights into Mesoporous Nitrogen-Rich Carbon Induced Synergy for the Selective Synthesis of Ethanol. *Carbon* 2020, 168, 337–353.
- (21) He, L.; Weniger, F.; Neumann, H.; Beller, M. Synthesis, Characterization, and Application of Metal Nanoparticles Supported on Nitrogen-Doped Carbon: Catalysis beyond Electrochemistry. Angew. Chem. Int. Ed. 2016, 55 (41), 12582–12594.
- (22) Cuervo, M. R.; Asedegbega-Nieto, E.; Díaz, E.; Ordóñez, S.; Vega, A.; Belén Dongil, A.; Rodríguez-Ramos, I. Modification of the Adsorption Properties of High Surface Area Graphites by Oxygen Functional Groups. Carbon 2008, 46 (15), 2096–2106.
- (23) Wei, J.; Geng, S.; Kumar, M.; Pitkänen, O.; Hietala, M.; Oksman, K. Investigation of Structure and Chemical Composition of Carbon Nanofibers Developed from Renewable Precursor. Front. Mater. 2019, 6, 334.
- (24) Gu, W.; Yushin, G. Review of Nanostructured Carbon Materials for Electrochemical Capacitor Applications: Advantages and Limitations of Activated Carbon, Carbide-Derived Carbon, Zeolite-Templated Carbon, Carbon Aerogels, Carbon Nanotubes, Onion-like Carbon, and Graphene. WIREs Energy Environ. 2014, 3 (5), 424–473.
- (25) Baumann, T. F.; Worsley, M. A.; Han, T. Y.-J.; Satcher Jr., J. H. High Surface Area Carbon Aerogel Monoliths with Hierarchical Porosity. *J. Non. Crust. Solids* **2008**, *354* (29), 3513–3515.
- (26) Carbon Materials for Catalysis, 1st ed.; Serp, P., Figueiredo, J. L., Eds.; John Wiley & Sons, Inc.: Hoboken, New Jersey, 2009.
- (27) Dannenberg, E. M. Bound Rubber and Carbon Black Reinforcement. Rubber Chem. Technol. 1986, 59(3), 512–524.
- (28) Serp, P.; Corrias, M.; Kalck, P. Carbon Nanotubes and Nanofibers in Catalysis. *Appl. Catal. A* **2003**, 253 (2), 337–358.
- (29) Shen, K.; Chen, X.; Chen, J.; Li, Y. Development of MOF-Derived Carbon-Based Nanomaterials for Efficient Catalysis. *ACS Catal.* **2016**, *6* (9), 5887–5903.
- (30) Moreno-Castilla, C.; Maldonado-Hódar, F. J. Carbon Aerogels for Catalysis Applications: An Overview. *Carbon* **2005**, *43* (3), 455–465.
- (31) Szczęśniak, B.; Choma, J.; Jaroniec, M. Major Advances in the Development of Ordered Mesoporous Materials. Chem. Commun. 2020, 56 (57), 7836–7848.
- (32) Zhang, P.; Zhu, H.; Dai, S. Porous Carbon Supports: Recent Advances with Various Morphologies and Compositions. *ChemCatChem* **2015**, *7* (18), 2788–2805.
- (33) Ma, T.-Y.; Liu, L.; Yuan, Z.-Y. Direct Synthesis of Ordered Mesoporous Carbons. Chem. Soc. Rev. 2013,

- 42 (9), 3977-4003.
- (34) Ryoo, R.; Joo, S. H.; Jun, S. Synthesis of Highly Ordered Carbon Molecular Sieves via Template-Mediated Structural Transformation. *J. Phys. Chem. B* **1999**, *103* (37), 7743–7746.
- (35) van Dam, H. E.; van Bekkum, H. Preparation of Platinum on Activated Carbon. *J. Catal.* **1991**, *131* (2), 335–349.
- (36) Aksoylu, A. E.; Madalena, M.; Freitas, A.; Pereira, M. F. R.; Figueiredo, J. L. Effects of Different Activated Carbon Supports and Support Modifications on the Properties of Pt/AC Catalysts. *Carbon* 2001, 39 (2), 175–185.
- (37) Stoller, M. D.; Park, S.; Zhu, Y.; An, J.; Ruoff, R. S. Graphene-Based Ultracapacitors. *Nano Lett.* **2008**, 8 (10), 3498–3502.
- (38) Qu, L.; Liu, Y.; Baek, J.-B.; Dai, L. Nitrogen-Doped Graphene as Efficient Metal-Free Electrocatalyst for Oxygen Reduction in Fuel Cells. ACS Nano 2010, 4 (3), 1321–1326.
- van den Berg, R.; Prieto, G.; Korpershoek, G.; van der Wal, L. I.; van Bunningen, A. J.; Lægsgaard-Jørgensen, S.; de Jongh, P. E.; de Jong, K. P. Structure Sensitivity of Cu and CuZn Catalysts Relevant to Industrial Methanol Synthesis. *Nat. Commun.* **2016**. *7*. 13057.
- (40) Furimsky, E. CO<sub>2</sub> Hydrogenation to Methanol and Methane over Carbon-Supported Catalysts. *Ind. Eng. Chem. Res.* **2020**, *59* (35), 15393–15423.
- (41) Xiao, K.; Bao, Z.; Qi, X.; Wang, X.; Zhong, L.; Fang, K.; Lin, M.; Sun, Y. Advances in Bifunctional Catalysis for Higher Alcohol Synthesis from Syngas. *Chin. J. Catal.* **2013**, *34* (1), 116–129.
- (42) Luk, H. T.; Mondelli, C.; Mitchell, S.; Siol, S.; Stewart, J. A.; Curulla Ferré, D.; Pérez-Ramírez, J. Role of Carbonaceous Supports and Potassium Promoter on Higher Alcohols Synthesis over Copper-Iron Catalysts. ACS Catal. 2018, 8 (10), 9604–9618.
- (43) Wang, J.; Chernavskii, P. A.; Wang, Y.; Khodakov, A. Y. Influence of the Support and Promotion on the Structure and Catalytic Performance of Copper-Cobalt Catalysts for Carbon Monoxide Hydrogenation. *Fuel* **2013**, *103*, 1111–1122.
- (44) Wang, P.; Zhang, J.; Bai, Y.; Xiao, H.; Tian, S.; Xie, H.; Yang, G.; Tsubaki, N.; Han, Y.; Tan, Y. Ternary Copper-Cobalt-Cerium Catalyst for the Production of Ethanol and Higher Alcohols through CO Hydrogenation. Appl. Catal. A 2016, 514, 14–23.
- (45) Wang, P.; Bai, Y.; Xiao, H.; Tian, S.; Zhang, Z.; Wu, Y.; Xie, H.; Yang, G.; Han, Y.; Tan, Y. Effect of the Dimensions of Carbon Nanotube Channels on Copper-Cobalt-Cerium Catalysts for Higher Alcohols Synthesis. *Catal. Commun.* **2016**, *75*, 92–97.
- (46) Dong, X.; Zhang, H.-B.; Lin, G.-D.; Yuan, Y.-Z.; Tsai, K. R. Highly Active CNT-Promoted Cu-ZnO-Al<sub>2</sub>O<sub>3</sub> Catalyst for Methanol Synthesis from H<sub>2</sub>/CO/CO<sub>2</sub>. *Catal. Lett.* **2003**, *85* (3–4), 237–246.
- (47) Dong, X.; Liang, X.-L.; Li, H.-Y.; Lin, G.-D.; Zhang, P.; Zhang, H.-B. Preparation and Characterization of Carbon Nanotube-Promoted Co-Cu Catalyst for Higher Alcohol Synthesis from Syngas. *Catal. Today* **2009**, *147* (2), 158–165.
- (48) Zhang, H.-B.; Dong, X.; Lin, G.-D.; Liang, X.-L.; Li, H.-Y. Carbon Nanotube-Promoted Co-Cu Catalyst for Highly Efficient Synthesis of Higher Alcohols from Syngas. *Chem. Commun.* 2005, No. 40, 5094– 5096.
- (49) Kandemir, T.; Schuster, M. E.; Senyshyn, A.; Behrens, M.; Schlögl, R. The Haber-Bosch Process Revisited: On the Real Structure and Stability of "Ammonia Iron" under Working Conditions. *Angew. Chem. Int. Ed.* 2013, 52 (48), 12723–12726.
- (50) Munnik, P.; de Jongh, P. E.; de Jong, K. P. Recent Developments in the Synthesis of Supported

- Catalysts. Chem. Rev. 2015, 115 (14), 6687-6718.
- Marceau, E.; Carrier, X.; Che, M. Impregnation and Drying. In *Synthesis of Solid Catalysts*; de Jong,
   K. P., Ed.; Wiley-VCH Verlag GmbH & Co. KGaA: Weinheim, Germany, 2009; pp 59–82.
- (52) Marceau, E.; Carrier, X.; Che, M.; Clause, O.; Marcilly, C. Ion Exchange and Impregnation. In *Handbook of Heterogeneous Catalysis*; Wiley-VCH Verlag GmbH & Co. KGaA: Weinheim, Germany, 2008; pp 467–484.
- (53) Eggenhuisen, T. M.; de Jongh, P. E. Supported Nanoparticles. In Nanoparticles: Workhorses of Nanoscience; De Mello Donegá, C., Ed.; Springer-Verlag: Berlin-Heidelberg, Germany, 2014; pp 121– 144.
- (54) Munnik, P.; Wolters, M.; Gabrielsson, A.; Pollington, S. D.; Headdock, G.; Bitter, J. H.; de Jongh, P. E.; de Jong, K. P. Copper Nitrate Redispersion to Arrive at Highly Active Silica-Supported Copper Catalysts. J. Phys. Chem. C 2011, 115 (30), 14698–14706.
- (55) Luk, H. T.; Mondelli, C.; Curulla Ferré, D.; Stewart, J. A.; Pérez-Ramírez, J. Status and Prospects in Higher Alcohols Synthesis from Syngas. *Chem. Soc. Rev.* **2017**, *46* (5), 1358–1426.
- (56) Khodakov, A. Y.; Chu, W.; Fongarland, P. Advances in the Development of Novel Cobalt Fischer-Tropsch Catalysts for Synthesis of Long-Chain Hydrocarbons and Clean Fuels. *Chem. Rev.* 2007, 107 (5), 1692–1744.
- (57) Heidenreich, S.; Foscolo, P. U. New Concepts in Biomass Gasification. Prog. Energy Combust. Sci. 2015, 46, 72–95.
- (58) Mondal, P.; Dang, G. S.; Garg, M. O. Syngas Production through Gasification and Cleanup for Downstream Applications - Recent Developments. Fuel Process. Technol. 2011, 92 (8), 1395–1410.
- (59) Grammelis, P.; Margaritis, N.; Karampinis, E. Solid Fuel Types for Energy Generation: Coal and Fossil Carbon-Derivative Solid Fuels. In *Fuel Flexible Energy Generation: Solid, Liquid and Gaseous Fuels*; Oakey, J., Ed.; Elsevier Ltd.: Cambridge, UK, 2016; pp 29–58.
- (60) Iaquaniello, G.; Cucchiella, B.; Antonetti, E. Method for Producing Synthesis Gas for Methanol Production. WO2013062413A1, 2013.
- (61) de Ruyck, J.; Delattin, F.; Bram, S. Co-Utilization of Biomass and Natural Gas in Combined Cycles through Primary Steam Reforming of the Natural Gas. *Energy* **2007**, *32* (4), 371–377.
- (62) Ratnasamy, C.; Wagner, J. P. Water Gas Shift Catalysis. Catal. Rev. 2009, 51 (3), 325-440.
- (63) Daniel Martínez, J.; Mahkamov, K.; Andrade, R. V.; Silva Lora, E. E. Syngas Production in Downdraft Biomass Gasifiers and Its Application Using Internal Combustion Engines. *Renew. Energy* 2012, 38 (1), 1–9.
- (64) Agragiotis, C.; Roeb, M.; Sattler, C. A Review on Solar Thermal Syngas Production via Redox Pair-Based Water/Carbon Dioxide Splitting Thermochemical Cycles. *Renew. Sustain. Energy Rev.* **2015**, 42, 254–285.
- (65) Sehested, J. Industrial and Scientific Directions of Methanol Catalyst Development. J. Catal. 2019, 371, 368–375.
- (66) Olah, G. A. Beyond Oil and Gas: The Methanol Economy. Angew. Chem. Int. Ed. 2005, 44 (18), 2636–2639.
- (67) Methanol Institute. Methanol price and supply/demand https://www.methanol.org/methanol-pricesupply-demand/ (accessed Jun 15, 2020).
- (68) Alvarado, M. The Changing Face of the Global Methanol Market. IHS Chem. Bull. 2016, No. 3, 1–2.
- (69) Mittasch, A.; Pier, M.; Winkler, K. Production of Oxygenated Organic Compounds. US1558559, 1925.

- (70) Mittasch, A.; Pier, M. Synthetic Manufacture of Methanol. US1569775, 1926.
- (71) Waugh, K. C. Methanol Synthesis. Catal. Lett. 2012, 142 (10), 1153–1166.
- (72) Jeong, Y. R.; Jung, H.; Kang, J.; Han, J. W.; Park, E. D. Continuous Synthesis of Methanol from Methane and Steam over Copper-Mordenite. *ACS Catal.* **2021**, *11*, 1065–1070.
- (73) Jin, Z.; Wang, L.; Zuidema, E.; Mondal, K.; Zhang, M.; Zhang, J.; Wang, C.; Meng, X.; Yang, H.; Mesters, C.; Xiao, F.-S. Hydrophobic Zeolite Modification for in Situ Peroxide Formation in Methane Oxidation to Methanol. *Science* 2020, 367 (6474), 193–197.
- (74) Dinh, K. T.; Sullivan, M. M.; Narsimhan, K.; Serna, P.; Meyer, R. J.; Dincă, M.; Román-Leshkov, Y. Continuous Partial Oxidation of Methane to Methanol Catalyzed by Diffusion-Paired Copper Dimers in Copper-Exchanged Zeolites. J. Am. Chem. Soc. 2019, 141 (29), 11641–11650.
- (75) Ravi, M.; Sushkevich, V. L.; Knorpp, A. J.; Newton, M. A.; Palagin, D.; Pinar, A. B.; Ranocchiari, M.; van Bokhoven, J. A. Misconceptions and Challenges in Methane-to-Methanol over Transition-Metal-Exchanged Zeolites. *Nat. Catal.* **2019**, *2*, 485–494.
- (76) Latimer, A. A.; Kakekhani, A.; Kulkarni, A. R.; Nørskov, J. K. Direct Methane to Methanol: The Selectivity-Conversion Limit and Design Strategies. *ACS Catal.* **2018**, *8* (8), 6894–6907.
- (77) Wu, C.; Lin, L.; Liu, J.; Zhang, J.; Zhang, F.; Zhou, T.; Rui, N.; Yao, S.; Deng, Y.; Yang, F.; Xu, W.; Luo, J.; Zhao, Y.; Yan, B.; Wen, X.-D.; Rodriguez, J. A.; Ma, D. Inverse ZrO<sub>2</sub>/Cu as a Highly Efficient Methanol Synthesis Catalyst from CO<sub>2</sub> Hydrogenation. Nat. Commun. 2020, 11, 5767.
- (78) Wang, L.-X.; Guan, E.; Wang, Z.; Wang, L.; Gong, Z.; Cui, Y.; Yang, Z.; Wang, C.; Zhang, J.; Meng, X.;
   Hu, P.; Gong, X.-Q.; Gates, B. C.; Xiao, F.-S. Dispersed Nickel Boosts Catalysis by Copper in CO<sub>2</sub>
   Hydrogenation. ACS Catal. 2020, 10 (16), 9261–9270.
- (79) Wang, L.; Guan, E.; Wang, Y.; Wang, L.; Gong, Z.; Cui, Y.; Meng, X.; Gates, B. C.; Xiao, F.-S. Silica Accelerates the Selective Hydrogenation of CO<sub>2</sub> to Methanol on Cobalt Catalysts. *Nat. Commun.* 2020, 11, 1033.
- (80) Zabilskiy, M.; Sushkevich, V. L.; Palagin, D.; Newton, M. A.; Krumeich, F.; Van Bokhoven, J. A. The Unique Interplay between Copper and Zinc during Catalytic Carbon Dioxide Hydrogenation to Methanol. *Nat. Commun.* 2020, 11, 2409.
- (81) Zabilskiy, M.; Sushkevich, V. L.; Newton, M. A.; van Bokhoven, J. A. Copper-Zinc Alloy-Free Synthesis of Methanol from Carbon Dioxide over Cu/ZnO/Faujasite. ACS Catal. 2020, 10, 14240–14244.
- (82) Guzmán, H.; Salomone, F.; Batuecas, E.; Tommasi, T.; Russo, N.; Bensaid, S.; Hernández, S. How to Make Sustainable CO<sub>2</sub> Conversion to Methanol: Thermocatalytic versus Electrocatalytic Technology. Chem. Eng. J. 2020, 127973.
- (83) Liu, Y.; Li, F.; Zhang, X.; Ji, X. Recent Progress on Electrochemical Reduction of CO<sub>2</sub> to Methanol. *Curr. Opin. Green Sustain. Chem.* **2020**, *23*, 10–17.
- (84) Wu, Y.; Zhang, J.; Zhang, T.; Sun, K.; Wang, L.; Xie, H.; Tan, Y. Effect of Potassium on the Regulation of C<sub>1</sub> Intermediates in Isobutyl Alcohol Synthesis from Syngas over CuLaZrO<sub>2</sub> Catalysts. *Ind. Eng. Chem. Res.* 2019, 58 (22), 9343–9351.
- (85) Lu, L.; Sun, X.; Ma, J.; Yang, D.; Wu, H.; Zhang, B.; Zhang, J.; Han, B. Highly Efficient Electroreduction of CO<sub>2</sub> to Methanol on Palladium-Copper Bimetallic Aerogels. Angew. Chem. Int. Ed. 2018, 57 (43), 14149–14153.
- (86) Almusaiteer, K. A.; Al-Hadhrami, A.; Abed, O.; Biausque, G.; Al-Amer, A. Catalysts and Methods for Methanol Synthesis from Direct Hydrogenation of Syngas and/or Carbon Dioxide. US20190076828A1, 2019.

- (87) Waugh, K. C. Methanol Synthesis. Catal. Today 1992, 15 (1), 51–75.
- (88) Prieto, G.; de Jong, K. P.; de Jongh, P. E. Towards "greener" Catalyst Manufacture: Reduction of Wastewater from the Preparation of Cu/ZnO/Al<sub>2</sub>O<sub>3</sub> Methanol Synthesis Catalysts. *Catal. Today* **2013**, 215, 142–151.
- (89) Behrens, M.; Studt, F.; Kasatkin, I.; Kühl, S.; Hävecker, M.; Abild-Pedersen, F.; Zander, S.; Girgsdies, F.; Kurr, P.; Kniep, B.-L.; Tovar, M.; Fischer, R. W.; Nørskov, J. K.; Schlögl, R. The Active Site of Methanol Synthesis over Cu/ZnO/Al<sub>2</sub>O<sub>3</sub> Industrial Catalysts. *Science* 2012, 336 (6083), 893–897.
- (90) Zhang, F.; Liu, Y.; Xu, X.; Yang, P.; Miao, P.; Zhang, Y.; Sun, Q. Effect of Al-Containing Precursors on Cu/ZnO/Al<sub>2</sub>O<sub>3</sub> Catalyst for Methanol Production. *Fuel Process. Technol.* **2018**, *178*, 148–155.
- (91) Guil-López, R.; Mota, N.; Llorente, J.; Millán, E.; Pawelec, B.; García, R.; Fierro, J. L. G.; Navarro, R. M. Structure and Activity of Cu/ZnO Catalysts Co-Modified with Aluminium and Gallium for Methanol Synthesis. Catal. Today 2020, 355, 870–881.
- (92) Chiche, D.; Diverchy, C.; Lucquin, A.-C.; Porcheron, F.; Defoort, F. Synthesis Gas Purification. Oil Gas Sci. Technol. Rev. d'IFP Energies Nouv. 2013. 68 (4), 707–723.
- (93) Lee, W. J.; Bordoloi, A.; Patel, J.; Bhatelia, T. The Effect of Metal Additives in Cu/Zn/Al<sub>2</sub>O<sub>3</sub> as a Catalyst for Low-Pressure Methanol Synthesis in an Oil-Cooled Annulus Reactor. *Catal. Today* 2020, 343, 183–190.
- (94) Klier, K.; Chatikavanij, V.; Herman, R. G.; Simmons, G. W. Catalytic Synthesis of Methanol from CO/H<sub>2</sub>: IV. The Effects of Carbon Dioxide. *J. Catal.* **1982**, *74* (2), 343–360.
- (95) Fichtl, M. B.; Schlereth, D.; Jacobsen, N.; Kasatkin, I.; Schumann, J.; Behrens, M.; Schlögl, R.; Hinrichsen, O. Kinetics of Deactivation on Cu/ZnO/Al<sub>2</sub>O<sub>3</sub> Methanol Synthesis Catalysts. *Appl. Catal.* A 2015, 502, 262–270.
- (96) Prieto, G.; Zečević, J.; Friedrich, H.; de Jong, K. P.; de Jongh, P. E. Towards Stable Catalysts by Controlling Collective Properties of Supported Metal Nanoparticles. *Nat. Mater.* **2013**, *12* (1), 34–39.
- (97) Pompe, C. E.; Slagter, M.; de Jongh, P. E.; de Jong, K. P. Impact of Heterogeneities in Silica-Supported Copper Catalysts on Their Stability for Methanol Synthesis. *J. Catal.* **2018**, *365*, 1–9.
- (98) Roine, A.; Lamberg, P.; Mansikka-aho, J.; Björklund, P.; Kentala, J.-P.; Talonen, T.; Kotiranta, T.; Ahlberg, R.; Gröhn, A.; Saarinen, O.; Myyri, J.; Sipilä, J.; Vartiainen, A. Metso Outotec HSC Chemistry v7.14 Software. Outetec, Research Center: Finland 2011.
- (99) Chase Jr., M. W.; Davies, C. A.; Downey Jr., J. R.; Frurip, D. J.; McDonald, R. A.; Syverud, A. N. JANAF Thermochemical Tables, Third Edition. *J. Phys. Chem. Ref. Data* **1985**, *14* (suppl. 1), 1–1856.
- (100) Frenkel, M.; Kabo, G. J.; Marsh, K. N.; Roganov, G. N.; Wilhoit, R. C. *Thermodynamics of Organic Compounds in the Gas State*, 1st ed.; CRC Press: Thermodynamics Research Center (TRC), 1994.
- (101) Landolt-Börnstein Group IV. Thermodynamic Properties of Inorganic Materials; Scientific Group Thermodata Europe (SGTE), Ed.; Springer-Verlag: Berlin-Heidelberg, Germany, 1999; Vol. 19.
- (102) Barin, I. *Thermodynamical Data of Pure Substances*, 3rd ed.; VCH Verlagsgesellschaft: Weinheim, Germany, 1995.
- (103) Liu, D.-M.; Lin, B.-W. Thermal Conductivity in Hot-Pressed Silicon Carbide. Ceram. Int. 1996, 22 (5), 407–414.
- (104) Sahibzada, M.; Metcalfe, I. S.; Chadwick, D. Methanol Synthesis from CO/CO<sub>2</sub>/H<sub>2</sub> over Cu/ZnO/Al<sub>2</sub>O<sub>3</sub> at Differential and Finite Conversions. J. Catal. 1998, 174 (2), 111–118.
- (105) Lee, J. S.; Lee, K. H.; Lee, S. Y.; Kim, Y. G. A Comparative Study of Methanol Synthesis from CO<sub>2</sub>/H<sub>2</sub> and CO/H<sub>2</sub> over a Cu/ZnO/Al<sub>2</sub>O<sub>3</sub> Catalyst. *J. Catal.* **1993**, *144* (2), 414–424.

- (106) Nielsen, N. D.; Jensen, A. D.; Christensen, J. M. The Roles of CO and CO<sub>2</sub> in High Pressure Methanol Synthesis over Cu-Based Catalysts. J. Catal. 2020, 393, 324–334.
- (107) Abbas, I.; Kim, H.; Shin, C.-H.; Yoon, S.; Jung, K.-D. Differences in Bifunctionality of ZnO and ZrO<sub>2</sub> in Cu/ZnO/ZrO<sub>2</sub>/Al<sub>2</sub>O<sub>3</sub> Catalysts in Hydrogenation of Carbon Oxides for Methanol Synthesis. Appl. Catal. B 2019, 258, 117971.
- (108) Studt, F.; Behrens, M.; Kunkes, E. L.; Thomas, N.; Zander, S.; Tarasov, A.; Schumann, J.; Frei, E.; Varley, J. B.; Abild-Pedersen, F.; Nørskov, J. K.; Schlögl, R. The Mechanism of CO and CO<sub>2</sub> Hydrogenation to Methanol over Cu-Based Catalysts. *ChemCatChem* **2015**, *7* (7), 1105–1111.
- (109) Yang, Y.; Mims, C. A.; Mei, D. H.; Peden, C. H. F.; Campbell, C. T. Mechanistic Studies of Methanol Synthesis over Cu from CO/CO<sub>2</sub>/H<sub>2</sub>/H<sub>2</sub>O Mixtures: The Source of C in Methanol and the Role of Water. *J. Catal.* **2013**, 298, 10–17.
- (110) Thrane, J.; Kuld, S.; Nielsen, N. D.; Jensen, A. D.; Sehested, J.; Christensen, J. M. Methanol-Assisted Autocatalysis in Catalytic Methanol Synthesis. *Angew. Chem. Int. Ed.* **2020**, *59* (41), 18189–18193.
- (111) Grabow, L. C.; Mavrikakis, M. Mechanism of Methanol Synthesis on Cu through CO<sub>2</sub> and CO Hydrogenation. *ACS Catal.* **2011**, *1* (4), 365–384.
- (112) Eurostat. Energy balances https://ec.europa.eu/eurostat/web/energy/data/energy-balances (accessed Mar 18, 2021).
- (113) Bui, M.; Adjiman, C. S.; Bardow, A.; Anthony, E. J.; Boston, A.; Brown, S.; Fennell, P. S.; Fuss, S.; Galindo, A.; Hackett, L. A.; Hallett, J. P.; Herzog, H. J.; Jackson, G.; Kemper, J.; Krevor, S.; Maitland, G. C.; Matuszweski, M.; Metcalfe, I. S.; Petit, C.; Puxty, G.; Reimer, J.; Reiner, D. M.; Rubin, E. S.; Scott, S. A.; Shah, N.; Smit, B.; Trusler, J. P. M.; Webley, P.; Wilcox, J.; Mac Dowell, N. Carbon Capture and Storage (CCS): The Way Forward. Energy Environ. Sci. 2018, 11 (5), 1062–1176.
- (114) Bae, Y.-S.; Snurr, R. Q. Development and Evaluation of Porous Materials for Carbon Dioxide Separation and Capture. *Angew. Chem. Int. Ed.* **2011**, *50* (49), 11586–11596.
- (115) Buhre, B. J. P.; Elliott, L. K.; Sheng, C. D.; Gupta, R. P.; Wall, T. F. Oxy-Fuel Combustion Technology for Coal-Fired Power Generation. *Prog. Energy Combust. Sci.* **2005**, *31* (4), 283–307.
- (116) Centi, G.; Perathoner, S. Opportunities and Prospects in the Chemical Recycling of Carbon Dioxide to Fuels. *Catal. Today* **2009**, *148* (3–4), 191–205.
- (117) Nielsen, D. U.; Hu, X.-M.; Daasbjerg, K.; Skrydstrup, T. Chemically and Electrochemically Catalysed Conversion of CO<sub>2</sub> to CO with Follow-up Utilization to Value-Added Chemicals. *Nat. Catal.* 2018, 1, 244–254.
- (118) Kattel, S.; Liu, P.; Chen, J. G. Tuning Selectivity of CO<sub>2</sub> Hydrogenation Reactions at the Metal/Oxide Interface. *J. Am. Chem. Soc.* **2017**, *139* (29), 9739–9754.
- (119) Saeidi, S.; Najari, S.; Fazlollahi, F.; Khoshtinat Nikoo, M.; Sefidkon, F.; Jaromír Klemeš, J.; Baxter, L. L. Mechanisms and Kinetics of CO<sub>2</sub> Hydrogenation to Value-Added Products: A Detailed Review on Current Status and Future Trends. Renew. Sustain. Energy Rev. 2017, 80, 1292–1311.
- (120) Porosoff, M. D.; Yan, B.; Chen, J. G. Catalytic Reduction of CO<sub>2</sub> by H<sub>2</sub> for Synthesis of CO, Methanol and Hydrocarbons: Challenges and Opportunities. *Energy Environ. Sci.* **2016**, *9* (1), 62–73.
- (121) Bansode, A.; Tidona, B.; van Rohr, P. R.; Urakawa, A. Impact of K and Ba Promoters on CO<sub>2</sub> Hydrogenation over Cu/Al<sub>2</sub>O<sub>3</sub> Catalysts at High Pressure. Catal. Sci. Technol. 2013, 3 (3), 767–778.
- (122) Kattel, S.; Yan, B.; Chen, J. G.; Liu, P. CO<sub>2</sub> Hydrogenation on Pt, Pt/SiO<sub>2</sub> and Pt/TiO<sub>2</sub>: Importance of Synergy between Pt and Oxide Support. *J. Catal.* **2016**, *343*, 115–126.
- (123) Fujitani, T.; Saito, M.; Kanai, Y.; Watanabe, T.; Nakamura, J.; Uchijima, T. Development of an Active

- Ga<sub>2</sub>O<sub>3</sub> Supported Palladium Catalyst for the Synthesis of Methanol from Carbon Dioxide and Hydrogen. *Appl. Catal. A* **1995**, *125* (2), L199–L202.
- (124) Büchel, R.; Baiker, A.; Pratsinis, S. E. Effect of Ba and K Addition and Controlled Spatial Deposition of Rh in Rh/Al<sub>2</sub>O<sub>3</sub> Catalysts for CO<sub>2</sub> Hydrogenation. *Appl. Catal. A* **2014**. *477*, 93–101.
- (125) Wu, J.; Saito, M.; Takeuchi, M.; Watanabe, T. The Stability of Cu/ZnO-Based Catalysts in Methanol Synthesis from a CO<sub>2</sub>-Rich Feed and from a CO-Rich Feed. *Appl. Catal. A* **2001**, *218* (1–2), 235–240.
- (126) Gupta, M.; Smith, M. L.; Spivey, J. J. Heterogeneous Catalytic Conversion of Dry Syngas to Ethanol and Higher Alcohols on Cu-Based Catalysts. *ACS Catal.* **2011**, *1* (6), 641–656.
- (127) Surisetty, V. R.; Dalai, A. K.; Kozinski, J. Alcohols as Alternative Fuels: An Overview. Appl. Catal. A 2011, 404 (1–2), 1–11.
- (128) Zaman, S.; Smith, K. J. A Review of Molybdenum Catalysts for Synthesis Gas Conversion to Alcohols: Catalysts, Mechanisms and Kinetics, Catal. Rev. Sci. Eng. 2012, 54, 41–132.
- (129) Ao, M.; Pham, G. H.; Sunarso, J.; Tade, M. O.; Liu, S. Active Centers of Catalysts for Higher Alcohol Synthesis from Syngas: A Review. *ACS Catal.* **2018**, *8* (8), 7025–7050.
- (130) Schubert, T. Production Routes of Advanced Renewable C1 to C4 Alcohols as Biofuel Components A Review. Biofuels Bioprod. Biorefining 2020, 14 (4), 845–878.
- (131) Khan, W. U.; Baharudin, L.; Choi, J.; Yip, A. C. K. Recent Progress in CO Hydrogenation over Bimetallic Catalysts for Higher Alcohol Synthesis. ChemCatChem 2020, 13 (1), 111–120.
- (132) Spivey, J. J.; Egbebi, A. Heterogeneous Catalytic Synthesis of Ethanol from Biomass-Derived Syngas. *Chem. Soc. Rev.* **2007**, *36* (9), 1514–1528.
- (133) Wang, J.; Chernavskii, P. A.; Khodakov, A. Y.; Wang, Y. Structure and Catalytic Performance of Alumina-Supported Copper-Cobalt Catalysts for Carbon Monoxide Hydrogenation. *J. Catal.* **2012**, 286, 51–61.
- (134) Xiaoding, X.; Doesburg, E. B. M.; Scholten, J. J. F. Synthesis of Higher Alcohols from Syngas Recently Patented Catalysts and Tentative Ideas on the Mechanism. *Catal. Today* 1987, 2 (1), 125–170.
- (135) Baker, J. E.; Burch, R.; Hibble, S. J.; Loader, P. K. Properties of Silica-Supported Cu/Co Bimetallic Catalysts in the Synthesis of Higher Alcohols. *Appl. Catal.* **1990**, *65* (1), 281–292.
- (136) Hu, J.; Wang, Y.; Cao, C.; Elliott, D. C.; Stevens, D. J.; White, J. F. Conversion of Biomass-Derived Syngas to Alcohols and C<sub>2</sub> Oxygenates Using Supported Rh Catalysts in a Microchannel Reactor. *Catal. Today* **2007**, *120* (1), 90–95.
- (137) showtheplanet inc. Daily metal prices https://www.dailymetalprice.com/ (accessed Dec 14, 2020).
- (138) Sugier, A.; Freund, E. Process for Manufacturing Alcohols, Particularly Linear Saturated Primary Alcohols, from Synthesis Gas. USP4122110, 1978.
- (139) Sugier, A.; Freund, E. Process for Manufacturing Alcohols and More Particularly Saturated Linear Primary Alcohols from Synthesis Gas. USP4291126, 1981.
- (140) Gao, F.; Liu, H.; Hu, X.; Chen, J.; Huang, Z.; Xia, C. Selective Hydrogenolysis of Furfuryl Alcohol to 1,5- and 1,2-Pentanediol over Cu-LaCoO<sub>3</sub> Catalysts with Balanced Cu<sup>0</sup>-CoO Sites. *Chin. J. Catal.* **2018**, 39 (10), 1711–1723.
- (141) Tien-Thao, N.; Zahedi-Niaki, M. H.; Alamdari, H.; Kaliaguine, S. Effect of Alkali Additives over Nanocrystalline Co-Cu-Based Perovskites as Catalysts for Higher-Alcohol Synthesis. J. Catal. 2007, 245 (2), 348–357.
- (142) Tien-Thao, N.; Alamdari, H.; Zahedi-Niaki, M. H.; Kaliaguine, S. LaCo<sub>1-x</sub>Cu<sub>x</sub>O<sub>3-δ</sub> Perovskite Catalysts for Higher Alcohol Synthesis. Appl. Catal. A 2006, 311, 204–212.

- (143) Fang, Y. Z.; Liu, Y.; Zhang, L. H. LaFeO<sub>3</sub>-Supported Nano Co-Cu Catalysts for Higher Alcohol Synthesis from Syngas. *Appl. Catal. A* **2011**, *397* (1–2), 183–191.
- (144) Tien-Thao, N.; Zahedi-Niaki, M. H.; Alamdari, H.; Kaliaguine, S. Conversion of Syngas to Higher Alcohols over Nanosized LaCoo 2Cuo 3O3 Perovskite Precursors. Appl. Catal. A 2007, 326 (2), 152–163.
- (145) Fang, Y.; Liu, Y.; Deng, W.; Liu, J. Cu-Co Bi-Metal Catalyst Prepared by Perovskite CuO/LaCoO<sub>3</sub> Used for Higher Alcohol Synthesis from Syngas. J. Energy Chem. 2014, 23 (4), 527–534.
- (146) Tien Thao, N.; Thanh Son, L. Production of Cobalt-Copper from Partial Reduction of La(Co,Cu)O<sub>3</sub> Perovskites for CO Hydrogenation. J. Sci. Adv. Mater. Devices 2016, 1 (3), 337–342.
- (147) Ao, M.; Pham, G. H.; Sage, V.; Pareek, V.; Liu, S. Perovskite-Derived Trimetallic Co-Ni-Cu Catalyst for Higher Alcohol Synthesis from Syngas. Fuel Process. Technol. 2019, 193, 141–148.
- (148) Subramanian, N. D.; Balaji, G.; Kumar, C. S. S. R.; Spivey, J. J. Development of Cobalt-Copper Nanoparticles as Catalysts for Higher Alcohol Synthesis from Syngas. *Catal. Today* **2009**, *147* (2), 100–106.
- (149) Lü, D.; Zhu, Y.; Sun, Y. Cu Nanoclusters Supported on Co Nanosheets for Selective Hydrogenation of CO. *Chin. J. Catal.* **2013**, *34* (11), 1998–2003.
- (150) Mendes, L. V. P.; Snider, J. L.; Fleischman, S. D.; Kibsgaard, J.; McEnaney, J. M.; Aranda, D. A. G.; Jaramillo, T. F. Polyol Synthesis of Cobalt-Copper Alloy Catalysts for Higher Alcohol Synthesis from Syngas. Catal. Lett. 2017, 147 (9), 2352–2359.
- (151) Sheffer, G. R.; Jacobson, R. A.; King, T. S. Chemical Nature of Alkali-Promoted Copper-Cobalt-Chromium Oxide Higher Alcohol Catalysts. J. Catal. 1989, 116 (1), 95–107.
- (152) Liu, G.-L.; Niu, T.; Cao, A.; Geng, Y.-X.; Zhang, Y.; Liu, Y. The Deactivation of Cu-Co Alloy Nanoparticles Supported on ZrO<sub>2</sub> for Higher Alcohols Synthesis from Syngas. *Fuel* **2016**, *176*, 1–10.
- (153) Sheffer, G. R.; King, T. S. Effect of Preparation Parameters on the Catalytic Nature of Potassium Promoted Cu-Co-Cr Higher Alcohol Catalysts. *Appl. Catal.* **1988**, *44*, 153–164.
- (154) Das, S.; Sengupta, M.; Bordoloi, A. Role of Caesium in Higher Alcohol Synthesis over Modified Copper-Cobalt Nanocomposites under Mild Conditions. *ChemCatChem* **2017**, *9* (10), 1845–1853.
- (155) Zhao, L.; Duan, J.; Zhang, Q.; Li, Y.; Fang, K. Preparation, Structural Characterization, and Catalytic Performance of Cu-Co Alloy Supported on Mn-Al Oxide for Higher Alcohol Synthesis via Syngas. *Ind. Eng. Chem. Res.* 2018, 57 (44), 14957–14966.
- (156) Luo, J.; Xuan, K.; Wang, Y.; Li, F.; Wang, F.; Pu, Y.; Li, L.; Zhao, N.; Xiao, F. Aerobic Oxidation of Fluorene to Fluorenone over Co-Cu Bimetal Oxides. *New J. Chem.* **2019**, *43* (22), 8428–8438.
- (157) Xiang, Y.; Kruse, N. Cobalt-Copper Based Catalysts for Higher Terminal Alcohols Synthesis via Fischer-Tropsch Reaction. J. Energy Chem. 2016, 25 (6), 895–906.
- (158) Yang, Y.; Qi, X.; Wang, X.; Lv, D.; Yu, F.; Zhong, L.; Wang, H.; Sun, Y. Deactivation Study of CuCo Catalyst for Higher Alcohol Synthesis via Syngas. Catal. Today 2016, 270, 101–107.
- (159) Mouaddib, N.; Perrichon, V.; Martin, G. A. Characterization of Copper-Cobalt Catalysts for Alcohol Synthesis from Syngas. Appl. Catal. A 1994, 118 (1), 63–72.
- (160) Guo, W.; Bi, J.; Zhu, Q.; Ma, J.; Yang, G.; Wu, H.; Sun, X.; Han, B. Highly Selective CO<sub>2</sub> Electroreduction to CO on Cu-Co Bimetallic Catalysts. ACS Sustain. Chem. Eng. 2020, 8 (33), 12561– 12567
- (161) Wu, S.; Guo, H.; Hui, K. S.; Hui, K. N. Rational Design of Integrated CuO@Co<sub>x</sub>Ni<sub>1-x</sub>(OH)<sub>2</sub> Nanowire Arrays on Copper Foam for High-Rate and Long-Life Supercapacitors. *Electrochim. Acta* 2019, 295, 759–768.

- (162) Ghouri, Z. K.; Barakat, N. A. M.; Kim, H. Y. Influence of Copper Content on the Electrocatalytic Activity toward Methanol Oxidation of Co<sub>v</sub>Cu<sub>v</sub> Allov Nanoparticles-Decorated CNFs. Sci. Rep. 2015. 5. 16695.
- (163) Call, A.; Casadevall, C.; Acuña-Parés, F.; Casitas, A.; Lloret-Fillol, J. Dual Cobalt-Copper Light-Driven Catalytic Reduction of Aldehydes and Aromatic Ketones in Aqueous Media. *Chem. Sci.* 2017, 8 (7), 4739–4749.
- (164) Jiang, Y.-W.; Chai, K.; Wang, Y.-Q.; Zhang, H.-D.; Xu, W.; Li, W.; Shi, Y. Mesoporous Silica-Supported CuCo<sub>2</sub>O<sub>4</sub> Mixed-Metal Oxides for the Aerobic Oxidation of Alcohols. *ACS Appl. Nano Mater.* **2019**, *2* (7), 4435–4442.
- (165) Hankare, P. P.; Kamble, P. D.; Maradur, S. P.; Kadam, M. R.; Sankpal, U. B.; Patil, R. P.; Nimat, R. K.; Lokhande, P. D. Ferrospinels Based on Cu and Co Prepared via Low Temperature Route as Efficient Catalysts for the Selective Oxidation of Alcohol. *J. Alloys Compd.* 2009, 487 (1–2), 730–734.
- (166) Zhang, Z.; Yao, S.; Wang, C.; Liu, M.; Zhang, F.; Hu, X.; Chen, H.; Gou, X.; Chen, K.; Zhu, Y.; Lu, X.; Ouyang, P.; Fu, J. CuZnCoO<sub>x</sub> Multifunctional Catalyst for in Situ Hydrogenation of 5-Hydroxymethylfurfural with Ethanol as Hydrogen Carrier. J. Catal. 2019, 373, 314–321.
- (167) Srivastava, S.; Mohanty, P.; Parikh, J. K.; Dalai, A. K.; Amritphale, S. S.; Khare, A. K. Cr-Free Co-Cu/SBA-15 Catalysts for Hydrogenation of Biomass-Derived α-, β-Unsaturated Aldehyde to Alcohol. *Chin. J. Catal.* 2015, 36 (7), 933–942.
- (168) Srivastava, S.; Jadeja, G. C.; Parikh, J. A Versatile Bi-Metallic Copper-Cobalt Catalyst for Liquid Phase Hydrogenation of Furfural to 2-Methylfuran. *RSC Adv.* **2016**, *6* (2), 1649–1658.
- (169) Golub, K. W.; Sulmonetti, T. P.; Darunte, L. A.; Shealy, M. S.; Jones, C. W. Metal-Organic-Framework-Derived Co/Cu-Carbon Nanoparticle Catalysts for Furfural Hydrogenation. ACS Appl. Nano Mater. 2019, 2 (9), 6040–6056.
- (170) Gou, X.; Okejiri, F.; Zhang, Z.; Liu, M.; Liu, J.; Chen, H.; Chen, K.; Lu, X.; Ouyang, P.; Fu, J. Tannin-Derived Bimetallic CuCo/C Catalysts for an Efficient in-Situ Hydrogenation of Lauric Acid in Methanol-Water Media. *Fuel Process. Technol.* **2020**, *205*, 106426.
- (171) Mathew, T.; Shylesh, S.; Devassy, B. M.; Vijayaraj, M.; Satyanarayana, C. V. V.; Rao, B. S.; Gopinath, C. S. Selective Production of Orthoalkyl Phenols on Cu<sub>0.5</sub>Co<sub>0.5</sub>Fe<sub>2</sub>O<sub>4</sub>: A Study of Catalysis and Characterization. Appl. Catal. A 2004, 273 (1–2), 35–45.
- (172) Cui, K.; Kumamoto, A.; Xiang, R.; An, H.; Wang, B.; Inoue, T.; Chiashi, S.; Ikuhara, Y.; Maruyama, S. Synthesis of Subnanometer-Diameter Vertically Aligned Single-Walled Carbon Nanotubes with Copper-Anchored Cobalt Catalysts. *Nanoscale* 2016, 8 (3), 1608–1617.
- (173) Prieto, G.; Beijer, S.; Smith, M. L.; He, M.; Au, Y.; Wang, Z.; Bruce, D. A.; de Jong, K. P.; Spivey, J. J.; de Jongh, P. E. Design and Synthesis of Copper-Cobalt Catalysts for the Selective Conversion of Synthesis Gas to Ethanol and Higher Alcohols. *Angew. Chem. Int. Ed.* 2014, 53 (25), 6397–6401.
- (174) Sun, K.; Tan, M.; Bai, Y.; Gao, X.; Wang, P.; Gong, N.; Zhang, T.; Yang, G.; Tan, Y. Design and Synthesis of Spherical-Platelike Ternary Copper-Cobalt-Manganese Catalysts for Direct Conversion of Syngas to Ethanol and Higher Alcohols. *J. Catal.* **2019**, *378*, 1–16.
- (175) Li, Z.; Zeng, Z.; Yao, D.; Fan, S.; Guo, S.; Lv, J.; Huang, S.; Wang, Y.; Ma, X. High-Performance CoCu Catalyst Encapsulated in KIT-6 for Higher Alcohol Synthesis from Syngas. *ACS Sustain. Chem. Eng.* **2020**, *8* (1), 200–209.
- (176) Göbel, C.; Schmidt, S.; Froese, C.; Fu, Q.; Chen, Y.-T.; Pan, Q.; Muhler, M. Structural Evolution of Bimetallic Co-Cu Catalysts in CO Hydrogenation to Higher Alcohols at High Pressure. *J. Catal.* **2020**, 383, 33–41.

- (177) Lin, T.; Qi, X.; Wang, X.; Xia, L.; Wang, C.; Yu, F.; Wang, H.; Li, S.; Zhong, L.; Sun, Y. Direct Production of Higher Oxygenates by Syngas Conversion over a Multifunctional Catalyst. *Angew. Chem. Int. Ed.* **2019**, *58* (14), 4627–4631.
- (178) Cao, A.; Schumann, J.; Wang, T.; Zhang, L.; Xiao, J.; Bothra, P.; Liu, Y.; Abild-Pedersen, F.; Nørskov, J. K. Mechanistic Insight into the Synthesis of Higher Alcohols from Syngas on CuCo Alloys. ACS Catal. 2018, 8 (11), 10148–10155.
- (179) Kesler, S. E.; Wilkinson, B. H. Earth's Copper Resources Estimated from Tectonic Diffusion of Porphyry Copper Deposits. *Geology* **2008**, *36* (3), 255–258.
- (180) Chernavskii, P. A.; Kazak, V. O.; Pankina, G. V.; Perfiliev, Y. D.; Li, T.; Virginie, M.; Khodakov, A. Y. Influence of Copper and Potassium on the Structure and Carbidisation of Supported Iron Catalysts for Fischer-Tropsch Synthesis. *Catal. Sci. Technol.* 2017, 7 (11), 2325–2334.
- (181) Xu, L.; Lin, J.; Bai, Y.; Mavrikakis, M. Atomic and Molecular Adsorption on Cu(111). *Top. Catal.* **2018**, *61* (9–11), 736–750.
- (182) Crabtree, R. H. *The Organometallic Chemistry of the Transition Metals*, 6th ed.; John Wiley & Sons, Inc.: Hoboken, New Jersey, 2014.
- (183) Müller, A.; Comas-Vives, A.; Copéret, C. Shape and Surface Morphology of Copper Nanoparticles under CO<sub>2</sub> Hydrogenation Conditions from First Principles. *J. Phys. Chem. C* **2021**, *125* (1), 396–409.
- (184) Lisiecki, I. Size, Shape, and Structural Control of Metallic Nanocrystals. *J. Phys. Chem. B* **2005**, *109* (25), 12231–12244.
- (185) Salzemann, C.; Lisiecki, I.; Brioude, A.; Urban, J.; Pileni, M. P. Collections of Copper Nanocrystals Characterized by Different Sizes and Shapes: Optical Response of These Nanoobjects. *J. Phys. Chem. B* **2004**, *108* (35), 13242–13248.
- (186) Tanori, J.; Pileni, M. P. Control of the Shape of Copper Metallic Particles by Using a Colloidal System as Template. *Langmuir* **1997**, *13* (4), 639–645.
- (187) Hansen, P. L.; Wagner, J. B.; Helveg, S.; Rostrup-Nielsen, J. R.; Clausen, B. S.; Topsøe, H. Atom-Resolved Imaging of Dynamic Shape Changes in Supported Copper Nanocrystals. *Science* 2002, 295 (5562), 2053–2055.
- (188) Vesborg, P. C. K.; Chorkendorff, I.; Knudsen, I.; Balmes, O.; Nerlov, J.; Molenbroek, A. M.; Clausen, B. S.; Helveg, S. Transient Behavior of Cu/ZnO-Based Methanol Synthesis Catalysts. *J. Catal.* 2009, 262 (1), 65–72.
- (189) Guisbiers, G.; Kazan, M.; van Overschelde, O.; Wautelet, M.; Pereira, S. Mechanical and Thermal Properties of Metallic and Semiconductive Nanostructures. *J. Phys. Chem. C* **2008**, *112* (11), 4097–4103.
- (190) Zhang, T.; Chen, Z.; Walsh, A. G.; Li, Y.; Zhang, P. Single-Atom Catalysts Supported by Crystalline Porous Materials: Views from the Inside. Adv. Mater. 2020, 32 (44), 2002910.
- (191) Zimmermann, P.; Peredkov, S.; Abdala, P. M.; DeBeer, S.; Tromp, M.; Müller, C.; van Bokhoven, J. A. Modern X-Ray Spectroscopy: XAS and XES in the Laboratory. Coord. Chem. Rev. 2020, 423, 213466.
- (192) Itié, J.-P.; Baudelet, F.; Rueff, J.-P. High Pressure XAS, XMCD and IXS. In X-ray Absorption and X-ray Emission Spectroscopy: Theory and Applications; van Bokhoven, J. A., Lamberti, C., Eds.; John Wiley & Sons, Inc.: Chichester, United Kingdom, 2016; pp 385–405.
- (193) Behrens, M.; Zander, S.; Kurr, P.; Jacobsen, N.; Senker, J.; Koch, G.; Ressler, T.; Fischer, R. W.; Schlögl, R. Performance Improvement of Nanocatalysts by Promoter-Induced Defects in the Support Material: Methanol Synthesis over Cu/ZnO:Al. J. Am. Chem. Soc. 2013, 135 (16), 6061–6068.

- (194) Bulavchenko, O. A.; Pochtar, A. A.; Gerasimov, E. Y.; Fedorov, A. V.; Chesalov, Y. A.; Saraev, A. A.; Yakovlev, V. A.; Kaichev, V. V. Chemical and Texture Promoters in Cu-Fe-Al Oxide Nanocomposite Catalysts for Combustion of Solid Fuel Gasification Products. Appl. Catal. A 2020, 590, 117364.
- (195) Rothenberg, G. Catalysis: Concepts and Green Applications, 1st ed.; Wiley-VCH Verlag GmbH & Co. KGaA: Weinheim, Germany, 2008.
- (196) Logadottir, A.; Nørskov, J. K. The Effect of Strain for N<sub>2</sub> Dissociation on Fe Surfaces. Surf. Sci. 2001, 489 (1-3), 135-143.
- (197) Ngantsoue-Hoc, W.; Zhang, Y.; O'Brien, R. J.; Luo, M.; Davis, B. H. Fischer-Tropsch Synthesis: Activity and Selectivity for Group I Alkali Promoted Iron-Based Catalysts. *Appl. Catal. A* **2002**, *236* (1–2), 77–89.
- (198) Gaube, J.; Klein, H. F. The Promoter Effect of Alkali in Fischer-Tropsch Iron and Cobalt Catalysts. Appl. Catal. A 2008, 350 (1), 126–132.
- (199) Ertl, G.; Lee, S. B.; Weiss, M. Adsorption of Nitrogen on Potassium Promoted Fe(111) and (100) Surfaces. Surf. Sci. 1982, 114 (2–3), 527–545.
- (200) Huš, M.; Hellman, A. Dipole Effect on Ethylene Epoxidation: Influence of Alkali Metals and Chlorine. J. Catal. 2018, 363, 18–25.
- (201) Connor, G. P.; Holland, P. L. Coordination Chemistry Insights into the Role of Alkali Metal Promoters in Dinitrogen Reduction. Catal. Today 2017, 286, 21–40.
- (202) Aqra, F.; Ayyad, A. Surface Free Energy of Alkali and Transition Metal Nanoparticles. Appl. Surf. Sci. 2014, 314, 308–313.
- (203) Egeberg, R. C.; Dahl, S.; Logadottir, A.; Larsen, J. H.; Nørskov, J. K.; Chorkendorff, I. N<sub>2</sub> Dissociation on Fe(1 1 0) and Fe/Ru(0 0 0 1): What Is the Role of Steps? Surf. Sci. 2001, 491 (1-2), 183-194.
- (204) Si, C.; Ban, H.; Chen, K.; Wang, X.; Cao, R.; Yi, Q.; Qin, Z.; Shi, L.; Li, Z.; Cai, W.; Li, C. Insight into the Positive Effect of Cu<sup>0</sup>/Cu<sup>+</sup> Ratio on the Stability of Cu-ZnO-CeO<sub>2</sub> Catalyst for Syngas Hydrogenation. *Appl. Catal. A* **2020**, *594*, 117466.
- (205) Hernández Mejía, C.; van Deelen, T. W.; de Jong, K. P. Activity Enhancement of Cobalt Catalysts by Tuning Metal-Support Interactions. *Nat. Commun.* **2018**, *9*, 4459.
- van den Berg, R.; Parmentier, T. E.; Elkjær, C. F.; Gommes, C. J.; Sehested, J.; Helveg, S.; de Jongh, P.
   E.; de Jong, K. P. Support Functionalization to Retard Ostwald Ripening in Copper Methanol Synthesis
   Catalysts. ACS Catal. 2015, 5 (7), 4439–4448.
- (207) Kołodziejczak-Radzimska, A.; Jesionowski, T. Zinc Oxide-from Synthesis to Application: A Review. Materials **2014**, 7 (4), 2833–2881.
- (208) Moezzi, A.; McDonagh, A. M.; Cortie, M. B. Zinc Oxide Particles: Synthesis, Properties and Applications, Chem. Eng. J. 2012, 185–186, 1–22.
- (209) Shi, Y.; Zhou, Y.; Yang, D.-R.; Xu, W.-X.; Wang, C.; Wang, F.-B.; Xu, J.-J.; Xia, X.-H.; Chen, H.-Y. Energy Level Engineering of MoS<sub>2</sub> by Transition-Metal Doping for Accelerating Hydrogen Evolution Reaction. *J. Am. Chem. Soc.* **2017**, *139* (43), 15479–15485.
- (210) Liu, T.; Liu, D.; Qu, F.; Wang, D.; Zhang, L.; Ge, R.; Hao, S.; Ma, Y.; Du, G.; Asiri, A. M.; Chen, L.; Sun, X. Enhanced Electrocatalysis for Energy-Efficient Hydrogen Production over CoP Catalyst with Nonelectroactive Zn as a Promoter. Adv. Energy Mater. 2017, 7 (15), 1700020.
- (211) Zhu, J.; Peng, X.; Yao, L.; Shen, J.; Tong, D.; Hu, C. The Promoting Effect of La, Mg, Co and Zn on the Activity and Stability of Ni/SiO<sub>2</sub> Catalyst for CO<sub>2</sub> Reforming of Methane. *Int. J. Hydrogen Energy* **2011**, *36* (12), 7094–7104.

- (212) Bollmann, L.; Ratts, J. L.; Joshi, A. M.; Williams, W. D.; Pazmino, J.; Joshi, Y. V.; Miller, J. T.; Kropf, A. J.; Delgass, W. N.; Ribeiro, F. H. Effect of Zn Addition on the Water-Gas Shift Reaction over Supported Palladium Catalysts. J. Catal. 2008, 257 (1), 43–54.
- (213) Li, S.; Li, A.; Krishnamoorthy, S.; Iglesia, E. Effects of Zn, Cu, and K Promoters on the Structure and on the Reduction, Carburization, and Catalytic Behavior of Iron-Based Fischer-Tropsch Synthesis Catalysts. Catal. Lett. 2001, 77 (4), 197–205.
- (214) Zhai, P.; Xu, C.; Gao, R.; Liu, X.; Li, M.; Li, W.; Fu, X.; Jia, C.; Xia, J.; Zhao, M.; Wang, X.; Li, Y.-W.; Zhang, Q.; Wen, X.-D.; Ma, D. Highly Tunable Selectivity for Syngas-Derived Alkenes over Zinc and Sodium-Modulated Fe<sub>5</sub>C<sub>2</sub> Catalyst. *Angew. Chem. Int. Ed.* 2016, 55 (34), 9902–9907.
- (215) Wang, H.; Yang, Y.; Xu, J.; Wang, H.; Ding, M.; Li, Y. Study of Bimetallic Interactions and Promoter Effects of FeZn, FeMn and FeCr Fischer-Tropsch Synthesis Catalysts. *J. Mol. Catal. A* **2010**, 326 (1–2), 29–40.
- (216) Brands, D. S.; Poels, E. K.; Bliek, A. Ester Hydrogenolysis over Promoted Cu/SiO<sub>2</sub> Catalysts. Appl. Catal. A 1999, 184 (2), 279–289.
- (217) Kurtz, M.; Strunk, J.; Hinrichsen, O.; Muhler, M.; Fink, K.; Meyer, B.; Wöll, C. Active Sites on Oxide Surfaces: ZnO-Catalyzed Synthesis of Methanol from CO and H<sub>2</sub>. Angew. Chem. Int. Ed. 2005, 44 (18), 2790–2794.
- (218) Wilmer, H.; Kurtz, M.; Klementiev, K. V.; Tkachenko, O. P.; Grünert, W.; Hinrichsen, O.; Birkner, A.; Rabe, S.; Merz, K.; Driess, M.; Wöll, C.; Muhler, M. Methanol Synthesis over ZnO: A Structure-Sensitive Reaction? *Phys. Chem. Chem. Phys.* 2003, 5 (20), 4736–4742.
- (219) Laudenschleger, D.; Ruland, H.; Muhler, M. Identifying the Nature of the Active Sites in Methanol Synthesis over Cu/ZnO/Al<sub>2</sub>O<sub>3</sub> Catalysts. *Nat. Commun.* **2020**, *11*, 3898.
- (220) Kuld, S.; Thorhauge, M.; Falsig, H.; Elkjær, C. F.; Helveg, S.; Chorkendorff, I.; Sehested, J. Quantifying the Promotion of Cu Catalysts by ZnO for Methanol Synthesis. *Science* **2016**, *352* (6288), 969–974.
- (221) Frei, E.; Gaur, A.; Lichtenberg, H.; Zwiener, L.; Scherzer, M.; Girgsdies, F.; Lunkenbein, T.; Schlögl, R. Cu-Zn Alloy Formation as Unfavored State for Efficient Methanol Catalysts. *ChemCatChem* 2020, 12 (16), 4029–4033.
- (222) Chinchen, G. C.; Waugh, K. C.; Whan, D. A. The Activity and State of the Copper Surface in Methanol Synthesis Catalysts. Appl. Catal. 1986, 25 (1–2), 101–107.
- (223) Pan, W. X.; Cao, R.; Roberts, D. L.; Griffin, G. L. Methanol Synthesis Activity of Cu/ZnO Catalysts. *J. Catal.* **1988**, *114* (2), 440–446.
- (224) Grunwaldt, J.-D.; Molenbroek, A. M.; Topsøe, N.-Y.; Topsøe, H.; Clausen, B. S. In Situ Investigations of Structural Changes in Cu/ZnO Catalysts. *J. Catal.* **2000**, *194* (2), 452–460.
- (225) Tisseraud, C.; Comminges, C.; Belin, T.; Ahouari, H.; Soualah, A.; Pouilloux, Y.; Le Valant, A. The Cu-ZnO Synergy in Methanol Synthesis from CO<sub>2</sub>, Part 2: Origin of the Methanol and CO Selectivities Explained by Experimental Studies and a Sphere Contact Quantification Model in Randomly Packed Binary Mixtures on Cu-ZnO Coprecipitate Catalysts. J. Catal. 2015, 330, 533–544.
- (226) Spencer, M. S. The Role of Zinc Oxide in Cu/ZnO Catalysts for Methanol Synthesis and the Water-Gas Shift Reaction. *Top. Catal.* **1999**, *8* (3–4), 259–266.
- (227) Le Valant, A.; Comminges, C.; Tisseraud, C.; Canaff, C.; Pinard, L.; Pouilloux, Y. The Cu-ZnO Synergy in Methanol Synthesis from CO<sub>2</sub>, Part 1: Origin of Active Site Explained by Experimental Studies and a Sphere Contact Quantification Model on Cu + ZnO Mechanical Mixtures. *J. Catal.* **2015**, *324*, 41–49.
- (228) Kattel, S.; Ramírez, P. J.; Chen, J. G.; Rodriguez, J. A.; Liu, P. Active Sites for CO<sub>2</sub> Hydrogenation to

- Methanol on Cu/ZnO Catalysts. Science 2017, 355 (6331), 1-4.
- (229) Nakamura, J.; Choi, Y.; Fujitani, T. On the Issue of the Active Site and the Role of ZnO in Cu/ZnO Methanol Synthesis Catalysts. *Top. Catal.* **2003**, *22* (3–4), 277–285.
- (230) Naumann d'Alnoncourt, R.; Xia, X.; Strunk, J.; Löffler, E.; Hinrichsen, O.; Muhler, M. The Influence of Strongly Reducing Conditions on Strong Metal-Support Interactions in Cu/ZnO Catalysts Used for Methanol Synthesis. *Phys. Chem. Chem. Phys.* 2006, 8 (13), 1525–1538.
- (231) Kuld, S.; Conradsen, C.; Moses, P. G.; Chorkendorff, I.; Sehested, J. Quantification of Zinc Atoms in a Surface Alloy on Copper in an Industrial-Type Methanol Synthesis Catalyst. *Angew. Chem. Int. Ed.* **2014**, *53* (23), 5941–5945.
- (232) Robinson, W. R. A. M.; Mol, J. C. Support Effects in Methanol Synthesis over Copper-Containing Catalysts. *Appl. Catal.* **1991**, *76* (1), 117–129.
- (233) Wang, G.; Zuo, Y.; Han, M.; Wang, J. Copper Crystallite Size and Methanol Synthesis Catalytic Property of Cu-Based Catalysts Promoted by Al, Zr and Mn. React. Kinet. Mech. Catal. 2010, 101 (2), 443–454.
- (234) Schumann, J.; Eichelbaum, M.; Lunkenbein, T.; Thomas, N.; Álvarez Galván, M. C.; Schlögl, R.; Behrens, M. Promoting Strong Metal Support Interaction: Doping ZnO for Enhanced Activity of Cu/ZnO:M (M = Al, Ga, Mg) Catalysts. *ACS Catal.* **2015**, *5* (6), 3260–3270.
- (235) Das, A. P.; Sukla, L. B.; Pradhan, N.; Nayak, S. Manganese Biomining: A Review. *Bioresour. Technol.* 2011, 102 (16), 7381–7387.
- (236) Badoga, S.; Kamath, G.; Dalai, A. Effects of Promoters (Mn, Mg, Co and Ni) on the Fischer-Tropsch Activity and Selectivity of KCuFe/Mesoporous-Alumina Catalyst. Appl. Catal. A 2020, 607, 117861.
- (237) Wang, X.; Zhang, C.; Chang, Q.; Wang, L.; Lv, B.; Xu, J.; Xiang, H.; Yang, Y.; Li, Y. Enhanced Fischer-Tropsch Synthesis Performances of Fe/h-BN Catalysts by Cu and Mn. *Catal. Today* **2020**, *343*, 91–100.
- (238) Ding, M.; Qiu, M.; Liu, J.; Li, Y.; Wang, T.; Ma, L.; Wu, C. Influence of Manganese Promoter on Co-Precipitated Fe-Cu Based Catalysts for Higher Alcohols Synthesis. Fuel 2013, 109, 21–27.
- (239) Han, X.; Fang, K.; Sun, Y. Effects of Metal Promotion on CuMgFe Catalysts Derived from Layered Double Hydroxides for Higher Alcohol Synthesis via Syngas. RSC Adv. 2015, 5 (64), 51868–51874.
- (240) Qian, W.; Wang, H.; Xu, Y.; Yang, X.; Zhai, G.; Zhang, H.; Ma, H.; Sun, Q.; Ying, W. In Situ DRIFTS Study of Homologous Reaction of Methanol and Higher Alcohols Synthesis over Mn Promoted Cu-Fe Catalysts. *Ind. Eng. Chem. Res.* **2019**, *58* (16), 6288–6297.
- (241) Heracleous, E.; Liakakou, E..; Lappas, A. A.; Lemonidou, A. A. Investigation of K-Promoted Cu-Zn-Al, Cu-X-Al and Cu-Zn-X (X = Cr, Mn) Catalysts for Carbon Monoxide Hydrogenation to Higher Alcohols. *Appl. Catal. A* **2013**, *455*, 145–154.
- (242) Liakakou, E. T.; Isaacs, M. A.; Wilson, K.; Lee, A. F.; Heracleous, E. On the Mn Promoted Synthesis of Higher Alcohols over Cu Derived Ternary Catalysts. Catal. Sci. Technol. 2017, 7 (4), 988–999.
- (243) Gupta, M.; Spivey, J. J. Electrodeposited Cu-ZnO and Mn-Cu-ZnO Nanowire/Tube Catalysts for Higher Alcohols from Syngas. *Catal. Today* **2009**, *147* (2), 126–132.
- (244) Zhang, R.; Wang, G.; Wang, B.; Ling, L. Insight into the Effect of Promoter Mn on Ethanol Formation from Syngas on a Mn-Promoted MnCu(211) Surface: A Comparison with a Cu(211) Surface. J. Phys. Chem. C 2014, 118 (10), 5243–5254.
- (245) Beiramar, J. M.; Griboval-Constant, A.; Khodakov, A. Y. Effects of Metal Promotion on the Performance of CuZnAl Catalysts for Alcohol Synthesis. *ChemCatChem* **2014**, *6* (6), 1788–1793.
- (246) Tan, Y.; Xie, H.; Cui, H.; Han, Y.; Zhong, B. Modification of Cu-Based Methanol Synthesis Catalyst for

- Dimethyl Ether Synthesis from Syngas in Slurry Phase. Catal. Today 2005, 104 (1), 25–29.
- (247) Zhou, X.; Meng, M.; Sun, Z.; Li, Q.; Jiang, Z. Prominent Enhancement of Mn or Co Addition on the Performance of Cu-Ce-O Catalyst Used for H<sub>2</sub> Production via Dimethyl Ether Steam Reforming. *Chem. Eng. J.* **2011**, *174* (1), 400–407.
- (248) Ye, T.; Ai, Y.; Chen, B.; Ye, Y.; Sun, J.; Qin, L.; Yao, X. Enhancement of Aldehyde-Water Shift Reaction over CuZnAl Catalyst by Mn Promoter. Catal. Commun. 2020, 149, 106262.
- (249) Tian, X.; Wang, S.; Wang, Z.-J.; Wang, H.; Zhou, Y.; Zhong, H.; Mao, Y. Understanding the Promotion Effect of Mn on CuO/Al<sub>2</sub>O<sub>3</sub> for Catalyzed HCl Oxidation to Cl<sub>2</sub>. *ChemCatChem* **2020**, *12* (12), 3240–3248.
- (250) Koh, M. K.; Wong, Y. J.; Chai, S. P.; Mohamed, A. R. Carbon Dioxide Hydrogenation to Methanol over Multi-Functional Catalyst: Effects of Reactants Adsorption and Metal-Oxide(s) Interfacial Area. *J. Ind. Eng. Chem.* 2018, 62, 156–165.
- (251) Zhan, H.; Li, F.; Xin, C.; Zhao, N.; Xiao, F.; Wei, W.; Sun, Y. Performance of the La-Mn-Zn-Cu-O Based Perovskite Precursors for Methanol Synthesis from CO<sub>2</sub> Hydrogenation. *Catal. Lett.* 2015, 145 (5), 1177–1185.
- (252) Słoczyński, J.; Grabowski, R.; Kozłowska, A.; Olszewski, P.; Lachowska, M.; Skrzypek, J.; Stoch, J. Effect of Mg and Mn Oxide Additions on Structural and Adsorptive Properties of Cu/ZnO/ZrO<sub>2</sub> Catalysts for the Methanol Synthesis from CO<sub>2</sub>, Appl. Catal. A 2003, 249 (1), 129–138.
- (253) Chen, H. Y.; Lin, J.; Tan, K. L.; Li, J. Comparative Studies of Manganese-Doped Copper-Based Catalysts: The Promoter Effect of Mn on Methanol Synthesis. *Appl. Surf. Sci.* **1998**, *126* (3–4), 323–331.
- (254) Acet, M.; Zähres, H.; Stamm, W.; Wassermann, E. F.; Pepperhoff, W. The Study of the Thermal Properties of v-Mn from Mn-Cu Allovs. *Phys. B Phys. Condens. Matter* **1989**, *161* (1–3), 67–71.
- (255) Li, J.-L.; Takeguchi, T.; Inui, T. Doping Effect of Potassium Permanganate on the Performance of a Copper/Zinc Oxide/Alumina Catalyst for Methanol Formation. Appl. Catal. A 1996, 139 (1–2), 97– 106.
- (256) Kilo, M.; Weigel, J.; Wokaun, A.; Koeppel, R. A.; Stoeckli, A.; Baiker, A. Effect of the Addition of Chromium- and Manganese Oxides on Structural and Catalytic Properties of Copper/Zirconia Catalysts for the Synthesis of Methanol from Carbon Dioxide. *J. Mol. Catal. A* **1997**, *126* (2–3), 169–184.
- (257) Hayward, J. S.; Smith, P. J.; Kondrat, S. A.; Bowker, M.; Hutchings, G. J. The Effects of Secondary Oxides on Copper-Based Catalysts for Green Methanol Synthesis. *ChemCatChem* **2017**, 9 (9), 1655–1662.
- (258) Blanco, H.; Hallen Lima, S.; de Oliveira Rodrigues, V.; Amparo Palacio, L.; da Costa Faro Jr., A. Copper-Manganese Catalysts with High Activity for Methanol Synthesis. *Appl. Catal. A* **2019**, *579*, 65–74.
- (259) Sharafutdinov, I.; Elkjær, C. F.; Pereira de Carvalho, H. W.; Gardini, D.; Chiarello, G. L.; Damsgaard, C. D.; Wagner, J. B.; Grunwaldt, J.-D.; Dahl, S.; Chorkendorff, I. Intermetallic Compounds of Ni and Ga as Catalysts for the Synthesis of Methanol. *J. Catal.* 2014, 320, 77–88.
- (260) Smitshuysen, T. E. L.; Nielsen, M. R.; Pruessmann, T.; Zimina, A.; Sheppard, T. L.; Grunwaldt, J.-D.; Chorkendorff, I.; Damsgaard, C. D. Optimizing Ni-Fe-Ga Alloys into Ni<sub>2</sub>FeGa for the Hydrogenation of CO<sub>2</sub> into Methanol. *ChemCatChem* 2020, *12* (12), 3265–3273.
- Fiordaliso, E. M.; Sharafutdinov, I.; Carvalho, H. W. P.; Grunwaldt, J.-D.; Hansen, T. W.; Chorkendorff,
   I.; Wagner, J. B.; Damsgaard, C. D. Intermetallic GaPd<sub>2</sub> Nanoparticles on SiO<sub>2</sub> for Low-Pressure CO<sub>2</sub>
   Hydrogenation to Methanol: Catalytic Performance and in Situ Characterization. ACS Catal. 2015, 5

- (10), 5827-5836.
- (262) Curulla-Ferré, D.; Drouilly, C.; Martin, O.; Mondelli, C.; Pérez-Ramírez, J.; Martin-Fernandez, A. J. Supported Indium Oxide Catalyst and Process for Methanol Synthesis Using the Same. US20200061582A1, 2020.
- (263) Agny, R. M.; Takoudis, C. G. Synthesis of Methanol from Carbon Monoxide and Hydrogen over a Copper-Zinc Oxide-Alumina Catalyst. Ind. Eng. Chem. Prod. Res. Dev. 1985, 24 (1), 50–55.
- (264) Nielsen, N. D.; Thrane, J.; Jensen, A. D.; Christensen, J. M. Bifunctional Synergy in CO Hydrogenation to Methanol with Supported Cu. *Catal. Lett.* **2019**, 1–7.
- (265) Zuo, Z.-J.; Han, P.-D.; Li, Z.; Hu, J.-S.; Huang, W. Can Methanol Be Synthesized from CO by Direct Hydrogenation over Cu/ZnO Catalysts? Appl. Surf. Sci. 2012, 261, 640–646.
- (266) Martin, O.; Pérez-Ramírez, J. New and Revisited Insights into the Promotion of Methanol Synthesis Catalysts by CO<sub>2</sub>. Catal. Sci. Technol. 2013, 3 (12), 3343–3352.
- (267) Prieto, G.; Meeldijk, J. D.; de Jong, K. P.; de Jongh, P. E. Interplay between Pore Size and Nanoparticle Spatial Distribution: Consequences for the Stability of CuZn/SiO<sub>2</sub> Methanol Synthesis Catalysts. *J. Catal.* 2013, 303, 31–40.
- (268) van den Berg, R.; Zečević, J.; Sehested, J.; Helveg, S.; de Jongh, P. E.; de Jong, K. P. Impact of the Synthesis Route of Supported Copper Catalysts on the Performance in the Methanol Synthesis Reaction. Catal. Todau 2016, 272, 87–93.
- (269) Lunkenbein, T.; Girgsdies, F.; Kandemir, T.; Thomas, N.; Behrens, M.; Schlögl, R.; Frei, E. Bridging the Time Gap: A Copper/Zinc Oxide/Aluminum Oxide Catalyst for Methanol Synthesis Studied under Industrially Relevant Conditions and Time Scales. *Angew. Chem. Int. Ed.* 2016, 55 (41), 12708–12712.
- (270) Chen, K.; Yu, J.; Liu, B.; Si, C.; Ban, H.; Cai, W.; Li, C.; Li, Z.; Fujimoto, K. Simple Strategy Synthesizing Stable CuZnO/SiO<sub>2</sub> Methanol Synthesis Catalyst. *J. Catal.* **2019**. *372*. 163–173.
- (271) Rasmussen, D. B.; Janssens, T. V. W.; Temel, B.; Bligaard, T.; Hinnemann, B.; Helveg, S.; Sehested, J. The Energies of Formation and Mobilities of Cu Surface Species on Cu and ZnO in Methanol and Water Gas Shift Atmospheres Studied by DFT. J. Catal. 2012, 293, 205–214.
- (272) Choi, Y.; Futagami, K.; Fujitani, T.; Nakamura, J. The Difference in the Active Sites for CO<sub>2</sub> and CO Hydrogenations on Cu/ZnO-Based Methanol Synthesis Catalysts. *Catal. Lett.* **2001**, *73* (1), 27–31.
- (273) Zander, S.; Kunkes, E. L.; Schuster, M. E.; Schumann, J.; Weinberg, G.; Teschner, D.; Jacobsen, N.; Schlögl, R.; Behrens, M. The Role of the Oxide Component in the Development of Copper Composite Catalysts for Methanol Synthesis. *Angew. Chem. Int. Ed.* 2013, 52 (25), 6536–6540.
- (274) Che, M.; Bennett, C. O. The Influence of Particle Size on the Catalytic Properties of Supported Metals. *Adv. Catal.* **1989**, *36*, 55–172.
- (275) Eslava, J. L.; Gallegos-Suárez, E.; Guerrerro-Ruiz, A.; Rodríguez-Ramos, I. Effect of Mo Promotion on the Activity and Selectivity of Ru/Graphite Catalysts for Fischer-Tropsch Synthesis. *Catal. Today* 2019, 357, 185–192.
- (276) Bian, J.; Xiao, M.; Wang, S.; Wang, X.; Lu, Y.; Meng, Y. Highly Effective Synthesis of Dimethyl Carbonate from Methanol and Carbon Dioxide Using a Novel Copper-Nickel/Graphite Bimetallic Nanocomposite Catalyst. Chem. Eng. J. 2009, 147 (2–3), 287–296.
- (277) Che, M.; Clause, O.; Marcilly, C. Preparation of Solid Catalysts: Supported Catalysts: Deposition of Active Component: Impregnation and Ion Exchange. In *Handbook of Heterogeneous Catalysis*; Ertl, G., Knözinger, H., Weitkamp, J., Eds.; VCH Verlagsgesellschaft mbH: Weinheim, Germany, 1997; pp 191–207.

- (278) Thommes, M.; Kaneko, K.; Neimark, A. V.; Olivier, J. P.; Rodriguez-Reinoso, F.; Rouquerol, J.; Sing, K. S. W. Physisorption of Gases, with Special Reference to the Evaluation of Surface Area and Pore Size Distribution (IUPAC Technical Report). *Pure Appl. Chem.* 2015, 87 (9–10), 1051–1069.
- (279) van den Bleek, C. M.; van der Wiele, K.; van den Berg, P. J. The Effect of Dilution on the Degree of Conversion in Fixed Bed Catalytic Reactors. Chem. Eng. Sci. 1969, 24 (4), 681–694.
- (280) Nunes, M.; Fernandez, D. M.; Morales, M. V.; Rodríguez-Ramos, I.; Guerrero-Ruiz, A.; Freire, C. Cu and Pd Nanoparticles Supported on a Graphitic Carbon Material as Bifunctional HER/ORR Electrocatalysts. Catal. Today 2019, 357, 279–290.
- (281) D'Halluin, M.; Mabit, T.; Fairley, N.; Fernandez, V.; Gawande, M. B.; Le Grognec, E.; Felpin, F.-X. Graphite-Supported Ultra-Small Copper Nanoparticles Preparation, Characterization and Catalysis Applications. Carbon 2015, 93, 974–983.
- (282) Robinson, I.; Harder, R. Coherent X-Ray Diffraction Imaging of Strain at the Nanoscale. *Nat. Mater.* **2009**, *8* (4), 291–298.
- (283) Harris, K. D. M.; Tremayne, M.; Kariuki, B. M. Contemporary Advances in the Use of Powder X-Ray Diffraction for Structure Determination. *Angew. Chem. Int. Ed.* **2001**, *40* (9), 1626–1651.
- (284) Lunkenbein, T.; Schumann, J.; Behrens, M.; Schlögl, R.; Willinger, M. G. Formation of a ZnO Overlayer in Industrial Cu/ZnO/Al<sub>2</sub>O<sub>3</sub> Catalysts Induced by Strong Metal-Support Interactions. *Angew. Chem. Int. Ed.* **2015**, *54* (15), 4544–4548.
- (285) Dieterich, V.; Buttler, A.; Hanel, A.; Spliethoff, H.; Fendt, S. Power-to-Liquid via Synthesis of Methanol, DME or Fischer-Tropsch-Fuels: A Review. *Energy Environ. Sci.* **2020**, *13* (10), 3207–3252.
- (286) Xie, J.; Torres Galvis, H. M.; Koeken, A. C. J.; Kirilin, A.; Iulian Dugulan, A.; Ruitenbeek, M.; de Jong, K. P. Size and Promoter Effects on Stability of Carbon-Nanofiber-Supported Iron-Based Fischer-Tropsch Catalysts. ACS Catal. 2016, 6 (6), 4017–4024.
- (287) Wöll, C. The Chemistry and Physics of Zinc Oxide Surfaces. Prog. Surf. Sci. 2007, 82 (2–3), 55–120.
- (288) Larina, O. V.; Kyriienko, P. I.; Balakin, D. Y.; Vorokhta, M.; Khalakhan, I.; Nychiporuk, Y. M.; Matolín, V.; Soloviev, S. O.; Orlyk, S. M. Effect of ZnO on Acid-Base Properties and Catalytic Performances of ZnO/ZrO<sub>2</sub>-SiO<sub>2</sub> Catalysts in 1,3-Butadiene Production from Ethanol-Water Mixture. *Catal. Sci. Technol.* 2019, 9 (15), 3964–3978.
- (289) Prieto, G.; Shakeri, M.; de Jong, K. P.; de Jongh, P. E. Quantitative Relationship between Support Porosity and the Stability of Pore-Confined Metal Nanoparticles Studied on CuZnO/SiO<sub>2</sub> Methanol Synthesis Catalysts. *ACS Nano* **2014**, *8* (3), 2522–2531.
- (290) Pompe, C. E.; van Uunen, D. L.; van der Wal, L. I.; van der Hoeven, J. E. S.; de Jong, K. P.; de Jongh, P. E. Stability of Mesocellular Foam Supported Copper Catalysts for Methanol Synthesis. *Catal. Today* 2019, 334, 79–89.
- (291) Dalebout, R.; Visser, N. L.; Pompe, C. E.; de Jong, K. P.; de Jongh, P. E. Interplay between Carbon Dioxide Enrichment and Zinc Oxide Promotion of Copper Catalysts in Methanol Synthesis. *J. Catal.* 2020, 392, 150–158.
- (292) Divins, N. J.; Kordus, D.; Timoshenko, J.; Sinev, I.; Zegkinoglou, I.; Bergmann, A.; Chee, S. W.; Widrinna, S.; Karshoğlu, O.; Mistry, H.; Lopez Luna, M.; Zhong, J. Q.; Hoffman, A. S.; Boubnov, A.; Boscoboinik, J. A.; Heggen, M.; Dunin-Borkowski, R. E.; Bare, S. R.; Roldan Cuenya, B. Operando High-Pressure Investigation of Size-Controlled CuZn Catalysts for the Methanol Synthesis Reaction. Nat. Commun. 2021, 12, 1435.
- (293) Nakamura, J.; Fujitani, T.; Kuld, S.; Helveg, S.; Chorkendorff, I.; Sehested, J. Comment on "Active Sites

- for CO<sub>2</sub> Hydrogenation to Methanol on Cu/ZnO Catalysts." Science 2017. 357 (6354).
- (294) Herman, R. G.; Klier, K.; Simmons, G. W.; Finn, B. P.; Bulko, J. B. Catalytic Synthesis of Methanol from CO/H<sub>2</sub> I. Phase Composition, Electronic Properties, and Activities of the Cu/ZnO/M<sub>2</sub>O<sub>3</sub> Catalysts. *J. Catal.* **1979**, *56* (3), 407–429.
- (295) Günter, M. M.; Ressler, T.; Bems, B.; Büscher, C.; Genger, T.; Hinrichsen, O.; Muhler, M.; Schlögl, R. Implication of the Microstructure of Binary Cu/ZnO Catalysts for Their Catalytic Activity in Methanol Synthesis. *Catal. Lett.* **2001**, *71* (1–2), 37–44.
- (296) Fujitani, T.; Nakamura, J. The Effect of ZnO in Methanol Synthesis Catalysts on Cu Dispersion and the Specific Activity. Catal. Lett. 1998, 56, 119–124.
- (297) Fujitani, T.; Nakamura, I.; Uchijima, T.; Nakamura, J. The Kinetics and Mechanism of Methanol Synthesis by Hydrogenation of CO<sub>2</sub> over a Zn-Deposited Cu(111) Surface. Surf. Sci. 1997, 383 (2–3), 285–298.
- (298) Kühl, S.; Tarasov, A.; Zander, S.; Kasatkin, I.; Behrens, M. Cu-Based Catalyst Resulting from a Cu,Zn,Al Hydrotalcite-like Compound: A Microstructural, Thermoanalytical, and in Situ XAS Study. Chem. Eur. J. 2014. 20 (13), 3782–3792.
- (299) Sun, Q.; Zhang, Y.-L.; Chen, H.-Y.; Deng, J.-F.; Wu, D.; Chen, S.-Y. A Novel Process for the Preparation of Cu/ZnO and Cu/ZnO/Al<sub>2</sub>O<sub>3</sub> Ultrafine Catalyst: Structure, Surface Properties, and Activity for Methanol Synthesis from CO<sub>2</sub> + H<sub>2</sub>. J. Catal. 1997, 167 (1), 92–105.
- (300) Clausen, B. S.; Lengeler, B.; Rasmussen, B. S. X-Ray Absorption Spectroscopy Study of Cu-Based Methanol Catalysts. 1. Calcined State. J. Phys. Chem. 1985, 89 (11), 2319–2324.
- (301) Großmann, D.; Klementiev, K.; Sinev, I.; Grünert, W. Surface Alloy or Metal-Cation Interaction-The State of Zn Promoting the Active Cu Sites in Methanol Synthesis Catalysts. *ChemCatChem* **2017**, *9* (2), 365–372.
- (302) Großmann, D.; Dreier, A.; Lehmann, C.; Grünert, W. Methanol Synthesis over Cu-ZnO Aggregates Supported on Carbon Nanotubes. Appl. Catal. A 2015, 504, 351–360.
- (303) Grandjean, D.; Pelipenko, V.; Batyrev, E. D.; van den Heuvel, J. C.; Khassin, A. A.; Yurieva, T. M.; Weckhuysen, B. M. Dynamic Cu/Zn Interaction in SiO<sub>2</sub> Supported Methanol Synthesis Catalysts Unraveled by in Situ XAFS. *J. Phys. Chem. C* **2011**, *115* (41), 20175–20191.
- (304) Frei, E.; Gaur, A.; Lichtenberg, H.; Heine, C.; Friedrich, M.; Greiner, M.; Lunkenbein, T.; Grunwaldt, J.-D.; Schlögl, R. Activating a Cu/ZnO:Al Catalyst Much More than Reduction: Decomposition, Self-Doping and Polymorphism. ChemCatChem 2019, 11 (6), 1587–1592.
- (305) Tohji, K.; Udagawa, Y.; Mizushima, T.; Ueno, A. The Structure of the Cu/ZnO Catalyst by an in-Situ EXAFS Study. *J. Phys. Chem.* **1985**, *89* (26), 5671–5676.
- (306) Kleymenov, E.; Sa, J.; Abu-Dahrieh, J.; Rooney, D.; van Bokhoven, J. A.; Troussard, E.; Szlachetko, J.; Safonova, O.; Nachtegaal, M. Structure of the Methanol Synthesis Catalyst Determined by in Situ HERFD XAS and EXAFS. Catal. Sci. Technol. 2012, 2 (2), 373–378.
- van den Berg, M. W. E.; Polarz, S.; Tkachenko, O. P.; Klementiev, K. V.; Bandyopadhyay, M.; Khodeir,
   L.; Gies, H.; Muhler, M.; Grünert, W. Cu/ZnO Aggregates in Siliceous Mesoporous Matrices:
   Development of a New Model Methanol Synthesis Catalyst. J. Catal. 2006, 241 (2), 446–455.
- (308) La Fontaine, C.; Belin, S.; Barthe, L.; Roudenko, O.; Briois, V. ROCK: A Beamline Tailored for Catalysis and Energy-Related Materials from Ms Time Resolution to Mm Spatial Resolution. *Synchrotron Radiat. News* **2020**, *33* (1), 20–25.
- (309) Takesue, M.; Hayashi, H.; Smith Jr., R. L. Thermal and Chemical Methods for Producing Zinc Silicate

- (Willemite): A Review. Prog. Cryst. Growth Charact. Mater. 2009, 55 (3-4), 98-124.
- (310) Ravel, B.; Newville, M. ATHENA, ARTEMIS, HEPHAESTUS: Data Analysis for X-Ray Absorption Spectroscopy Using IFEFFIT. *J. Synchrotron Radiat.* **2005**, *12* (4), 537–541.
- (311) Yu, J.; Yang, M.; Zhang, J.; Ge, Q.; Zimina, A.; Pruessmann, T.; Zheng, L.; Grunwaldt, J.-D.; Sun, J. Stabilizing Cu<sup>+</sup> in Cu/SiO<sub>2</sub> Catalysts with a Shattuckite-like Structure Boosts CO<sub>2</sub> Hydrogenation into Methanol. ACS Catal. 2020, 10, 14694–14706.
- (312) Wang, L.; Lu, X.; Huang, Y. Determination of Zn Distribution and Speciation in Basic Oxygen Furnace Sludge by Synchrotron Radiation Induced μ-XRF and μ-XANES Microspectroscopy. X-Ray Spectrom. 2013, 42 (6), 423–428.
- (313) Rose, J.; Moulin, I.; Masion, A.; Bertsch, P. M.; Wiesner, M. R.; Bottero, J.-Y.; Mosnier, F.; Haehnel,
   C. X-Ray Absorption Spectroscopy Study of Immobilization Processes for Heavy Metals in Calcium
   Silicate Hydrates. 2. Zinc. Langmuir 2001, 17 (12), 3658–3665.
- (314) Veiga, J. P.; Figueiredo, M. O. A XANES Study on the Structural Role of Zinc in Ancient Tile Glazes of Portuguese Origin. *X-Ray Spectrom.* **2008**, *37* (4), 458.461.
- van den Berg, M. W. E.; Polarz, S.; Tkachenko, O. P.; Kähler, K.; Muhler, M.; Grünert, W. Dynamical Changes in the Cu-ZnO<sub>x</sub> Interaction Observed in a Model Methanol Synthesis Catalyst. *Catal. Lett.* **2009**. *128* (1–2), 49–56.
- (316) Okamoto, H. Supplemental Literature Review of Binary Phase Diagrams: Ag-Ni, Ag-Zr, Au-Bi, B-Ni, Co-Sb, Cu-Mn, Cu-Si, Cu-Zn, Fe-Zr, Li-Sb, Mg-Pu, and Si-Zr. *J. Phase Equilibria Diffus.* **2018**, *39*, 87–100.
- (317) Zhou, Y.; Jin, C.; Li, Y.; Shen, W. Dynamic Behavior of Metal Nanoparticles for Catalysis. *Nano Today* **2018**, *20*, 101–120.
- (318) Spencer, M. S. α-Brass Formation in Copper/Zinc Oxide Catalysts: II. Diffusion of Zinc in Copper and α-Brass under Reaction Conditions. *Surf. Sci.* **1987**, *192* (2–3), 329–335.
- (319) Guisbiers, G.; Buchaillot, L. Size and Shape Effects on Creep and Diffusion at the Nanoscale. *Nanotechnology* **2008**, *19* (43), 435701.
- (320) Koel, B. E.; Kim, J. Promoters and Poisons. In *Handbook of Heterogeneous Catalysis*; Wiley-VCH Verlag GmbH & Co. KGaA, 2008; pp 1593–1624.
- (321) Coadsorption, Promoters and Poisons; King, D. A., Woodruff, D. P., Eds.; Elsevier, 1993; Vol. 6.
- (322) Fichtl, M. B.; Schumann, J.; Kasatkin, I.; Jacobsen, N.; Behrens, M.; Schlögl, R.; Muhler, M.; Hinrichsen, O. Counting of Oxygen Defects versus Metal Surface Sites in Methanol Synthesis Catalysts by Different Probe Molecules. *Angew. Chem. Int. Ed.* 2014, 53 (27), 7043–7047.
- (323) Graciani, J.; Mudiyanselage, K.; Xu, F.; Baber, A. E.; Evans, J.; Senanayake, S. D.; Stacchiola, D. J.; Liu, P.; Hrbek, J.; Fernández Sanz, J.; Rodriguez, J. A. Highly Active Copper-Ceria and Copper-Ceria-Titania Catalysts for Methanol Synthesis from CO<sub>2</sub>. Science **2014**, 345 (6196), 546–550.
- (324) Martin, O.; Martín, A. J.; Mondelli, C.; Mitchell, S.; Segawa, T. F.; Hauert, R.; Drouilly, C.; Curulla-Ferré, D.; Pérez-Ramírez, J. Indium Oxide as a Superior Catalyst for Methanol Synthesis by CO<sub>2</sub> Hydrogenation. *Angew. Chem. Int. Ed.* **2016**, *55* (21), 6261–6265.
- (325) Pinto, F. M.; Suzuki, V. Y.; Silva, R. C.; La Porta, F. A. Oxygen Defects and Surface Chemistry of Reducible Oxides. Front. Mater. 2019, 6, 260.
- (326) Kattel, S.; Yan, B.; Yang, Y.; Chen, J. G.; Liu, P. Optimizing Binding Energies of Key Intermediates for CO<sub>2</sub> Hydrogenation to Methanol over Oxide-Supported Copper. J. Am. Chem. Soc. 2016, 138 (38), 12440–12450.

- (327) Qin, Y.; Fan, S.; Li, X.; Gan, G.; Wang, L.; Yin, Z.; Guo, X.; Tadé, M. O.; Liu, S. Peanut-Shaped Cu-Mn Nano-Hollow Spinel with Oxygen Vacancies as Catalysts for Low-Temperature NO Redution by CO. *ACS Appl. Nano Mater.* **2021**, *4* (11), 11969–11979.
- (328) Wang, G.; Mao, D.; Guo, X.; Yu, J. Methanol Synthesis from CO<sub>2</sub> Hydrogenation over CuO-ZnO-ZrO<sub>2</sub>-M<sub>x</sub>O<sub>y</sub> Catalysts (M=Cr, Mo and W). *Int. J. Hydrogen Energy* **2019**, *44* (8), 4197–4207.
- (329) Dasireddy, V. D. B. C.; Štefančič, N. S.; Huš, M.; Likozar, B. Effect of Alkaline Earth Metal Oxide (MO) Cu/MO/Al<sub>2</sub>O<sub>3</sub> Catalysts on Methanol Synthesis Activity and Selectivity via CO<sub>2</sub> Reduction. *Fuel* **2018**, 233, 103–112.
- (330) González-Arias, J.; Gonzálex-Cataño, M.; Elena Sánchez, M.; Cara-Jiménez, J.; Arellano-García, H. Valorization of Biomass-Derived CO<sub>2</sub> Residues with Cu-MnO<sub>x</sub> Catalysts for RWGS Reaction. *Renew. Energy* **2022**, *182*, 443–451.
- (331) Shi, X.; Lin, X.; Luo, R.; Wu, S.; Li, L.; Zhao, Z.-J.; Gong, J. Dynamics of Heterogeneous Catalytic Processes at Operando Conditions. *JACS Au* **2021**, *1* (12), 2100–2120.
- (332) Johnson, G. R.; Werner, S.; Bell, A. T. An Investigation into the Effects of Mn Promotion on the Activity and Selectivity of Co/SiO<sub>2</sub> for Fischer-Tropsch Synthesis: Evidence for Enhanced CO Adsorption and Dissociation. ACS Catal. 2015. 5 (10), 5888–5903.
- (333) Totarella, G.; Beerthuis, R.; Masoud, N.; Louis, C.; Delannoy, L.; de Jongh, P. E. Supported Cu Nanoparticles as Selective and Stable Catalysts for the Gas Phase Hydrogenation of 1,3-Butadiene in Alkene-Rich Feeds. *J. Phys. Chem. C* **2021**, *125* (1), 366–375.
- (334) Beerthuis, R.; de Rijk, J. W.; Deeley, J. M. S.; Sunley, G. J.; de Jong, K. P.; de Jongh, P. E. Particle Size Effects in Copper-Catalyzed Hydrogenation of Ethyl Acetate. *J. Catal.* **2020**, *388*, 30–37.
- (335) Smith, M. L.; Campos, A.; Spivey, J. J. Reduction Processes in Cu/SiO<sub>2</sub>, Co/SiO<sub>2</sub>, and CuCo/SiO<sub>2</sub> Catalysts. *Catal. Today* **2012**, *182* (1), 60–66.
- (336) Fierro, G.; Lo Jacono, M.; Inversi, M.; Porta, P.; Cioci, F.; Lavecchia, R. Study of the Reducibility of Copper in CuO-ZnO Catalysts by Temperature-Programmed Reduction. Appl. Catal. A 1996, 137 (2), 327\_348
- (337) Stynes, D. V. Misinterpretation of Isosbestic Points: Ambident Properties of Imidazole. *Inorg. Chem.* **1975**, *14* (2), 453–454.
- (338) Kofstad, P. Diffusional Transport in MnO. Solid State Ionics 1984, 12, 101–111.
- (339) Liu, Y.; Murata, K.; Inaba, M.; Takahara, I.; Okabe, K. Synthesis of Ethanol from Syngas over Rh/Ce<sub>1-x</sub>Zr<sub>x</sub>O<sub>2</sub> Catalysts. *Catal. Today* **2011**, *164* (1), 308–314.
- (340) Wang, J.; Liu, C.; Feng, J.; Cheng, D.; Zhang, C.; Yao, Y.; Gu, Z.; Hu, W.; Wan, J.; Yu, C. MOFs Derived Co/Cu Bimetallic Nanoparticles Embedded in Graphitized Carbon Nanocubes as Efficient Fenton Catalysts. *J. Hazard. Mater.* **2020**, *394*, 122567.
- (341) Guo, R.; Zhu, Y.; Cheng, X.; Li, J.; Crittenden, J. C. Efficient Degradation of Lomefloxacin by Co-Cu-LDH Activating Peroxymonosulfate Process: Optimization, Dynamics, Degradation Pathway and Mechanism. J. Hazard. Mater. 2020, 399, 122966.
- (342) Huang, Z.; Zhang, Y.; Li, H.; Liu, Y. A Novel Immobilized Cobalt(II)/Copper(II) Bimetallic Catalyst for Atom Transfer Radical Polymerization (ATRP) of Methyl Methacrylate. Appl. Catal. A 2007, 332 (2), 192–199.
- (343) Xu, W.; Chen, X.; Chen, J.; Jia, H. Bimetal Oxide CuO/Co<sub>3</sub>O<sub>4</sub> Derived from Cu Ions Partly-Substituted Framework of ZIF-67 for Toluene Catalytic Oxidation. *J. Hazard. Mater.* **2021**, *403*, 123869.
- (344) Lu, L.; Liu, Y.; Fan, J.; Wang, L.; Lin, Y.; Xu, D.; Dai, Z.; Han, M. Engineering Bimetal Cu, Co Sites on

- 3D N-Doped Porous Carbon Nanosheets for Enhanced Oxygen Reduction Electrocatalysis. *Chem. Commun.* **2020**, *56* (69), 10010–10013.
- (345) Turchanin, M. A.; Agraval, P. G. Phase Equilibria and Thermodynamics of Binary Copper Systems with 3d-Metals. V. Copper-Cobalt System. *Powder Metall. Met. Ceram.* **2007**, *46* (1–2), 77–89.
- (346) Nishizawa, T.; Ishida, K. The Co-Cu (Cobalt-Copper) System. *Bull. Alloy Phase Diagrams* **1984**, *5* (2), 161–165.
- Yeshchenko, O. A.; Dmitruk, I. M.; Alexeenko, A. A.; Dmytruk, A. M. Size-Dependent Melting of Spherical Copper Nanoparticles Embedded in a Silica Matrix. *Phys. Rev. B* 2007, 75, 085434.
- (348) Li, Z.; Yang, T.; Zhao, W.; Xu, T.; Wei, L.; Feng, J.; Yang, X.; Ren, H.; Wu, M. Structural Modulation of Co Catalyzed Carbon Nanotubes with Cu-Co Bimetal Active Center to Inspire Oxygen Reduction Reaction. ACS Appl. Mater. Interfaces 2019, 11 (4), 3937–3945.
- (349) Niu, W.; Shi, J.; Ju, L.; Li, Z.; Orlovskaya, N.; Liu, Y.; Yang, Y. Understanding Synergism of Cobalt Metal and Copper Oxide toward Highly Efficient Electrocatalytic Oxygen Evolution. ACS Catal. 2018, 8 (12), 12030–12040.
- (350) Feng, X.; Bo, X.; Guo, L. CoM(M=Fe,Cu,Ni)-Embedded Nitrogen-Enriched Porous Carbon Framework for Efficient Oxygen and Hydrogen Evolution Reactions. J. Power Sources 2018, 389, 249–259.
- (351) Chen, J.; Wang, Z.; Zhao, J.; Ling, L.; Zhang, R.; Wang, B. The Active Site of Ethanol Formation from Syngas over Cu<sub>4</sub> Cluster Modified MoS<sub>2</sub> Catalyst: A Theoretical Investigation. Appl. Surf. Sci. 2021, 540 (P1), 148301.
- (352) Chen, S. Te; Liu, Y. Y.; Chen, G. S. Ultrathin Cobalt-Alloyed Barrier Layers for Copper Metallization by a New Seeding and Electroless-Deposition Process. *Appl. Surf. Sci.* **2015**, *354* (part A), 144–147.
- (353) Shacham-Diamand, Y.; Lopatin, S. Integrated Electroless Metallization for ULSI. *Electrochim. Acta* **1999**, 44 (21–22), 3639–3649.
- (354) da Silva, A. G. M.; Rodrigues, T. S.; Haigh, S. J.; Camargo, P. H. C. Galvanic Replacement Reaction: Recent Developments for Engineering Metal Nanostructures towards Catalytic Applications. *Chem. Commun.* 2017, 53 (53), 7135–7148.
- (355) Lu, X.; Tuan, H.-Y.; Chen, J.; Li, Z.-Y.; Korgel, B. A.; Xia, Y. Mechanistic Studies on the Galvanic Replacement Reaction between Multiply Twinned Particles of Ag and HAuCl<sub>4</sub> in an Organic Medium. J. Am. Chem. Soc. **2007**, 129 (6), 1733–1742.
- (356) Nafria, R.; Genç, A.; Ibáñez, M.; Arbiol, J.; Ramírez de la Piscina, P.; Homs, N.; Cabot, A. Co-Cu Nanoparticles: Synthesis by Galvanic Replacement and Phase Rearrangement during Catalytic Activation, *Langmuir* 2016, 32 (9), 2267–2276.
- (357) Atkins, P. W.; Overton, T. L.; Rourke, J. P.; Weller, M. T.; Armstrong, F. A. Shriver & Atkins' Inorganic Chemistru. fifth.: W.H. Freeman and Company: New York, 2010.
- (358) Zhu, Y.; Ji, H.; Cheng, H.-M.; Ruoff, R. S. Mass Production and Industrial Applications of Graphene Materials. Natl. Sci. Rev. 2018, 5 (1), 90–101.
- (359) den Breejen, J. P.; Radstake, P. B.; Bezemer, G. L.; Bitter, J. H.; Frøseth, V.; Holmen, A.; de Jong, K. P. On the Origin of the Cobalt Particle Size Effects in Fischer-Tropsch Catalysis. *J. Am. Chem. Soc.* 2009, 131 (20), 7197–7203.
- (360) Gawande, M. B.; Goswami, A.; Felpin, F.-X.; Asefa, T.; Huang, X.; Silva, R.; Zou, X.; Zboril, R.; Varma,
   R. S. Cu and Cu-Based Nanoparticles: Synthesis and Applications in Catalysis. *Chem. Rev.* 2016, 116
   (6), 3722–3811.
- (361) van den Berg, R.; Parmentier, T. E.; Elkjær, C. F.; Gommes, C. J.; Sehested, J.; Helveg, S.; de Jongh, P.

- E.; de Jong, K. P. Support Functionalization to Retard Ostwald Ripening in Copper Methanol Synthesis Catalysts. *ACS Catal.* **2015**. *5* (7), 4439–4448.
- (362) Hong, J.; Marceau, E.; Khodakov, A. Y.; Gaberová, L.; Griboval-Constant, A.; Girardon, J.-S.; La Fontaine, C.; Briois, V. Speciation of Ruthenium as a Reduction Promoter of Silica-Supported Co Catalysts: A Time-Resolved in Situ XAS Investigation. *ACS Catal.* **2015**, *5* (2), 1273–1282.
- (363) Carenco, S.; Tuxen, A.; Chintapalli, M.; Pach, E.; Escudero, C.; Ewers, T. D.; Jiang, P.; Borondics, F.; Thornton, G.; Alivisatos, A. P.; Bluhm, H.; Guo, J.; Salmeron, M. Dealloying of Cobalt from CuCo Nanoparticles under Syngas Exposure. *J. Phys. Chem. C* **2013**, *117* (12), 6259–6266.
- (364) Egry, I.; Herlach, D.; Kolbe, M.; Ratke, L.; Reutzel, S.; Perrin, C.; Chatain, D. Surface Tension, Phase Separation, and Solidification of Undercooled Cobalt-Copper Alloys. *Adv. Eng. Mater.* **2003**, *5* (11), 819–823.

## **Acknowledgments / Dankwoord**

Dear reader.

Thank you that you have read my entire dissertation from the start until this very end (but you may have started reading this acknowledgments section as one of the first sections when you received this thesis). This is highly understandable as completing a PhD pathway is not an easy task and cannot be completed at your own. Many researchers, colleagues, friends, and family were needed to help, guide, and motivate me to deliver this final product. After each chapter I already wrote several words for the persons who significantly helped me for that particular chapter, but here I would like to spotlight everyone.

Als eerste zou ik graag mijn promotor *Petra* willen bedanken voor de kans dat ik onder haar supervisie mijn onderzoek heb mogen uitvoeren. Je bent altijd enthousiast over alles en iedereen en dat weet je ook altijd goed over te dragen, zowel als promotor die mij begeleidde als hoogleraar die college gaf. Niet alleen heb je me veel geholpen bij het schrijven van artikelen en het op de rails houden van mijn focus, maar bijvoorbeeld ook met de 'beam trip' naar SOLEIL waarbij we hele mooie resultaten hebben behaald.

Daarnaast was *Krijn* mijn tweede promotor die ik ook graag in het zonnetje wil zetten. Je was van mening dat er geen twee kapiteins op één schip kunnen staan (daar ben ik het ook helemaal mee eens), en hield je daarom langs de zijlijn in mijn project. Daarbij gaf je me wel heel erg fijn, verfrissend en goed advies. Ik heb altijd enorm genoten van al je anekdotes en verhalende beschrijvingen, en dat betuigt dan ook maar weer eens de sterke overbrengingskracht die je hebt bij het geven van colleges.

The Flowrence®, the multi-reactor system, was the setup I frequently used in my research, and *Rolf* and technician *Jan Willem* helped me a lot with starting up the first experiments. Later *Nienke*, *Laura*, and *Oscar* joined the 'Flowrence-2 team' and together we made a lot of data (Excel sheets of many, many megabytes). I would like to thank you all for keeping such a complicated apparatus up

and running (for most of the time), and for cheering each other up if something was not initially working the way we expected.

Electron microscopy was an important characterization technique used in my dissertation for which *Savannah*, *Nienke*, *Nynke*, *Mark*, *Lars*, *Jessi*, and *Min* but also technicians *Hans* and *Chris* helped me a lot, especially for making colorful EDX maps showing the metal distribution in my catalysts on the nanoscale. Here, I would like to thank *Giorgio* as well for making ultrathin slices of catalysts embedded in an epoxy resin, resulting in beautiful microscopy images.

'Time-resolved X-ray absorption spectroscopy (XAS), simultaneously at two K-edges and at high temperature and pressure' is a mouth full of words, which implies that this is a state-of-the-art technique and that is actually the case. *Baira* and *Jessi* introduced me to this synchrotron-based XAS technique at the DUBBLE beamline at the ESRF in Grenoble. Also, *Eric Marceau* and his 'beam team' from the University of Lille showed me how measuring catalysts at a synchrotron is like at the AILES beamline at the SOLEIL synchrotron near Paris. Thank you all.

During my PhD project we planned a trip to the ROCK beamline at the SOLEIL synchrotron to perform the just mentioned complicated XAS experiments, which was made possible by the on-site beamline scientists *Camille La Fontaine* and *Valérie Briois*. The people who helped me with obtaining the data (the 'beam team') were *Petra*, *Laura*, and *Giorgio* from the Utrecht University and *Xavier Carrier* from the Sorbonne University. All the raw data had to be analyzed for which I would really like to thank *Camille* for the initial data conversion at SOLEIL and *Laura*, *Florian*, *Giorgio*, *Ad*, and *Frank* for the in-depth analysis. This successful beam trip resulted in sufficient data that is used in two chapters of this dissertation, which could never have been achieved without all your help for which I would like to thank you all.

Collaborations connect people. *Benjamin Mockenhaupt* and *Fatih Özcan* from the former group of *Malte Behrens* at the University of Duisburg-Essen worked together with me using the Flowrence® in search for methanol and higher alcohols with their own catalysts, which was really inspiring, and I always enjoyed working together with you. I am also very grateful that I could measure the porosity of polymer-based materials for *Sjaak Jong*, a very fruitful collaboration which resulted in two papers. Thank you!

Het vele werk had nooit kunnen slagen zonder alle technische ondersteuning van de technici. Daarvoor zou ik in het bijzonder de technici *Jan Willem, Dennie, Hans, Pascal* en *Ad* willen bedanken voor hun hulp met het onderhoud aan de Flowrence®, aan de apparatuur voor materiaalkarakerisatie en aan de elektronenmicroscopen, met het plaatsen en regelen van bestellingen, met het veilig leren werken in het lab en alle andere technische zaken. Ook technici *Ad Mens, Fouad, Herrick, Jochem, Joris, Marjan, Oscar* en *Ramon* zou ik willen bedanken voor hun

hulp en dat ze altijd klaar stonden voor vragen. Daarnaast waren de administratieve zaken van het secretariaat zeer goed geregeld en dat had zeker niet gekund zonder *Dymph*, *Ilonka* en *Sylvia*.

Een onderdeel van het doen van een PhD is het geven van onderwijs, waaronder dus ook het begeleiden van studenten in hun project valt. Veel van het werk van *Willem* en *Brecht* op de galvanische vervanging als preparatiemethode voor katalysatoren zijn uiteindelijk in hoofdstuk 5 terecht gekomen: dank jullie wel voor al jullie werk in jullie projecten. Ook de katalysatoren gemaakt door *Nienke* als masterstudente zijn gebruikt in hoofdstuk 3, en dat mooie werk is niet onopgemerkt gebleven want je bent een van mijn collega's geweest. Tenslotte heb ik erg fijn samengewerkt met studenten *Robin*, *Yevkeni* en *Liselotte* en ik hoop dat ik jullie veel heb kunnen leren.

Next to all the hard work in the labs, which goes hand in hand with doing a PhD, I needed to have a daily lunch. So, we started to have a daily lunch group, which finally consisted of *Laurens*, *Koen*, *Roozbeh*, *Maarten*, *Bas*, *Laura*, *Giorgio*, *Francesco*, *Valerio*, *Oscar*, *Savannah*, *Christia*, *Silvia*, and *Abi*. Many times, I brought a special loaf of bread I got from the penguin at the bakery, which was always quite some fun. Thank you all for the fun times outside of the labs, not only during lunch but also with the nights going out.

I already mentioned many names in this section, but the group was even much larger. I always enjoyed working in this cohesive group, where everyone was easily approachable and functioned at the nearly the same level of hierarchy. Many of my other colleagues involved *Anne-Eva*, *Baira*, *Carlos*, *Christa*, *Claudi*, *Guusje*, *Henrik*, *Ioanis*, *Jeroen*, *Jogchum*, *Johan*, *Jongkook*, *Jovana*, *JX*, *Kai*, *Kris*, *Laura de Kort*, *Lennart*, *Lisette*, *Luc*, *Luke*, *Maaike*, *Mahnaz*, *Marisol*, *Matt*, *Miguel*, *Nazila*, *Nikos*, *Nynke*, *Oscar Brandt Corstius*, *Peter Bramwell*, *Peter Ngene*, *Petra Keijzer*, *Roy*, *Sander*, *Suzan*, *Tom*, *Wouter*, and *Yuang*. Thank you all for the wonderful time at this group, both in the labs for questions as well as during after-work drinks.

Het heeft even geduurd voordat mijn proefschrift volledig en wel klaarlag op de stoep, en daarvoor waren veel motivatieoppeppers nodig geweest. *Mama*, *papa* en mijn broer *Martijn* (ja, ik noem je nu geen broertje) zijn altijd enthousiast en vooral trots op mij dat ik het überhaupt zo ver heb geschopt. Vaak als ik thuiskwam hoorde ik: "En is je katalysator al af? Doet-ie het al? Wat heb je gemaakt?". Een promotie doen is erg ongrijpbaar, omdat je eigenlijk niet echt iets heel fysieks maakt (al maakte ik wel katalysatoren in een lab). Het gaat dan ook vooral om het bijeenbrengen van kennis en dit vastleggen op ('digitaal') papier, iets wat nu eenmaal weinig letterlijk 'houvast' geeft. Je promotieonderzoek uitleggen is al niet eenvoudig en zeker niet als het over best wel fundamentele chemie gaat. Vaak legde ik mijn onderzoek aan jullie uit alsof ik vanuit bomen alcohol maakte met behulp van Phillip Cocu. Nu is er uiteindelijk wel een eindproduct op tafel en is 'de katalysator (ofwel mijn promotieonderzoek)' klaar en afgesloten.

Zeuren, wat heb ik dat veel gedaan. Jaar in, jaar uit heeft mijn vriendin *Emma* dit van mij moeten aanhoren, maar ik ben o zo blij en trots op haar dat ze me telkens weer die motivatie gaf om door te zetten. Samen hebben we ook veel moois meegemaakt, zoals een mooie reis door Sri Lanka, lekker met de auto toeren naar Frankrijk en Italië, en vele stedentrips. Ondertussen hebben we een prachtige koopwoning in de wacht weten te slepen in Rosmalen en ik kijk er helemaal naar uit wat voor moois de toekomst voor in ons petto heeft. Dankjewel! En ik hou van je.

# List of publications and presentations

#### This thesis is partially based on the following publications

Dalebout, R.; Visser, N.L.; Pompe, C.E.; de Jong, K.P.; de Jongh, P.E. Interplay between Carbon Dioxide Enrichment and Zinc Oxide Promotion of Copper Catalysts in Methanol Synthesis. *J. Catal.* **2020**, *392*, 150-158. (chapter 2)

Dalebout, R.; Barberis L.; Totarella, G.; Turner, S.J.; La Fontaine, C.; de Groot, F.M.F.; Carrier, X.; van der Eerden, A.M.J.; Meirer, F.; de Jongh, P.E. Insight into the Nature of the ZnO<sub>x</sub> Promoter during Methanol Synthesis. *ACS Catal.* **2022**, *12*, 6628-6639. (chapter 3)

Dalebout, R.; Barberis L.; Visser, N.L.; van der Hoeven, J.E.S.; van der Eerden, A.M.J.; Stewart, J.A.; Meirer, F.; de Jong, K.P.; de Jongh, P.E. Manganese Oxide as a Promoter for Copper Catalysts in CO<sub>2</sub> and CO Hydrogenation, *ChemCatChem*, **2022**, *accepted*. (chapter 4)

#### Other publications

Jong, J.A.W.; Guo, Y.; Veenhoven, C.; Moret, M.-E.; van der Zwan, J.; Paioni, A.L.; Scheiner, K.C.; Dalebout, R.; van Steenbergn, M.J.; Verhaar, M.C.; Smakman, R.; Hennink, W.E.; Gerritsen, K.G.F.; van Nostrum, C.F. Phenylglyoxaldehyde-Functionalized Polymeric Sorbents for Urea Removal from Aqueous Solutions. *ACS Appl. Polym. Mater.* **2020**, *2* (2), 515-527.

Jong, J.A.W.; Guo, Y.; Hazenbrink, D.; Douka, S.; Verdijk, D.; van der Zwan, J.; Houben, K.; Baldus, M.; Scheiner, K.C.; Dalebout, R.; Verhaar, M.C.; Smakman, R.; Hennink, W.E.; Gerritsen, K.G.F.; van Nostrum, C.F. A Ninhydrin-Type Urea Sorbent for the Development of a Wearable Artificial Kidney. *Macromol. Biosci.* **2020**, *20* (3), 1900396.

Guadix-Montero, S.; Alshammari, H.; Dalebout, R.; Nowicka, E.; Morgan, D.J.; Shaw, G.; He, Q.; Sankar, M. Deactivation Studies of Bimetallic AuPd Nanoparticles Supported on MgO during Selective Aerobic Oxidation of Alcohols. *Appl. Catal. A* **2017**, *546*, 58-66.

#### **Oral presentations**

Dalebout, R.; de Jong, K.P.; de Jongh, P.E. The Effect of CO<sub>2</sub> Concentration and ZnO<sub>x</sub> Promotion on Cu/C-Catalyzed Methanol Synthesis, 17<sup>th</sup> International Congress on Catalysis (ICC), San Diego (USA), 14-19 June **2020**, *cancelled conference*.

Dalebout, R.; de Jong, K.P.; de Jongh, P.E. The Effect of CO<sub>2</sub> Concentration and ZnO<sub>x</sub> Promotion on Cu/C-Catalyzed Methanol Synthesis, XXIst Netherlands' Catalysis and Chemistry Conference (NCCC), Noordwijkerhout (the Netherlands), 2-4 March **2020**.

Dalebout, R.; de Jong, K.P.; de Jongh, P.E. The Effect of  $CO_2$  Concentration and  $ZnO_x$  Promotion on Cu/C-Catalyzed Methanol Synthesis, CHemistry As INnovating Science (CHAINS) conference, Veldhoven (the Netherlands), 10-11 December **2019**.

Dalebout, R.; de Jong, K.P.; de Jongh, P.E. The Effect of  $ZnO_x$  Promotion and  $CO_2$  on Cu/C-Catalyzed Methanol Synthesis, 14<sup>th</sup> European Congress on Catalysis (EuropaCat), Aachen (Germany), 18-23 August **2019**.

Dalebout, R.; de Jong, K.P.; de Jongh, P.E. The Effect of  $ZnO_x$  Promotion and  $CO_2$  on Cu/C-Catalyzed Methanol Synthesis,  $8^{th}$  Asia Pacific Congress on Catalysis (APCAT), Bangkok (Thailand), 4-7 August **2019**.

#### **Poster presentations**

Dalebout, R.; Krans, N.A.; de Jong, K.P.; de Jongh, P.E. The Effect of ZnO<sub>x</sub> Promotion and Syngas Composition on Cu/C-Catalyzed Methanol Synthesis, XX<sup>st</sup> Netherlands' Catalysis and Chemistry Conference (NCCC), Noordwijkerhout (the Netherlands), 4-6 March **2019**.

Dalebout, R.; de Jong, K.P.; de Jongh, P.E. Carbon-Supported CuCo Catalysts for CO Hydrogenation to Higher Alcohols, XIX<sup>st</sup> Netherlands' Catalysis and Chemistry Conference (NCCC), Noordwijkerhout (the Netherlands), 5-7 March **2018**.

### Curriculum vitae

Remco Dalebout was born on the 25<sup>th</sup> of September 1993 in Gorinchem, the Netherlands. After he completed his preuniversity education (vwo) at the Oosterlicht College at the Vianen and Nieuwegein locations, he started his bachelor studies in chemistry at the Utrecht University in 2011. Within three years he completed his thesis named 'Valorization of lignin-derived catechol by iron(III)-catalyzed deoxygenation and ethenolysis' in the Inorganic Chemistry and Catalysis group under supervision of Prof. Dr. P.C.A. Bruijnincx, thereby obtaining his bachelor's degree with a *cum laude* 



distinction in 2014. He continued with his master studies *Nanomaterials: Chemistry and Physics* at the Utrecht University and investigated the stability and promoter effects of carbon-supported, copper-based catalysts in the Inorganic Chemistry and Catalysis group under supervision of Prof. Dr. P.E. de Jongh. During these two years he also visited the Cardiff University and performed a project entitled 'Solvent-free selective oxidation of benzyl alcohol with molecular oxygen over palladium-based bimetallic catalysts' in the group of Dr. M. Sankar. Meanwhile, he conceptualized and organized student-for-a-day programs for future chemistry students at the Utrecht University. He finished his master's degree with a *cum laude* distinction in 2016.

In October 2016, Remco started as a PhD researcher in the group of Materials Chemistry and Catalysis under supervision of Prof. Dr. P.E. de Jongh and Prof. Dr. Ir. K.P. de Jong. He worked on understanding the effects of the catalyst support and the zinc-, manganese-, and cobalt-based promoters on copper catalysts used for hydrogenation reactions. During his PhD research he investigated and identified relationships between catalyst properties and performance, delivering opportunities to optimize industrial catalyst design. He also taught, supervised, and motivated bachelor and master students during courses and laboratory projects. Part of the work discussed in this thesis has been published in peer-reviewed journals and has been presented in international conferences.

In his free time Remco likes cycling, cooking, and spending time in his garden. Since June 2021 he works as a staff member in the group of Materials Chemistry and Catalysis.

